

6-25-2010

Fluvial sedimentation in continental half-graben basins

Sean Connell

Follow this and additional works at: https://digitalrepository.unm.edu/eps_etds

Recommended Citation

Connell, Sean. "Fluvial sedimentation in continental half-graben basins." (2010). https://digitalrepository.unm.edu/eps_etds/12

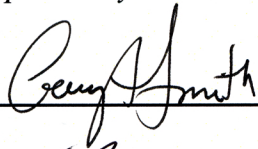
This Dissertation is brought to you for free and open access by the Electronic Theses and Dissertations at UNM Digital Repository. It has been accepted for inclusion in Earth and Planetary Sciences ETDs by an authorized administrator of UNM Digital Repository. For more information, please contact disc@unm.edu.

Sean David Connell
Candidate

Earth and Planetary Sciences
Department

This dissertation is approved, and it is acceptable in quality and form for publication:

Approved by the Dissertation Committee:

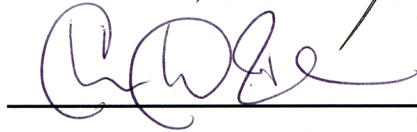


, Chairperson









**FLUVIAL SEDIMENTATION IN CONTINENTAL
HALF-GRABEN BASINS**

BY

SEAN DAVID CONNELL

B.S. Geology, California State University, Northridge, 1988
M.S. Geology, University of California, Riverside, 1995

DISSERTATION

Submitted in Partial Fulfillment of the
Requirements for the Degree of

**Doctor of Philosophy
Earth and Planetary Sciences**

The University of New Mexico
Albuquerque, New Mexico

May, 2010

©2010, Sean David Connell

ACKNOWLEDGEMENTS

The completion of this dissertation was supported by the New Mexico Bureau of Geology and Mineral Resources (Peter A. Scholle, director), the National Science Foundation (EAR-0344146), the New Mexico Geological Society, and the Saint Anthony Falls Industrial Consortium, consisting of Chevron, Conoco-Phillips, Exxon-Mobil Upstream Research Corporation, Japan Oil, Gas and Metals National Corporation (JOGMEC), and Royal-Dutch Shell Corporation. Although each chapter contains separate acknowledgments, I would like to thank those who provided valuable assistance, advice, and technical expertise for the completion of this project.

I thank my dissertation committee, Gary Smith, Chris Paola, John Geissman, Grant Meyer, and Laura Crossey, for their advice and guidance. In particular, I would like to thank Gary Smith, Chris Paola, and Wonsuck Kim for sharing their insights on natural and experimental sedimentary systems. Dr. Kim also provided valuable assistance during the design, execution, and analysis of the physical stratigraphy experiments. I am also grateful to Jim Mullin, Chris Ellis, and Dick Christopher for their help with the experiments at the Saint Anthony Falls Laboratory.

Geologic mapping and $^{40}\text{Ar}/^{39}\text{Ar}$ age determinations were supported by the New Mexico Bureau of Geology and Mineral Resources, and the New Mexico Statemap Program component of the National Cooperative Geologic Mapping Act of 1992, which is administered by the U.S. Geological Survey. Volcanic samples were analyzed at the New Mexico Geochronological Research Laboratory (Matt Heizler, William C. McIntosh, Rich Esser, and Lisa Peters). Analyses of magnetic properties were conducted at the University of New Mexico Paleomagnetic and Rock Magnetic Laboratory (John Geissman and Tim Wawrzyniec). Holly Buehler, Teresa Connell, Linda Donohoo-Hurley, Scott Muggleton, Travis Naibert, Mitchell Reese, and Kate Ziegler helped with the acquisition, preparation, and analysis of paleomagnetic specimens. Rita Case helped me to keep my references straight. The Pueblos of Cochiti, Isleta, Jemez, Sandia, San Felipe, Santo Domingo, and Zia graciously provided access to tribal lands. Ivan Benavidez, King Brothers Ranch, Village of Los Lunas, New Mexico State Land Office, and the former Westland Corporation provided access rights to field sites.

DEDICATION

This dissertation is dedicated to my three Muses: Teresa, Kathleen, and Harriet.

**FLUVIAL SEDIMENTATION IN CONTINENTAL
HALF-GRABEN BASINS**

BY

SEAN DAVID CONNELL

ABSTRACT OF DISSERTATION

Submitted in Partial Fulfillment of the
Requirements for the Degree of

**Doctor of Philosophy
Earth and Planetary Sciences**

The University of New Mexico
Albuquerque, New Mexico

May, 2010

FLUVIAL SEDIMENTATION IN CONTINENTAL HALF-GRABEN BASINS

by

Sean David Connell

B.S., Geology, California State University, Northridge, 1988

M.S., Geology, University of California, Riverside, 1995

Ph.D., Earth and Planetary Sciences, University of New Mexico, 2010

ABSTRACT

The stratigraphic architecture of intracontinental rift basins is defined by a dynamic relationship between depositional belts associated with the basin floor and flanking tributary streams on the piedmont. Spatiotemporal distributions of these deposits are sensitive to basin geometry, subsidence rate, and discharge. Understanding how these depositional belts respond to allogenic forcing is examined using experimental and field approaches.

Physical experiments focused on the geomorphic evolution of drainage and the resulting stratigraphic architecture in an asymmetrically subsiding basin based on the form of a simple half graben with four interacting supply points of sediment and water that produced an axial fan and longitudinal channel flanked by transverse fans. Imposition of various combinations of lateral and axial sediment flux showed that the locations and widths of the deposits were controlled by relative sediment discharges and not by the location of the subsidence maximum. Except during the highest of axial sediment discharges in the experiment, the axial drainage was dominated by transverse sources through toe cutting. Footwall fans persisted under conditions of high axial-

sediment discharge, aided by topographic inheritance and steeper deposit slopes. The hanging-wall fan responded to changes in sediment discharge more slowly than the footwall.

Field comparisons focused on a study of Plio-Pleistocene deposits in the tectonically active Albuquerque Basin of New Mexico. Deposits on the distal hanging-wall ramp overlapped a widespread Miocene erosion surface, burying it by 3.0 Ma. These deposits coarsened after 2.6 Ma, forming a broad sheet of amalgamated channel deposits that prograded into the basin until 1.8 Ma. Axial-river deposition focused near the eastern master-fault system until piedmont deposits prograded away from the basin border after 1.8 Ma. Basin-fill deposition ceased when the axial river began incising shortly after 0.8 Ma. The asynchronous progradation of coarse-grained, margin-sourced detritus may be a consequence of half-graben basin shape that promoted extensive bypass of sediment. Integration of the axial drainage and development of this Plio-Pleistocene sequence likely formed as a result of increased discharge due to late Pliocene and early Pleistocene climatic changes.

TABLE OF CONTENTS

ACKNOWLEDGEMENTS.....	iv
DEDICATION.....	v
ABSTRACT.....	vii
TABLE OF CONTENTS.....	ix
LIST OF FIGURES.....	xi
LIST OF TABLES.....	xiv
LIST OF APPENDICES.....	xv
PREFACE.....	xvi
CHAPTER 1. FLUVIAL SEDIMENTATION IN CONTINENTAL HALF-GRABEN BASINS	
BASINS.....	1
Introduction.....	1
Approach and Methods.....	8
Chapter References.....	11
CHAPTER 2. CLIMATIC CONTROLS ON NONMARINE DEPOSITIONAL SEQUENCES IN THE ALBUQUERQUE BASIN, RIO GRANDE RIFT, NORTH-CENTRAL NEW MEXICO	
Chapter Abstract.....	17
Introduction.....	18
Study Area.....	22
Geochronology.....	29
⁴⁰ Ar/ ³⁹ Ar Methods and Results.....	29
Paleomagnetic Methods.....	39
Rock-Magnetic Results.....	42
Paleomagnetic Results.....	54
Stratigraphy.....	59
Miocene Deposits.....	62
Ceja Formation.....	68
<i>Geochronology</i>	73
Sierra Ladrones Formation.....	82
<i>Geochronology</i>	84
Plio-Pleistocene Deposits.....	87
Sediment-Accumulation Rates.....	90
Paleosurfaces.....	95
Alluvial Sequences.....	100
Miocene Sedimentation.....	101
Plio-Pleistocene Sedimentation and Axial-drainage Development.....	102
Depositional Patterns.....	105
Climatic Implications.....	108
Chapter Summary and Conclusions.....	111
Chapter Acknowledgments.....	113
Chapter References.....	114
CHAPTER 3. EXPERIMENTAL STUDY OF INTERACTING DRAINAGES IN A SEDIMENTARY BASIN: SURFACE MORPHOLOGY	
Chapter Abstract.....	131

Introduction	133
Methods	136
Experimental EarthScape Facility.....	136
Experimental Design.....	138
Sediment	143
Experimental Stages.....	143
Data Collection	145
Surface Morphology	148
Axial Drainage.....	154
Transverse Drainage	157
Axial-Transverse Drainage Interactions	162
Sediment Mass Balance.....	165
Model Results	168
Discussion.....	172
Axial-Drainage Morphology.....	172
Transverse-Fan Morphology.....	177
Drainage Interactions.....	180
Chapter Conclusions.....	181
Chapter Acknowledgements.....	183
Chapter References.....	183
CHAPTER 4. EXPERIMENTAL STUDY OF INTERACTING DRAINAGES IN A SEDIMENTARY BASIN: STRATIGRAPHIC ARCHITECTURE AND SEDIMENT TRANSPORT	191
Chapter Abstract.....	191
Introduction	192
Methods	194
Experimental EarthScape Facility.....	194
Experimental Design and Data Collection.....	194
Image Analysis.....	199
Stratigraphy	201
Isochrons	208
Depositional patterns	210
Sediment Mass Balance	211
Intra-stage Variations.....	216
Grain Composition	221
Discussion.....	232
Chapter Conclusions.....	241
Chapter Acknowledgements.....	242
Chapter References.....	243
CHAPTER 5. CONCLUSIONS	248
Conclusions	248
Research Directions.....	252
Chapter References.....	254
APPENDIX.....	256

LIST OF FIGURES

Figure 1.1. Diagram illustrating major depositional belts within half-graben basins.....	1
Figure 1.2. Results of numerical simulations.....	4
Figure 1.3. Basins of the Rio Grande in Colorado and New Mexico	7
Figure 1.4. Schematic plan-view map and cross sections of the experimental setup	10
Figure 2.1. Diagram illustrating major depositional systems	19
Figure 2.2. Basins of the Rio Grande in Colorado and New Mexico	24
Figure 2.3. Shaded-relief map of the central and northern parts of the Albuquerque Basin	25
Figure 2.4. Simplified geologic cross section A-A'	27
Figure 2.5. Age and correlation of stratigraphic units in the Albuquerque Basin	28
Figure 2.6. Summary of $^{40}\text{Ar}/^{39}\text{Ar}$ age determinations (N = 32) for the unit of San Clemente, Ceja, Cochiti, Arroyo Ojito, and Cerro Conejo Formations.....	37
Figure 2.7. Summary of $^{40}\text{Ar}/^{39}\text{Ar}$ age determinations (N = 46) for the Lava Creek B in an inset terrace of the Rio Grande (Qr), Sierra Ladrones Formation, and a Miocene axial-river deposit	38
Figure 2.8. Photographs of a weakly cemented sample site and prepared specimens....	41
Figure 2.9. Box and whisker plots of median, quartile, and outlier values of bulk magnetic susceptibility.....	44
Figure 2.10. Normalized demagnetization response curves	46
Figure 2.11. Normalized demagnetization response curves for specimens.....	47
Figure 2.12. Plots showing thermal demagnetization response curves for three-component isothermal remanent magnetization	48
Figure 2.13. Examples of alternating-field and thermal demagnetization results	52
Figure 2.14. Equal-area projections showing site and grand-mean directions for accepted sites	57
Figure 2.15. Stratigraphic fence diagram, illustrating correlations of measured stratigraphic sections.....	60
Figure 2.16. Stratigraphic fence diagram, illustrating correlations to the GPTS.....	61
Figure 2.17. Simplified geologic map along part of the Ceja del Rio Puerco and western margin of the Albuquerque Basin	65
Figure 2.18. Simplified geologic map of the eastern part of the San Felipe volcanic field and eastern margin of the Albuquerque Basin	70
Figure 2.19. Photographs of deposits in the study area.	71
Figure 2.20. Lithostratigraphy and magnetic polarity stratigraphy of the CDRP3 stratigraphic section	75
Figure 2.21. Lithostratigraphy and magnetic polarity stratigraphy of County Line (CDRP-CL) stratigraphic section.....	76
Figure 2.22. Lithostratigraphy and magnetic polarity stratigraphy of Zia Fault (ZF) stratigraphic section	77
Figure 2.23. Geology of El Cerro de Los Lunas.....	78
Figure 2.24. Lithostratigraphy and magnetic polarity stratigraphy of the Los Lunas volcano (LLV) composite section.....	80
Figure 2.25. Geology of Tijeras Arroyo and Hell Canyon Wash	86

Figure 2.26. Lithostratigraphy and magnetic-polarity stratigraphy of CSA and PLU composite sections	89
Figure 2.27. Stratigraphic fence diagram, illustrating physical correlations of stratigraphic sections in Tijeras Arroyo.....	90
Figure 2.28. Sediment accumulation rates and major depositional events since late Miocene time	94
Figure 2.29. Chronostratigraphic diagram.....	97
Figure 2.30. Schematic cross sections (left) and paleogeographic diagrams (right) illustrating the history of subsidence and sedimentation in the Albuquerque Basin since middle Miocene time (14-1 Ma).....	104
Figure 3.1. Diagram illustrating major depositional belts	134
Figure 3.2. Schematic plan-view map and cross sections of the experimental setup, depicting dimensions of the tank and locations of sediment input points	137
Figure 3.3. Variables for XES06 stages and substages.....	140
Figure 3.4. Orthorectified overhead photographic images	147
Figure 3.5. Harmonic-mean positions of the transverse hanging-wall and footwall fans and approximate shoreline position	149
Figure 3.6. Harmonic-mean positions of the shoreline.....	150
Figure 3.7. Mean fan areas and centroid locations (from Figure 3.5), and contour maps of basement depth at the end of each experimental stage.....	153
Figure 3.8. Plots of dimensionless deposit-surface slope (vertical/horizontal) versus deposit area and sediment discharge determined from topographic scans	155
Figure 3.9. Maps of (arithmetic) mean flow occupation	156
Figure 3.10. Overhead photographic images illustrating the axial river, hanging-wall (HW) fan, and the upstream (FW-1) and downstream (FW-2) footwall fans during the experiment	158
Figure 3.11. Circular histograms (rose diagrams) of mean flow-directions.....	160
Figure 3.12. Plots of mean width $\pm 2\sigma$ and maximum width of the axial river versus basin distance.....	163
Figure 3.13. Definition diagram of circular fan boundary used to determine fan area and sediment volume	166
Figure 3.14. Spline-interpolated circular areas modeled for hypothetical semi-circular fans.....	170
Figure 3.15. Plots illustrating mapped and model deposit areas.....	171
Figure 3.16. Shaded-relief map of upper Rio Grande drainage.....	173
Figure 3.17. Simplified geologic map of the Albuquerque Basin	176
Figure 3.18. Circular histograms	179

Figure 4.1. Schematic plan-view map and cross sections of the setup for XE06	196
Figure 4.2. Parameters used for XES06 experimental stages	198
Figure 4.3. Shaded-relief block diagrams	202
Figure 4.4. Images of strike slice ($x = 2500$ mm), synthetic dip slice ($y = 2000$ mm)	204
Figure 4.5. Natural-color images of two regions of strike slice $x = 2500$ mm	205
Figure 4.6. Outlines of strike sections down-basin (x -axis).....	206
Figure 4.7. Harmonic mean positions of mapped hanging-wall and footwall fans overlain on isopach maps	213
Figure 4.8. Summary plots of sediment volume and sediment discharge	214
Figure 4.9. Bar graphs illustrating sediment volume and experimental stage	215
Figure 4.10. Intra-stage variations in sediment volume and shoreline	217
Figure 4.11. Axial-transverse boundaries interpreted for two cross sections ($x = 2500$ and $x = 3400$ mm, see inset map), and chronostratigraphic diagrams	218
Figure 4.12. Color distribution of coal, sand, and color-coded sand	222
Figure 4.13. Images of strike section at $x = 1600$ mm	225
Figure 4.14. Images of strike section at $x = 2500$ mm	226
Figure 4.15. Images of strike section at $x = 3400$ mm	227
Figure 4.16. Color-enhanced images	228
Figure 4.17. Stacked column plot of mapped coal, sand and colored sand	229
Figure 4.18. Axial- and transverse-sourced sediment.....	231
Figure 4.19. Generalized geologic cross sections.....	237
Figure 4.20. Detrital sandstone compositions.....	239

LIST OF TABLES

Table 2.1. Summary of age determinations from published sources.....	31
Table 2.2. Summary of $^{40}\text{Ar}/^{39}\text{Ar}$ RFIH results.....	32
Table 2.3. Summary of $^{40}\text{Ar}/^{39}\text{Ar}$ SCLF results.....	33
Table 2.4. Statistical parameters for class I sites.....	56
Table 2.5. Statistical parameters for rotated class I sites.....	58
Table 3.1. Summary of XES06 discharge parameters.....	142
Table 3.2. Summary of XES06 results.....	151
Table 3.3. Summary of XES06 deposit areas.....	169
Table 4.1. Summary of XES06 experimental parameters.....	196
Table 4.2. Descriptive statistics of sediment size.....	198
Table 4.3. Summary of mapped and model volume.....	212
Table 4.4. Descriptive statistics of deposit color.....	221

LIST OF APPENDICES

Appendix A. Rock-magnetic data for Chapter 2	Supplementary files
Appendix B. Paleomagnetic site results.....	257
Appendix C. Supplemental data for stratigraphic sections.....	268
Appendix D. Time-lapse movies	Supplementary files
Appendix E. Gridded elevation data.....	Supplementary files
Appendix F. Areal extents of mapped fans from overhead images...	Supplementary files
Appendix G. Threshold images for flow-occupation maps.....	Supplementary files
Appendix H. Images of deposit slices.....	Supplementary files
Appendix I. Matlab™ computer application scripts.....	Supplementary files
Appendix J. Graphical files for chapter figures.	Supplementary files

PREFACE

The chapters included in this dissertation are related to a common theme of sedimentation in fluvially dominated intracontinental rift basins. Chapter 1 introduces basic concepts of basin sedimentation and the research approaches used to examine sedimentation in fluvially dominated intracontinental rift basins. Chapters 2-4 are stand-alone manuscripts written for publication, and thus contain repeated material. These three chapters have separate abstracts, introductions, methods, results, discussions, and references sections. The collaborating coauthors are listed for these chapters, and their specific contributions are detailed below. I am the lead author on all of these chapters because I conducted the majority of field work, sample collection and analysis, data interpretation, and writing. This research was conducted while I was a Field Geologist at the New Mexico Bureau of Geology and Mineral Resources, a Division of the New Mexico Institute of Mining and Technology.

Chapter 2 utilizes $^{40}\text{Ar}/^{39}\text{Ar}$ geochronology data by William C. McIntosh and colleagues at the New Mexico Geochronological Research Laboratory (NMGRL), New Mexico Institute of Mining and Technology. Many of the volcanic rocks analyzed at the NMGRL were co-collected by me, Steve Cather, Dave Love, and Dan Koning. These colleagues also provided sample data that have been included in this chapter. The $^{40}\text{Ar}/^{39}\text{Ar}$ geochronology data is summarized in tables in this chapter. Full descriptions of the analytical methods and results will be included as an appendix in the final published report, which has been accepted for publication by the Geological Society of America in a Special Paper, entitled *New Perspectives on the Rio Grande rift: from tectonics to groundwater*, edited by Mark R. Hudson and V.J.S. Grauch. Chapters 3 and

4 utilize data collected during experiments conducted at Saint Anthony Falls Laboratory at the University of Minnesota. Data collection and interpretation was assisted by Wonsuck Kim, Chris Paola, Jim Mullin, Chris Ellis, and Dick Christopher. Chapter 5 summarizes the conclusions of the field and experimental research and makes recommendations for future research. Much of the data used in this study is included in the Appendix. Additional data on the XES06 experiment is available through the National Center for EarthSurface Dynamics (NCED) data repository at the University of Minnesota (<https://repository.nced.umn.edu>).

CHAPTER 1. FLUVIAL SEDIMENTATION IN CONTINENTAL HALF-GRABEN BASINS

Introduction

Rift basins are important tectonic elements within continental regions that have been subjected to crustal extension. The stratigraphic architecture of intracontinental rift basins is defined by three depositional belts associated with the basin floor and flanking tributaries that drain the footwall uplift and traverse the hanging-wall ramp (Fig. 1.1). The spatiotemporal distribution of these depositional belts are sensitive to a variety of factors, including basin geometry, subsidence and sediment delivery rate, effective moisture, catchment morphology, and rock type (Gawthorpe and Leeder, 2000; and Paola, 2000).

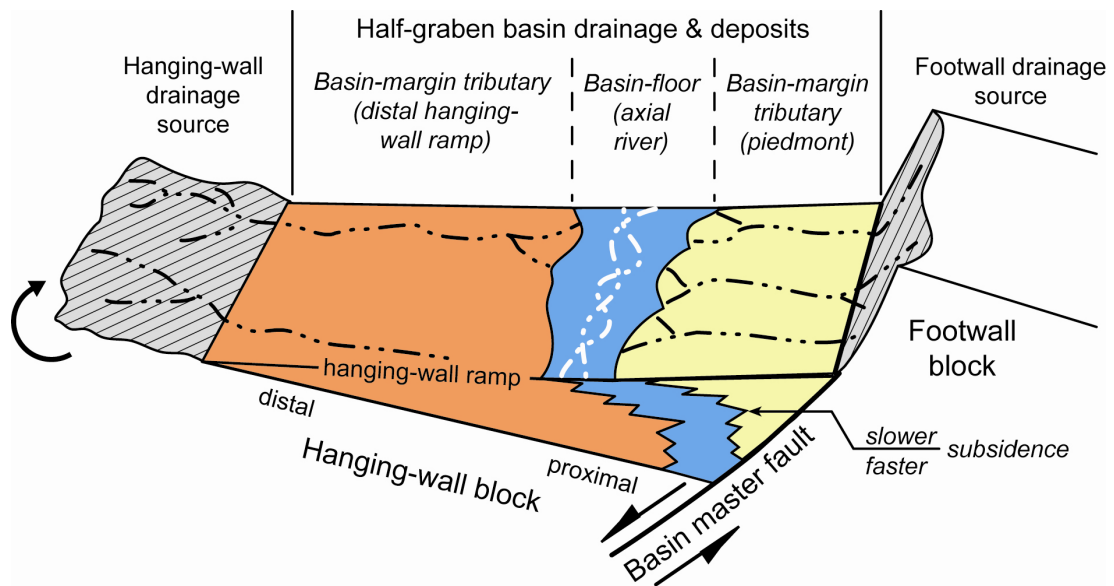


Figure 1.1. Diagram illustrating major depositional belts within half-graben basins (modified from Mack and Seager, 1990). The basin axis contains sediments associated with a through-going axial drainage (axial river, in blue) that is flanked by tributary deposits on the hanging-wall ramp (orange) and originating from the uplifted footwall block (yellow).

Models of basin filling are principally concerned with the timing and partitioning of sediment into stratigraphic sequences that describe first-order patterns in the stratigraphic architecture (Schlische and Olsen, 1990; Kendall et al., 1991; Travis and Nunn, 1994; Lawrence, 1994; Shanley and McCabe, 1994; and Contreras et al., 1997). Quantification of how sediments are distributed within extensional basins would help in understanding how alluvial successions develop autogenically and respond to allogenic forcing. Nonmarine depositional sequences are well known from coastal settings, where changes in relative sea level dominate the stratigraphic architecture (e.g., Shanley and McCabe, 1994). Many intracontinental rift-basins are sufficiently upstream of the coastline where they are far from eustatic effects on base level, so that the upper limit of fluvial deposition is set by changes in discharge regimes, sediment supply, and tectonism (e.g., Blum and Törnqvist, 2000).

The asymmetrical subsidence pattern of half-graben basins should influence the accumulation and preservation of all three depositional elements; however, most studies of half-graben sedimentation have focused on sedimentary successions associated with the footwall-adjacent piedmont-slope and basin-floor (Bridge and Leeder, 1981; Leeder and Gawthorpe, 1987; Blair and Bilodeau, 1988; Frostick and Reid, 1989; Heller and Paola, 1992; Mack and Seager, 1990; Paola et al., 1992; Bridge and MacKey, 1993; and Leeder et al., 1996). Footwall-sourced deposition is primarily controlled by the activity of the basin master-fault and sediment flux (Gawthorpe and Leeder, 2000, and references therein). The axial-river appears to act passively relative to the smaller drainages of the transverse belts, so its position indicates tectonic activity (e.g., Blair and Bilodeau, 1988; Peakall, 1998; Peakall et al., 2000; and Smith et al., 2001). The

hanging-wall dip-slope is typically portrayed as a passive depositional ramp whose sedimentary record is generally considered insignificant in the evolution of the basin. This depositional component is important because it is typically the most areally extensive and voluminous part of the basin-fill system and it commonly occupies less structurally complicated areas compared to the footwall uplift (e.g., Dart et al., 1995; and Gawthorpe and Hurst, 1993).

Computational models of basin filling reveal allogenic controls on the distribution of sediment across simple half-graben basins where mass is conserved (Paola et al., 1992; and Marr et al., 2000). Progradation of coarse-grained sediment coincides with increased sediment flux or diminished subsidence where sediment is introduced at the master fault (Fig. 1.2A & B). Where sediment is introduced opposite the master fault (Fig. 1.2C), progradation occurs in response to increased basin subsidence. Geometrically superposing these subsidence modeling results (Fig. 1.2B-C) suggest that the sediments delivered off the footwall block prograde as complementary, tributary deposits retreat up the hanging-wall block during times of diminished subsidence (Fig. 1.2D). This implies that the progradation of coarse-grained sediment from opposite sides of the model basin may respond differently to the same tectonic forcing. Progradation of coarse-grained, margin-sourced, sedimentary wedges may also be related to climatically driven discharge increases or drainage-basin enlargement (e.g., Smith, 1994; and Fraser and DeCelles, 1992). Thus, it is important to understand how basin-margin and basin-axis depositional belts interact and respond to tectonic and climatic stimuli.

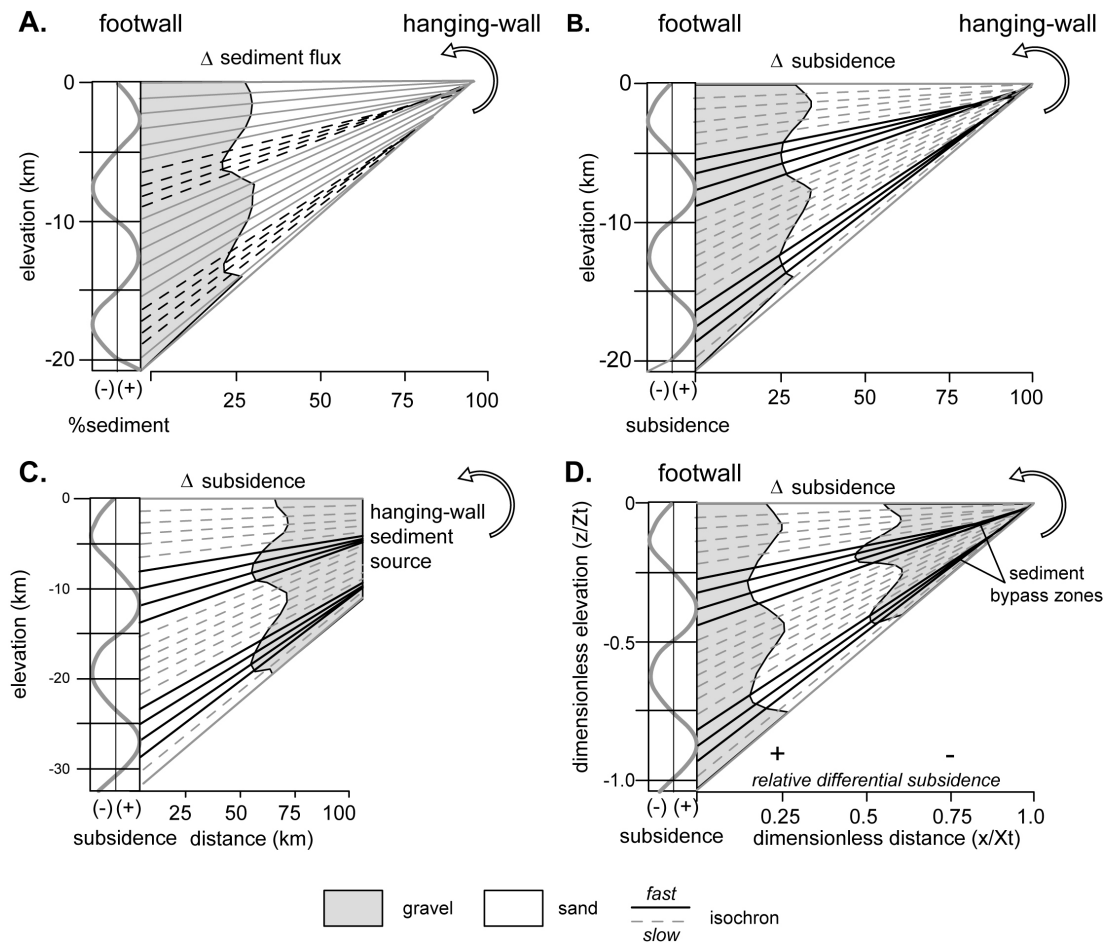


Figure 1.2. Results of numerical simulations of variable sediment flux and subsidence on sedimentation in actively subsiding basins where sediment is conserved (modified from Paola et al., 1992; and Marr et al., 2000). The master fault is on the left side of each diagram. Lines represent isochrons that are subdivided into intervals associated with slow (dashed) and rapid (solid) sinusoidal variations in sediment discharge or subsidence. A & B: Back-tilted basin cases where basin accommodation decreases away from the master fault and sediment source. C: Fore-tilted instance of distal hanging-wall ramp sedimentation where sediment source is opposite the master fault. D: Hypothetical transposition of cases B and C, illustrating sediment delivery at opposite sides of the basin. Sediment delivered to the model basin is not conserved in case D.

The research presented herein integrates field and experimental approaches in an attempt to elucidate tectonic and climatic controls on the development of alluvial sequences within intracontinental half-graben basins. A major objective of this research was to examine the roles of asymmetrical tilting of the basin-floor and sediment delivery

on the development of alluvial depositional successions. Is tectonic tilt a major control on location of the depositional belts, or are these belts influenced by differences in sediment discharge? Other objectives included the examination of the major controls on the position of the axial river system, how intrabasinal unconformities form, and how transverse sediments can bypass the basin margins. How efficiently can the axial river transport water and sediment through the basin, and does the river preferentially extract sediment from fans draining the footwall or those on the distal hanging-wall ramp? Other objectives included examination of the origin of obliquely oriented tributary drainage in half-graben basins. These objectives were addressed through experimentation and comparison to field sites, with an emphasis on Plio-Pleistocene sedimentation patterns within the Albuquerque Basin of New Mexico.

Research objectives are addressed in three stand-alone chapters (Chapters 2-4). Chapter 2 interprets an alluvial succession preserved within the Albuquerque Basin in the intracontinental Rio Grande rift. Field-based geomorphic, stratigraphic, and geochronologic studies examined the spatiotemporal evolution of the three main depositional elements in a fluvially dominated half-graben basin. Chapters 3 and 4 describe the results of a series of stratigraphic experiments that explored the evolution of surface morphology and stratigraphic architecture in a basin based on the form of a simple half graben. Chapter 3 examines the geomorphic evolution of deposit geomorphology in the experimental basin. Chapter 4 explores the stratigraphic architecture of the deposits preserved in the experimental basin with a focus on how the axial stream transports sediment through the basin. These two chapters on experimental stratigraphy compare results with field cases, including those of Chapter 2. Chapter 5

summarizes the conclusions of the experiments and field-study, and where appropriate, comparing these diverse datasets.

The physical experiments were motivated by a desire to understand how the three major depositional components in fluvially dominated half-graben basins respond to changes in subsidence and sediment supply. Specifically, we examined how tributary piedmont drainage can influence the position of the longitudinal (or axial) river and how it can transfer sediment through the basin. The ability of the axial drainage system to move sediment was examined using a simple sediment mass-balance model and comparing it to the total sediment input, mapped depositional belts, and using distinctive tracer grains.

A field component addressed the development of a Plio-Pleistocene alluvial succession preserved in the Albuquerque Basin of the Rio Grande rift in north-central New Mexico (Fig. 1.3). This succession was investigated using combined geomorphic, stratigraphic, sedimentologic, and geochronologic approaches. New $^{40}\text{Ar}/^{39}\text{Ar}$ age determinations and magnetic-polarity stratigraphy refine the ages of the synrift basin fill in order to allow correlations of the depositional belts to be made. The development of a robust magnetic-polarity stratigraphy refined the ages of the alluvial sequence, allowing correlation of major stratigraphic units to be made across the basin. A major motivation in this field study was to develop a comprehensive understanding of why distinct depositional belts occupy different parts of a basin at different times, with an emphasis on deposits on the distal hanging-wall ramp. Another objective was to examine structural and geomorphic controls on the development of drainage patterns, unconformities and

sediment bypass surfaces, and conditions leading to the eventual entrenchment of the synrift succession.

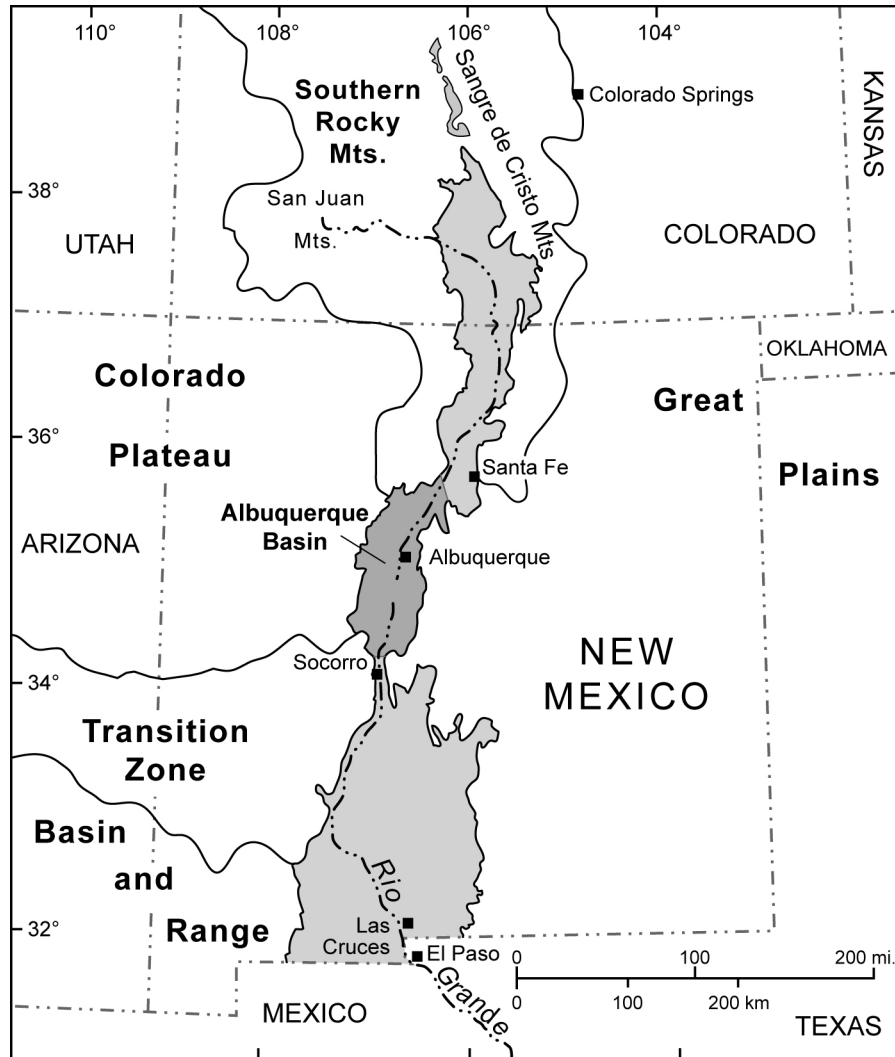


Figure 1.3. Basins of the Rio Grande in Colorado and New Mexico (light-gray) and the Albuquerque Basin (dark gray; modified from Thorn et al., 1993).

Understanding basin-scale patterns of sedimentation is important in evaluating the geomorphic and structural development of ancient extensional basins where later tectonic events or burial may have obscured the character of the original basin. The distribution of the component depositional belts in half-graben basins is important

because their contrasting three-dimensional facies-stacking arrangements broadly define reservoir (or aquifer) anisotropy, heterogeneity, and permeability (e.g., Davis et al., 1993; Bryant et al., 1995; Heller and Paola, 1996; and Smith, 2000). Rift basins in semi-arid regions, such as in southwestern North America, provide an essential source of groundwater (e.g., Bartolino and Cole, 2002). As potable water becomes scarcer, more robust models of extensional basin-fill architecture will aid in the management of these resources, as recently exemplified in the Rio Grande rift (e.g., McAda and Barroll, 2002).

Approach and Methods

This interdisciplinary project incorporates sedimentologic, stratigraphic, and geomorphic field studies with physical modeling of deposition in order to elucidate controls on the development of stratigraphic successions within half-graben basins. Experimentation is a forward approach to physical modeling that offers a unique view of how sedimentary systems change under well-controlled boundary conditions and carefully monitored surface topography (Paola et al., 2001; Van Heijst and Postma, 2001; Sheets et al., 2002; Hickson et al., 2005; and Martin et al., 2009). Because there are no practical ways to scale certain physical aspects of basin filling, such as grain size and fluid viscosity (Peakall et al., 1996; and Paola, 2000), the value of the experimental approach relies on the similarity of processes that establish topography and distribute sediment. For instance, model experiments create landscapes that bear remarkable similarity to natural environments (Hasbargen and Paola, 2000). Braided channel networks are easily created and maintained in experimental basins, exhibit similar

geometry over many spatial scales, and have similar spatial organization relative to natural distributary networks (Sapazhnikov and Foufoula-Georgiou, 1996; Foufoula-Georgiou and Sapazhnikov, 1998 and 2001; and Edmonds et al., 2007).

The pairing of field and experimental study of half-graben sedimentation provides unique opportunities to examine the complicated interplay of depositional systems from different perspectives. Experimentation can be used to explore and quantify linkages between surface processes and sedimentary architecture that are largely unavailable in field-based studies, which are commonly under-constrained because of incomplete exposures, poor geochronological resolution, and abundant stratigraphic lacunae. Physical experiments should not be considered “analog models” of field cases, but rather they are useful in providing independent sources of insight into how complicated depositional systems interact and respond to allogenic forcing.

Experiments were performed using the Experimental EarthScape (XES) facility at Saint Anthony Falls Laboratory, University of Minnesota. The XES is an experimental basin built to examine sedimentation under conditions of programmable differential subsidence (Paola et al., 2001). These experiments examined fluvial processes and stratigraphy created by four interacting sediment sources filling a basin that resembles a simple half graben (Fig. 1.4). The relative supplies of water and sediment to the axial and transverse fans were determined in part from field observations. Sediment discharge controls were emphasized in order to better understand the upstream controls on fluvial geomorphology and sedimentation.

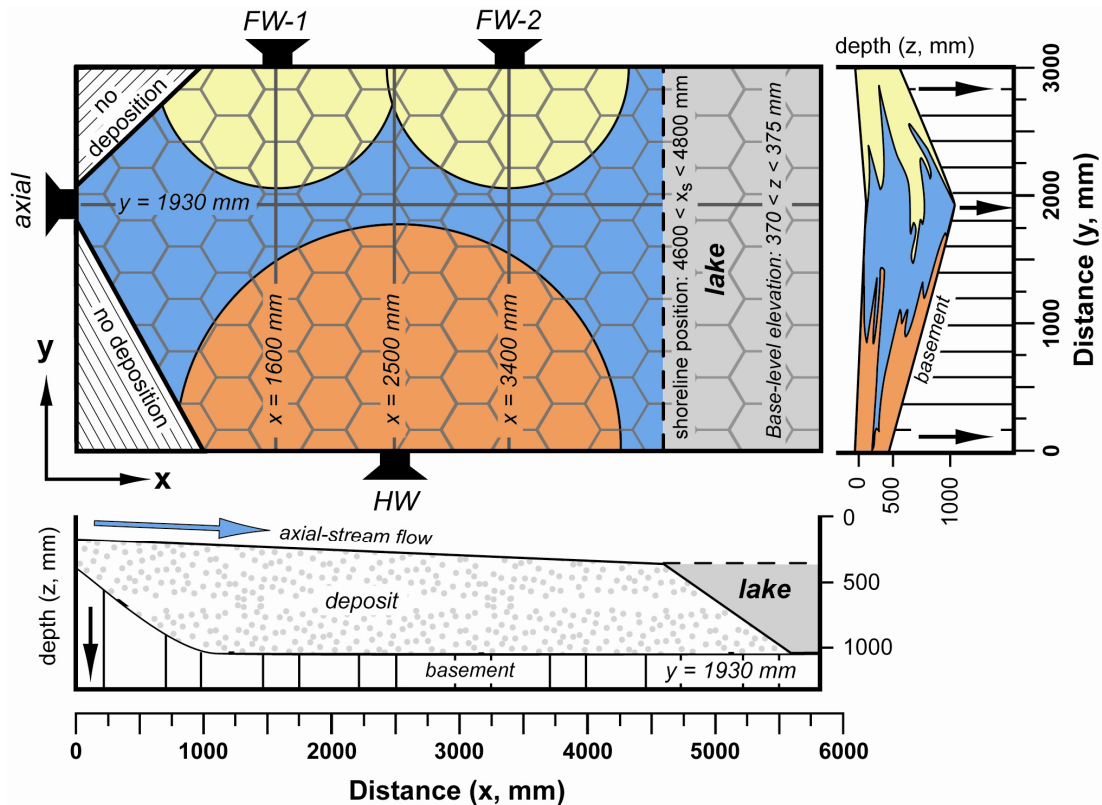


Figure 1.4. Schematic plan-view map and cross sections of the experimental setup, depicting dimensions of the tank and locations of sediment input points. Schematic cross sections illustrate geometry of basin subsidence. The four sediment feed points are analogous to the axial, hanging-wall (HW), and footwall sources in half-graben basins. The footwall contains upstream (FW-1) and downstream (FW-2) inputs. The honeycomb pattern represents the active subsidence cells that control basin subsidence. The light-gray shading denotes standing water that controls base level.

Experimental results were compared to the Albuquerque Basin field study (Fig. 1.3) and to other basins described in the following chapters. The Albuquerque Basin is well suited for field study because of extensive geologic mapping, and previous stratigraphic, biostratigraphic, and geochronologic studies (Bachman and Mehnert, 1978; Baldrige et al., 1980 & 1987; Connell, 2004, 2008a & b; Connell et al., 1999, 2002, 2005 & 2007; Hawley et al., 1995; Lozinsky, 1994; Morgan and Lucas, 2003; Maldonado et al., 2006 & 2007; and Williams and Cole, 2007). New age determinations provide important temporal control for the development of a magnetic-polarity

stratigraphy that refines the geochronology of the Plio-Pleistocene Ceja and Sierra Ladrones Formations in the Albuquerque Basin. Previous studies of the magnetic properties of deposits in the Rio Grande rift demonstrated that these alluvial sediments are suitable for the development of a robust polarity stratigraphy (e.g., Mack et al., 1993; Tedford and Barghoorn, 1999; and Hudson et al., 2008).

Chapter References

- Bachman, G.O., and Mehnert, H.H., 1978, New K-Ar dates and the late Pliocene to Holocene geomorphic history of the central Rio Grande region, New Mexico: Geological Society of America Bulletin, v. 89, p. 283-292.
- Baldrige, W.S., Damon, P.E., Shafiqullah, M., and Bridwell, R.J., 1980, Evolution of the central Rio Grande rift, New Mexico: New Potassium-argon ages: Earth and Planetary Sciences Letters, v. 51, n. 2, p. 309-321.
- Baldrige, W.S., Perry, F.V., and Shafiqullah, M., 1987, Late Cenozoic volcanism of the southeastern Colorado Plateau: I. Volcanic geology of the Lucero area, New Mexico: Geological Society of America Bulletin, v. 99, n. 10, p. 463-470.
- Bartolino, D.P., and Cole, J.C., 2002, Ground-water resources of the middle Rio Grande basin, New Mexico: U.S. Geological Survey, Circular 1222, 132 p.
- Blair, T.C., and Bilodeau, W.L., 1988, Development of tectonic cyclothem in rift, pull-aparts, and foreland basins: sedimentary response to episodic tectonism: Geology, v. 16, p. 517-520.
- Blum, M.D., and Törnqvist, T.E., 2000, Fluvial responses to climate and sea-level change; a review and look forward: Sedimentology, v. 47, Suppl. 1, p. 2-48.
- Bridge, J.S., and Leeder, M.R., 1979, A simulation model of alluvial stratigraphy: Sedimentology, v. 26, p. 617-644.
- Bridge, J.S., and MacKey, S.D., 1993, A revised alluvial stratigraphy model, in Marzo, M., and Puigdefabregas, C., eds., Alluvial Sedimentation: International Association of Sedimentologists, Special Publication 17, p. 319-336.
- Bryant, M., Falk, P., and Paola, C., 1995, Experimental study of avulsion frequency and rate of deposition: Geology, v. 23, p. 365-368.

- Chapin, C.E., and Cather, S.M., 1994, Tectonic setting of the axial basins of the northern and central Rio Grande rift: Geological Society of America, Special Paper 291, p. 5-25.
- Connell, S.D., 2004, Geology of the Albuquerque Basin and tectonic development of the Rio Grande rift, north-central New Mexico, in Mack, G.H., and Giles, K.J., eds., *The Geology of New Mexico, A geologic history*: New Mexico: New Mexico Geological Society, Special Publication 11, p. 359-388.
- Connell, S.D., 2008a, Geologic map of the Albuquerque-Rio Rancho metropolitan area, Bernalillo and Sandoval County, New Mexico: New Mexico Bureau of Geology and Mineral Resources, Geologic Map GM-78, scale 1:50,000, 2 pls.
- Connell, S.D., 2008b, Refinements to the stratigraphic nomenclature of the Santa Fe Group, northwestern Albuquerque Basin, New Mexico: *New Mexico Geology*, v. 30, n. 1, p. 14-35.
- Connell, S.D., Koning, D.J., and Cather, S.M., 1999, Revisions to the stratigraphic nomenclature of the Santa Fe Group, northwestern Albuquerque Basin, New Mexico, in Pazzaglia, F.J., and Lucas, S.G., eds., *Albuquerque Geology: New Mexico Geological Society, Guidebook 50*, p. 337-353.
- Connell, S.D., Cather, S.M., Dunbar, N., McIntosh, W.C., and Peters, L., 2002, Stratigraphy of the Tanos and Blackshare Formations (lower Santa Fe Group), Hagan embayment, Rio Grande rift, New Mexico: *New Mexico Geology*, v. 24, n. 4, p. 107-119.
- Connell, S.D., Hawley, J.W., and Love, D.W., 2005, Late Cenozoic drainage development in the southeastern Basin and Range of New Mexico, southeasternmost Arizona, and western Texas, in Lucas, S.G., Morgan, G.S., and Zeigler, K.E., eds., *New Mexico's Ice Ages: New Mexico Museum of Natural History and Science, Bulletin No. 28*, p. 125-150.
- Connell, S.D., Love D.W., and Dunbar, N.W., 2007, Geomorphology and stratigraphy of inset fluvial deposits along the Rio Grande valley in the central Albuquerque Basin, New Mexico: *New Mexico Geology*, v. 29, n. 1, p. 13-31.
- Contreras, J., Scholz, C.H., and King, G.C.P., 1997, A model of rift basin evolution constrained by first-order stratigraphic observations: *Journal of Geophysical Research*, v. 102, n. B4, p. 7673-7690.
- Davis, J. M., Lohmann, R. C., Phillips, F. M., Wilson, J. L., and Love, D. W., 1993, Architecture of the Sierra Ladrones Formation, central New Mexico: Depositional controls on the permeability correlation structure: *Geological Society of America Bulletin*, v. 105, p. 998-1007.

- Dart, C., Cohen, H.A., Akyüz, H.S., Barka, A., 1995, Basinward migration of rift-border faults: Implications for facies distribution and preservation potential: *Geology*, v. 23, n. 1, p. 69-72.
- Edmonds, D.A., Hoyal, D.C., Sheets, B., and Bloch, R.B., 2007, On the nature of delta distributary fill (abstract): *American Association of Petroleum Geologists, Annual Meeting Abstracts*, v. 16, p. 40.
- Foufoula-Georgiou, E., and V. B. Sapazhnikov, 1998, Anisotropic scaling in braided rivers: An integrated theoretical framework and results from application to an experimental river: *Water Resources Research*, v. 34, p. 863–867, doi:10.1029/98WR00216.
- Foufoula-Georgiou, E., and V. B. Sapazhnikov, 2001, Scale invariances in the morphology and evolution of braided rivers: *Mathematical Geology*, v. 33, p. 273–291, doi:10.1023/A:1007682005786.
- Fraser, G.S., and DeCelles, P.G., 1992, Geomorphic controls on sediment accumulation at margins of foreland basins: *Basin Research*, v. 4, p. 233-252.
- Frostick, L.E., and Reid, I., 1989, Is structure the main control of river drainage and sedimentation in rifts?: *Journal of African Earth Sciences*, v. 11, p. 165-182.
- Gawthorpe, R.L., and Hurst, J.M., 1993, Transfer zones in extensional basins: their structural style and influence on drainage development and stratigraphy: *Journal of the Geological Society*, v. 150, p. 1137-1152.
- Gawthorpe, R.L., and Leeder, M.R., 2000, Tectono-sedimentary evolution of active extensional basins: *Basin Research*, v. 12, p. 195-218.
- Hasbargen, L.E., and Paola, C., 2000, Landscape instability in an experimental drainage basin: *Geology*, v. 28, n. 12, p. 1067-1070.
- Hawley, J.W., Haase, C.S., Lozinsky, R.P., 1995, An underground view of the Albuquerque Basin: *New Mexico Water Resources Research Institute, Report 290*, p. 27-55.
- Heller, P.L., and Paola, C., 1992, The large-scale dynamics of grain-size variation in alluvial basins, 2: application to syntectonic conglomerate: *Basin Research*, v. 4, p. 91-102.
- Heller, P.L., and Paola, C., 1996, Downstream changes in alluvial architecture: An exploration of controls on channel-stacking patterns, *Journal of Sedimentary Research*, v. 66, 297-306.

- Hudson, M.R., Grauch, V.J.S., and Minor, S.A., 2008, Rock magnetic characterization of faulted sediments with associated magnetic anomalies in the Albuquerque Basin, Rio Grande rift, New Mexico: *Geological Society of America Bulletin*, v. 120, n. 5/6, p. 641-658; doi: 10.1130/B26213.1.
- Hickson, T. A., B. A. Sheets, C. Paola, and M. Kelberer, 2005, Experimental test of tectonic controls on three-dimensional alluvial facies architecture: *Journal of Sedimentary Research*, v. 75, p. 710–722, doi:10.2110/jsr.2005.057.
- Kendall, C.G. St. C., Strobel, J., Cannon, R., Bezdek, J., and Biswas, G., 1991, The simulation of the sedimentary fill of basins: *Journal of Geophysical Research*, v. 96, p. 6911-6929.
- Lawrence, D.T., 1994, Evaluation of eustasy, subsidence, and sediment input as controls on depositional sequence geometries and the synchronicity of sequence boundaries, in Weimer, P., and Posamentier, H.W., eds., *Siliclastic sequence stratigraphy; recent developments and applications: American Association of Petroleum Geologists Memoir 58*, p. 337-367.
- Leeder, M.R., and Gawthorpe, R.L., 1987, Sedimentary models for extensional tilt block/half graben basins, in Coward, M.P., Dewey, J.F., and Hancock, P.L., eds., *Continental Extensional Tectonics, Geological Society of London Special Publication 28*, p.139-152.
- Leeder, M.R., Mack, G.H., Peakall, J., and Salyards, S.L., 1996, First quantitative test of alluvial stratigraphic models: *Southern Rio Grande rift, New Mexico: Geology*, v. 24, n. 1, p. 87-90.
- Lozinsky, R.P., 1994, Cenozoic stratigraphy, sandstone petrology, and depositional history of the Albuquerque basin, central New Mexico: *Geological Society of America, Special Paper 291*, p. 73-82.
- Mack, G.H. and Seager, W.R., 1990, Tectonic controls on facies distribution of the Camp Rice and Palomas Formations (Pliocene-Pleistocene) in the southern Rio Grande rift: *Geological Society of America Bulletin*, v. 102, p. 45-53.
- Mack, G.H., Salyards, S.L., and James, W.C., 1993, Magnetostratigraphy of the Plio-Pleistocene Camp Rice and Palomas Formations in the Rio Grande rift of southern New Mexico: *American Journal of Science*, v. 293, p. 47-77.
- Maldonado, F., Budahn, J.R., Peters, L., and Unruh, D.M., 2006, Geology, geochronology, and geochemistry of basaltic flows of the Cat Hills, Cat Mesa, Wind Mesa, Cerro Verde, and Mesita Negra, central New Mexico: *Canadian Journal of Earth Sciences*, v. 43, n. 9, p. 1251-1268.

- Maldonado, F., Slate, J.L., Love, D.W., Connell, S.D., Cole, J.C., and Karlstrom, K.E., 2007, Geologic map of the Pueblo of Isleta tribal lands and vicinity, Bernalillo, Tarrant, and Valencia Counties, central New Mexico: U.S. Geological Survey Scientific Investigations Map 2913, 35-p. pamphlet, 1 plate, scale 1:50,000.
- Marr, J.G., Swenson, J.B., Paola, C., and Voller, V.R., 2000, A two-dimensional model of fluvial stratigraphy in closed depositional basins: *Basin Research*, v. 12, p. 381-398.
- Martin, J., Paola, C., Abreu, V., Neal, J., and Sheets, B., 2009, Sequence stratigraphy of experimental strata under known conditions of differential subsidence and variable base level: *American Association of Petroleum Geologists Bulletin*, v. 93, n. 4, p. 503-533.
- McAda, D.P., and Barroll, P., 2002, Simulation of ground-water flow in the middle Rio Grande Basin between Cochiti and San Acacia, New Mexico: U.S. Geological Survey, Water-Resources Investigations Report 02-4200, 81 p.
- Morgan G.S., and Lucas, S.G., 2003, Mammalian biochronology of Blancan and Irvingtonian (Pliocene and early Pleistocene) faunas from New Mexico: *American Museum of Natural History Bulletin*, v. 13, n. 279, p. 269-320.
- Paola, C., 2000, Quantitative models of sedimentary basin filling: *Sedimentology*, v. 47, p. 121-178.
- Paola, C., Heller, P.L., and Angevine, C.L., 1992, The large-scale dynamics of grain-size variation in alluvial basins, 1: Theory: *Basin Research*, v. 4, p. 73-90.
- Paola, C., Mullin, J., Ellis, C., Mohrig, D.C., Swenson, J.B., Parker, G., Hickson, T., Heller, P.L., Pratson, L., Syvitski, J., Sheets, B., and Strong, N., 2001, Experimental Stratigraphy: *GSA Today*, v. 11, p. 4-9.
- Peakall, J., 1998, Axial river evolution in response to half-graben faulting, Carson River, Nevada, U.S.A.: *Journal of Sedimentary Research*, v. 68, n. 5, p. 788-799.
- Peakall, J., Ashworth, P.J., and Best, J.L., 1996, Physical modeling in fluvial geomorphology: principals, applications and unresolved issues, in Rhodes, B.L., and Thorn, C.E., eds., *The scientific geomorphology: 27th Binghamton symposium in Geomorphology, Proceedings of the Annual Geomorphology Symposia Series*, Binghamton, New York, p. 221-253.
- Peakall, J., Leeder, M., Best, J., and Ashworth, P., 2000, River responses to lateral ground tilting: a synthesis and some important implications for the modeling of alluvial architecture in extensional basins: *Basin Research*, v. 12, p. 413-424.

- Sapozhnikov, V. B., and E. Foufoula-Georgiou, 1996, Self affinity in braided rivers: *Water Resources Research*, v. 32, p. 1429–1439, doi:10.1029/96WR00490.
- Schlische, R.W., and Olsen, P.E., 1990, Quantitative filling model for continental extensional basins with applications to early Mesozoic rifts of eastern North America: *The Journal of Geology*, v. 98, n. 3, p. 135-155.
- Shanley, K.W., and McCabe, P.J., 1994, Perspectives on the sequence stratigraphy of continental strata: *American Association of Petroleum Geologists Bulletin*, v. 78, p. 544-568.
- Sheets, B., T. Hickson, and C. Paola, 2002, Assembling the stratigraphic record: Depositional patterns and timescales in an experimental alluvial basin: *Basin Research*, v.14, p. 287–301, doi:10.1046/j.1365-2117.2002.00185.x.
- Smith, G.A., 2000, Recognition and significance of streamflow-dominated piedmont facies in extensional basins: *Basin Research*, v. 12, p. 399-411.
- Smith, G.A., 1994, Climatic influences on continental deposition during late-stage filling of an extensional basin, southeastern Arizona: *Geological Society of America Bulletin*, v. 106, n. 8, p. 1212-1228.
- Smith, G.A., McIntosh, W.C., and Kuhle, A.J., 2001, Sedimentologic and geomorphic evidence for sea-saw subsidence of the Santo Domingo accommodation-zone basin, Rio Grande rift, New Mexico: *Geological Society of America, Bulletin*, v. 113, n. 5, p. 561-574.
- Tedford, R.H., and Barghoorn, S., 1999, Santa Fe Group (Neogene), Ceja del Rio Puerco, northwestern Albuquerque Basin, Sandoval County, New Mexico: *New Mexico Geological Society, Guidebook 50*, p. 327-335.
- Travis, C.J., and Nunn, J.A., 1994, Stratigraphic architecture of extensional basins: Insights from a numerical model of sedimentation in evolving half grabens: *Journal of Geophysical Research*, v. 99, n. B8, p. 15,653-15,666.
- Van Heijst, M. W. I. M., and G. Postma, 2001, Fluvial response to sea-level changes: A quantitative analog, experimental approach: *Basin Research*, v. 13, p. 269–292, doi:10.1046/j.1365-2117.2001.00149.x.
- Williams, P.L., and Cole, J.C., 2007, Geologic map of the Albuquerque 30' x 60' quadrangle, north-central New Mexico: U.S. Geological Survey, Scientific Investigations Map 2946, 31 p., scale 1:100,000.

**CHAPTER 2. CLIMATIC CONTROLS ON NONMARINE DEPOSITIONAL
SEQUENCES IN THE ALBUQUERQUE BASIN, RIO GRANDE RIFT, NORTH-
CENTRAL NEW MEXICO**

Sean D. Connell^{1,2}, Gary A. Smith¹, John W. Geissman¹, and William C. McIntosh²

¹*Department of Earth and Planetary Sciences, MSC03 2040, University of New Mexico,
Albuquerque, New Mexico 87131 USA*

²*New Mexico Bureau of Geology and Mineral Resources, New Mexico Institute of
Mining and Technology, 801 Leroy Place, Socorro, New Mexico 87801 USA*

Chapter Abstract

We investigated a Plio-Pleistocene alluvial succession in the Albuquerque Basin of the Rio Grande rift in New Mexico using geomorphic, stratigraphic, sedimentologic, geochronologic, and magnetostratigraphic data. New ⁴⁰Ar/³⁹Ar age determinations and magnetic-polarity stratigraphy refine the ages of the synrift Santa Fe Group. The Pliocene Ceja Formation lies on the distal hanging-wall ramp across much of the Albuquerque Basin. It overlapped widespread, upper Miocene erosion surfaces (Rincones and lower Ortiz paleosurfaces), burying them by 3.0 Ma. Sediment accumulation rates in the Ceja Formation decreased after 3.0 Ma, and the Ceja formed broad sheets of amalgamated channel deposits that prograded into the basin after about 2.6 Ma. Ceja deposition ceased shortly after 1.8 Ma, forming the Llano de Albuquerque surface. Deposition of the ancestral Rio Grande in the Sierra Ladrones Formation focused near the eastern master-fault system before piedmont deposits (Sierra Ladrones Fm) began prograding away from the border faults between 1.8 and 1.6 Ma. Widespread basin filling ceased when the Rio Grande began cutting its valley, shortly after 0.78 Ma.

Although the Albuquerque Basin is tectonically active, the development of through-going drainage of the ancestral Rio Grande, burial of Miocene unconformities, and coarsening of upper Santa Fe Group basin fill were likely driven by climatic changes. Valley incision was approximately coeval with increased northern hemisphere climatic cyclicity and magnitude and was also likely related to climatic changes. Asynchronous progradation of coarse-grained, margin-sourced detritus may be a consequence of basin shape, where the basinward tilting of the hanging-wall promoted extensive sediment bypass of coarse-grained, margin-sourced sediment across the basin.

Introduction

Rift basins are important tectonic elements within continental regions subjected to crustal extension. The stratigraphic architecture of intracontinental rift basins is defined by three depositional belts associated with the basin floor and two sets of flanking tributaries from the footwall uplift and on the hanging-wall ramp (Fig. 2.1). The distributions of these depositional belts are sensitive to several factors, including basin geometry, subsidence and sediment delivery rate, effective moisture, catchment morphology, and rock type (e.g., Fraser and DeCelles, 1992; Leeder and Jackson, 1993; Gawthorpe and Leeder, 2000; and Paola, 2000).

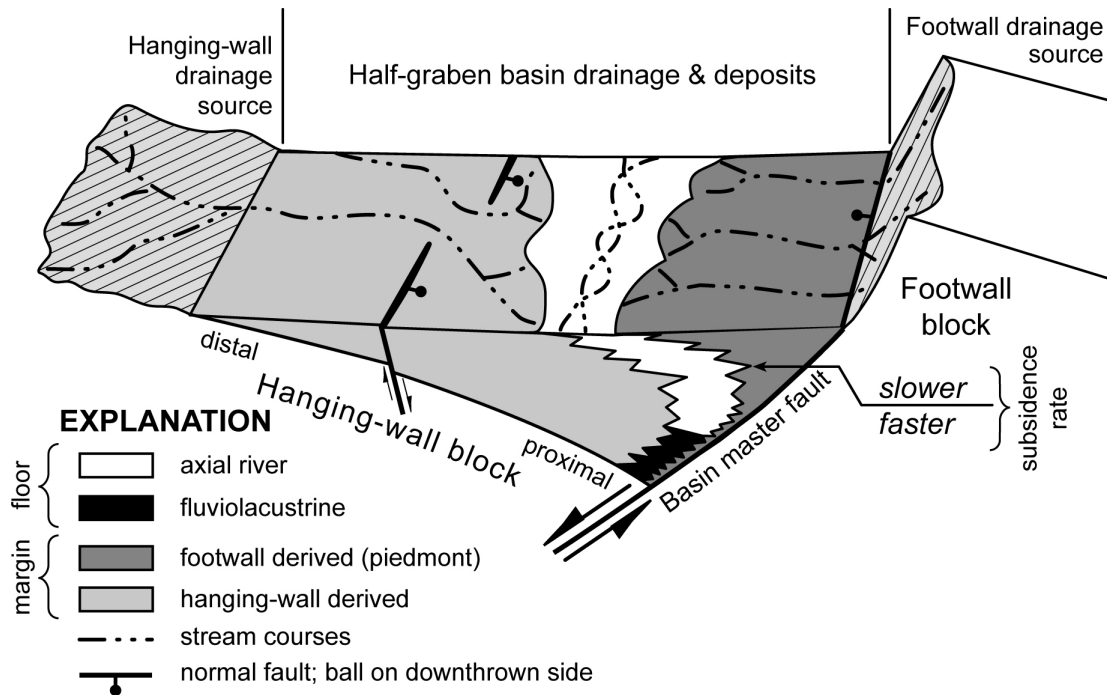


Figure 2.1. Diagram illustrating major depositional systems within a half-graben basin (modified from Mack and Seager, 1990; and Schlische, 1995). The basin axis contains sediments associated with internal surface drainage (fluviolacustrine) or through-going axial drainage (axial river) that are flanked by sets of tributary deposits originating from the footwall (piedmont slope) and distal hanging-wall ramp. The basin-floor/piedmont-slope boundary is sensitive to subsidence along the basin master fault (Leeder and Gawthorpe, 1987). Intrabasinal faults cut the hanging-wall ramp and allow steepening of the basement (rollover) towards the basin master fault (e.g., Xiao and Suppe, 1992). The asymmetric geometry of half-graben basins promotes the development slightly angular (fore-tilted) unconformities on the hanging-wall ramp that and strongly angular (back-tilted) unconformities next to the footwall cut off.

Most studies of half-graben sedimentation focused on (footwall-derived) piedmont-slope and basin-floor successions that were deposited near the master fault system (Bridge and Leeder, 1981; Leeder and Gawthorpe, 1987; Blair and Bilodeau, 1988; Frostick and Reid, 1989; Mack and Seager, 1990; Heller and Paola, 1992; Paola et al., 1992; Bridge and MacKey, 1993; Leeder et al., 1996; Peakall, 1998; Peakall et al., 2000; Marr et al., 2000; Leeder and Mack, 2001; and Smith et al., 2001). Quantitative models of fault development and basin filling describe first-order patterns in the

stratigraphic architecture of rift basins (Schlische, 1991; Travis and Nunn, 1994; and Contreras et al., 1997). Computational models suggest that sediments derived from the footwall block prograde into the basin as complementary tributary deposits retreat up the hanging-wall block during times of diminished subsidence (Paola et al., 1992; and Marr et al., 2000).

Understanding sedimentation patterns in half-graben basins can be accomplished by examining the timing of progradation of transverse (tributary) deposits derived from facing structural margins. We demonstrate the utility of combined sequence-stratigraphic, sedimentologic, and geomorphologic approaches to interpreting alluvial sequences developed within fluvially dominated intracontinental rift basins, such as the Albuquerque Basin of north-central New Mexico. Our primary motivation is to develop a comprehensive understanding of why certain facies belts occupy different parts of a basin at different times, with an emphasis on deposits on the distal hanging-wall ramp. This depositional belt should be sensitive to the activity of the basin master fault because progressive basinward tilting (fore-tilting) of the hanging wall increases the fan-surface area and stream gradients, thereby promoting erosion of distal areas and progradation of sediment towards the master fault (Leeder and Gawthorpe, 1987). Deposits on the hanging-wall ramp also tend to be well exposed and occupy less structurally complicated areas relative to their depositional counterpart adjacent to the footwall block (e.g., Dart et al., 1995; and Gawthorpe and Hurst, 1993). Nonmarine depositional sequences are well known from coastal settings, where changes in relative sea level dominate the stratigraphic architecture (e.g., Shanley and McCabe, 1994). Fluvial basins of the Rio Grande rift in New Mexico are more than 1500 km upstream of the coastline and are far

from eustatic effects on base level. Thus, the upper limit of fluvial deposition is controlled by changes in discharge regimes, sediment supply, and tectonism (Blum and Törnqvist, 2000).

The Albuquerque Basin of north-central New Mexico (Fig. 2.2) is well suited for investigation because excellent exposures have permitted extensive geologic mapping, biostratigraphic, stratigraphic, and geochronologic studies (Bachman and Mehnert, 1978; Baldrige et al., 1980 & 1987; Cole et al., 2007; Connell, 2004, 2008a & b; Connell and Wells, 1999; Connell et al., 1998, 1999, 2000, 2001a-d, 2002, 2005 & 2007a & b; Hawley, 1996; Hawley and Haase, 1992; Hawley et al., 1995; Lozinsky, 1994; Love and Connell, 2005; Love et al., 2001a-c; Lucas et al., 1993; Morgan and Lucas, 2003; Maldonado et al., 1999, 2006 & 2007a & b; Stone et al., 1998; Tedford and Barghoorn, 1999; and Williams and Cole, 2007). New $^{40}\text{Ar}/^{39}\text{Ar}$ age determinations provide important temporal control for the development of a magnetic-polarity stratigraphy that refines the geochronology of the Plio-Pleistocene Ceja and Sierra Ladrones Formations. Previous studies of the magnetic properties of deposits in the Rio Grande rift show that alluvial sediments are suitable for the development of a robust polarity stratigraphy (Mack et al., 1993; Tedford and Barghoorn, 1999; and Hudson et al., 2008). Rift basins in semi-arid regions, such as in southwestern North America, provide an essential source of groundwater (Bartolino and Cole, 2002). As potable water becomes scarcer, more robust models of extensional basin-fill architecture will aid in the management of these resources, as recently exemplified in the Rio Grande rift (McAda and Barroll, 2002).

Study Area

The Albuquerque Basin is part of the intracontinental Rio Grande rift, a chain of structurally and topographically linked extensional basins within a broader region of Neogene extension in the western United States and northern Mexico (Bryan, 1938; Kelley, 1952 & 1979; Chapin, 1971; and Chapin and Cather, 1994). The basin is flanked by the Colorado Plateau and Great Plains, and lies between the west-tilted Española and Socorro basins (Fig. 2.2). The eastern flank abuts the rift-flank uplifts of the Sandia, Manzanita, and Manzano Mountains. The northwestern flank has little surface relief, and the southwestern margin is marked by the rift-flanking uplifts of the Sierra Lucero and Ladron Mountains.

The Albuquerque Basin resembles a single physiographic basin; however, underlying geologic structure is complicated, and the basin has been segmented into a least three distinct sub-basins (*cf.* Russell and Snelson, 1994; and Grauch et al., 1999). These sub-basins are, from north to south: the Santo Domingo sub-basin (or basin, e.g., Smith et al., 2001), Calabacillas sub-basin, and the Belen sub-basin. Most of the study area is within the Calabacillas sub-basin and the northern part of the Belen sub-basin (Fig. 2.2), where the basin-fill generally dips eastward towards the Sandia, Manzanita, and Manzano Mountains.

The basin has relatively low topographic relief that is punctuated by two large, longitudinal river valleys and elongate tablelands (Fig. 2.3). The Ceja del Rio Puerco is a west-facing erosional escarpment that defines the eastern edge of the Rio Puerco valley (a southeastward-flowing tributary to the Rio Grande) and the western edge of the Llano de Albuquerque. La Ceja is a north-facing escarpment at the northern end of the Llano

de Albuquerque. Other major landforms in the Albuquerque Basin include the Hubbell bench, a structural bench along the western flanks of the Manzanita and Manzano Mountains, and the Hagan embayment, a structural re-entrant at the northeastern margin of the basin (Kelley, 1977). The central part of the study area (in the Calabacillas sub-basin) is in a half graben cut by numerous intrabasinal faults (Fig. 2.4), many of which remain tectonically active and have slip rates of 0.2-0.01 mm/a (Machette et al., 1998). The western flank of the study area forms a shallowly buried structural bench (Laguna bench of Russell and Snelson, 1994) that is defined by the San Ysidro, and Cat Mesa fault zones and the western basin-border faults.

The sedimentary fill and interbedded volcanic deposits of Rio Grande rift basins are collectively known as the Santa Fe Group (Fig. 2.5). Regionally these strata accumulated between late Oligocene and early Pleistocene time (Kelley, 1977; Hawley, 1978; Gile et al., 1981, 1995; Chapin and Cather, 1994). Deposition of the Santa Fe Group ceased as a result of incision of the present valleys (Spiegel and Baldwin, 1963). In the Albuquerque Basin, the Santa Fe Group is generally less than one kilometer thick along the western margin, but it thickens to nearly 5 km next to the eastern structural margin (Fig. 2.4; Lozinsky, 1994).

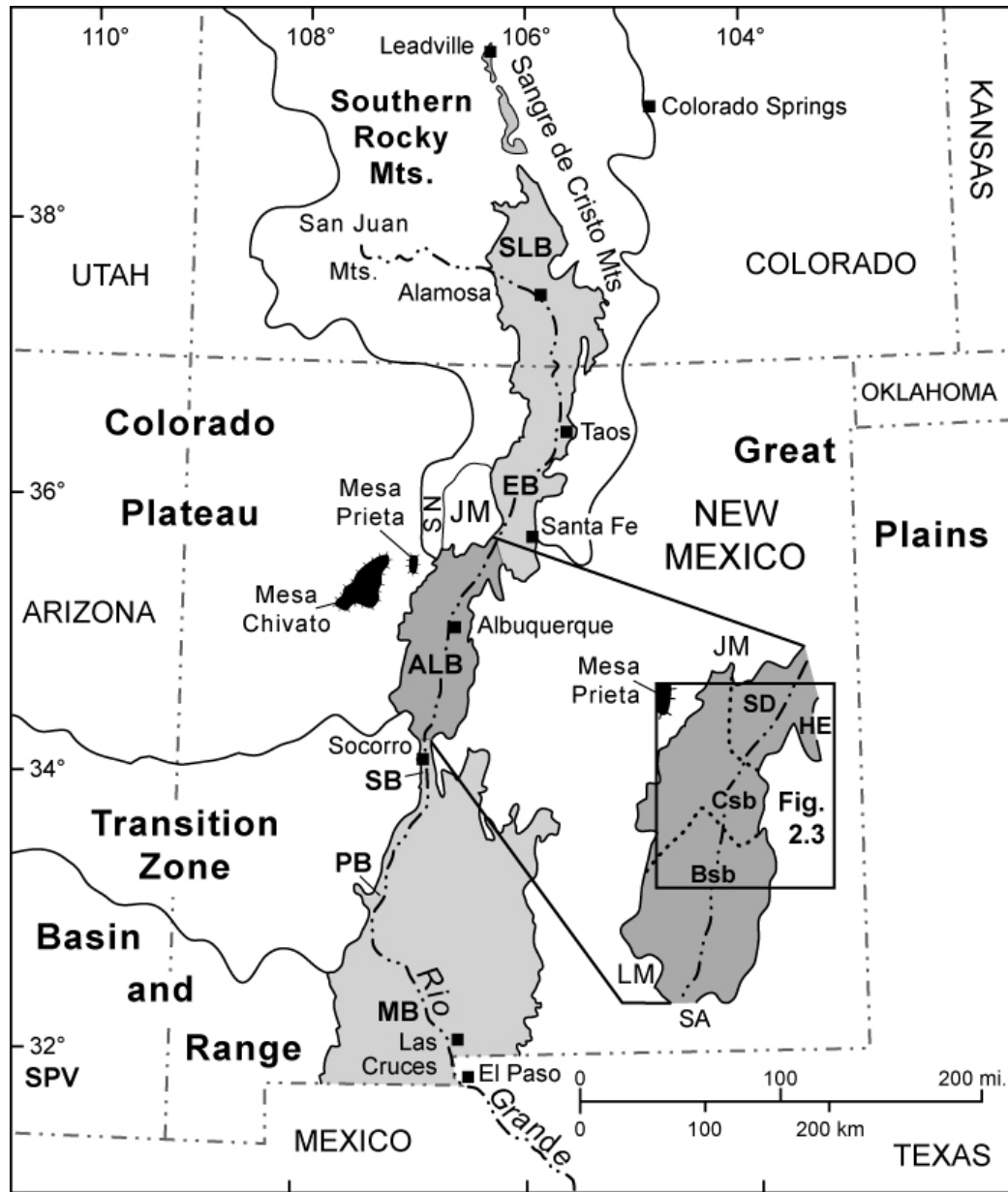
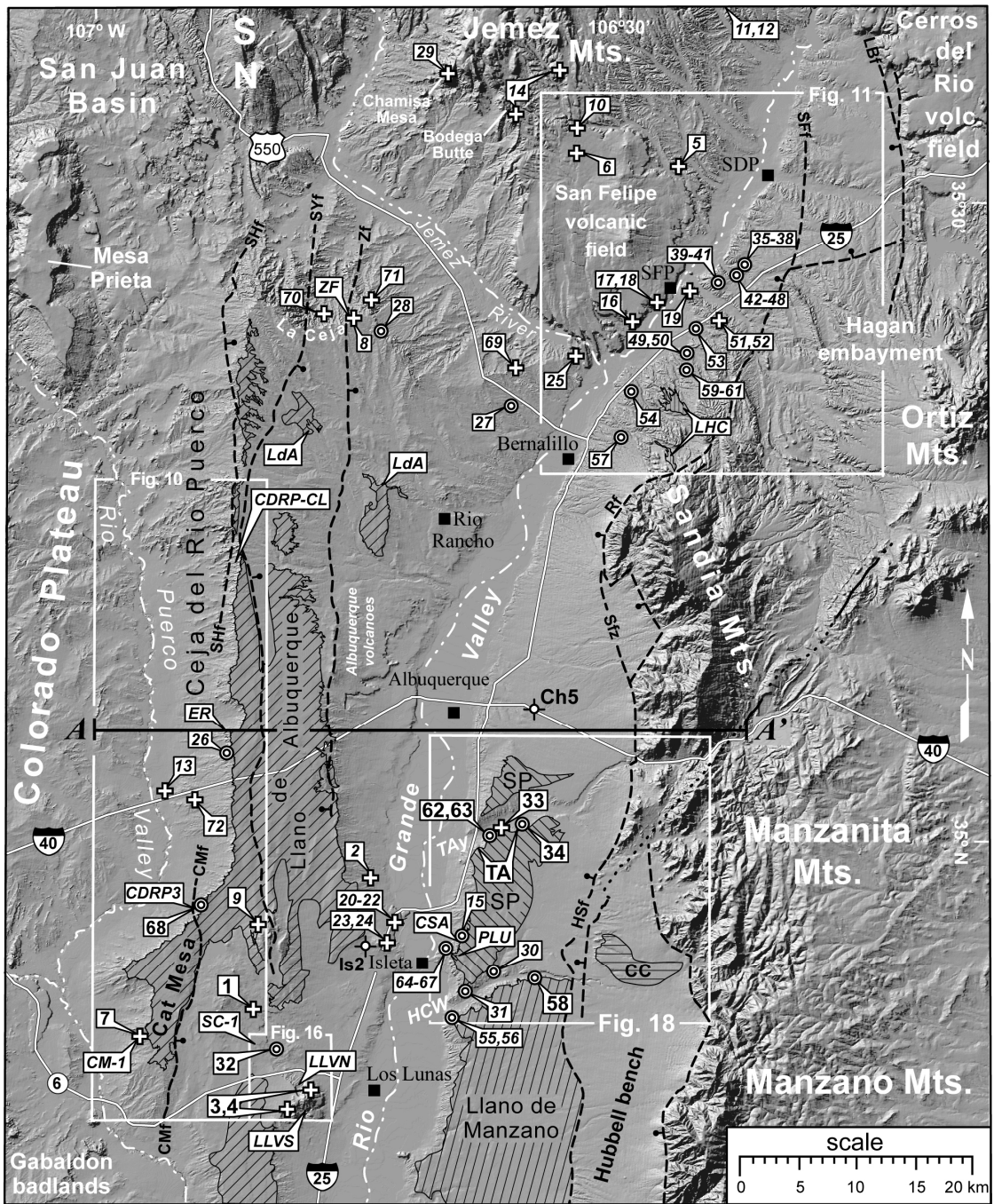


Figure 2.2. Basins of the Rio Grande in Colorado and New Mexico shaded in gray (modified from Thorn et al., 1993). Major basins include the: San Luis Basin (SLB), Española Basin (EB), Albuquerque Basin (ALB), Socorro Basin (SB), Palomas Basin (PB), and Mesilla Basin (MB). The approximate location of the San Pedro Valley (SPV) of southeastern Arizona is also shown. Inset map denotes the outline of Albuquerque Basin and approximate boundary of the study area in Figure 2.3, including the Hagan embayment (HE) and approximate boundaries of the Santo Domingo basin (or sub-basin, SD), Calabacillas sub-basin (Csb), and Belen sub-basin (Bsb; modified from Grauch et al., 1999). Abbreviations denote physiographic features surrounding the Albuquerque Basin, including the Jemez Mountains (JM), Ladron Mountains (LM), and Sierra Nacimiento (SN).

Figure 2.3 (following page). Shaded-relief map of the central and northern parts of the Albuquerque Basin, showing major physiographic features, towns, and study area locations. Towns include Albuquerque, Bernalillo, Isleta Pueblo, Los Lunas, San Felipe Pueblo (SFP), and Santo Domingo Pueblo (SDP). Geomorphic surfaces include the Cañada Colorada (CC), Las Huertas (LHC), Llano de Albuquerque (LdA), Llano de Manzano, and Sunport (SP). Selected major faults (thick dashed lines) include: La Bajada fault zone (LBf), Cat Mesa fault (CMf), Hubbell Spring fault zone (HSf), Sand Hill fault (SHf), Sandia fault zone (Sfz), San Francisco fault (Sff), San Ysidro fault (SYf), and Zia and County Dump faults (Zf). Other features include the Sierra Nacimiento (SN), the mouths of Hell Canyon Wash (HCW) and Tijeras Arroyo (TAy), Hubbell bench, San Felipe volcanic field, Cerros del Rio volcanic field, La Ceja, and the Ceja del Rio Puerco. Cross section A-A' is shown on Figure 2.4. Wells include the Charles Wells well #5 (Ch5), and Shell Isleta #2 (Is2). Stratigraphic locations include CDRP3, CDRP-CL, CM-1, CSA-PLU, LLV, SC-1, TA, and ZF. The type section of the Ceja Formation is at El Rincón (ER, Connell, 2008a). White-bordered boxes denote locations of geologic maps (Figs. 2.10, 2.11, 2.16 & 2.18). Numbers denote geochronologic sample sites listed on Tables 2.1-2.3. The “plus” symbol denotes volcanic materials primary fallout, lava flows, and intrusions that represent emplacement or depositional ages. The circle-in-circle symbol denotes fluvially recycled volcanic materials that represent maximum ages.



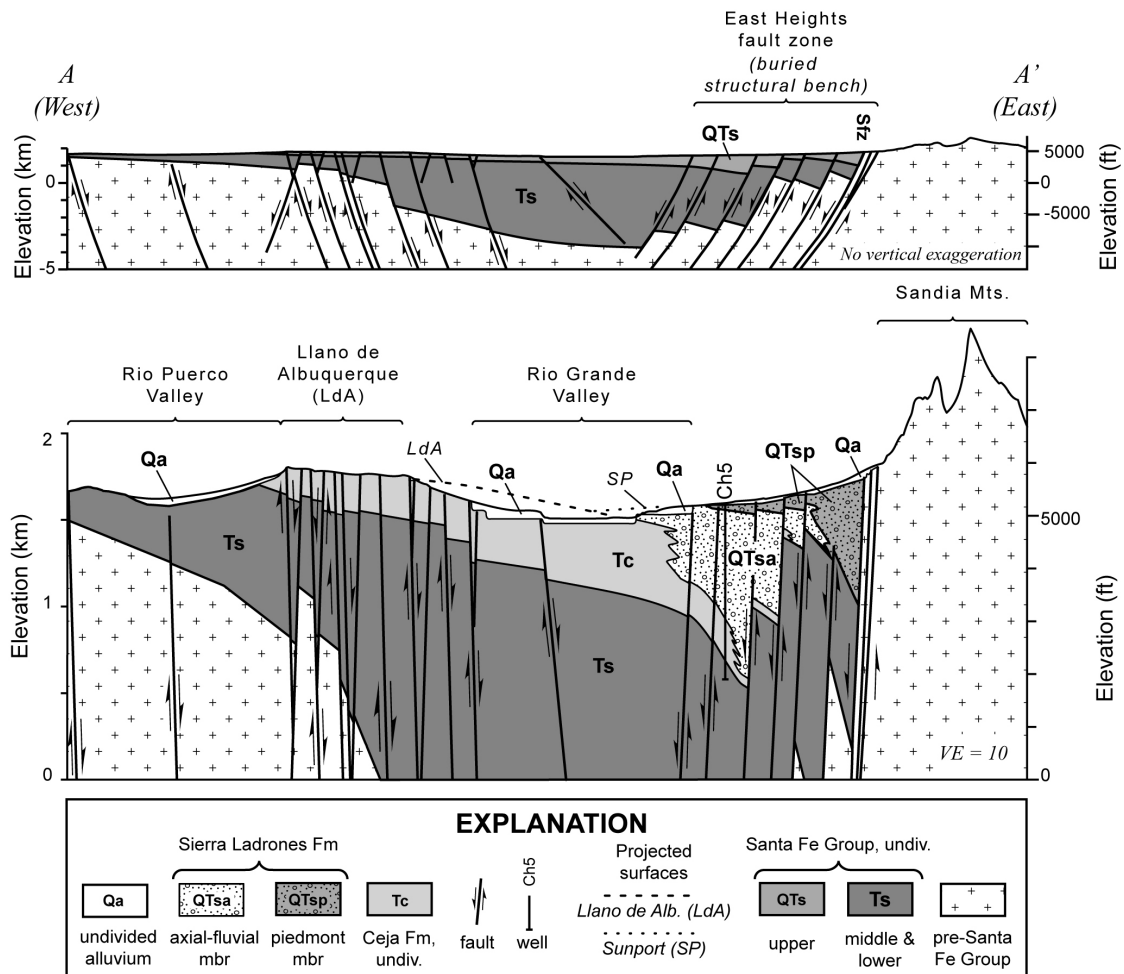


Figure 2.4. Simplified geologic cross section A-A' across the Albuquerque Basin (modified after Connell, 2008b). See Figure 2.3 for cross section location. Top: structure section with no vertical exaggeration, illustrating the overall east-tilted character of the basin. Bottom: vertically exaggerated cross section A-A' (VE = 10), illustrating the Ceja Formation and the axial-fluvial and piedmont members of the Sierra Ladrones Formation. Surficial deposits are diagrammatically shown and faults are highly generalized. The basin master fault is a zone of normal faults that lie along the eastern edge of the basin. Numerous intrabasinal faults cut the basin fill and probably control the position of the eastern part of the axial-fluvial member of the Sierra Ladrones Formation (QTsa). Projections of the Llano de Albuquerque and Sunport geomorphic surfaces denoted by dashed and dotted lines, respectively.

Geochronology

The stratigraphic architecture of the Albuquerque Basin is examined through physical correlation of strata and bounding surfaces, $^{40}\text{Ar}/^{39}\text{Ar}$ age determinations, biostratigraphy, and magnetic-polarity stratigraphy. Neogene deposits of the Albuquerque Basin yielded a rich array of biostratigraphically useful vertebrate fossil remains that have been summarized by Morgan and Lucas (2003) and Tedford et al. (2004). The Arroyo Ojito, Cerro Conejo, Popotosa, and Zia Formations contain interbedded volcanic material and sparse age-diagnostic fossils of Miocene age (Lozinsky and Tedford, 1991; Tedford and Barghoorn, 1999; and Connell, 2004). The Ceja Formation locally contains fossils indicative of late Pliocene age (3.5-2.2 Ma). The Sierra Ladrones Formation contains early Pleistocene fossils (Lucas et al., 1993) and Pliocene lava exposed in the adjacent Socorro Basin (Machette, 1978). Numerous isotopic age determinations and tephrochronologic correlations on ash and fluvially recycled pyroclastic rocks have been previously reported in the Albuquerque Basin and surrounding areas (Bachman and Mehnert, 1978; Baldrige et al., 1980; Connell, 2004 & 2008b; Connell et al., 1999 & 2002; Smith et al., 2001; Dunbar et al., 2001; Maldonado et al., 2006 & 2007; and Chamberlin and McIntosh, 2007).

$^{40}\text{Ar}/^{39}\text{Ar}$ Methods and Results

We use 20 previously reported $^{40}\text{Ar}/^{39}\text{Ar}$ and tephrochronologic age determinations (Table 2.1) and report 58 new $^{40}\text{Ar}/^{39}\text{Ar}$ age determinations to refine the ages of upper Miocene through lower Pleistocene strata in the Albuquerque Basin (Figs. 2.6 & 2.7 and Tables 2.2 & 2.3). Although some of the age determinations were

informally reported on geologic maps and reports, details of the $^{40}\text{Ar}/^{39}\text{Ar}$ analyses are first presented herein (Cather and Connell, 1998; Connell, 2004, 2008a & b; Connell et al., 1999 & 2005; Koning and Personius; 2002; Maldonado et al., 1999 & 2006; and Williams and Cole, 2007). Samples were analyzed at the New Mexico Geochronological Research Laboratory at the New Mexico Institute of Mining and Technology in Socorro, New Mexico. Fish Canyon Tuff sanidine (28.02 Ma, Renne et al., 1998) was used as a monitor for reducing the analytical data. The previously reported age determinations in Table 2.1 have been adjusted to the revised standard of Renne et al. (1998). Complete analytical data, including age-spectra and age-probability distribution diagrams (Deino and Potts, 1992) are available in Connell et al. (*in press*).

Volcanic rocks sampled for geochronology include tholeiitic basalt, trachyandesite, dacite, rhyodacite, and rhyolite associated with hydromagmatic tuff, fallout ash and lapilli, lava flows, and shallow intrusive rocks (Kelley and Kudo, 1978; Dunbar et al., 2001; Maldonado et al., 2006 & 2007; and Connell, 2008b). The ages of 15 samples were determined by resistance-furnace incremental-heating (RFIH) of groundmass concentrate or hornblende (Table 2.2). The ages of 43 samples containing sanidine were dated by single-crystal laser-fusion (SCLF) methods (Table 2.3). One sample containing plagioclase was dated by SCLF methods.

Table 2.1. Summary of age determinations from published sources.

Map No.	Unit	Age $\pm 2\sigma$ (Ma)	Method	Sample No.	Comments
1	Qch	0.099 \pm 0.002	RFIH	³ CH-21-1	Youngest lava flow of Cat Hills volcanic field.
2	Qrl	0.643 \pm 0.002	GCC	⁵ Gutierrez quarry	Lava Creek B ash; ⁴⁰ Ar/ ³⁹ Ar age from Lanphere et al. (2002).
3	Qlv	1.26 \pm 0.02	RFIH	^{2,4} S9a	Younger trachyandesite at El Cerro de los Lunas.
4	Tlv	3.83 \pm 0.10	RFIH	^{2,4} S26	Younger trachyandesite at El Cerro de los Lunas.
5	Tbs	2.43 \pm 0.03	RFIH	⁸ NMGRL 8364-1	NE flank of San Felipe volcanic field.
6	Tbs	2.46 \pm 0.22	RFIH	⁷ NMGRL 50139-1	NW flank of San Felipe volcanic field
7	Tcm	3.02 \pm 0.10	RFIH	³ CM-01A	Cat Mesa lava flow.
8	Tc	\sim 3.28	GCC	¹ SA-14	Nomlaki Tuff, fallout ash.
9	Twm	4.04 \pm 0.16	RFIH	³ WM-01A	Wind Mesa basalt.
SA	Tvsa	4.76 \pm 0.04	RFIH	⁶ San Acacia	Trachyandesite at San Acacia; not on map.
10	QTct	6.29 \pm 0.04	SCLF	⁷ NMGRL 50523-1	Younger Peralta Tuff.
11	QTct	6.23 \pm 0.06	SCLF	⁸ NMGRL 8353	Younger Peralta Tuff; north of study area.
12	QTsa	6.86-6.92	SCLF	⁸ NMGRL 7870, 7160, 7165	Older Peralta Tuff (n = 3); north of study area.
13	Tbm	8.16 \pm 0.05	RFIH	³ CH-13	Basaltic lava flow at La Mesita Negra.
14	Tcc	9.04-9.25	RFIH	⁷ NMGRL 9739, 50101, 50104, 50105	Basalt of Bodega Butte; overlies Cerro Conejo Fm (n = 4).

Notes: Map number refers to Figures 3, 6-11, 13, and 15-20.

Map units include: Cat Hills volcanic field (Qch), Lomas Negras Formation (Qrl) of Connell et al. (2007a), Los Lunas volcano (younger = Qlv, older = Tlv), Atrisco Member of the Ceja Formation (Tca), Ceja Formation, undivided (Tc), San Felipe volcanic field (Tbs), basaltic lava at Cat Mesa (Tcm), Wind Mesa volcanic field (Twm), Trachyandesite at San Acacia (Tvsa, not shown on maps), Cochiti Formation (QTct), and basaltic lava at La Mesita Negra (Tbm).

Methods include resistance furnace incremental heating (RFIH), single crystal laser fusion (SCLF), and geochemical correlation (GCC). ⁴⁰Ar/³⁹Ar age determinations recalculated to revised Fish Canyon sanidine standard (Renne et al., 1998).

Sources include: ¹Connell et al. (1999), ²Dunbar et al. (2001), ³Maldonado et al. (2006); ⁴Maldonado et al. (2007), ⁵Connell et al. (2007a), ⁶Chamberlin et al. (2001), ⁷Chamberlin and McIntosh (2007), and ⁸Smith et al. (2001).

Table 2.2. Summary of $^{40}\text{Ar}/^{39}\text{Ar}$ resistance furnace incremental heating (RFIH) results.

Map No.	Sample	Map unit	Lat. (°N)	Lon. (°W)	Lab. No.	Method	Material	Irad.	N	MSWD	Date $\pm 2\sigma$ (Ma)	K/Ca $\pm 2\sigma$	Comment
15*	S14	QTsa	34.9233	-106.6552	53930	RFIH	obsidian	NM162	7	4.87	1.44 \pm 0.01	18.4 \pm 0.8	Rabbit Mtn. obsidian pebble.
16	SF-Bas3	Tb	35.4029	-106.4867	8928	RFIH	groundmass	NM86	7	3.76	1.85 \pm 0.16	0.2 \pm 0.2	San Felipe vf., SE mesa.
17	SF-Bas2	Tb	35.4174	-106.4654	8927	RFIH	groundmass	NM86	5	4.23	2.28 \pm 0.09	0.2 \pm 0.0	San Felipe vf, boulder below SE flank
18	SF-bas1	QTsa	35.4176	-106.4653	8926	RFIH	groundmass	NM86	4	2.34	2.28 \pm 0.14	0.2 \pm 0.1	Same as No. 17.
19	TQA-4	Tb	35.4283	-106.4255	51967	RFIH	groundmass	NM33	7	6.67	2.57 \pm 0.11	0.2 \pm 0.2	San Felipe vf., in QTsa
20	125NE	Tb	34.9419	-106.7055	8406	RFIH	groundmass	NM78	6	3.63	2.79 \pm 0.05	0.5 \pm 0.6	S17: Black Mesa flow, in Tcrp
21	IV1	Tb	34.9326	-106.7169	8387	RFIH	groundmass	NM77	3	1.76	2.80 \pm 0.03	0.8 \pm 0.3	S20: Isleta volcano, in Tcrp
22	85	Tb	34.9202	-106.7058	8409	RFIH	groundmass	NM78	5	5.27	2.82 \pm 0.05	0.5 \pm 0.2	S18: Isleta volcano, in Tcrp
23	225 block	Tb	35.9168	-106.7210	8407	RFIH	groundmass	NM78	6	1.51	2.84 \pm 0.03	0.3 \pm 0.3	S21: Isleta volc., base surge.
24	125S	Tb	35.9168	-106.7210	8404	RFIH	groundmass	NM78	4	2.46	2.86 \pm 0.07	0.2 \pm 0.2	S19: Isleta volc.
25	022098-161-SANA	Tcs	35.3806	-106.5435	8977	RFIH	hornblende	NM86	4	1.64	3.81 \pm 0.23	0.1 \pm 0.0	SA15: ash 42 m below Pliocene lavas
26*	030100-ER3a	Tcrp	35.0659	-106.8742	51448	RFIH	groundmass	NM127	5	1.86	4.23 \pm 0.21	0.5 \pm 0.4	SA16: Basaltic cobble
27*	011598-31BERN	Tcs	35.3373	-106.6047	50483	RFIH	hornblende	NM110	3	6.09	4.81 \pm 0.26	0.1 \pm 0.0	SA18: Rhyodacite cobble
28*	8h-1	Top	35.4033	-106.7309	50485	RFIH	hornblende	NM110	3	2.37	6.56 \pm 0.33	0.3 \pm 0.1	SA19: Cobble 20 m below top.
29	0903998-JP	Tcc	35.5955	-106.6643	52286	RFIH	groundmass	NM137	3	1.64	9.67 \pm 0.14	0.1 \pm 0.1	Chamisa Mesa

Notes: See Table 3 for details.

Table 2.3. Summary of $^{40}\text{Ar}/^{39}\text{Ar}$ single crystal laser fusion (SCLF) results.

Map No.	Sample	Map unit	Lat. (°N)	Lon. (°W)	Lab. No.	Method	Material	Ir.	N	MSWD	Date $\pm 2\sigma$ (Ma)	K/Ca $\pm 2\sigma$	Comment
30*	Is10 (S10)	QTsa	34.9006	-106.6219	6198	SCLF	sanidine	NM45	11	1.42	1.23 \pm 0.01	56.0 \pm 7.5	Rhyolitic pumice
31*	Is4 (S11)	QTsa	34.8870	-106.6486	6197	SCLF	sanidine	NM45	15	2.25	1.24 \pm 0.01	25.0 \pm 10.0	Rhyolitic pumice
32*	99DS1	Qsc	34.8382	-106.8281	51932	SCLF	sanidine	NM133	9	0.52	1.24 \pm 0.02	52.9 \pm 30.4	Upper Bandelier pumice
33	011700-ALE3	QTsa	35.0094	-106.6151	57256	SCLF	sanidine	NM123	11	1.92	1.28 \pm 0.02	41.6 \pm 24.2	SA2: Tshirege ash
34*	102998-A-ALE	QTsa	35.0111	-106.5963	50256	SCLF	sanidine	NM105	14	2.00	1.34 \pm 0.04	2.4 \pm 0.6	Rhyolitic pumice
35*	SF-ac22	QTsa	35.4462	-106.3828	9175	SCLF	sanidine	NM89	23	0.20	1.18 \pm 0.18	29.3 \pm 25.3	Rhyolitic pumice
36*	SF-ac12	QTsa	35.4423	-106.3857	8933	SCLF	sanidine	NM86	14	2.41	1.38 \pm 0.03	37.4 \pm 8.9	Rhyolitic pumice
37*	SF-ac11	QTsa	35.4423	-106.3857	8935	SCLF	sanidine	NM86	8	4.79	1.46 \pm 0.25	20.5 \pm 26.5	Rhyolitic pumice
38*	SF-ac21	QTsa	35.4458	-106.3885	9174	SCLF	sanidine	NM89	30	0.40	1.62 \pm 0.09	52.4 \pm 64.8	Rhyolitic pumice
39*	SF-18psm	QTsa	35.4326	-106.4016	9172	SCLF	sanidine	NM89	9	0.37	1.45 \pm 0.12	40.6 \pm 38.4	Rhyolitic pumice
40*	SF-ac19	QTsa	35.4312	-106.4066	9176	SCLF	sanidine	NM89	5	0.07	1.49 \pm 0.06	18.5 \pm 0.4	Rhyolitic pumice
41*	SF-ac17	QTsa	35.4329	-106.4082	9171	SCLF	sanidine	NM89	30	1.15	1.70 \pm 0.06	36.0 \pm 31.4	Rhyolitic pumice
42*	SF-ac9	QTsa	35.4388	-106.3902	8920	SCLF	sanidine	NM86	13	3.99	1.49 \pm 0.03	39.3 \pm 9.9	Rhyolitic pumice
43*	SF-ac8	QTsa	35.4388	-106.3902	8919	SCLF	sanidine	NM86	6	0.48	1.41 \pm 0.04	38.1 \pm 6.8	Rhyolitic pumice
44*	SF-ac6	QTsa	35.4388	-106.3915	8917	SCLF	sanidine	NM86	13	2.28	1.55 \pm 0.01	29.5 \pm 11.4	Rhyolitic pumice
45*	SF-ac4	QTsa	35.4388	-106.3915	8915	SCLF	sanidine	NM86	12	0.41	1.61 \pm 0.05	30.9 \pm 15.7	Rhyolitic pumice
46*	SF-ac5	QTsa	35.4388	-106.3915	8916	SCLF	sanidine	NM86	14	0.67	1.63 \pm 0.04	36.6 \pm 21.8	Rhyolitic pumice
47*	SF-ac7	QTsa	35.4388	-106.3915	8918	SCLF	sanidine	NM86	14	2.08	1.66 \pm 0.01	31.5 \pm 4.3	Rhyolitic pumice
48*	SF-ac20	QTsa	35.4377	-106.3977	9173	SCLF	sanidine	NM89	14	0.41	1.65 \pm 0.09	35.4 \pm 11.2	Rhyolitic pumice
49*	SF-ac2	QTsa	35.3972	-106.4293	8912	SCLF	sanidine	NM86	12	0.67	1.54 \pm 0.07	38.7 \pm 12.8	Rhyolitic pumice
50*	SF-ac1	QTsa	35.3966	-106.4316	8911	SCLF	sanidine	NM86	10	2.17	1.71 \pm 0.04	30.9 \pm 9.6	Rhyolitic pumice

Table 2.3 (continued).

Map No.	Sample	Map unit	Lat. (°N)	Lon. (°W)	Lab. No.	Method	Material	Ir.	N	MSWD	Date ± 2σ (Ma)	K/Ca ± 2σ	Comment
51	Casino ash	QTsp	35.4107	-106.3995	9749	SCLF	sanidine	NM105	14	1.67	1.57 ± 0.09	38.8 ± 30.7	SA3: 3 m above QTsa
52	12199728-SFP	QTsp	35.4031	-106.4089	8924	SCLF	sanidine	NM86	15	8.49	1.60 ± 0.06	50.7 ± 8.3	Casino ash (SA3)
53*	PL-PS-1	QTsa	35.3651	-106.4382	8934	SCLF	sanidine	NM86	11	6.13	1.60 ± 0.02	44.4 ± 19.7	Rhyolitic pumice
54*	QTsa	QTsa	35.3488	-106.4907	7615	SCLF	sanidine	NM63	12	4.14	1.62 ± 0.03	32.9 ± 18.0	Rhyolitic pumice
55*	Placitas S5725 or LL3	QTsa	34.8658	-106.6637	51941	SCLF	sanidine	NM133	2	1.18	1.56 ± 0.09	46.7 ± 3.8	S8: Rhyolitic pumice
56*	99LLS1	QTsa	34.8659	-106.6677	51937	SCLF	sanidine	NM133	7	1.94	1.64 ± 0.03	35.0 ± 11.8	Rhyolitic pumice
57*	PL-asc2	QTsa	35.3132	-106.5010	2340	SCLF	sanidine	NM23	8	1.40	1.68 ± 0.02	33.7 ± 3.9	SA5: Rhyo. pumice
58*	Hell Cyn	QTsa	34.8961	-106.5820	51223	SCLF	sanidine	NM123	28	6.59	1.72 ± 0.04	33.2 ± 10.5	Rhyolitic pumice
59*	SF-acs16	QTsa	35.3780	-106.4379	8923	SCLF	sanidine	NM86	14	7.92	1.65 ± 0.03	33.2 ± 10.5	Rhyolitic pumice
60*	SF-acs14	QTsa	35.3780	-106.4379	8921	SCLF	sanidine	NM86	5	0.48	1.92 ± 0.09	31.6 ± 17.0	Rhyolitic pumice
61*	SF-acs15	QTsa	35.3780	-106.4379	8922	SCLF	sanidine	NM86	22	2.98	1.92 ± 0.19	30.4 ± 16.1	Rhyolitic pumice
62*	011700-ALE2	QTsa	35.0065	-106.6219	51257	SCLF	sanidine	NM123	13	4.43	1.68 ± 0.03	29.6 ± 11.9	Rhyolitic pumice
63*	011700-ALE1	QTsa	35.0069	-106.6237	51940	SCLF	sanidine	NM133	7	1.28	2.00 ± 0.04	16.5 ± 9.7	Pumiceous sand
64*	99IS10	QTsa	34.9261	-106.6572	51936	SCLF	sanidine	NM133	14	3.69	1.67 ± 0.04	31.4 ± 16.8	Rhyolitic pumice
65*	99IS3	Tca	34.9187	-106.6575	51933	SCLF	sanidine	NM133	12	3.83	2.63 ± 0.05	18.5 ± 27.6	Dacitic pumice

Table 2.3 (continued).

Map No.	Sample	Map unit	Lat. (°N)	Lon. (°W)	Lab. No.	Method	Material	Ir.	N	MSWD	Age ± 2σ (Ma)	K/Ca ± 2σ	Comment
66*	99IS6, 23Ayo	Tca	34.9139	-106.6737	51934	SCLF	sanidine	NM133	11	1.69	2.70 ± 0.06	60.2 ± 212	Dacitic pumice
67*	99IS8	Tca	34.9408	-106.6584	51935	SCLF	sanidine	NM133	2	0.85	2.77 ± 0.05	18.7 ± 0.0	Dacitic pumice
68*	CH33A	Tca	34.9592	-106.8949	8144	SCLF	sanidine	NM71	8	5.72	3.18 ± 0.10	152.5 ± 65.1	Dacitic pumice, 4m above base of Tca
69	021798-130-BERN	Tob	35.3668	-106.6090	8925	SCLF	sanidine	NM86	14	4.67	6.83 ± 0.04	6.6 ± 31.0	SA21: Peralta Tuff 100 m below top.
70	090198-U12-SVNE	Tob	35.4076	-106.7760	9473	SCLF	sanidine	NM93	14	0.89	6.85 ± 0.13	49.4 ± 7.0	SA20: Peralta Tuff
71	11E	Tob	35.4196	-106.7318	50516	SCLF	sanidine	NM110	5	0.67	7.06 ± 0.06	58.8 ± 35.1	SA22: Peralta Tuff
72	6F	Ton	35.0294	-106.9051	8945	SCLF	plagioclase	NM86	6	0.14	7.16 ± 0.47	37.7 ± 65.2	Cerro Colorado dacite

Notes: See Appendix A for detailed description and data tables. Map number refers to Figures 3, 6-11, 13, and 15-20. Asterisk(*) denotes fluvially recycled pyroclastic material, and represents a maximum age for the deposit. Sample S denotes sample localities in Maldonado et al. (2007). Sample SA denotes sample localities in Connell (2006, 2008b). Method is single crystal laser fusion (SCLF) or resistance furnace incremental heating (RFIH). N is the number of individual crystals analyzed (SCLF), or the number of heating steps used to calculate weighted mean age (RFIH). Sample material is groundmass concentrate, hornblende, obsidian, plagioclase, or sanidine. K/Ca is the molar ratio calculated from K-derived ³⁹Ar and Ca-derived ³⁷Ar. MSWD denotes Mean sum weighted deviates.

Methods: Sample preparation: sanidine, plagioclase, biotite—crushing, LST heavy liquid, Franz, HF; groundmass concentrate—crushing, picking. Irradiation: four separate in vacuo 7–14 hr irradiations (NM23, NM45, NM63, NM71, NM77, NM78, NM86, NM89, NM93, NM105, NM110, NM123, NM127, NM133, NM137, and NM162), D3 position, Nuclear Science Center, College Station, TX. Neutron flux monitor inter-laboratory standard Fish Canyon Tuff sanidine (FC-2) with an assigned age of 28.02 Ma (Renee et al., 1998); samples and monitors irradiated in alternating holes in machined Al discs.

Laboratory: New Mexico Geochronology Research Laboratory, Socorro, NM. Instrumentation: Mass Analyzer Products 215-50 mass spectrometer on line with automated, all metal extraction system. Heating: sanidine—SCLF, 10W continuous CO₂ laser; RFIH—25–45 mg aliquots in resistance furnace. Reactive gas cleanup: SAES GP-50 getters operated at 20°C and ~450 °C; SCLF—1–2 minutes, RFIH—9 minutes. Error calculation: all errors reported at ± 2 σ, mean ages calculated using inverse variance weighting of Samson and Alexander (1987), Decay constant and isotopic abundances: Steiger and Jäger (1977). Complete data set presented in Data Repository.

Analytical parameters: Electron multiplier sensitivity = 1 to 3 x 10¹⁷ moles/pA; typical system blanks were 470, 3, 0.6, 3, 3.0 x 10¹⁸ moles (laser) and at 1,730, 37, 2, 6, 9 (furnace) at masses 40, 39, 38, 37, 36 respectively; J-factors determined to a precision of ± 0.2% using SCLF of 4 to 6 crystals from each of 4 to 6 radial positions around irradiation vessel. Correction factors for interfering nuclear reactions, determined using K-glass and CaF₂ are provided in the Data Repository.

Map units include: Cerro Conejo Formation (Tcc), Navajo Draw (Ton), Loma Barbon (Tob), and Picuda Peak (Top) Members of the Arroyo Ojito Formation; axial-fluvial (QTsa) and piedmont (QTsp) member of the Sierra Ladrones Formation; Rio Puerco (Tcrp), Atrisco (Tca), and Santa Ana Mesa (Tcs) Members of the Ceja Formation; San Clemente alluvium (Qsc); Cat Hills volcanic field (Qch); and San Felipe volcanic field (Tbs).

Age determinations for 18 samples (taken from volcanic fallout or lava flows) represent emplacement or depositional ages. The remaining samples taken from fluvially recycled pyroclastic material, ranging from pumiceous sand to pebbles and cobbles of pumice and welded tuff, represent maximum ages of deposition. Six samples of Miocene rocks provided maximum bounding ages for the overlying Plio-Pleistocene succession. Wherever possible the dense crystalline cores of mafic lava flows were sampled. Volcanic gravel was scraped clean of adhered sand grains at the time of collection, and interior parts of samples were collected for analysis.

Figure 2.6 displays the stratigraphic assignments of age determinations for the Cerro Conejo, Arroyo Ojito, Cochiti, and Ceja Formations, and the unit of San Clemente, listed in increasing order of age. Four dacitic pumice pebbles in the Ceja Formation yielded late Pliocene dates that are similar to the age of the Pliocene Tschicoma volcanic field in the Jemez Mountains (Broxton et al., 2007). Three rhyolitic lapilli and ash beds in the Arroyo Ojito Formation yielded late Miocene age determinations that correlate to the *ca.* 6.1-7.0 Ma Peralta Tuff Member of the Bearhead Rhyolite on the southeastern flanks of the Jemez Mountains (McIntosh and Quade, 1995; Justet and Spell, 2001; Smith, 2001; Smith et al., 2001; and Chamberlin and McIntosh, 2007).

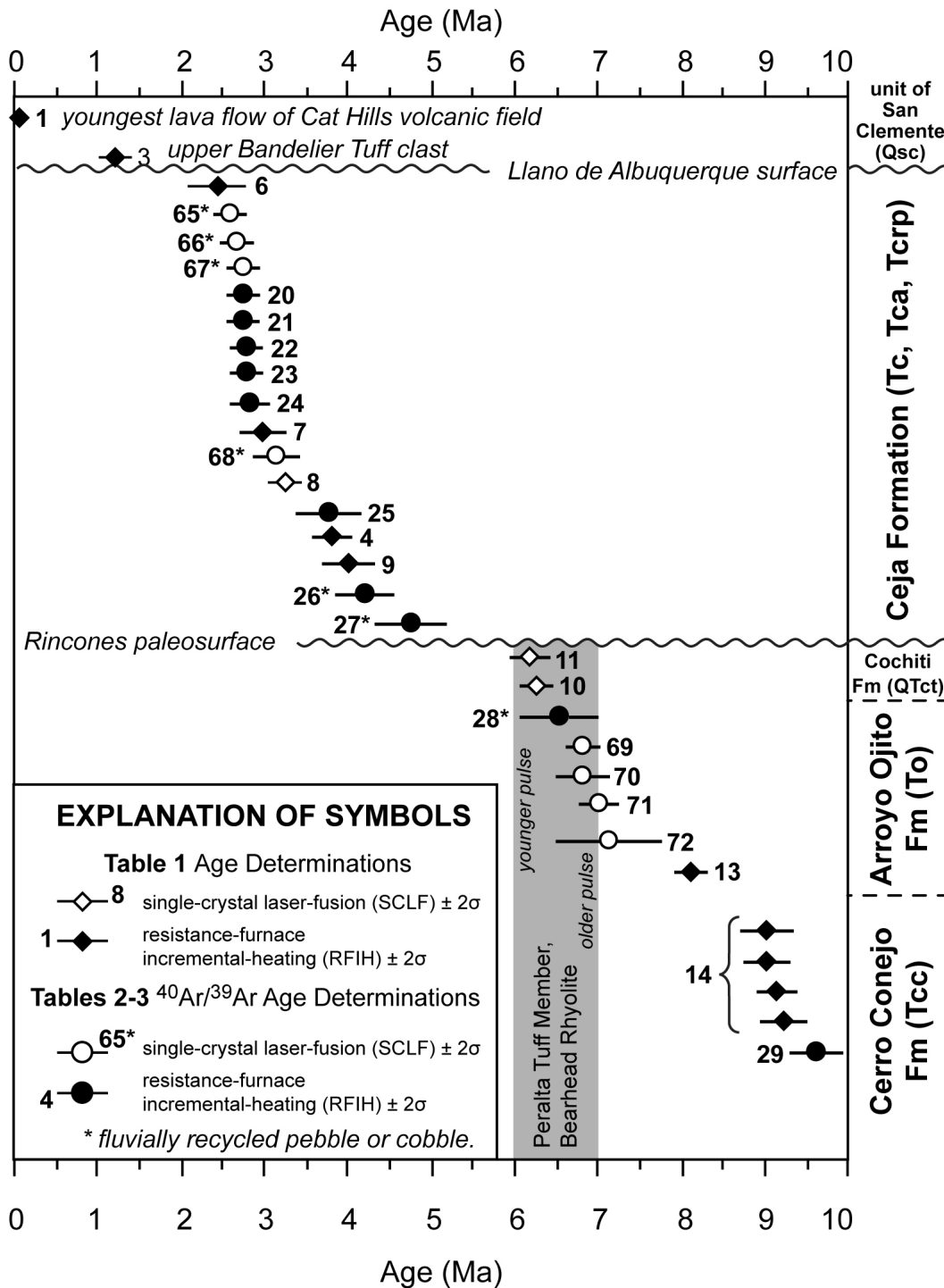


Figure 2.6. Summary of $^{40}\text{Ar}/^{39}\text{Ar}$ age determinations ($N = 32$) for the unit of San Clemente, Ceja, Cochiti, Arroyo Ojito, and Cerro Conejo Formations, showing mean sample ages and $\pm 2\sigma$ uncertainties, and sample numbers (Tables 2.1-2.3). Gray bar denotes range of the Peralta Tuff. Stratigraphic discontinuities are the Llano de Albuquerque and Rincones paleosurfaces. Asterisks denote fluviually recycled volcanic gravel that provides maximum ages of the deposits. Plagioclase was analyzed in sample 72; hornblende was analyzed in sample 25.

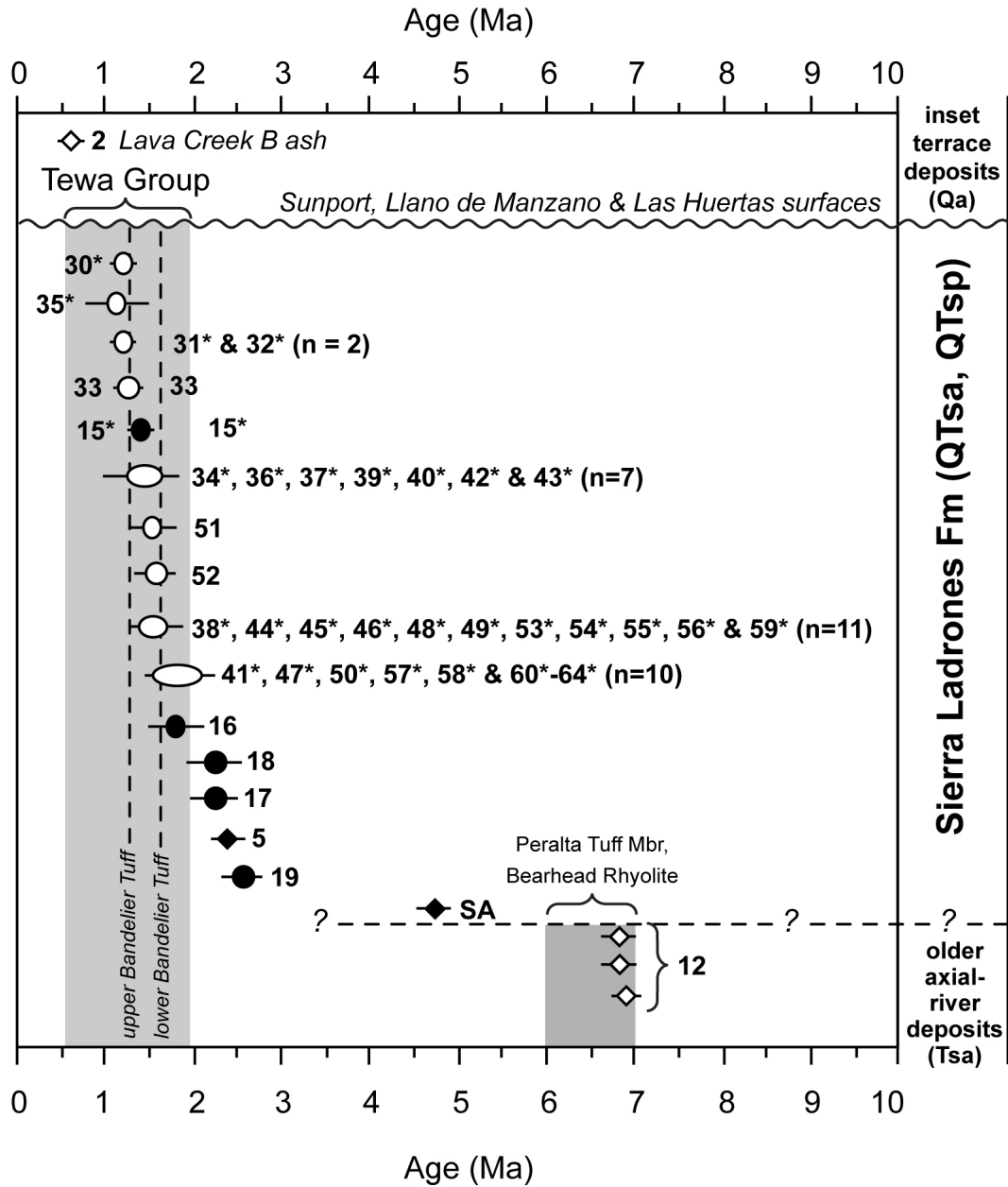


Figure 2.7. Summary of $^{40}\text{Ar}/^{39}\text{Ar}$ age determinations (N = 46) for the Lava Creek B in an inset terrace of the Rio Grande (Qr), Sierra Ladrones Formation, and a Miocene axial-river deposit, showing mean sample ages and $\pm 2\sigma$ uncertainties, and sample numbers (Tables 2.1-2.3). Refer to Figure 2.6 for explanation of symbols. Gray bars denote age ranges of the Tewa Group and Peralta Tuff. The trachyandesite at San Acacia (SA) lies near the boundary between the Socorro and Albuquerque basins.

Figure 2.7 displays the stratigraphic assignments of age determinations for late Miocene axial-river deposits, the Sierra Ladrões Formation, and an inset terrace deposit of the ancestral Rio Grande. Age determinations of 36 rhyolitic pumice and ash samples (Table 2.3) are mostly within the reported ages of early Pleistocene eruptions that formed the 1.9-0.6 Ma Tewa Group in the Jemez Mountains (Goff and Gardner, 2004), including the 1.85 ± 0.08 Ma tuff of San Diego Canyon (Spell et al., 1990), 1.26 ± 0.01 Ma Tshirege (upper) and 1.61 ± 0.01 Ma Otowi (lower) Members of the Bandelier Tuff (Izett and Obradovich, 1994; and Phillips et al., 2007), and the intracaldera 1.6-1.2 Ma Cerro Toledo Rhyolite (Spell et al., 1990 & 1996). Three rhyolitic samples yielded dates that are slightly older than the San Diego Canyon Tuff (Table 2.3). Other tephra include the 0.639 ± 0.002 Ma Lava Creek B ash (Lanphere et al., 2002), and the *ca.* 3.28 Ma Nomlaki Tuff of the Tuscan and Tehama Formations of California (Sarna-Wojcicki et al., 1991; and Connell et al., 1999).

Paleomagnetic Methods

Oriented-block samples were collected from 171 paleomagnetic sampling sites in alluvial sediments. At each site, multiple, independently oriented block samples were collected. The sampling interval averaged about 2.3 m between sites, but varied from 0.2 m to 9.0 m in order to obtain suitable fine-grained sediments. Stratal tilts were rotated to horizontal along bedding strike to correct the *in situ* magnetic remanence into stratigraphic (paleohorizontal) coordinates. Samples were collected following modifications to the approach of Lindsay et al. (1987). Most samples consisted of weakly cemented sand, silt, mud, and clay; well-cemented sediments were sampled at 10

sites. Weakly cemented sand and silt required outcrop modification and impregnation with dilute (by about 50 percent with water) sodium-silicate solution ($\text{Na}_2\text{Si}_3\text{O}_7$) before collection (Fig. 2.8A). Three to eight oriented blocks were typically obtained in the field. Specimens were dry-cut into cube-shaped ($1\text{-}4\text{ cm}^3$) oriented specimens (Fig. 2.8B) using a non-magnetic diamond-tipped saw blade. Analyses were conducted at the University of New Mexico Paleomagnetism and Rock Magnetism Laboratory in Albuquerque, New Mexico. Six to eleven specimens per site were analyzed, and at least one specimen was analyzed per sampled block. Raw specimen data are available in Appendix A.

Progressive alternating-field (AF) and thermal demagnetization were applied to 1327 specimens to investigate the character of the natural remanent magnetization (NRM). All measurements of specimen NRM were made in a magnetically shielded room using a 2G Enterprises Model 760R superconducting rock magnetometer, equipped with direct-current superconducting quantum interference devices (DC SQUIDS) with a magnetic-moment noise level of about $1.0\text{ to }3.0 \times 10^{-12}\text{ Am}^2$. Bulk magnetic susceptibility (MS) was measured using a Kappa Bridge KLY4S unit. The means of at least three specimens were divided by the specimen volume to obtain mean MS values for each site.



Figure 2.8. Photographs of a weakly cemented sample site and prepared specimens. A: Sand sample in the Ceja Formation at El Cerro de Los Lunas; 10-cm gradations on Jacob staff at left side. A reference surface was planed and orientation marks were cut using non-magnetic tools. The sediment was then impregnated with a dilute solution of sodium silicate before large blocks were removed from the site. B: Specimens from LLVN composite section cut into cubes (about 1.5-cm per side shown here), showing labels and orientations marked with a high-temperature, nonmagnetic ceramic coating (Zircar™).

At least one specimen from each sample was treated using progressive AF demagnetization. These specimens were subjected to initially low AF treatment at 2, 4, 6, 8, and 10 mT peak fields to remove viscous magnetization and to test for the possibility of lightning-induced isothermal remanent magnetization (IRM); some specimens were treated at 3, 6, and 9 mT steps. At least one specimen per site was subjected to further AF demagnetization in 5- and 10-mT steps, ending at a peak field between 65 and 115 mT. At least three specimens per site were subjected to thermal demagnetization using an ASC-48 thermal demagnetizer. Specimens were demagnetized by stepwise heating at 20 to 60° C intervals starting at 100 or 150° C and ending below 600° C, or where demagnetization trajectories became erratic. Specimens having more than 10 percent of the NRM not unblocked by 580° C were subjected to continued thermal treatments at 20° C intervals to 680° C.

The dominant magnetic mineral phases were investigated by subjecting selected specimens to anhysteretic remanent magnetization (ARM) acquisition in a peak alternating field of 95 mT and a biasing direct-current (DC) field of 0.1 mT and subsequent progressive AF demagnetization, followed by acquisition of isothermal remanent magnetization (IRM), to saturation of IRM (SIRM), and backfield (BIRM) DC demagnetization of SIRM. IRM acquisition tests were conducted with a pulse magnetizer that provided a DC field up to 2.97 Tesla, capable of saturating magnetite and approaching the saturation of hematite. A suite of specimens previously subjected to AF demagnetization of NRM, ARM, and SIRM, were given IRMs in peak DC fields of 2.97, 0.3, and 0.03 T along orthogonal directions and then progressively thermally demagnetized following the approach of Lowrie (1990).

Rock-Magnetic Results

Bulk magnetic susceptibility (MS) was measured for 348 specimens from 72 sites in the Ceja Formation, focusing on stratigraphic sections at Los Lunas volcano and at CDRP3 (Fig. 2.9). Site mean MS values (SI volume) were compared to gross deposit texture (i.e., mudstone and sandstone) and magnetic polarity (i.e., normal and reverse polarity), where they varied by about an order of magnitude (Fig. 2.9). The lack of a difference between MS values for normal and reverse polarity populations of specimens suggests that little or no systematic post-depositional alteration of the magnetic mineralogy took place that would remagnetize or alter the polarity of the remanence. The MS of mudstone in the Ceja Formation is $4.16 \times 10^{-4} \pm 4.89 \times 10^{-5}$ (geometric mean \pm standard error, in SI volume), and is about 60 percent of the sandstone population

($7.08 \times 10^{-4} \pm 1.03 \times 10^{-4}$). The MS data we obtained showed a narrower range in MS values than observed in mostly older sediments in the basin, as reported by Hudson et al. (2008). This narrower range of MS may simply be a result of restricting sampling to finer grain sizes of the sedimentary deposits.

Eighteen specimens from the sample sets that had been used for AF and thermal demagnetization were subjected to combined ARM acquisition and AF demagnetization, IRM acquisition and backfield demagnetization, and AF demagnetization of SIRM experiments to better understand the overall character of the remanence carrying magnetic mineralogy (Figs. 2.10 & 2.11). Response to progressive AF demagnetization of NRM was variable, with the median destructive field ranging from about 10 to over 40 mT (Fig. 2.10A). Progressive thermal demagnetization of NRM revealed that the NRM is associated with distributed laboratory unblocking temperatures and little evidence of considerable NRM unblocking above the maximum unblocking temperature of magnetite (about 580° C) (Fig. 2.10B). For most specimens, a small fraction of the NRM continued to be unblocked above 580° C, suggesting that a small part of the NRM is carried in either hematite or maghemite.

With the exception of specimen LLVN36-3C, the AF demagnetization response of ARM is very uniform among all specimens, with median destructive field between about 18 and 21 mT (Fig. 2.11A). We interpret this behavior to indicate a relatively uniform population of magnetic grains with coercivities less than about 95 mT among these specimens. The observed median destructive fields for ARM are suggestive of an abundance of reasonably fine-grained (less than a few tens of microns) magnetite grains present in these materials. The AF demagnetization response of saturation IRM (Fig.

2.11B) shows a greater range of responses, with the SIRM of some specimens (e.g., LLVN40-1A) requiring a considerably higher demagnetizing field than others.

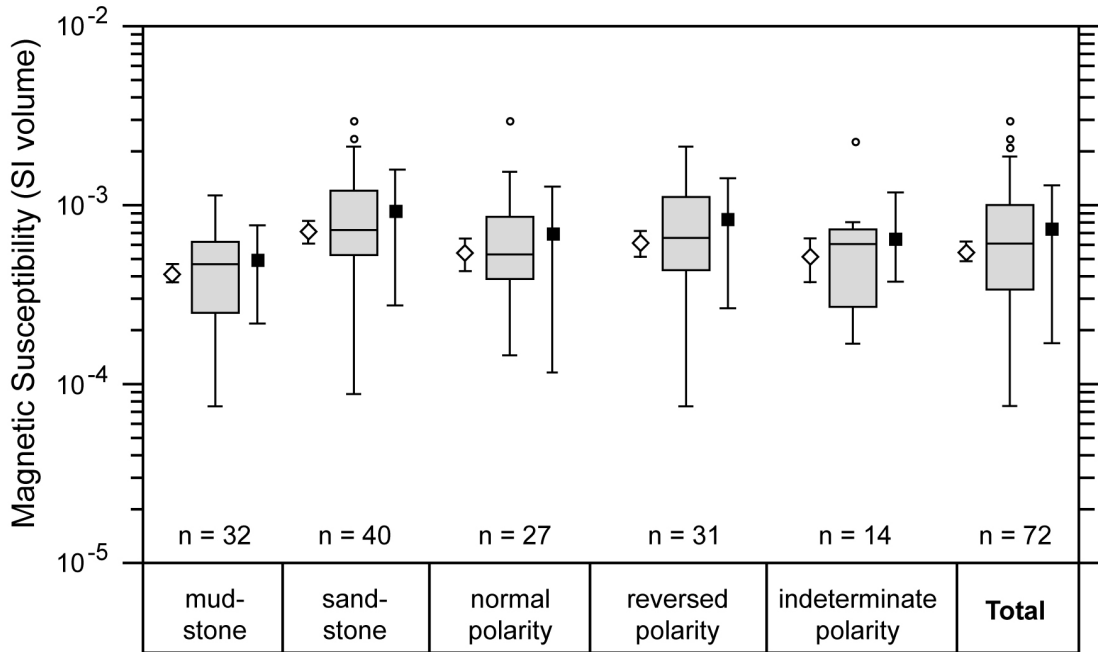
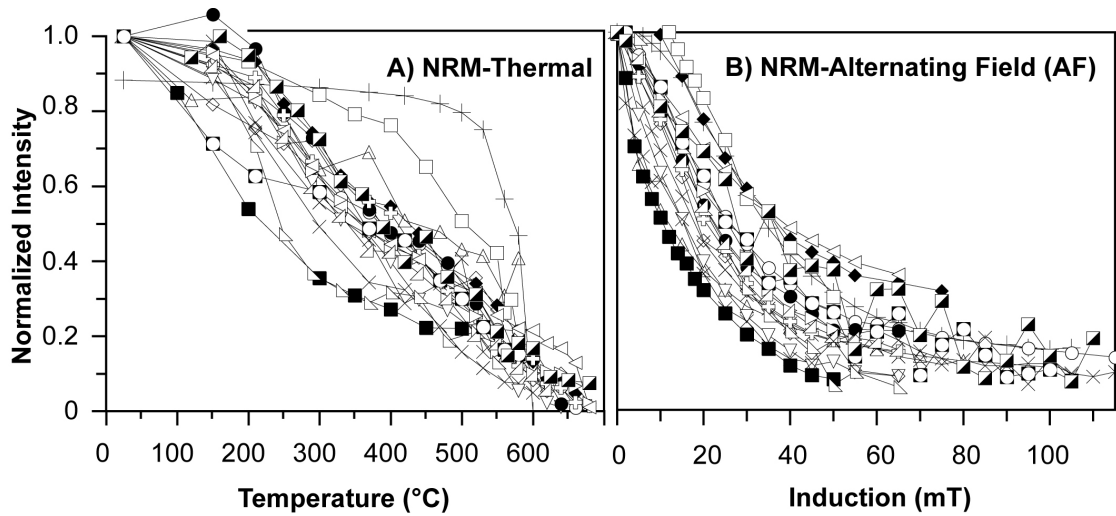


Figure 2.9. Box and whisker plots of median, quartile, and outlier values of bulk magnetic susceptibility for mudstone and sandstone in the Ceja Formation (N = 72 sites, 348 total measurements), including subsets illustrating normal, reversed, and indeterminate polarity sites. Each site represents the mean of at three to twelve specimens analyzed from the Los Lunas North (LLVN), Los Lunas South (LLVS), and CDRP-3 stratigraphic sections. The central line is the median, the gray box encompasses the 25th and 75th percentiles, and whiskers encompass the 10th and 90th percentiles. The white circles denote outliers. White diamonds are geometric means with standard errors represented by vertical bars. Black squares are arithmetic means and standard deviation.

The AF demagnetization of SIRM results showed a broader range of median destructive fields than shown by AF demagnetization of ARM (Fig. 2.11A-B). The modified Lowrie-Fuller test (Johnson et al. 1975) represents a way of better understanding the nature of the magnetic mineralogy in geologic materials and, specifically, if a population of relatively high- or low-coercivity phases dominate the remanence. This test, originally intended for igneous rocks with thermoremanent

magnetization (TRM), is applicable to magnetite-dominated materials where the ARM acquired in a field of about 100 mT activates most of the population of magnetite grains. The comparison of AF demagnetization responses of normalized NRM, ARM, and SIRM is based on the experimental observation that the AF demagnetization response of weak-field TRM (i.e., NRM) differs from that of strong-field TRM (i.e., SIRM) for assemblages dominated by single-domain and multi-domain particles. Notably, for populations dominated by large, multi-domain grains, SIRM requires higher destructive fields than ARM to reach the same normalized level. Overall, comparison of AF demagnetization response of ARM and SIRM by the 18 specimens is inconclusive and suggests that most of the materials selected for these tests are a mixture of relatively fine-grained, higher-coercivity grains, and some coarser-grained magnetic phases.

In IRM acquisition experiments, fifteen of these specimens showed saturation by about 0.5 T or less (Fig. 2.11C), indicating magnetite as the dominant magnetic phase. Three mudstone specimens (LLVN40-1a, TA3-20-4b, and CSA04e2) required fields above about 1.75 T, and showed less than 2 to 13 percent unblocking above 250° C, indicating that hematite is an important phase in some of the mudstones. With the exception of specimen LLVN40-1A (Fig. 2.11C-D), all specimens reveal a coercivity of remanence below about 70 mT, indicating that magnetite is the dominant magnetic phase in these materials.



EXPLANATION		
—+— Z4-1d: Tc (Nomlaki Tuff, R, A)	—□— PLU4b-3: Tca (ms, R, B)	—◁— LLVN36-3C: Tcrp (ss, R, C)
—X— CDRP3-21-2c: Tcrp (ms, N, A)	—■— PLU11a5: QTsa (ms, N, B)	—▷— LLVS02-3c: Tcl (ss, R, B)
—△— CSA04e2: Tca (ms, N, B)	—○— TA3-20-4b: QTsa (ms, R, A)	—◁— LLVS05-1a: Tcl (ss, R, A)
—▽— LLVN24-2C: Tca (ms, N, A)	—●— LLVN09-2A: Tca (ss, R, A)	—X— CDRP3-22-1a: Tcrp (ss, N, C)
—◇— LLVN25-1D: Tca (ms, N, A)	—⊕— LLVN20-1D: Tca (ss, N, B)	—□— CDRP3-2b: To (ss, N, C)
—◆— LLVN40-1A: Qsc (ms, R, B)	—▷— LLVN22B-3A: Tca (ss, R, A)	—■— CDRP-CL23c-3: Tcrp (ss, R, C)

Figure 2.10. Normalized demagnetization response curves for mudstone (ms), sandstone (ss), and volcanic ash (Nomlaki tuff) specimens taken from the Ceja (Tca and Tcrp) and Sierra Ladrones (QTsa) Formations. Also indicated are normal (N) and reverse (R) polarity specimens and quality assignments (A-C). A: Thermal demagnetization of natural remanent magnetization (NRM-thermal). B: Alternating-field demagnetization of natural remanent magnetization (NRM-AF).

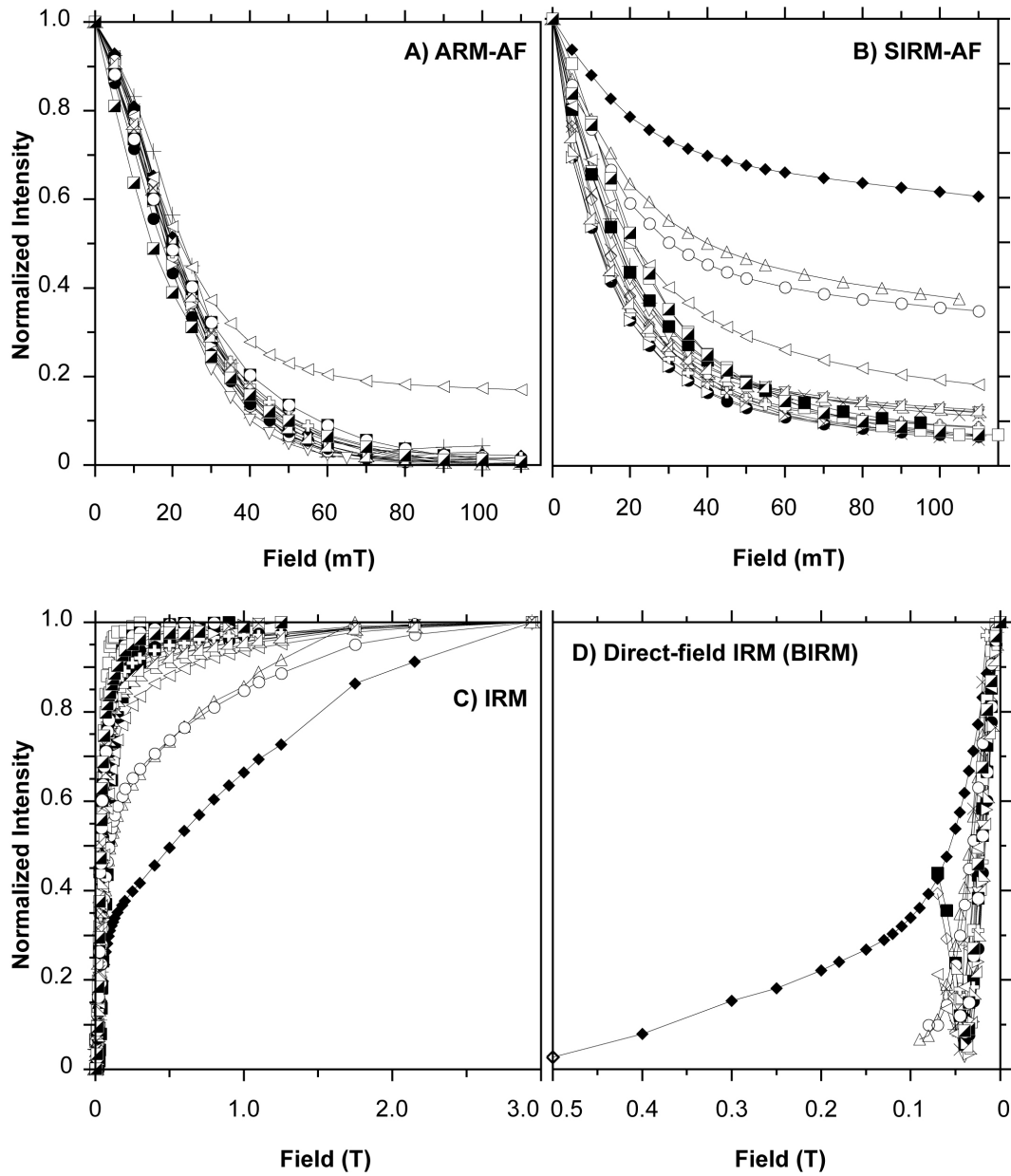


Figure 2.11. Normalized demagnetization response curves for specimens. Labels, polarity, and texture are listed on Figure 2.10. A: Alternating-field demagnetization of anhysteretic remanent magnetization (ARM-AF). B: alternating-field demagnetization of saturation isothermal remanent magnetization (SIRM-AF). C: Acquisition of isothermal remanent magnetization (IRM). D: Direct-field demagnetization of IRM (BIRM).

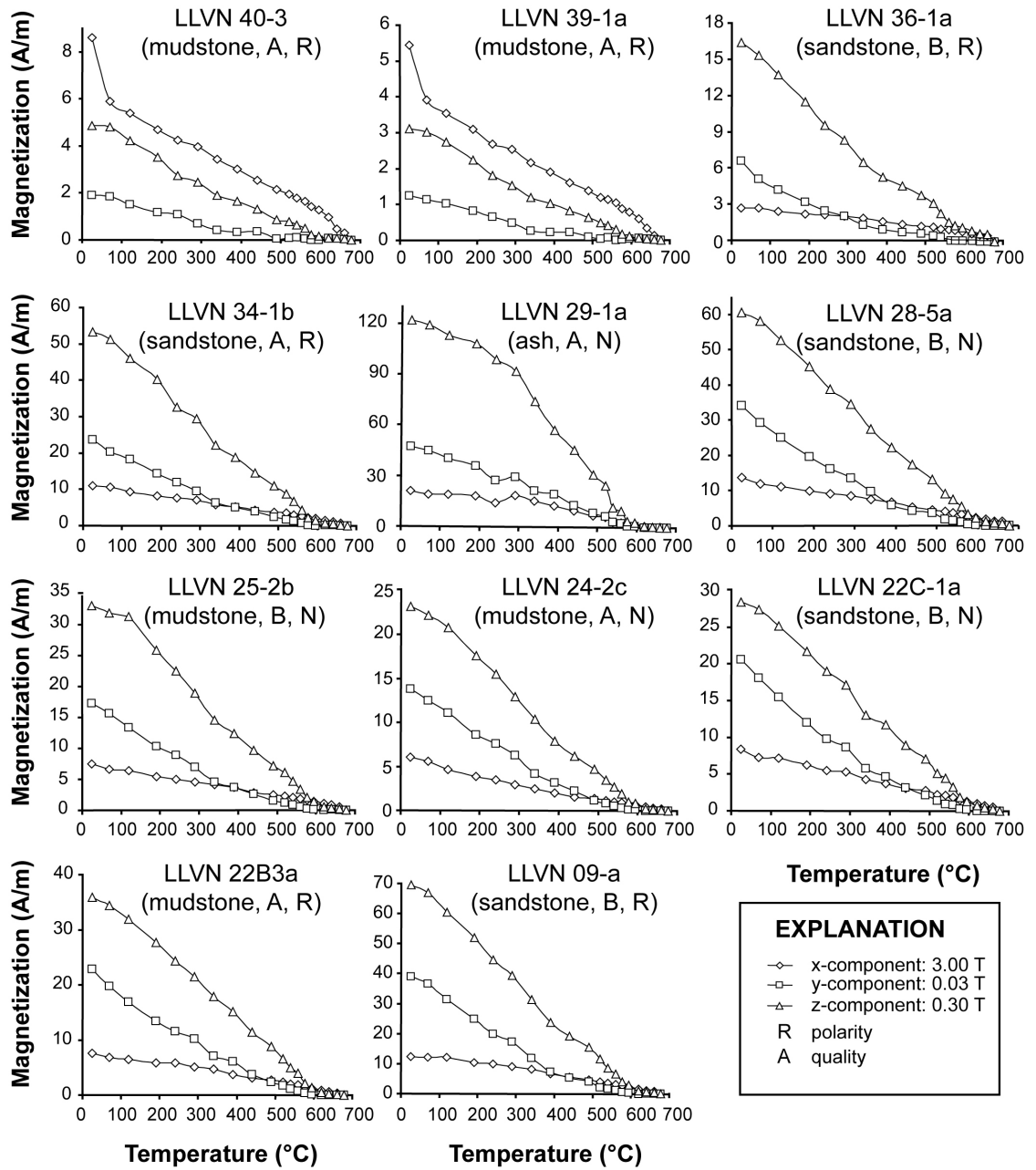


Figure 2.12. Plots showing thermal demagnetization response curves for three-component isothermal remanent magnetization (IRM) acquired in DC fields of 3.0, 0.3, and 0.03 T, following the approach of Lowrie (1990). Specimens include mudstone, sandstone, and volcanic ash yielding normal (N) and reverse (R) polarity magnetization and A-C quality assignments.

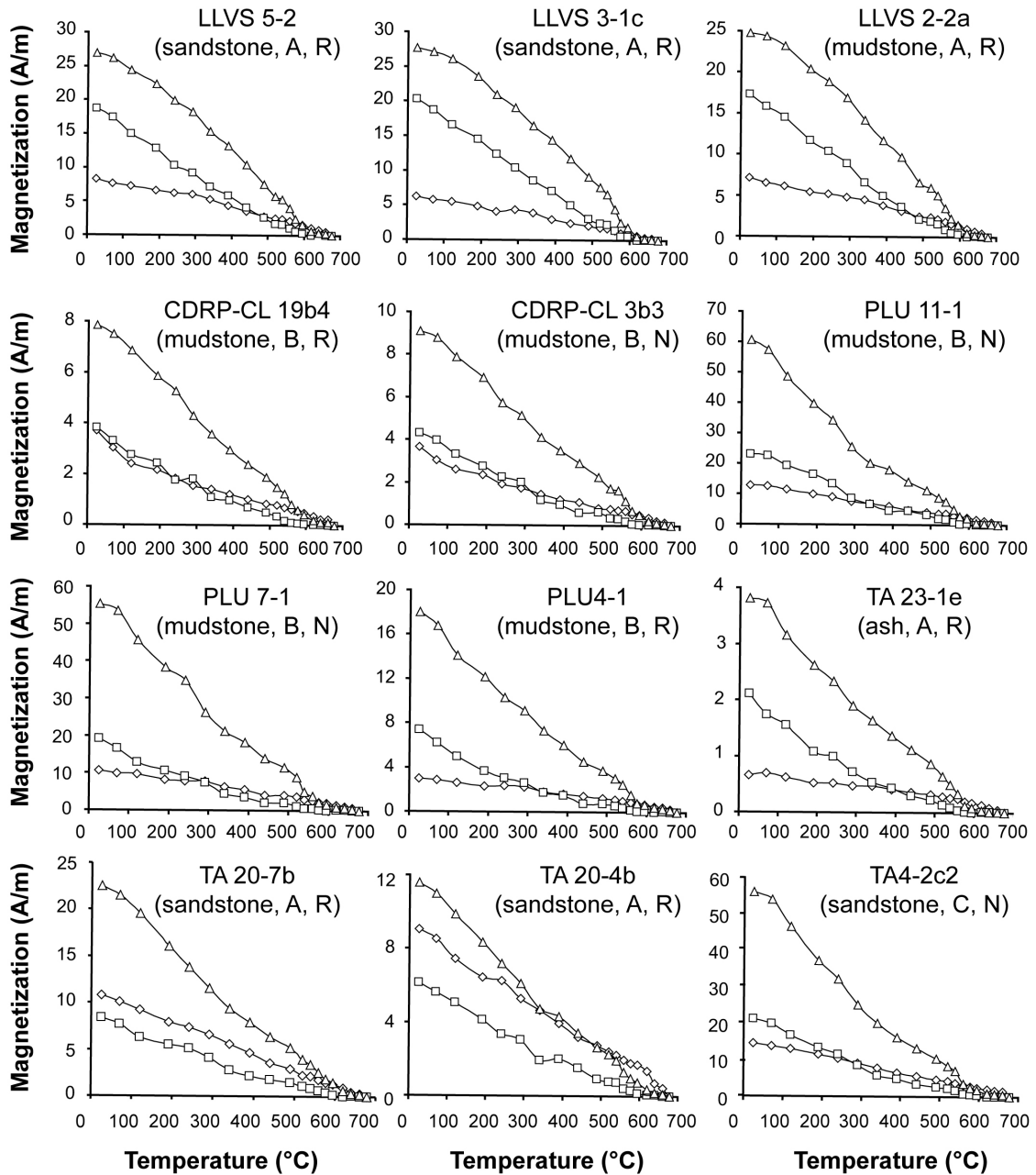


Figure 2.12 (continued).

Twenty-three specimens subjected to thermal demagnetization of three-component IRM (Lowrie, 1990) reveal overall consistent behavior (Fig. 2.12). For most of the specimens, the dominant IRM was that imparted parallel to the 0.3 T field. This magnetization was more than 95 percent unblocked by about 580° C. The next dominant

component was that imparted parallel to the 0.03 T field, and was also at least 95 percent unblocked by 580° C. The IRM component imparted parallel to the high coercivity (about 3.0 T) field showed minimal unblocking below about 580° C, and became the highest intensity component above 600° C.

Response to thermal demagnetization of the three-component IRM is interpreted to indicate that a magnetic phase in most of these materials is magnetite and titanomagnetite of relatively fine-grained size (of a few tens of microns maximum diameter), and thus of intermediate coercivity. The observation that the IRM component acquired at 0.03 T was never dominant implies the lack of very coarse-grained, low-coercivity magnetite/titanomagnetite as the magnetic carrier. Specimens LVN39-1 and LVN40-3 are exceptions and are consistent with the IRM acquisition data as the dominant component was acquired in a field of 3.0 T. This magnetization was partially unblocked below 100° C, with a very gradual decrease to full unblocking near 680° C. Hematite, and possibly goethite, is the dominant magnetic phase in the deposits represented by these specimens, which were taken from paleosols that were subjected to post-depositional modification (e.g., paleosols).

The quality of the response to progressive AF and thermal demagnetization, and thus the quality of our interpretation of the magnetic polarity in these deposits, are assigned using a simple four-tier quality assessment using orthogonal vector diagrams (Zijderveld, 1967), based in part on the approach used by Hudson et al. (1999). Figure 2.13 shows examples of orthogonal vector diagrams of AF and thermal results for normal and reverse polarity specimens. Specimen polarities were assigned the highest quality (A) if they had linear or slightly curvilinear trajectories that trended toward the

origin on orthogonal vector diagrams and if more than half of the natural remanence was randomized over the 15-65 mT interval or unblocked between about 100 and 580° C. Specimens were rejected where the mean angular dispersion exceeded 15 degrees. Quality A specimens (representing 22% of all specimens) show unambiguous polarities with stable endpoint trajectories and mean angular dispersions of unanchored linear fits of less than 10 degrees. Quality B specimens (24%) showed a defined polarity, but had irregular or partly curved demagnetization trajectories that typically trended toward the origin. Specimens with quality B polarities also have mean angular dispersions of less than 15 degrees. Low quality (quality C, 18%) specimens exhibit erratic trajectories, but still yield a relatively consistent polarity at the site level. Assigning polarities to quality C specimens is more subjective than for the higher quality specimens. In rare cases, polarity was assigned on basis of stratigraphic position relative to higher quality neighboring sites. Specimens yielding incoherent or un-interpretable demagnetization behavior, or yielding mixed polarity results are assigned quality D (36% of the specimens measured) and are rejected from further analysis.

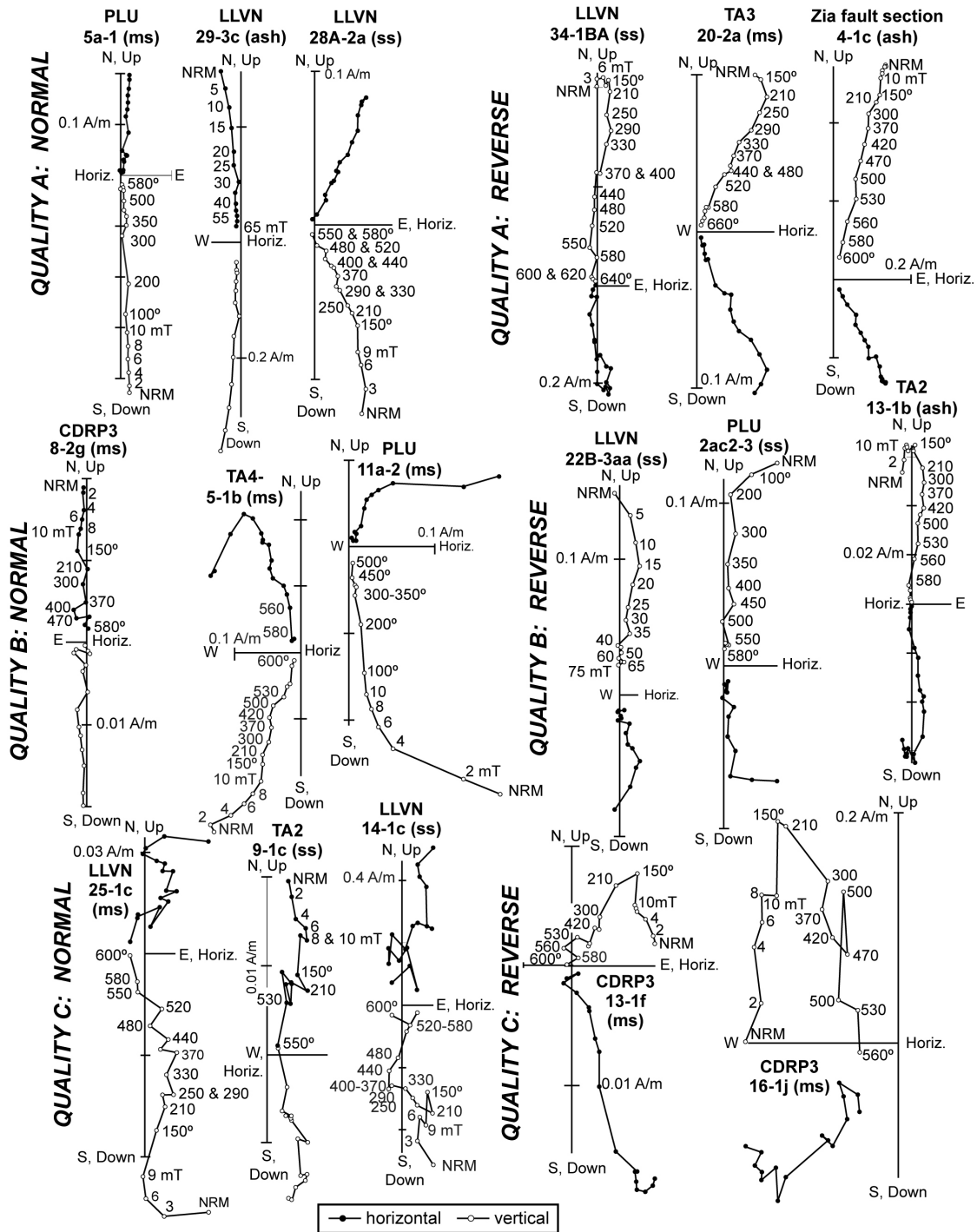


Figure 2.13. Examples of alternating-field and thermal demagnetization results for normal and reverse polarity specimens from sections CDRP-CL, CDRP3, LLVN, LLVS, CSA, PLU, and TA2. Orthogonal demagnetization diagrams (Zijderveld, 1967) show the endpoint of the magnetization vector (in stratigraphically corrected coordinates) plotted onto the horizontal plane (filled circles) and the true vertical plane (open circles). Typical quality A, B and C results for volcanic ash (ash), mudstone (ms), and sandstone (ss) specimens are shown.

Sites were grouped into four classes following the approaches of Opdyke et al. (1977) and Johnson et al. (1982). Class I sites have at least three statistically significant directions from three or more independent samples and have α_{95} confidence limits less than 20 degrees (Appendix B). Class II sites have 3 or more statistically significant directions that are not significant at the 95 percent confidence level, but the polarity determination is not in doubt. Sites are of class III status if the α_{95} confidence limit exceeded 35 degrees. Class III sites have dispersed vectors and were only used to corroborate polarity from stratigraphically adjacent class I sites. Class IV sites are defined by only one accepted specimen and are also only used to corroborate polarity with stratigraphically adjacent class I sites. A fifth category (class V) involves sites that contain specimens of poor quality (C or D) or yielded multiple polarity interpretations were rejected.

For each specimen, principal component analysis was used to determine the least-squares best-fit line of the characteristic component of magnetization (Kirschvink, 1980; and Jones, 2002). Demagnetization quality and magnetic polarity were interpreted using orthogonal vector diagrams (Fig. 2.13). The greatest weight in assigning polarity was given to the demagnetization response over the interval between 15 mT and 115 mT or about 120° and 580° C. Cubic spinel minerals, such as magnetite that would most likely carry an early acquired detrital remanence, typically are randomized or unblocked over these intervals. Many specimens contained a low-coercivity, positive-inclination component of probable viscous origin that was removed above 15 mT or 120° C. Response to thermal demagnetization shows the removal of a low-temperature overprint (possibly carried in goethite) by 200° C (Liu et al., 2006). At successively higher

temperatures, consistent magnetization directions were generally isolated between 420° and 560° C, above which large decreases in magnetization intensity or sporadic directional changes were observed. This behavior supports the conclusion that magnetite is the primary carrier of the characteristic remanent magnetization for nearly all of the specimens, and is supported by AF demagnetization of ARM and IRM acquisition experiments (Fig. 2.11). After treatment of specimens to 580° C, some retain a higher unblocking temperature component that is probably carried by hematite.

Specimen data were combined using Fisher (1953) statistics to determine mean site directions (Table 2.4). For a site comprised of three specimens, a Fisher R value greater than 2.62 is statistically significant at the 95 percent confidence level. Site mean-directions typically show interpretable magnetic polarity (Fig. 2.14). The assignment of normal polarities for specimens was more rigorously scrutinized than for reverse polarities because of the possibility of strong viscous overprinting or diagenetic modification during the Brunhes normal-polarity chron. Virtual geomagnetic pole (VGP) latitude (and inclination) values are calculated from the site mean directions and are used where the interpretation of directional data is ambiguous (Appendix B).

Paleomagnetic Results

A total of 171 sites were collected in the upper Miocene through Pleistocene alluvial deposits across 425 m of stratigraphic thickness. Five sites were collected from the underlying Navajo Draw Member of the Miocene Arroyo Ojito Formation, and three sites were collected in the Pleistocene unit of San Clemente. Within the Ceja and Sierra Ladrones Formations, 108 (63%) sites were class I, 16 (9%) sites were class II, 1 (<1%)

site was class III, 2 (1%) sites were class IV, and 44 (26%) sites were class V. Two out of three sites were accepted in the unit of San Clemente, and three out of five sites were accepted in the Navajo Draw Member. Of the 31 sites in the Sierra Ladrones Formation, nearly 60 percent were suitable for polarity interpretation. The remaining sites, comprising about 77 percent of the total sample population, were taken from the Ceja Formation; 67 percent of those sites were accepted for polarity interpretation. Mean site declination, inclination and virtual geomagnetic pole (VGP) values are reported for class I and II sites in Appendix B.

Mean orientations of all class I sites are listed in Table 2.4. The tilt-corrected mean of all class I normal polarity sites is $D = 2.8^\circ$, $I = 45.0^\circ$ ($N = 58$ sites), and all class I reverse polarity sites is $D = 180.2^\circ$, $I = -41.7^\circ$ ($N = 50$ sites; Fig. 2.14). The combined, tilt-corrected mean of all class I sites, after rotating the reverse polarity directions to the northern hemisphere ($D = 1.6^\circ$, $I = 43.5^\circ$, $N = 108$ sites, Table 2.5) is within a few degrees of all class I sites (Fig. 2.14). The tilt-corrected mean of all class I sites is 19 degrees shallower than the present-day field ($D = 10.0^\circ$, $I = 62.4^\circ$, NOAA Geophysical Data Center, 2005), and 8 degrees shallower than the time-averaged inclination of the dipole field ($I = 54.5^\circ$; Fig. 2.14). The tilt-corrected mean of all class I sites for the Sierra Ladrones Formation ($D = 0.8^\circ$, $I = 53.3^\circ$, $N = 15$ sites, Table 2.5) is similar to the time-averaged inclination of the dipole field and is about 11 degrees steeper than the tilt-corrected mean inclination of the Ceja Formation ($D = 1.6^\circ$, $I = 42.5^\circ$, $N = 48$ sites, Table 2.5).

Table 2.4. Statistical parameters for class I sites.

Section		N	R	K	α_{95} (°)	Dec. (°)	Inc. (°)
<u>All sites (N)</u>							
	Geo	58	53.5	12.76	5.4	3.5	47.1
	Strat	58	53.9	13.74	5.2	2.8	45.0
<u>All sites (R)</u>							
	Geo	50	45.4	10.64	6.5	181.9	-45.6
	Strat	50	45.4	10.69	6.5	180.2	-41.7
<u>All sites (R)*</u>							
	Geo	48	44.7	14.04	5.7	179.7	-47.1
	Strat	48	44.6	14.01	5.7	178.1	-43.2
<u>All Ceja Fm (N)</u>							
	Geo	47	43.7	13.94	5.8	4.2	44.7
	Strat	47	44.1	15.73	5.4	2.9	42.3
<u>All Ceja Fm (R)</u>							
	Geo	38	34.9	12.07	7.0	181.9	-47.0
	Strat	38	34.9	12.07	7.0	180.0	-42.6
<u>All Sierra Ladrones Fm (N)</u>							
	Geo	7	6.6	14.83	16.2	14.9	60.3
	Strat	7	6.6	15.03	16.1	17.8	59.5
<u>All Sierra Ladrones Fm (R)</u>							
	Geo	8	7.9	65.52	6.9	169.3	-46.7
	Strat	8	7.9	60.85	7.2	170.4	-46.6

Notes: N—number of sites averaged; R—Fisher statistic; *k*—precision parameter; α_{95} —cone of confidence; Dec—declination; Inc—inclination. Geographic (Geo) and tilt-corrected (Strat) declination and inclinations shown. (N) = normal sites; (R) = reversed sites. Asterisk (*) denotes removal of 2 outliers (CLS sites S11 & S25 in section CDRP-CL) with southward declination with positive inclination.

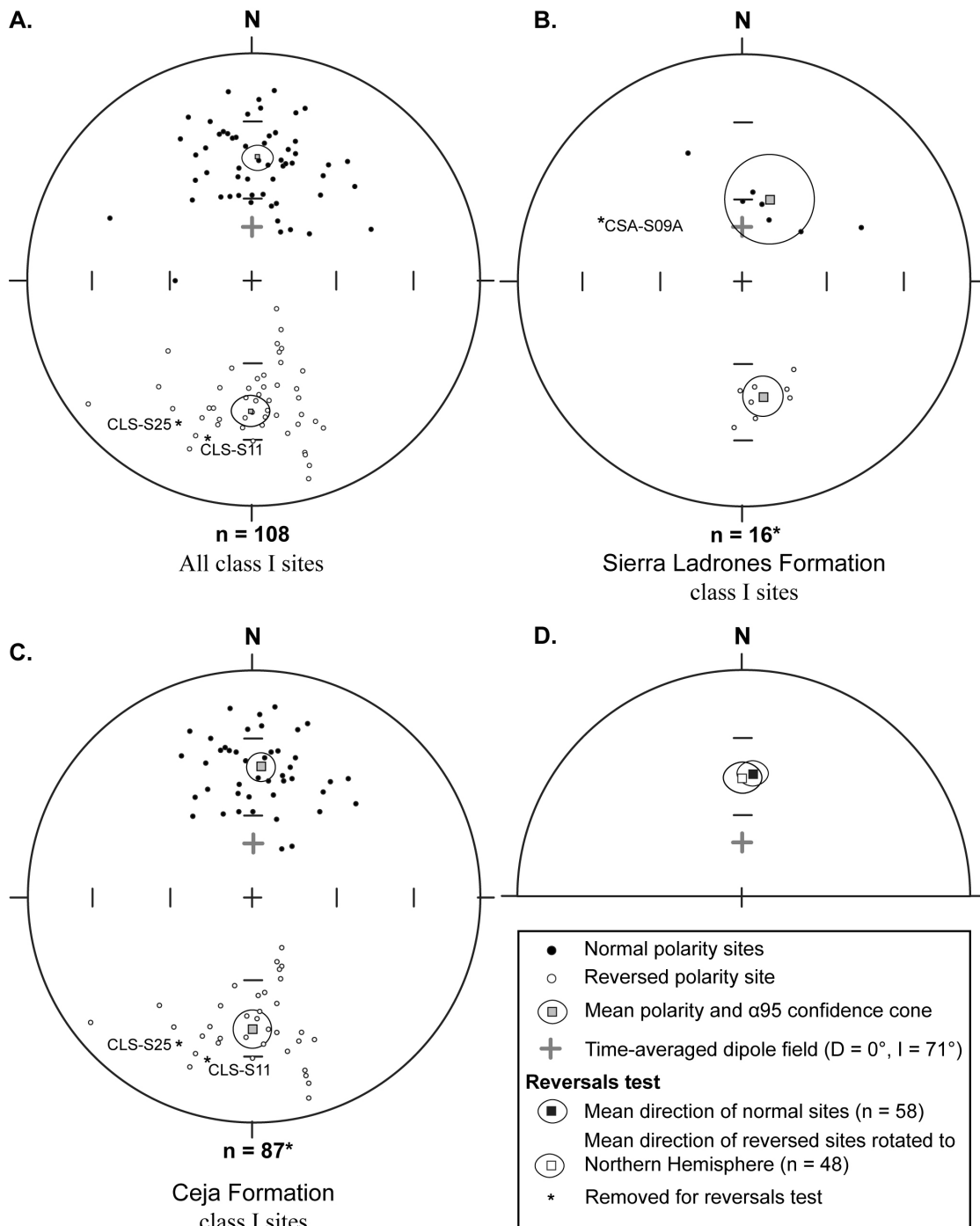


Figure 2.14. Equal-area projections showing site and grand-mean directions for accepted sites. A: All class I sites. B: Class I sites in the Sierra Ladrone Formation. C: Class I sites in the Ceja Formation. D: Reversals test (McFadden and McElhinny, 1990) showing grand mean direction of all class I sites, with reverse polarity sites inverted through origin to the lower hemisphere. Asterisks denote sites removed for reversals test. CLS refers to stratigraphic section CDRP-CL.

Table 2.5. Statistical parameters for rotated class I sites.

Section		N	R	<i>K</i>	α_{95} (°)	Dec. (°)	Inc. (°)
<u>All sites</u>							
	Geo	108	98.9	11.77	4.1	2.7	46.4
	Strat	108	99.2	12.18	4.1	1.6	43.5
<u>All reverse sites*</u>							
	Geo	48	47.9	15.73	5.4	0.7	47.9
	Strat	48	44.9	15.27	5.4	359.1	44.0
<u>Ceja Fm sites</u>							
	Geo	85	78.6	13.15	4.4	3.2	45.8
	Strat	85	79.0	13.99	4.3	1.6	42.5
<u>Sierra Ladrones Fm sites</u>							
	Geo	15	14.3	19.06	9.0	358.9	53.5
	Strat	15	14.3	18.73	9.1	0.8	53.3

Notes: N—number of sites averaged; R—Fisher statistic; *k*—precision parameter; α_{95} —cone of confidence; Dec—declination; Inc—inclination. Geographic (Geo) and tilt-corrected (Strat) declination and inclinations shown. (N) = normal sites; (R) = reversed sites. Asterisk (*) denotes removal of 2 outliers (CLS sites S11 & S25 in section CDRP-CL) with southward declination with positive inclination.

The shallower inclination values for class I sites relative to the present-day and time-averaged dipole fields probably reflects a shallowing of inclination due to sediment compaction (e.g., Sun and Kodama, 1992). Combined mean inclinations, with reverse polarity directions inverted to north-seeking, positive-inclination values, in the Sierra Ladrones Formation are about 21 percent steeper than those in the Ceja Formation, which may have been compacted by nearly one-fifth of its original thickness (see below).

To determine if the normal and reversed populations are statistically antipodal at the 95 percent confidence level, a reversals test was conducted on all class I sites (Fig. 2.14D & Table 2.5), following the approach of McFadden and McElhinny (1990). The calculated critical angle γ_c of 8.17 degrees between the mean directions of the two populations provides a positive reversals test with a calculated observed angle γ_o of 3.77 degrees. A reversals test conducted on 95 class I sites within the Ceja Formation also resulted in a positive test with a calculated critical angle γ_c of 8.62 degrees and observed

angle γ_0 of 2.20 degrees. A reversals test of 13 class I sites in the Sierra Ladrones Formation was inconclusive because of the low number of accepted sites.

Stratigraphy

Measured stratigraphic sections and geochronologic data provide a robust framework for developing a magnetic-polarity reversal chronology in the Ceja and Sierra Ladrones Formations. Stratigraphic correlations were established using geologically mapped boundaries and dated volcanic material as datum planes (Fig. 2.15). Many stratigraphic surfaces possess strongly developed calcic paleosols (Machette, 1985; Connell, 2008b; and Maldonado et al., 2007) that were described using pedogenic carbonate morphologic stages (Birkeland, 1999).

The stratigraphic nomenclature for the Santa Fe Group in the Albuquerque Basin was summarized by Connell (2004). Later refinements by Connell et al. (2007a & b) and Connell (2008a) are used in this study (Fig. 2.5). The Santa Fe Group is locally divided into three subgroups. The lower and middle subgroups include the Arroyo Ojito, Blackshare, Cerro Conejo, Popotosa, Tanos, and Zia Formations. These upper Oligocene through Miocene units were deposited within internally drained basins, where streams flowed off emerging uplifts and terminated onto ephemeral and intermittent playa lakes (Chapin and Cather, 1994). The upper part of the Santa Fe Group was deposited after establishment of through-going axial drainage (ancestral Rio Grande) that linked adjacent basins (Machette, 1978; Gile et al., 1981; Chapin and Cather, 1994; and Connell et al., 2005). These deposits include the Ceja, Cochiti, Sierra Ladrones, and Tuerto Formations. The Ceja and Sierra Ladrones Formations contain fluvial deposits

related to the development of the ancestral Rio Grande and its tributaries (Machette, 1978; and Connell, 2008a). Widespread, but thin, conglomeratic sandstone commonly overlie widespread, basin-flanking unconformities (Connell, 2004 & 2008a). Accumulations of alluvial, colluvial, and eolian sediment, such as the unit of San Clemente, are preserved in local structural depressions.

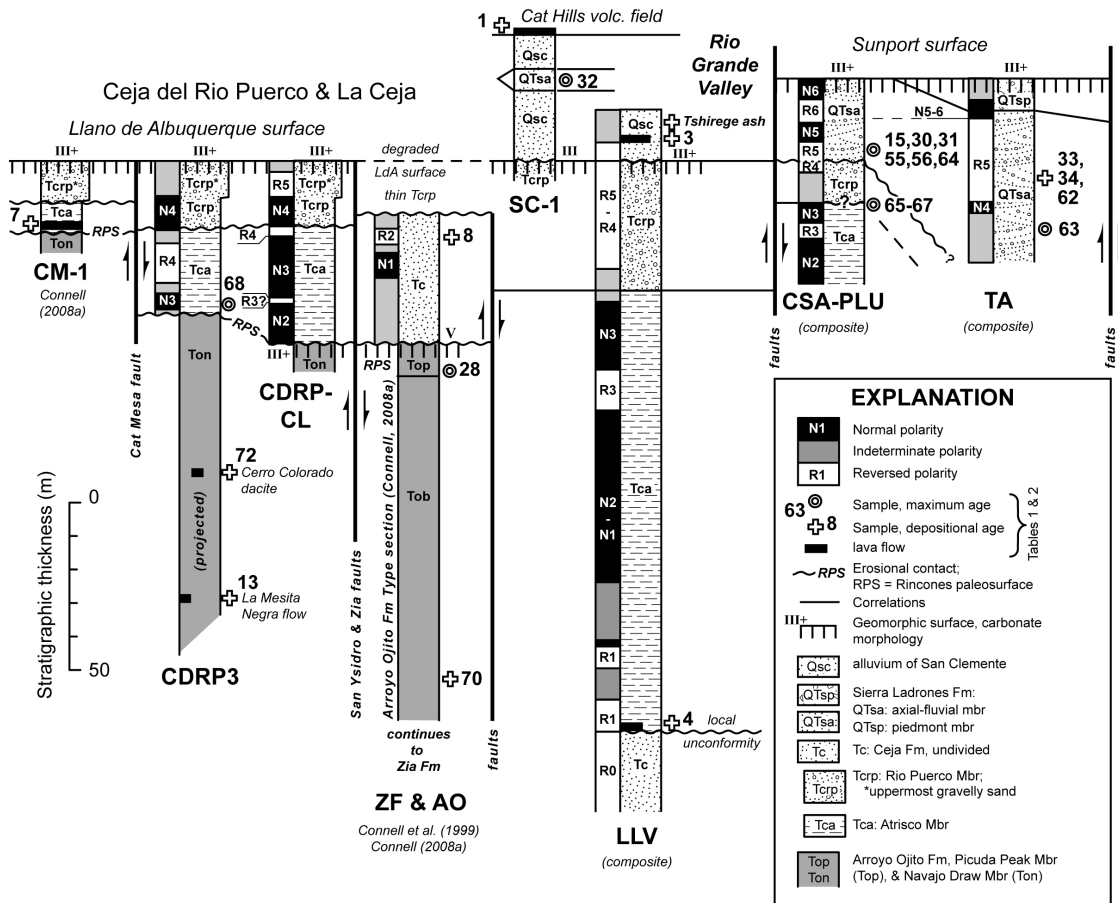


Figure 2.15. Stratigraphic fence diagram, illustrating correlations of measured stratigraphic sections. Measured sections were correlated using age determinations (Tables 2.1-2.3), the Rincones paleosurface, and the Llano de Albuquerque and Sunport geomorphic surfaces as stratigraphic datum planes. The Arroyo Ojito (AO), Zia fault (ZF), Cat Mesa (CM-1), and San Clemente stratigraphic sections (SC-1) were modified from previous studies (Connell et al., 1999; 2001c; and Connell, 2008a).

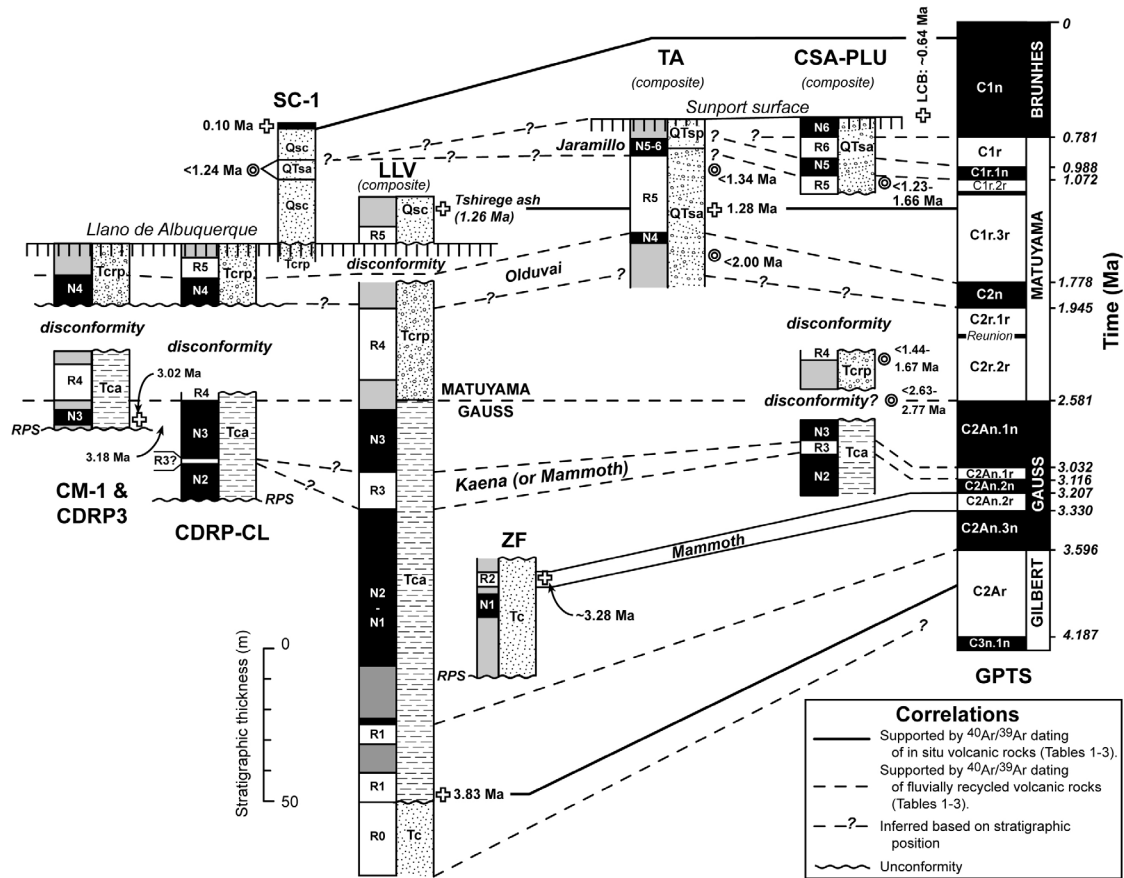


Figure 2.16. Stratigraphic fence diagram, illustrating correlations to the global geomagnetic polarity time scale (GPTS, Gradstein et al., 2005). Measured sections were correlated using the Gauss-Matuyama chron boundary, the Llano de Albuquerque and Sunport surfaces, and a 1.27 Ma ash correlated to the Tshirege Member of the Bandelier Tuff (Table 2.3). Stratigraphic sections are vertically separated across documented or inferred disconformities. The abbreviation LCB refers to the Lava Creek B tephra found within an inset terrace deposit of the Rio Grande (Connell et al., 2007a).

The geochronology of the Arroyo Ojito, Ceja, and Sierra Ladrones Formations was refined through correlation of the measured stratigraphic sections to the geomagnetic polarity time scale (GPTS, Gradstein et al., 2005) using dated temporal reference points that range from 9.7 to 0.1 Ma (Fig. 2.16, Tables 2.1-2.3). Twenty-three polarity intervals longer than 20 ka have been documented globally since the start of the Pliocene and are part of the GPTS. Nearly all of the major polarity chrons (and subchrons) in the past 4 Ma were recorded in this study. The Llano de Albuquerque and

Sunport surfaces, the 2.581-Ma Gauss-Matuyama chron boundary, and an early Pleistocene volcanic ash (Bandelier Tuff, Tewa Group) provide important chronostratigraphic datum controls for intrabasinal correlation (Fig. 2.16). The Réunion and Cobb Mountain subchrons (< 20 ka) were not recognized in this study. The preservation of such short-lived subchrons in an extensively channelized fluvial environment is probably low. The absence of these subchrons is supported by earlier estimates of Plio-Pleistocene sediment accumulation, which ranged from 22 to 33 m/Ma (Lozinsky, 1994). These rates would require sampling intervals of 0.4-0.7 m to capture these subchrons. Thus, the average sampling interval (see above) would have likely been too coarse to capture these short-lived subchrons.

Miocene Deposits

Exposed Miocene sections in the Albuquerque Basin contain alluvial, eolian, and volcanoclastic deposits of the Arroyo Ojito, Blackshare, Cerro Conejo, Cochiti, Popotosa, Tanos, and Zia Formations (Fig. 2.5). The Tanos and Blackshare Formations (Connell et al., 2002) are well exposed along the northeastern flank of the basin and in the Hagan embayment. The lower to middle Miocene Zia Formation is exposed along the northwestern flank of the basin (Connell, 2004). It consists of eolian and fluvial sandstone and mudstone that represents deposition in a predominantly eolian setting with scattered interdune ponds and streams (Tedford and Barghoorn, 1999). Fluvial deposits of the Popotosa Formation are exposed in the southern part of the basin, and are also recognized in drill holes (Is2 on Fig. 2.3; Machette, 1978; Lozinsky, 1994; Cather et al., 1994; Connell et al., 2005; and Maldonado et al., 1999 & 2007). Popotosa mudstone

has been reported in deep oil-test wells near Los Lunas and Isleta Pueblo (Lozinsky, 1994), but has not been recognized farther north in drill holes beneath Albuquerque (Hawley and Haase, 1992, section IV).

The middle Miocene Cerro Conejo Formation is exposed along the northwestern flank of the Albuquerque Basin, where it contains eolian and fluvial sand and interbedded mudstone that was deposited between 14.5 and 9.5 Ma (Tedford and Barghoorn, 1999; and Connell, 2008a). This unit represents a transition from the largely eolian Zia Formation to the predominantly fluvial Arroyo Ojito Formation (Connell et al., 1999). The Cochiti Formation is a Miocene through lower Pleistocene succession of volcanic-bearing sandstone and conglomerate exposed along the southern flank of the Jemez Mountains (Smith and Lavine, 1996).

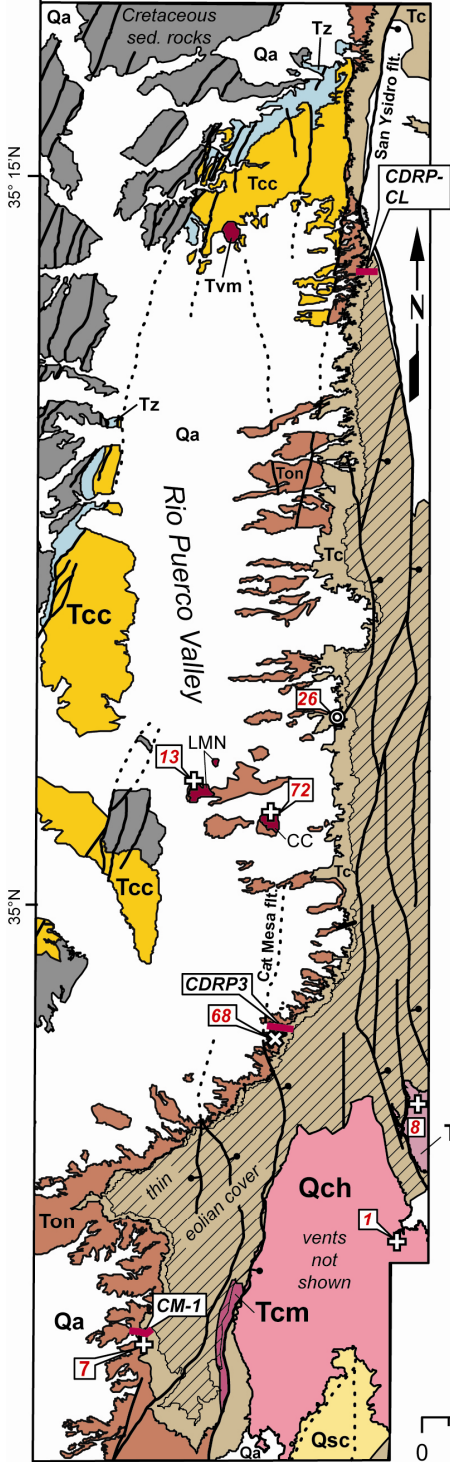
The Arroyo Ojito Formation is exposed along the western flank of the Albuquerque Basin. It was deposited between 9.0 and 6.3 Ma by southeast-flowing streams that originated on the Colorado Plateau and nearby uplifts, such as the Sierra Nacimiento (Connell et al., 1999). A widespread erosion surface called the Rincones paleosurface marks the top of the Arroyo Ojito Formation (Connell, 2008a). The age of the lower part of the Arroyo Ojito Formation is determined by upper Miocene basaltic lavas exposed near the top of the underlying Cerro Conejo Formation (Pazzaglia et al., 1998; Smith et al., 2001; and Chamberlin and McIntosh, 2007). Basaltic lava flows at Chamisa Mesa and Bodega Butte (Fig. 2.3), along the southern flank of the Jemez Mountains, yielded groundmass $^{40}\text{Ar}/^{39}\text{Ar}$ age determinations ranging between 9.67 and 9.04 Ma (Fig. 2.6, sample 14, Table 2.1; and sample 29, Table 2.2).

Other age control for the Arroyo Ojito Formation comes from the Rio Puerco Valley, where a basaltic lava flow at La Mesita Negra (Fig. 2.17) is interbedded with sandstone of the Navajo Draw Member. This flow yielded a $^{40}\text{Ar}/^{39}\text{Ar}$ age determination of 8.16 ± 0.05 Ma (Fig. 2.6, sample 13, Table 2.1; Maldonado et al., 2006). A dacitic volcanic vent at Cerro Colorado, about 3 km southeast of La Mesita Negra, yielded an age determination of 7.16 ± 0.47 Ma (Fig. 2.6, sample 72, Table 2.3). The basal edges of this feature rest on Navajo Draw sandstone, about 43-55 m below the Rincones paleosurface of Connell (2008a). The Loma Barbon Member of the Arroyo Ojito Formation contains ashes that range in age from 6.83 to 7.06 Ma (Fig. 2.6, samples 10-12, Table 2.1; and samples 69-71, Table 2.3). These ashes correlate to the Peralta Tuff Member of the Bearhead Rhyolite (e.g., Smith, 2001), which interfinger with the Arroyo Ojito Formation and lower parts of the Cochiti Formation in the northern part of the Albuquerque Basin and southeastern flank of the Jemez Mountains.

The Arroyo Ojito Formation generally coarsens up-section of the older (7.1-6.8 Ma) Peralta ashes (Connell, 2008b), culminating in deposition of the conglomeratic Picuda Peak Member by about 6.3 Ma. Lozinsky and Tedford (1991) reported an upward-coarsening trend in a 7-9 Ma section of the Popotosa Formation in the Gabaldon badlands, just southwest of the study area (Fig. 2.3). A maximum age of the top of the Arroyo Ojito Formation comes from a basaltic cobble about 20 m below the top of the Picuda Peak Member that yielded a groundmass $^{40}\text{Ar}/^{39}\text{Ar}$ age determination of 6.56 ± 0.33 Ma (Fig. 2.6, sample 28, Table 2.2).

Figure 2.17 (following page). Simplified geologic map along part of the Ceja del Rio Puerco and western margin of the Albuquerque Basin, illustrating the locations of major faults, volcanic features (LMN: La Mesita Negra; CC: Cerro Colorado), age-determination sample sites (Tables 2.1-2.3), and measured stratigraphic sections (described in text). Primary sample (“plus” symbol) denotes age determinations of volcanic fallout tephra or lava flows that represent emplacement or depositional ages. Samples of fluviably recycled tephra (“circle-in-circle” symbol) represent maximum ages. The Ceja Formation disconformably overlies the lower part of the Arroyo Ojito Formation (i.e., Navajo Draw Member) and the Cerro Conejo Formation. The Cat Mesa lava flow and CM-1 section are on the footwall of the Cat Mesa fault; section CDRP3 is northeast of the hanging wall. CDRP-CL is on the footwall of the San Ysidro fault.

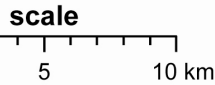
107° W



EXPLANATION

- Qa** Quaternary alluvium, undivided
- Qsc** Unit of San Clemente
- unconformity*
- QTg** Plio-Pleistocene gravels
Tuerto Fm & gravel of Lookout park
- unconformity*
- Llano de Manzano, Sunport, & Las Huertas surfaces; commonly covered by eolian sand
- QTsp** Sierra Ladrones Fm
piedmont member
- QTsa** Sierra Ladrones Fm
axial-fluvial member
- QTct** Cochiti Fm
- Llano de Albuquerque surface; commonly covered by Pleistocene & Holocene eolian sand
- Tc** Ceja Fm: Santa Ana Mesa Mbr (Tcs), Atrisco Mbr (Tca), Rio Puerco Mbr (Tcrp)
- Rincones paleosurface*
- Ts** Santa Fe Group, undivided
- Ton** Arroyo Ojito Fm, Navajo Draw Mbr
- Tcc** Cerro Conejo Fm
- unconformity*
- Tz** Zia Fm
- unconformity*
- pre-Santa Fe Group deposits
- Volcanic rocks**
- Qch** Cat Hills volcanic field (99-111 ka)
- Tcm** Cat Mesa lava flow (3.02 Ma)
- Twm** Wind Mesa lava flow (4.04 Ma)
- Tbs** Pliocene basaltic lavas (2.57-1.85 Ma)
- Tvm** Miocene volcanic rocks (8.16-7.16 Ma)

	horizontal bedding
	inclined bedding
	normal fault
*	vent
	primary age sample
	secondary age sample
	stratigraphic section
	cross section
	well & label



An important age determination for the Miocene succession comes from a bed of rhyolitic pumice in the Cochiti Formation exposed along the northern flank of the San Felipe volcanic field (Fig. 2.18). This pumice yielded a $^{40}\text{Ar}/^{39}\text{Ar}$ age on sanidine of 6.29 ± 0.08 Ma (Fig. 2.6, sample 10, Table 2.1) that correlates to the Cerrito Yelo tephra of the Peralta Tuff (Chamberlin and McIntosh, 2007). It is about 20-m below the 2.46-2.43 Ma basaltic lavas of the San Felipe volcanic field (Figs. 2.6 & 2.7, samples 5 and 6, Table 2.1; samples 16-19, Table 2.2; Smith et al., 2001). The age of this tephra suggests the presence of an unconformity or condensed stratigraphic section between upper Miocene and upper Pliocene rocks (Fig. 2.18). Geologic mapping north of the San Felipe volcanic field did not recognize any widespread unconformities within the Cochiti Formation (Smith et al., 2001); however, other workers reported multiple Miocene unconformities to the west (Chamberlin and McIntosh, 2007). The earlier (basinward) mapping of Smith et al. (2001) took place before dating of the Cerrito Yelo tephra and recognition of the Rincones paleosurface (described below), so it is not clear if the Cochiti Formation contains a widespread and mappable unconformity, or if it is a condensed section.

Over 1 km of Miocene through lower Pleistocene conglomerate and sandstone is exposed across a faulted relay ramp that formed between the northern flank of the Sandia Mountains and the Hagan embayment (Fig. 2.3; Kelley, 1977 & 1982; May et al., 1994; and Russell and Snelson, 1994). These deposits form a generally conformable stratigraphic succession that records unroofing of the adjacent Sandia Mountains (Connell and Wells, 1999).

Ceja Formation

The Ceja Formation contains fluvial sandstone, conglomerate, and mudstone deposited by large southeast-flowing streams and fluvial fans that drained the southeastern Colorado Plateau, San Juan Basin, Sierra Nacimiento, and southern Jemez Mountains (Connell, 2008a). Streams of the Ceja Formation drained roughly the same region as the Arroyo Ojito Formation; however, the Ceja Formation contains a greater variety of rock types than the Arroyo Ojito Formation and represents deeper unroofing of the western flanks of the Albuquerque Basin (Connell et al., 1999). The Ceja Formation thickens to the east (from about 20 m to over 420 m) and is bounded by a basal erosional surface (Rincones paleosurface), and an upper relict depositional surface called the Llano de Albuquerque surface (see below).

The Ceja Formation is divided into the Santa Ana Mesa, Atrisco, and Rio Puerco Members (Fig. 2.5). The Atrisco and Santa Ana Mesa Members contain sandstone and mudstone with minor pebbly sandstone interbeds. The Atrisco Member contains thickly bedded, mottled and massive to well-sorted, fine-grained, eolian sand (Figs. 2.19A & D). The Santa Ana Mesa Member is generally redder in color and contains coarser gravel than the Atrisco Member. The Rio Puerco Member is dominated by coarse-grained, medium to very thickly bedded, pebbly to cobbly sand with scattered cobbles and small boulders. The contact between the Atrisco and Rio Puerco Members is sharp and erosional along the Ceja del Rio Puerco. Gravelly beds in the Rio Puerco Member form overlapping, laterally and vertically stacked channels that commonly contain laminated to thinly bedded, low-angle, planar and locally trough cross-stratified sand and pebbly sand (Fig. 2.19B).

The Ceja Formation generally coarsens up-section, culminating in mesa-capping gravels of the Rio Puerco Member and a nearly 2-m thick accumulation of petrocalcic soils of the Llano de Albuquerque surface (Fig. 2.19A). Using borehole geophysical logs, Connell et al. (1998) interpreted an overall upward-coarsening trend in deposits overlying the Atrisco Member. This coarsening trend in the Ceja Formation was confirmed here by measuring the relative proportions of mud, sand, and gravel sizes along the Ceja del Rio Puerco and at El Cerro de los Lunas, or Los Lunas volcano (Fig. 2.3; Appendix C). Mudstone (12-24% of the section) and sandstone (72-81%) beds dominate the Atrisco Member along the Ceja del Rio Puerco, but gravels are a minor constituent (4-7%). The overlying Rio Puerco Member is dominated by gravel (35-48%) and sand (49-59%) with minor mud beds (3-6%).

This upward-coarsening trend is also reflected by gravel size (Appendix C). The lower part of the Atrisco Member contain medium pebbles (7 ± 3 cm, mean intermediate diameter of 5 ± 2 cm, N = 67 measurements), whereas, the upper part contains medium to coarse pebbles (17 ± 4 cm, mean intermediate diameter of 11 ± 3 cm, N = 26). The Rio Puerco Member contains coarse pebbles (21 ± 9 cm, mean intermediate diameter of 15 ± 6 cm, N = 42). Very coarse pebbles and coarse cobbles (40 to 110 cm in maximum diameter) are scattered at the top of the Rio Puerco Member.

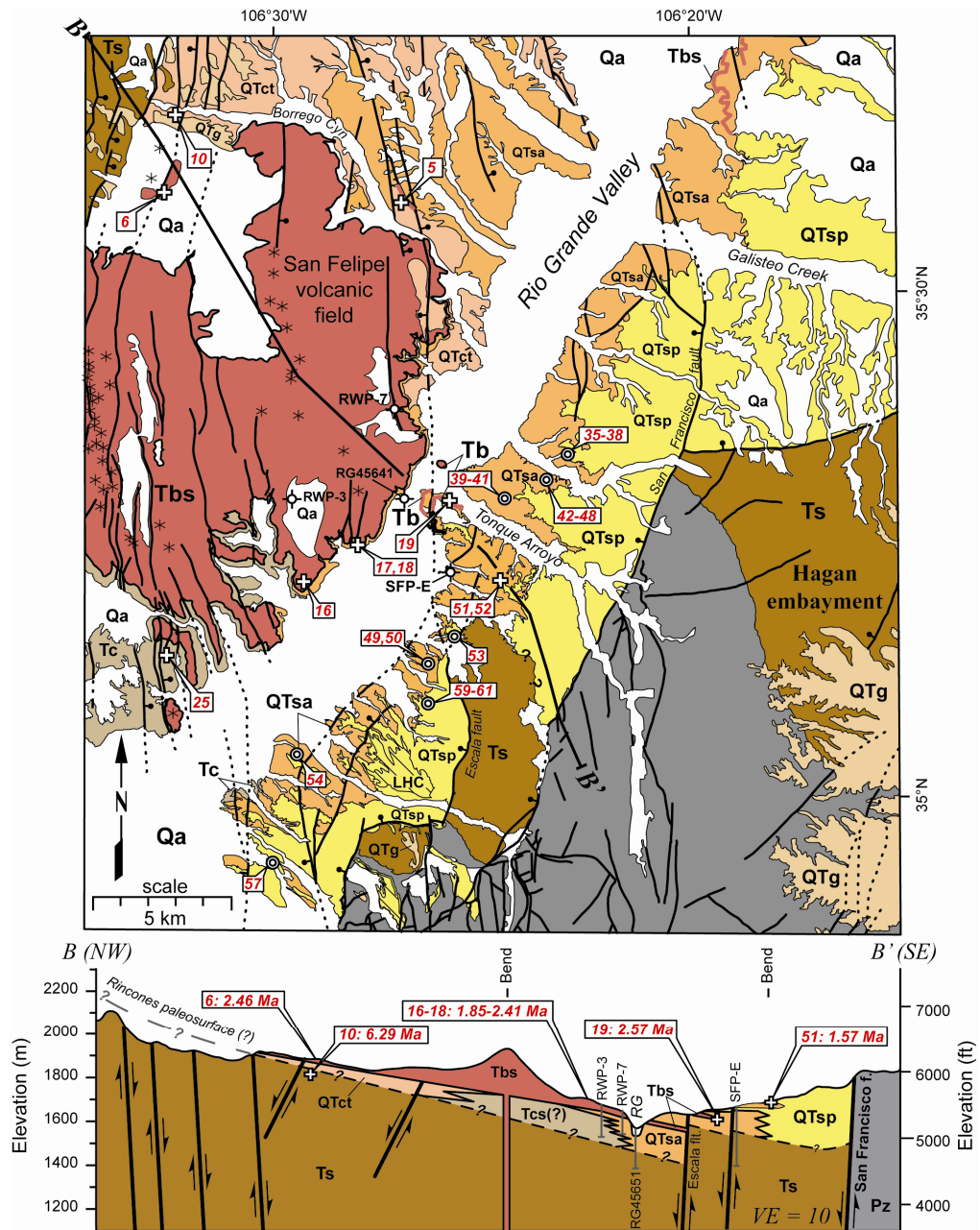
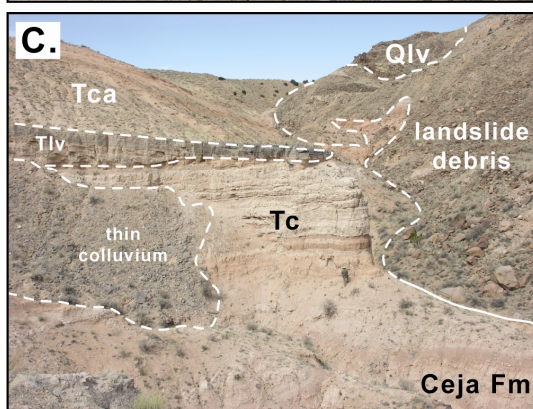
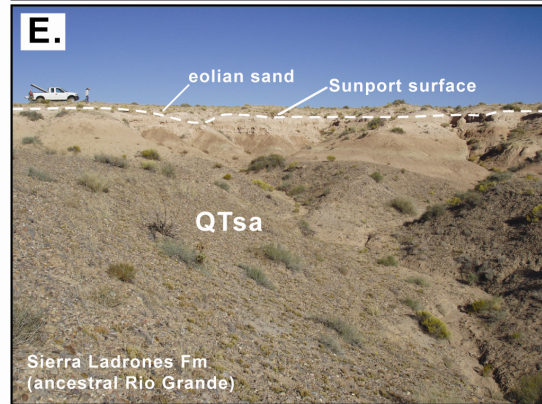
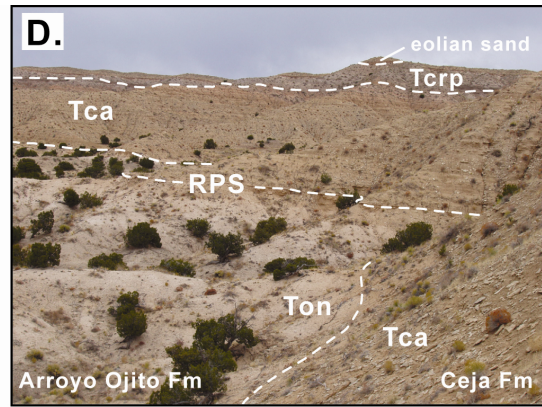


Figure 2.18. Simplified geologic map of the eastern part of the San Felipe volcanic field and eastern margin of the Albuquerque Basin (modified from Smith et al., 2001; and Connell, 2008b). Top Geologic Map. Numeric labels denote $^{40}\text{Ar}/^{39}\text{Ar}$ age determination sites on Tables 2.1-2.3. Explanation of map units and symbols are on Figure 2.17; additional units include the Santa Ana Mesa Member (Tcs) of the Ceja Formation. Las Huertas geomorphic surface (LHC, diagonal lines) marks a local depositional top of the Sierra Ladrones Formation. Bottom: Vertically exaggerated cross section B-B' (VE = 10) based on previous geologic mapping (Chamberlin et al., 1999; Smith et al., 2001; and Connell, 2008b). The cross section location is on the top figure. Stratigraphic interpretations of wells used in cross section were taken from a digital database (Connell, 2006).

Figure 2.19 (following page). Photographs of deposits in the study area. Units include the Navajo Draw Member (Ton) of the Arroyo Ojito Formation, Rio Puerco (Tcrp) and Atrisco (Tca) Members of the Ceja Formation (Tc), axial-fluvial (QTsa) and piedmont (QTsp) members of the Sierra Ladrones Formation, and the older (Tlv) and younger (Qlv) trachyandesitic lapilli tuff and lava flows at El Cerro de Los Lunas (Los Lunas volcano). Geologic contacts denoted by white lines. A: View to north of the Ceja del Rio Puerco (near the CDRP-CL section), an approximately 55-m high escarpment exposing Atrisco (Tca) and Rio Puerco (Tcrp) Members of the Ceja Formation that disconformably overlie upper Miocene sandstone of the Navajo Draw Member (Ton) of the Arroyo Ojito Formation. B: Cross-stratified pebbly sand in Rio Puerco Member (Tcrp) near the top of County Line section (CDRP-CL); 10 cm gradations on Jacob Staff. C: View to north of black lapilli of the older Los Lunas tuff (Tlv) overlying the LLVS section, and underlying the Atrisco Member (Tca) and younger trachyandesitic flows (Qlv) at Los Lunas volcano; 1.9-m tall person for scale. D: View to north of white petrocalcic paleosols with stage III+ pedogenic carbonate morphology developed on the Rincones paleosurface (RPS) along the Ceja del Rio Puerco, near the CDRP-CL section; trees and shrubs are less than 3 m tall. E: View to east of upper pumice-bearing, gravelly sand and mudstone of the axial-fluvial member of the PLU section and white petrocalcic soils of the Sunport surface (stage III+); truck is about 5 m long. F: Sharp boundary of gravelly sand of axial-fluvial member (QTsa) and overlying muddy sand of piedmont member (QTsa) of Sierra Ladrones Formation, at a gravel quarry northeast of Bernalillo, New Mexico. Exposures are about 15 m high.



Geochronology

Lava flows and fluvially recycled volcanic gravel in the Ceja Formation demonstrate a Pliocene age of deposition (Connell, 2008a; and Maldonado et al., 2007). The age of the Ceja Formation is refined by integrating isotopic and biostratigraphic age data into five composite stratigraphic sections that were sampled for magnetic polarity: CDRP3, CDRP-CL, CSA-PLU, LLV, and ZF (Figs. 2.20-2.22, 2.24, 2.26 & 2.27). The age of the base of the Atrisco Member increases into the basin across intrabasinal normal faults (Fig. 2.16). The 3.02-Ma Cat Mesa lava flow marks the base of the Atrisco Member on Cat Mesa and along the Ceja del Rio Puerco (Fig. 2.6, sample 7, Table 2.1). A volcanic ash adjacent to the Zia fault at La Ceja at the ZF section (Fig. 2.22) was geochemically correlated to the *ca.* 3.28 Ma Nomlaki Tuff (sample 8, Table 2.1). This ash yielded a reverse-polarity magnetization that is consistent with polarity data for the Nomlaki Tuff in eastern California (Reheis et al., 1991).

The Atrisco Member at CDRP3 and CDRP-CL contains normal- and reverse-polarity sites (Figs. 2.20 & 2.20) that indicate deposition during parts of the Gauss and Matuyama chrons (Fig. 2.16). The Santa Ana Mesa Member is locally capped by basaltic lavas of the San Felipe volcanic field (at Santa Ana Mesa), which yielded groundmass $^{40}\text{Ar}/^{39}\text{Ar}$ age determinations of 2.57 ± 0.11 Ma and 1.85 ± 0.10 Ma (Fig. 2.6, samples 19 and 16, Table 2.2). The Santa Ana Mesa Member contains an ash exposed in the spillway of the Jemez River dam that is about 42 m below these Pliocene basaltic lavas (Fig. 2.18). This spillway ash yielded a single-crystal $^{40}\text{Ar}/^{39}\text{Ar}$ age determination on hornblende of 3.81 ± 0.23 Ma (Fig. 2.6, sample 25, Table 2.3).

The thickest, most complete and accessible exposures of the Ceja Formation in the study area are along the flanks of El Cerro de los Lunas, also called Los Lunas volcano (Fig. 2.23; Kelley and Kudo, 1978; Love et al., 1998; Maldonado et al., 2007). A 210-m thick composite stratigraphic section was assembled by correlating distinctive marker beds and an angular unconformity (Fig. 2.24). El Cerro de los Lunas contains two overlapping trachyandesitic volcanoes that yielded groundmass $^{40}\text{Ar}/^{39}\text{Ar}$ age determinations of 3.83 ± 0.10 Ma and 1.26 ± 0.02 Ma (Fig. 2.7, samples 3 and 4, Table 2.1; Dunbar et al., 2001). The older event locally deformed a similarly aged bed of black lapilli tuff that was used to correlate the lower and upper parts of the LLV composite section (Figs. 2.19C & 2.23). This tuff overlies an unconformity having an angularity of about 45 degrees along the northern flank of the younger volcano. This boundary is subparallel to bedding where exposed at the southern flank. The abrupt change in the character of this stratal discontinuity and doming around the volcanoes suggest that this unconformity formed during emplacement, rather than representing a buried correlative of the Rincones paleosurface. Strata underlying the older lava flow yielded reverse polarity directions that are consistent with deposition during the later part of the Gilbert polarity chron, and after the normal polarity Cochiti subchron, at 4.187 Ma (Fig. 2.16). The top of the Ceja section contains a buried paleosol that is considered to be a buried correlative of the Llano de Albuquerque surface (Figs. 2.15 & 2.24). A bed of angular volcanic lapilli and blocks in the unit of San Clemente was deposited during the younger Los Lunas eruption.

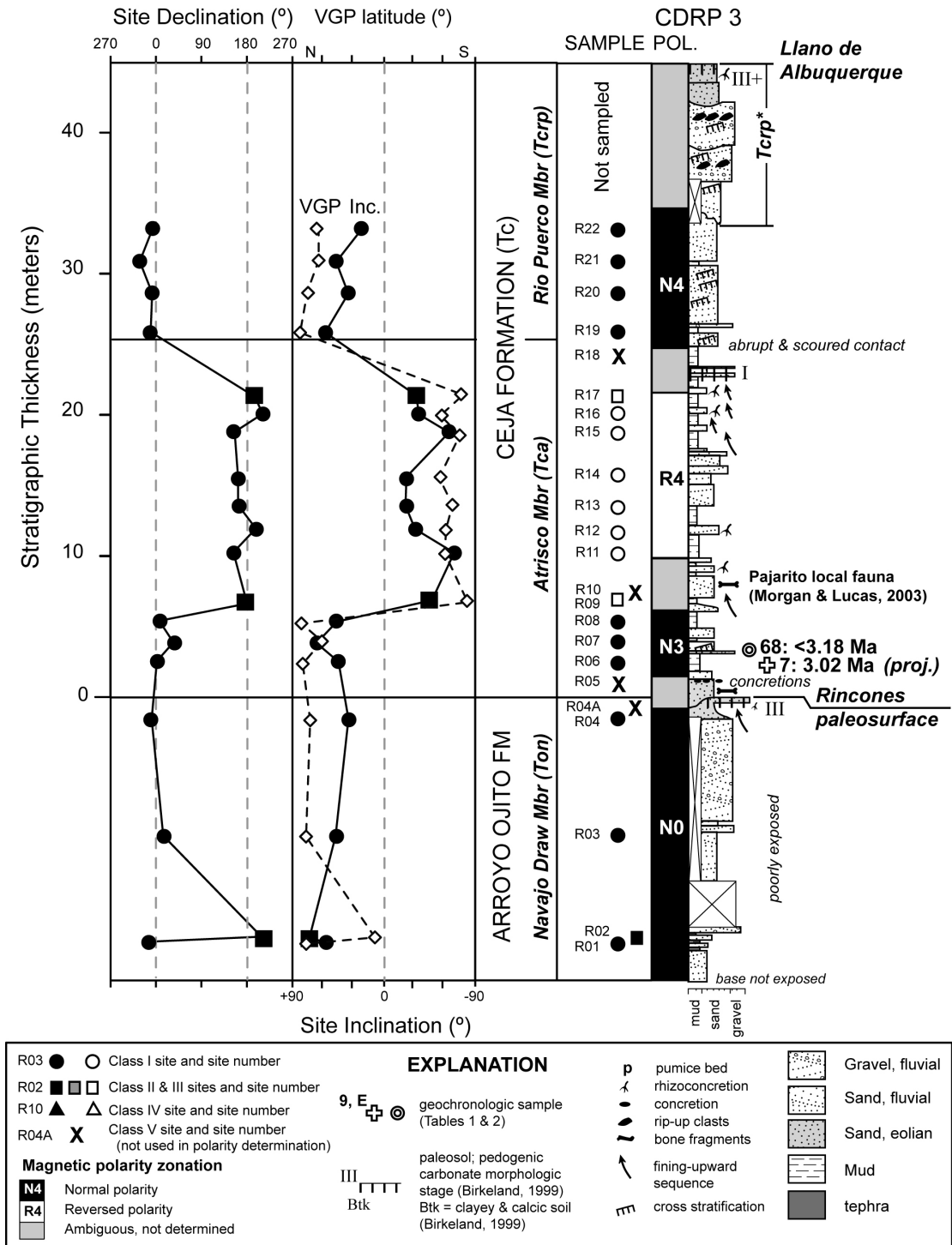


Figure 2.20. Lithostratigraphy and magnetic polarity stratigraphy of the CDRP3 stratigraphic section, magnetostratigraphic composite section (VGP = virtual geomagnetic pole latitude; Inc. = site inclination), and provisional magnetic polarity zonation. Lines connect stratigraphically consecutive sites. Age determination sites on Tables 2.1-2.3. Unit Tcrp* refers to the gravelly top of the Rio Puerco Member. Roman numerals denote pedogenic carbonate morphologic stage (Birkeland, 1999).

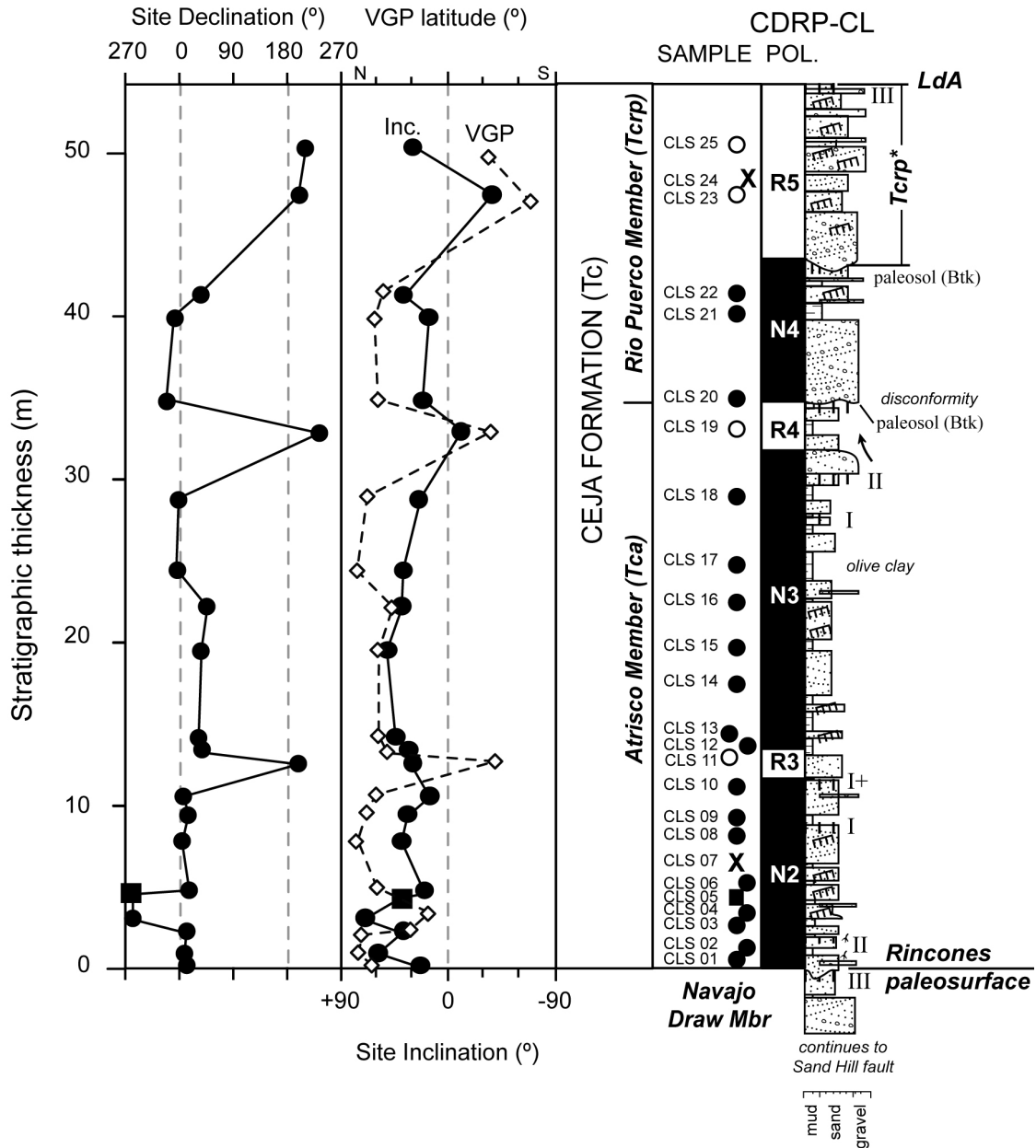


Figure 2.21. Lithostratigraphy and magnetic polarity stratigraphy of County Line (CDRP-CL) stratigraphic section, magnetostratigraphic composite section (VGP = virtual geomagnetic pole latitude; Inc. = site inclination), and correlation to a provisional magnetic polarity zonation. Lines connect stratigraphically consecutive sites. Refer to Figure 2.20 for explanation of symbols. Unit Tcrp* refers to the gravelly top of the Rio Puerco Member. Age determination sites on Tables 2.1-2.3. Roman numerals denote pedogenic carbonate morphologic stages; Btk refers to soil horizons in a buried paleosol with translocated clay and carbonate (Birkeland, 1999).

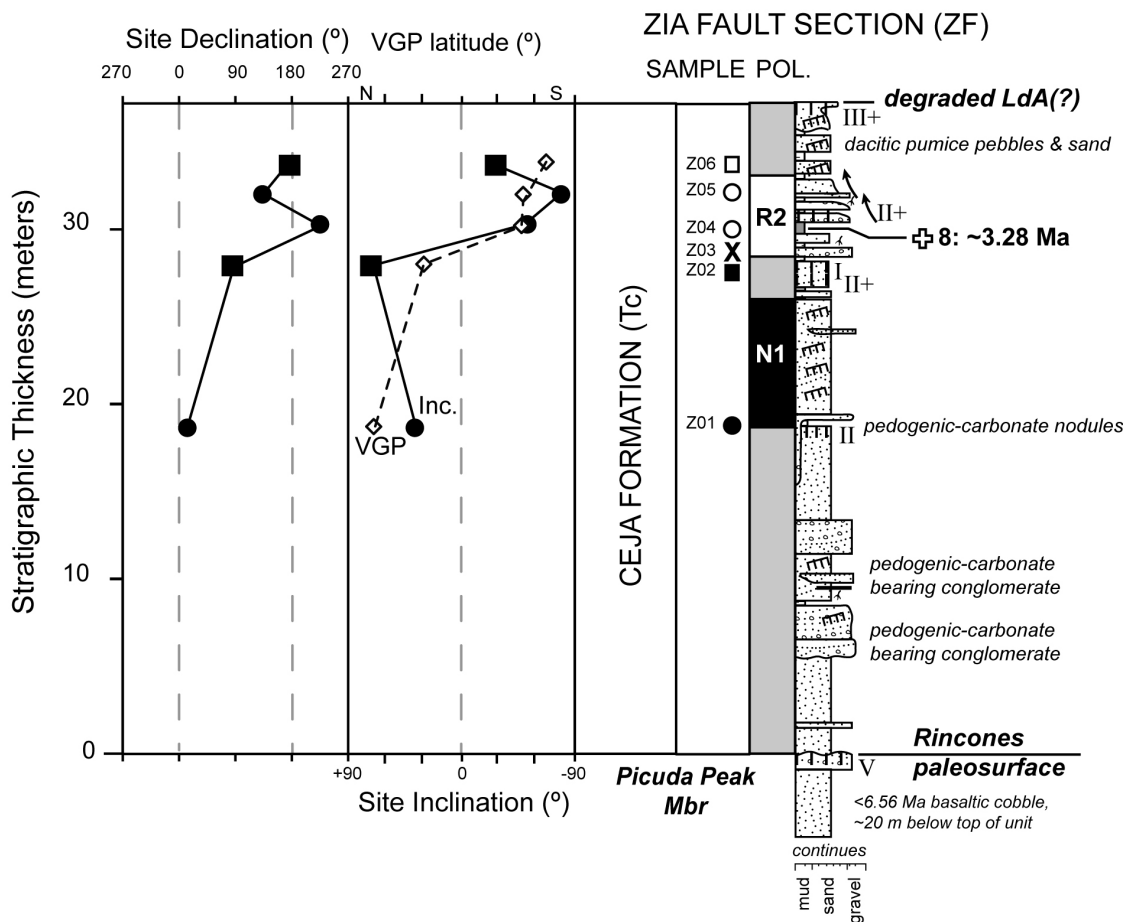


Figure 2.22. Lithostratigraphy and magnetic polarity stratigraphy of Zia Fault (ZF) stratigraphic section, magnetostratigraphic composite section (VGP = virtual geomagnetic pole latitude; Inc. = site inclination), and correlation to a provisional magnetic polarity zonation. Lines connect stratigraphically consecutive sites. The volcanic ash (sample 8, Table 2.1) was geochemically correlated to the *ca.* 3.28 Ma Nomlaki Tuff. Refer to Figure 2.20 for explanation of symbols. Age determination sites on Tables 2.1-2.3. Roman numerals denote pedogenic carbonate morphologic stages (Birkeland, 1999).

Figure 2.23 (following page). Geology of El Cerro de Los Lunas (Los Lunas volcano) and vicinity (modified from Love et al., 2001b). Top: Geologic map. Bottom: Vertically exaggerated geologic cross section C-C' (VE = 10; simplified from Love et al., 2001c) illustrates stratigraphic relationships among the younger (Qlv) and older (Tlv) emplacement events at Los Lunas volcano, the Ceja Formation (Tc, including undivided Atrisco and Rio Puerco Members), unit of San Clemente (Qsc), and younger basaltic lava flows of the Cat Hills volcanic field (Qch). Hachured lines denote a buried Llano de Albuquerque surface. The interpreted extent of now eroded deposits of Qsc and Tc are shown in cross section by faint shading and parenthetical unit symbols. The San Clemente section (SC-1, Fig. 2.15) contains a 1.5-3 m lens of pumice-bearing pebbly sand, containing rounded pebbles of upper Bandelier Tuff that is about 23 m stratigraphically above the Llano de Albuquerque surface. Refer to Figure 2.17 for explanation of other symbols and Tables 2.1-2.3 for age determinations.

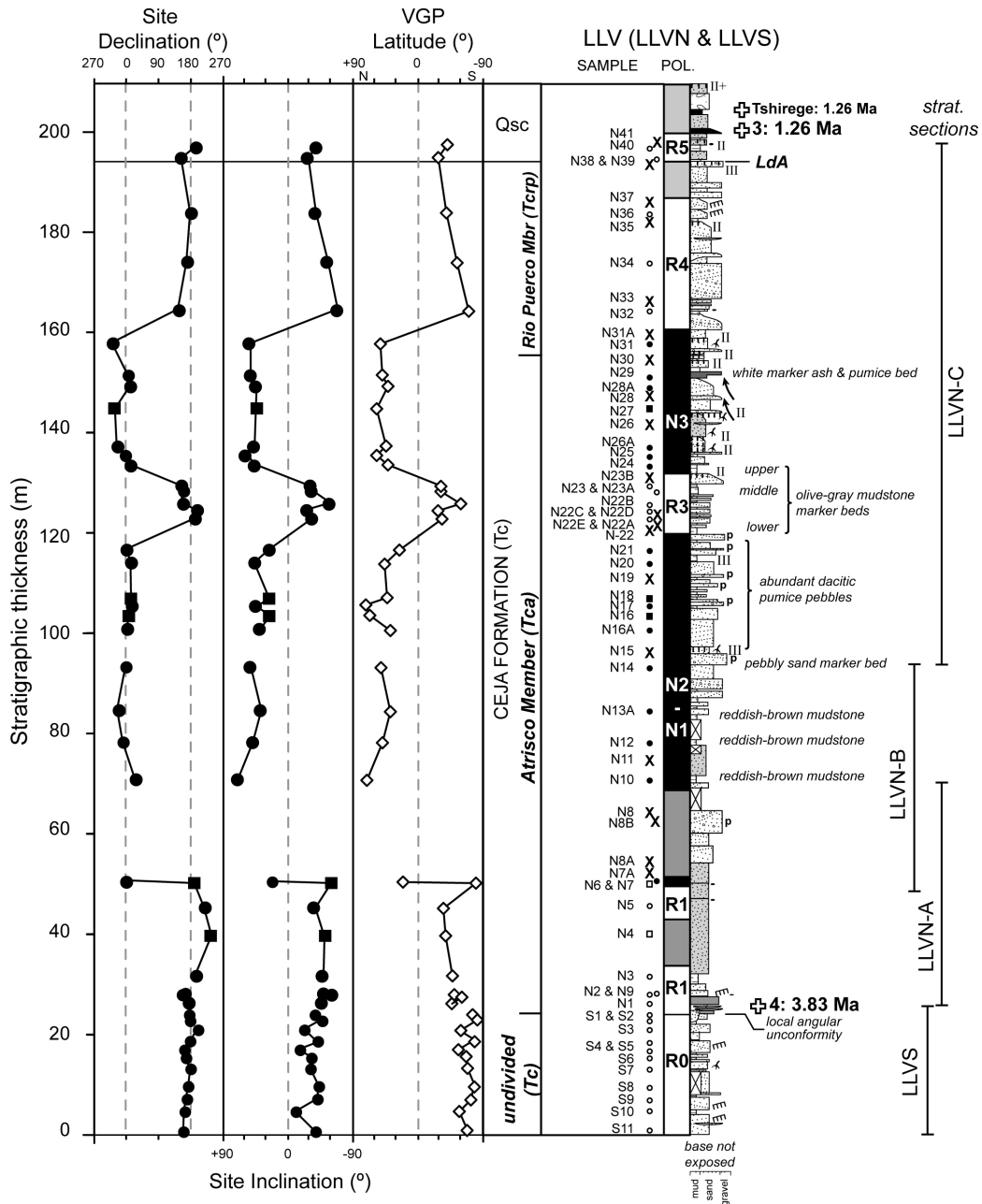


Figure 2.24. Lithostratigraphy and magnetic polarity stratigraphy of the Los Lunas volcano (LLV) composite section, magnetostratigraphic composite section (VGP = virtual geomagnetic pole latitude; Inc. = site inclination), and correlation to a provisional magnetic polarity zonation. Lines connect stratigraphically consecutive sites. Individual sections were correlated using distinctive marker beds: LLVS and LLVN-A were correlated by a dark-gray andesitic fallout tephra that overlies an angular unconformity; LLVN-A and LLVN-B were correlated by comparing a similar succession of sandstone beds; LLVN-B and LLVN-C were correlated using a prominent pebbly sandstone marker bed. Refer to Figure 2.20 for explanation of symbols. Age determination sites on Tables 2.1-2.3. Roman numerals denote pedogenic carbonate morphologic stages.

The easternmost exposures of the Ceja Formation were sampled in faulted blocks exposed along the flanks of the Rio Grande Valley (Fig. 2.25). Basaltic cinders from Perea Mesa (Isleta volcano, Kelley and Kudo, 1978) are exposed along the eastern edge of the Rio Grande Valley (Fig. 2.6, samples 21-23, Table 2.2), about 4 km northwest of Isleta Pueblo (Fig. 2.3). These 2.8-2.9 Ma basaltic tephra are stratigraphically below the CSU-PLU measured sections (Figs. 2.25 & 2.26; Fig. 2-1 in Connell et al., 2001d). Gray dacitic pumice pebbles, scattered throughout much of the Ceja Formation, yielded $^{40}\text{Ar}/^{39}\text{Ar}$ age determinations of 2.63 to 2.77 Ma (Fig. 2.6, samples 65-67, Table 2.3). These maximum ages support correlation of the lower part of the CSA-PLU section to the upper Gauss and Matuyama chrons (Fig. 2.16).

The Rio Puerco Member at CDRP3 and CDRP-CL contains a normal-polarity interval that is interpreted as part of the 1.945-1.778 Ma Olduvai subchron (Fig. 2.16). This interval is less than 10 m in thickness and probably did not record the geologically short (< 10 ka) Réunion subchron. Assignment to the Réunion subchron would require sedimentation rates that would be two to five times greater than the highest known accumulation rates estimated by Lozinsky (1994).

Assignment of thin, reverse-polarity intervals in the CDRP-CL, LLV, and CSA-PLU sections to GPTS subchrons are ambiguous because of a lack of adequate age control. Two thin (<4.5 m), reverse-polarity magnetozones at CDRP-CL may represent the Matuyama chron, or the Mammoth or Kaena subchrons. A 4.5-m thick succession of sand and laminated silty sand in the Atrisco Member is disconformably overlain by the Rio Puerco Member at CDRP-CL. The estimated site mean direction ($D = 233^\circ$; $I = -11^\circ$; VGP latitude = -33° , Appendix B) supports a reverse polarity interpretation, and the

stratigraphic position of this site (below the Rio Puerco Member) supports assignment to the lower part of the Matuyama chron. Thus, this stratigraphically lower reverse-polarity magnetozone (site 11) records either the Mammoth or Kaena subchrons (Fig. 2.21). Assignment to the Kaena subchron is preferred here because of the structurally higher position of the CDRP-CL section (on the footwall of the San Ysidro fault) and similar stratigraphic position relative to the Cat Mesa flow (CM-1, Fig. 2.16). Assignment of a thin, reverse-polarity magnetozone in the LLV and CSA-PLU composite sections (Figs. 2.24 & 2.26) to the Kaena subchron is based on the presence of dacitic pumice pebbles. Although dacitic pebbles in the LLV section did not yield interpretable age determinations, similar volcanic pebbles in CDRP3 and CSA-PLU yielded age determinations that are younger than the 3.3-3.2 Ma Mammoth subchron.

Sierra Ladrones Formation

The Sierra Ladrones Formation, which is dominated by fluvial sandstone and conglomerate, represents a major change in basin drainage with the establishment of through-going axial drainage (i.e., the ancestral Rio Grande) into southern New Mexico. The base of the Sierra Ladrones Formation is unconformable with older strata where exposed along the basin flanks (Machette, 1978; Lozinsky and Tedford, 1991; and Cather et al., 1994). Much of the Sierra Ladrones Formation is poorly exposed in the study area, but it is as much as 580 m thick in wells beneath Albuquerque (Hawley et al., 1995; and Connell et al., 1998).

The Sierra Ladrones Formation is informally divided into two interfingering members (Fig. 2.5; Machette, 1978): an axial-fluvial member (the ancestral Rio Grande),

and a piedmont-slope member associated with tributary drainages from the rift-flanking uplifts. The axial-fluvial member contains trough cross-stratified sand and gravel with sparse muddy interbeds representing ancestral Rio Grande deposition (Fig. 2.19E). Sand and gravel typically form multilateral and multistory channel sands in a 5- to 14-km wide depositional belt that, in the study area, lies almost entirely east of the present Rio Grande Valley. The eastern edge of this depositional belt is 1- to 5-km west of the Hubbell bench and the basin-bordering Sandia Mountains (Connell, 2008b, and Maldonado et al., 2007).

The top of the Sierra Ladrones Formation is defined by pedogenically modified depositional tops of the Cañada Colorada, Las Huertas, Llano de Manzano, and Sunport geomorphic surfaces (described below). The piedmont member forms a narrow belt of conglomerate and sandstone derived from the basin-flanking uplifts of the Sandia, Manzanita, and Manzano Mountains (Figs. 2.18 & 2.25). The uppermost part of the piedmont-member forms a coarse-grained depositional wedge that prograded (west) into the basin by 5 to 20 km, where it buried axial-fluvial deposits of the ancestral Rio Grande (Figs. 2.18, 2.19F, 2.25 & 2.27; Connell et al., 2001c & d). Gravels of the axial-fluvial member coarsen stratigraphically above the lavas of the San Felipe volcanic field (Brandes, 2002). Water-supply wells in Albuquerque show a coarsening of the axial-fluvial member in the upper 317 m of the section (Ch5, Figs. 2.3 & 2.4; Hawley, 1996; Connell, 2006 & 2008b). This coarsening also reflects the progradation of basin-margin alluvial fans and alluvial slopes over the axial-river deposits.

Geochronology

The Sierra Ladrones Formation is generally considered to range from Pliocene to early Pleistocene in age (4.7-0.8 Ma; Figs. 2.6 & 2.16); however, late Miocene age determinations have been reported for axial-fluvial deposits in the northern part of the basin (Smith et al., 2001). Volcanic-bearing fluvial deposits of possible extrabasinal origin have been reported beneath the Atrisco Member of the Ceja Formation in water-supply wells beneath Albuquerque (Hawley and Haase, 1992, section IV). Pliocene lava flows of the San Felipe volcanic field are interbedded with axial-fluvial deposits (2.57 ± 0.11 Ma, Fig. 2.7, sample 19, Table 2.2). To the south, Pliocene-aged trachyandesitic lava lay above the projected base of the Sierra Ladrones Formation at San Acacia (Machette, 1978), about 60 km south of the study area. Chamberlin et al. (2001) reported a $^{40}\text{Ar}/^{39}\text{Ar}$ age determination of 4.76 ± 0.04 Ma for this volcanic feature (Fig. 2.7, sample SA, Table 2.1).

The top of the Sierra Ladrones Formation is well exposed at the mouth of Tijeras Arroyo (Figs. 2.25 & 2.27), where axial-fluvial deposits contain an early Pleistocene flora and vertebrate fauna that is older than about 0.8 Ma (Lucas et al., 1993; Morgan and Lucas, 2003; and Bell et al., 2004). The axial-fluvial member contains abundant fluvially recycled, rhyolitic pumice and rounded obsidian pebbles and cobbles, some of which were dated or geochemically correlated to known eruptive sources (Fig. 2.7; Love et al., 2001a; and Maldonado et al., 1999 & 2007). These pumice-bearing beds were likely laid down by floods originating in the Jemez Mountains, where voluminous rhyolitic volcanism and river damming has occurred (e.g., Smith et al., 1970; and Reneau and Dethier, 1996). Pumice-bearing Plio-Pleistocene flood deposits have also

been reported in ancestral Rio Grande deposits nearly 300 km downstream of Tijeras Arroyo (Mack et al., 1996).

A bed of white volcanic ash (1.28 ± 0.2 Ma, Fig. 2.7, sample 33, Table 2.3) has been geochemically correlated with the Tshirege Member of the Bandelier Tuff (Nelia Dunbar, 2001, personal communication). Beneath this ash lies a bed of nearly pure, medium-grained, gray and white, pumiceous sand that yielded a single-crystal $^{40}\text{Ar}/^{39}\text{Ar}$ age determination on sanidine of 2.00 ± 0.04 Ma (Fig. 2.7, sample 63, Table 2.3). This lower pumiceous interval lies within a normal polarity magnetozone that is nearly 14 m stratigraphically below the Tshirege ash (Fig. 2.27) and is assigned to part of the 1.945-1.778 Ma Olduvai subchron (Fig. 2.16). The presence of the Olduvai subchron demonstrates that deposition in the upper part of the Ceja Formation was contemporaneous with the axial-fluvial member of the Sierra Ladrones Formation, even though they are locally separated by a disconformity exposed along the flanks of the Rio Grande Valley (Fig. 2.15).

The age of the top of the Sierra Ladrones Formation comes from the CSA-PLU composite section (Fig. 2.26), between Tijeras Arroyo and Hell Canyon Wash (Fig. 2.25). The upper part of this section contains abundant rhyolitic and pumiceous gravel that yielded ages of 1.44 to 1.67 Ma (Fig. 2.7, sample 15 and 64, Table 2.3). Deposits of the axial-fluvial member are exposed in Hell Canyon Wash, where rhyolitic, pumice-bearing fluvial cobbles yielded a $^{40}\text{Ar}/^{39}\text{Ar}$ age determination on sanidine of 1.72 ± 0.04 Ma (Fig. 2.7, sample 58, Table 2.3).

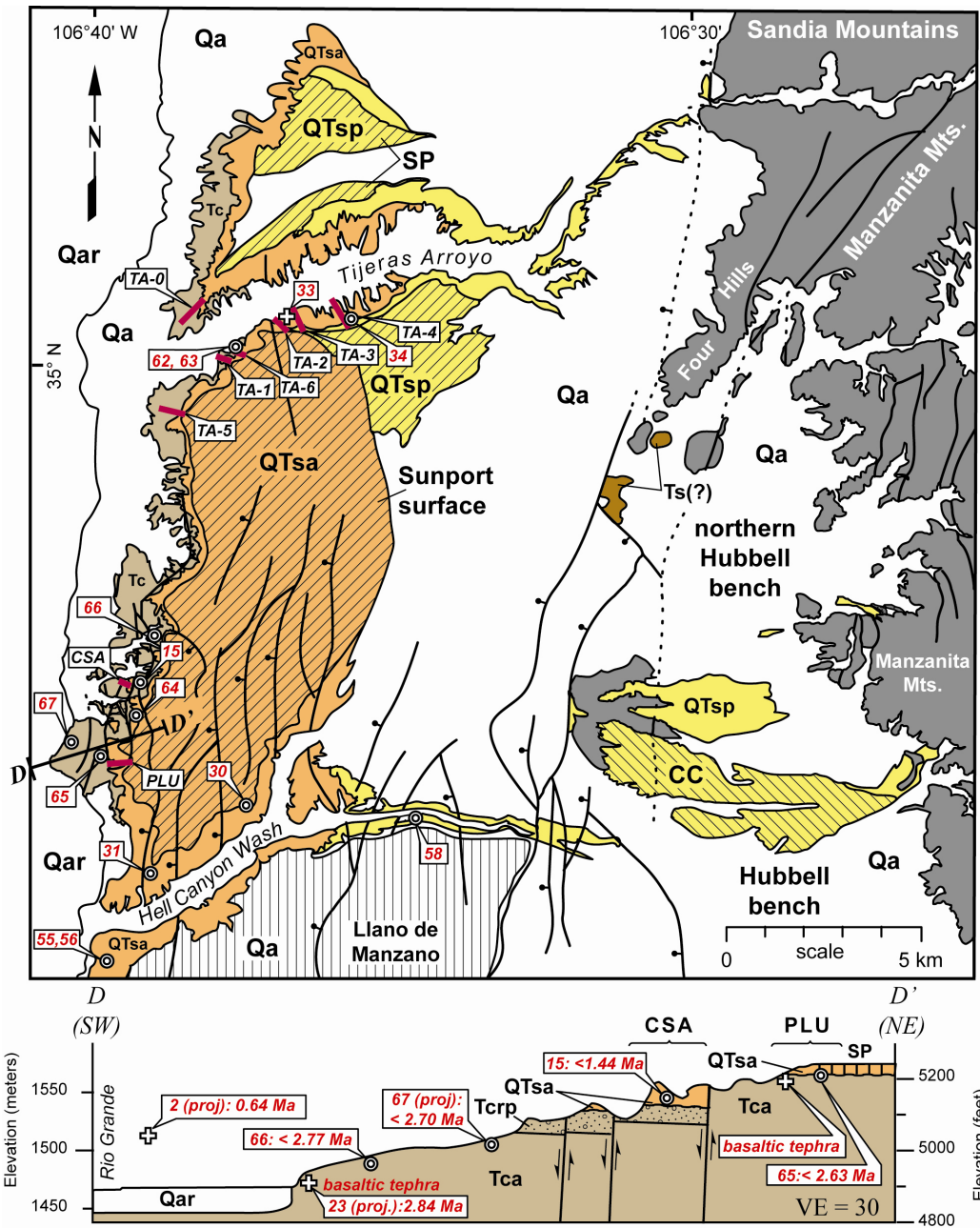


Figure 2.25. Geology of Tijeras Arroyo and Hell Canyon Wash. Top: Generalized geologic map, illustrating the locations of measured stratigraphic sections in Tijeras Arroyo (TA-0 through TA-6), and Isleta Powerline (PLU) and Casino (CSA). Unit Qar denotes alluvium of the Rio Grande Valley and floodplain. Depositional tops of the Sierra Ladrones Formation (and younger alluvium) locally delineated by hachured lines and include the Cañada Colorada (CC), Sunport (SP), and Llano de Manzano geomorphic surfaces. Bottom: Vertically exaggerated (VE = 30) geologic cross section D-D' across eastern margin of Rio Grande Valley (modified from Connell et al., 2001c), illustrating projections of the CSA and PLU stratigraphic sections and dated pumice pebbles. Explanation of units on Figure 2.17, and age determination sites on Tables 2.1-2.3.

An olive-green and reddish-brown sequence of mudstone, locally preserved against an intrabasinal fault, caps the Sierra Ladrones axial-fluvial succession at section PLU (Fig. 2.26). These mudstone beds contain a normal-polarity magnetozone that correlate to the early part of the Brunhes chron (0.781 Ma to present, Gradstein et al., 2005). A terrace deposit containing the 0.64 Ma Lava Creek B ash is inset about 60 m against the Sierra Ladrones Formation (Fig. 2.25; Connell et al., 2007a). Thus, deposition of the Sierra Ladrones Formation ended with the entrenchment of the Rio Grande Valley, which occurred shortly after 0.8 Ma and was well underway by 0.6 Ma.

Few direct age determinations are available for the piedmont member of the Sierra Ladrones Formation. Just south of Tonque Arroyo (Fig. 2.18), a volcanic ash bed sits 3 m above the piedmont/axial-fluvial contact (Cather and Connell, 1998; and Brandes, 2002). This ash yielded single-crystal $^{40}\text{Ar}/^{39}\text{Ar}$ age determinations on sanidine of 1.57 ± 0.09 Ma and 1.60 ± 0.06 Ma (Fig. 2.7, sample 51 and 52, Table 2.3). Piedmont member deposits prograded by as much as 10 km towards the Rio Grande after 1.7-1.6 Ma and buried most of the axial-fluvial member deposits (Figs. 2.18 & 2.25).

Plio-Pleistocene Deposits

Gravelly deposits exposed along the faulted and structurally elevated flanks of the Albuquerque Basin are inset against Miocene basin fill and older parts of the Ceja and Sierra Ladrones Formations (e.g., Connell and Wells, 1999; and Smith et al., 2001). The Tuerto Formation (Tuerto gravels of Stearns, 1953) is a thin and areally extensive, subhorizontally bedded succession of gravel and sand on the northern flank of the Sandia Mountains and in the Hagan embayment that overlies an angular unconformity marked

by the lower Ortiz paleosurface (see below). The Tuerto Formation is dominated by amalgamated conglomeratic sandstone (Koning et al., 2001) that locally encloses basaltic lava flows of the Pliocene Cerros del Rio volcanic field, near the Albuquerque-Española Basin boundary. Bachman and Mehnert (1978) report a K-Ar age determination of 2.8 ± 0.1 Ma for a lava flow at the base of the Tuerto Formation.

The unit of San Clemente was described by Love et al. (1998) for deposits of sand, mud and gravel that overlie the Ceja Formation in structural depressions on the Llano de Albuquerque (Fig. 2.23). The unit of San Clemente is about 36 m thick and disconformably overlies the Llano de Albuquerque surface (Fig. 2.24; Connell et al., 2001c). The top of this section is marked by well-developed calcic paleosols that are locally capped by lava flows of the middle Pleistocene Cat Hills volcanic field (99-111 ka; Kelley and Kudo, 1978; and Maldonado et al., 2006 and 2007). Sparse gravel in this unit typically resembles those of the underlying Ceja Formation, except for a nearly 3-m thick lens of cross-stratified, pumice-bearing pebbly sand about 22 m above the westward projection of the Llano de Albuquerque surface (Fig. 2.15 & Fig. 2.23 bottom). Rhyolitic pumice pebbles in this interval yielded a maximum age of 1.24 ± 0.02 Ma (Fig. 2.7, sample 32, Table 2.3) and are geochemically similar to the Tshirege Member of the Bandelier Tuff (N. Dunbar, personal communication, 2001). The most likely source of this pumice-bearing bed was from the ancestral Rio Grande.

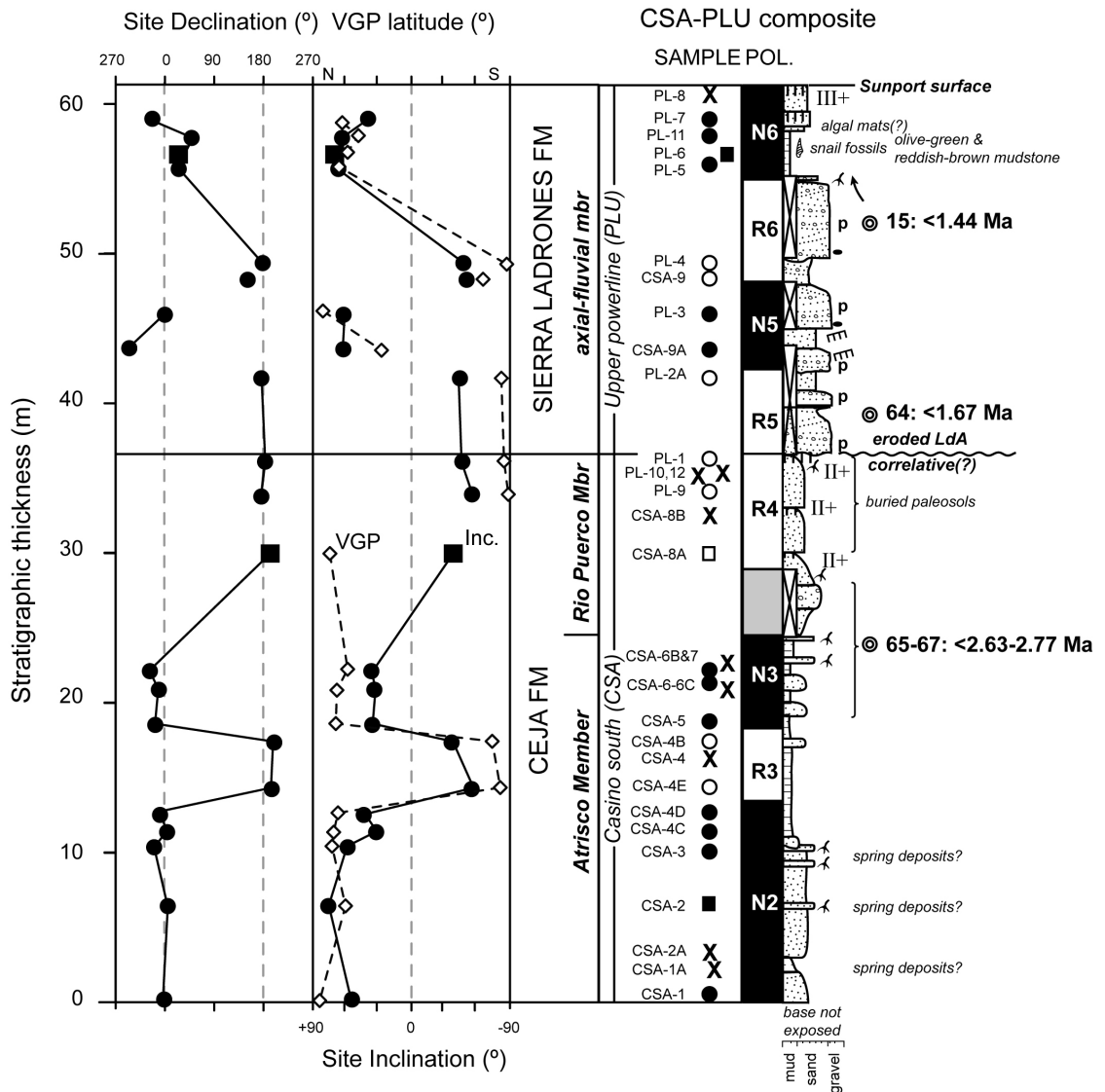


Figure 2.26. Lithostratigraphy and magnetic-polarity stratigraphy of CSA and PLU composite sections, magnetostratigraphic composite section (VGP = virtual geomagnetic pole latitude; Inc. = site inclination), and correlation to a provisional magnetic polarity zonation. Lines connect stratigraphically consecutive sites. Refer to Figure 2.20 for explanation of symbols. Age determination sites on Tables 2.1-2.3. Roman numerals denote pedogenic carbonate morphologic stages (Birkeland, 1999).

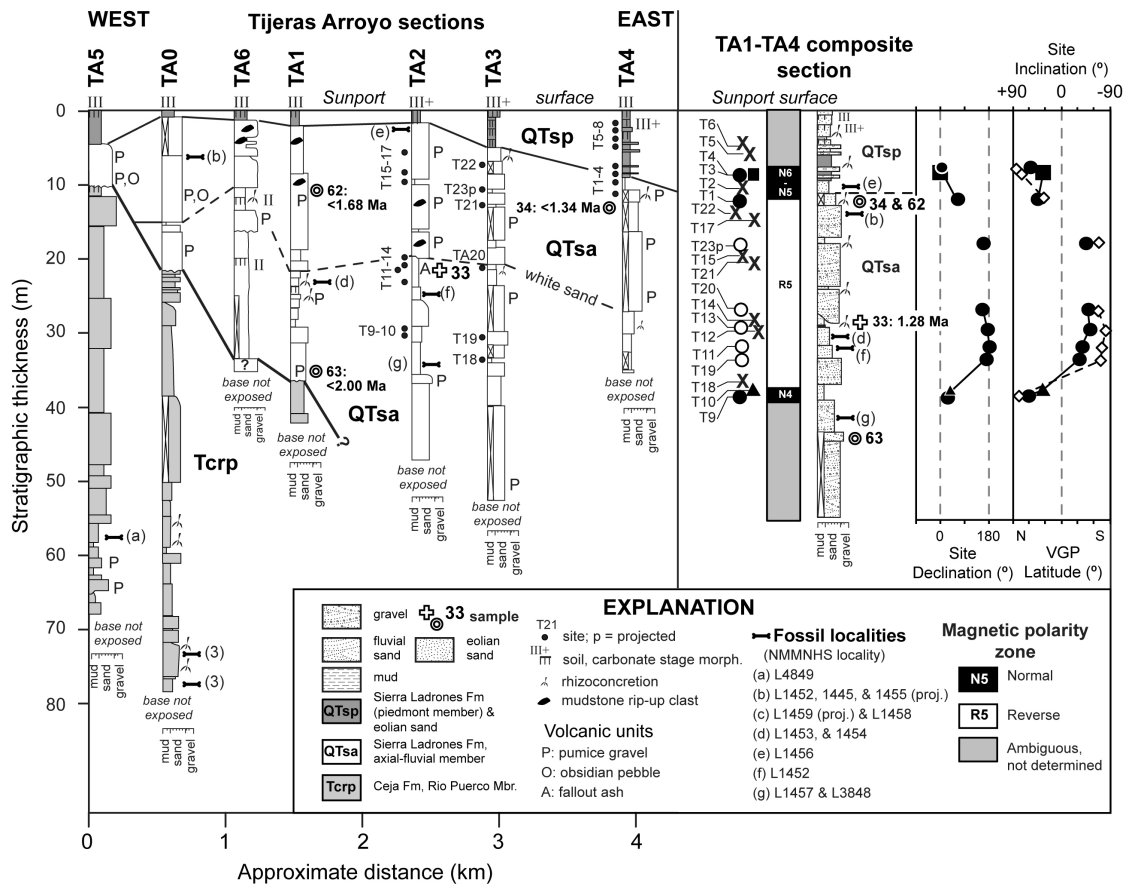


Figure 2.27. Stratigraphic fence diagram, illustrating physical correlations of stratigraphic sections in Tijeras Arroyo. Section TA5 was re-measured from previous studies (i.e., Lambert, 1968; and Lucas et al., 1993). Vertebrate fossil localities of the New Mexico Museum of Natural History and Science (NMMNHS, Lucas et al., 1993; and Morgan and Lucas, 2003) are also shown. Site T23p is a volcanic ash projected about 3 km south into Tijeras Arroyo. Right-side of figure portrays the generalized lithostratigraphy and magnetic polarity stratigraphy of TA composite section and correlation to a provisional magnetic polarity zonation (VGP = virtual geomagnetic pole latitude; Inc. = site inclination); lines connect stratigraphically consecutive sites. Age determination sites on Tables 2.1-2.3. Roman numerals denote pedogenic carbonate morphologic stages (Birkeland, 1999).

Sediment-Accumulation Rates

Rates of sediment accumulation were estimated for parts of the Ceja and Sierra Ladrones succession using the measured stratigraphic sections, data from a deep water-supply well beneath Albuquerque (Ch5, Fig. 2.3), and available age control (Fig. 2.28). Plio-Pleistocene deposits are poorly consolidated and have undergone little diagenetic

alteration beyond minor interstitial calcium-carbonate cementation and pedogenic alteration. Precise determinations of accumulation rates are difficult because of incomplete geochronologic control, exposure, and preservation. Truncation of magnetozones by disconformities would result in higher estimated rates. Accumulation rates for measured sections thinner than 60 m were adjusted for compaction using the approximation method of Van Hinte (1978), and porosity-depth relationships from Albuquerque area wells (Haneberg, 1995). The thicker section in this water-supply well was decompacted by applying an integral method described in Angevine et al. (1990) to the porosity-depth curves of Haneberg (1995).

On the basis of sparse age control, Lozinsky (1994) reported undecompressed sediment accumulation rates of 200-600 m/Ma for Miocene strata, although his highest estimated rates are probably much lower (Fig. 2.28A; Connell, 2004). The type section of the Arroyo Ojito Formation is 478 m thick (Connell et al., 1999) and accumulated between 9.0 and 6.3 Ma, yielding a long-term (undecompressed) accumulation rate of about 177 m/Ma (478 m/2.7 Ma). At the Arroyo Ojito type area, a 6.85 Ma ash is 328 m above the base, and about 150 m below the top (Connell et al., 1999; and Connell, 2008a). This ash and the 9 Ma estimated age of the base of the Arroyo Ojito Formation yield an undecompressed rate of about 153 m/Ma (328 m/2.15 Ma). The stratigraphic interval between the Peralta ashes and the assumed 6.3 Ma upper estimate for the Arroyo Ojito Formation yields a higher undecompressed rate of about 252 m/Ma (151 m/0.6 Ma). A slower rate of accumulation for the Picuda Peak Member (20 m/0.31 Ma = 65 m/Ma) was estimated using the ages of the 6.6 Ma basaltic cobble in the Picuda Peak Member and the 6.3 Ma Cerrito Yelo ash in the Cochiti Formation.

Plio-Pleistocene accumulation rates were estimated using age determinations and magnetic-polarity stratigraphy (Fig. 2.28B-C). Compaction errors at LLV are negligible in the upper 60 m (post-3.0 Ma) of the section. The lower part of this section was adjusted for compaction, yielding rates that were a factor of 1.2 to 1.4 higher than the uncompact rates. An uncompact rate between the older and younger Los Lunas eruptive products was about 32 m/Ma, which is similar to the sedimentation rates determined by Lozinsky (1994) and to rates reported by Mack et al. (1993) for comparably aged rift-basin fill in southern New Mexico.

The absence of a normal polarity magnetozone in the Gilbert-aged part of the LLVS (Fig. 2.24) suggests that deposition occurred after the Cochiti subchron (C3n.1n) at 4.187 Ma. This age constraint resulted in a decompact rate 100 m/Ma (uncompact rate of *ca.* 66 m/Ma). Decompact accumulation rates ranged from 168-183 m/Ma between 3.8 and 3.0 Ma (uncompact rate of 114-155 m/Ma for the same time interval). Accumulation rates in the Ceja Formation decreased by about 66 percent between 3.8 and 3.0 Ma, and by about 80 percent (59-12 m/Ma) between 3.0 and 1.8 Ma (Fig. 2.28). Miscorrelation of the Kaena (or Mammoth) subchron would only result in decreasing accumulation rates after 3.3 Ma, rather than after 3.0 Ma.

Accumulation rates for the CDRP3, CDRP-CL, CSA-PLU, TA, and SC-1 sections demonstrate an overall decrease in the rate of sediment accumulation by a factor of three or four since 3.0 Ma (12-59 m/Ma) and are similar to the rates estimated for the Ceja Formation in the Los Lunas volcano sections (Fig. 2.28B-C). This decrease in sedimentation rate occurred nearly 0.5 Ma before the Ceja section became much coarser grained (i.e., in the Rio Puerco Member). Decreases in sedimentation rates after 3 Ma

were punctuated by short intervals of relatively rapid accumulation in gravelly beds in CDRP3 and CDRP-CL. These faster rates may be the result of rapid deposition by river channels or they may merely be an artifact of shorter sampling (and time) intervals (Sadler, 1981). Accumulation rates estimated for the Sierra Ladrones Formation at the CSA-PLU and TA sections range from 12 to 43 m/Ma (Fig. 2.28D) and are in general agreement with estimates by Lozinsky (1994).

The Charles Wells #5 well (Ch5) penetrated the base of the Atrisco Member (at 872 m below land surface; Connell et al., 1998) near its deepest known level in the basin. Although the top of the Sierra Ladrones Formation is not preserved in this well, the land surface is less than 27 m below the projection of the Sunport surface (Connell, 2008b). Thus, Ch5 contains the thickest known accumulation of Sierra Ladrones deposits in the Albuquerque Basin. A decompacted sediment thickness for this entire succession is 917 m, and yields an average sediment accumulation rate of 167 or 229 m/Ma (Fig. 2.28A), depending on the ages selected for the base (i.e., 6.3-0.8 Ma or 4.8-0.8 Ma); undecompacked rates are 158 or 218 m/Ma. Higher accumulation rates would result if the Sierra Ladrones succession was younger than 4.8 Ma near the well. These long-term rates are greater than those determined for the measured sections, which are 12 to 30 km away from the master fault and thus, represent minimum estimates. The lower rates estimated towards the western basin margin may be a result of reduced accommodation up the hanging-wall ramp in this part of the basin.

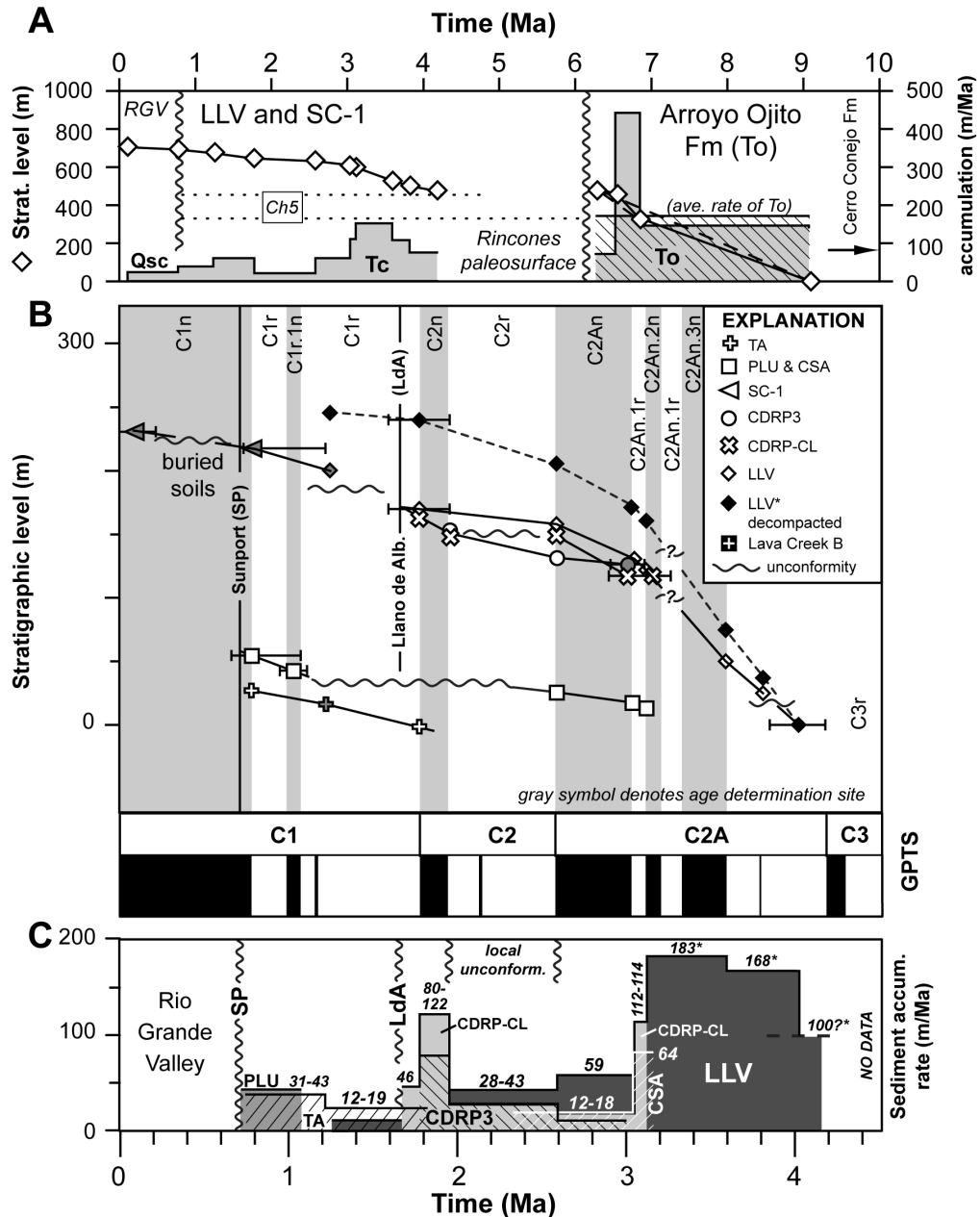


Figure 2.28. Sediment accumulation rates and major depositional events since late Miocene time. A: Plot of stratigraphic level and age (diamonds), and uncompact sediment accumulation rates for the Arroyo Ojito, Ceja, and Sierra Ladrones Formations. Black arrow denotes the mean accumulation rate estimated for the Cerro Conejo Formation (Tedford and Barghoorn, 1999). Two dotted lines denote decompact sediment accumulation rates for Charles Wells #5 well (Ch5) using different ages for the inferred base of the Ceja Formation. B: Plot of deposit age against stratigraphic level (thickness) and global polarity timescale (GPTS) for the Ceja and Sierra Ladrones Formations using stratigraphic sections CDRP3, CDRP-CL, CSA-PLU, LLV, and TA. C: Plot of sediment accumulation rates since 4.1 Ma; decompact rates are noted by an asterisk.

Paleosurfaces

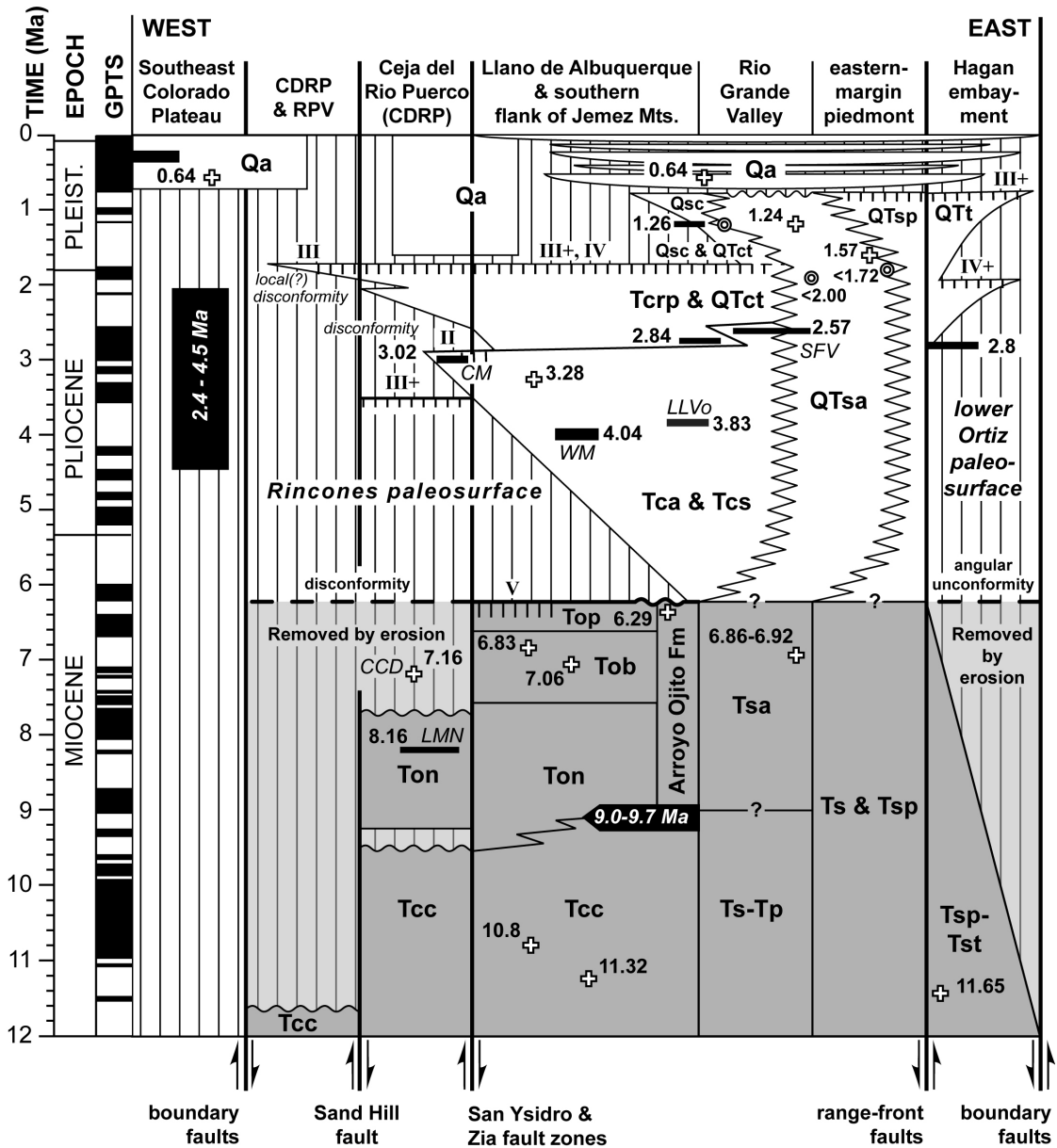
The Plio-Pleistocene alluvial succession in the Albuquerque Basin is defined by a set of upper and lower bounding surfaces (Fig. 2.29). The lower boundary is defined by the Rincones and lower Ortiz paleosurfaces. The upper boundaries are locally defined by a set of depositional (constructional) geomorphic surfaces developed on the Ceja, Sierra Ladrones, and Tuerto Formations. The Rincones paleosurface was named by for a disconformity between Miocene and Pliocene deposits in the Albuquerque Basin (Connell, 2008a). This discontinuity is exposed beneath the Ceja Formation, along the western and northern flanks of the Llano de Albuquerque and La Ceja, where as much of 450 m of the subjacent Miocene strata is missing. It is commonly disconformable (but forms angular unconformities near major intrabasinal faults), and locally contains strongly developed petrocalcic paleosols that exhibit stage III+ and V pedogenic carbonate morphology, depending on structural position. Elsewhere this boundary is marked by a pinkish, mottled, and bioturbated sand with scattered pebbles (e.g., Fig. 2.20).

The Ortiz paleosurface is an angular unconformity between Miocene and Pliocene strata in the Albuquerque and Española basins (Bryan, 1938; and Bryan and McCann, 1938). Bryan and co-workers (Bryan and McCann, 1938; Wright, 1946; and Stearns, 1979) considered the Ortiz paleosurface to represent a regional surface of erosion that divided moderately deformed Miocene strata from less deformed Plio-Pleistocene strata. The subjacent Miocene strata were tilted by as much as 32 degrees and were subjected to several hundred meters of erosion before being buried by subhorizontally bedded Plio-Pleistocene fluvial deposits of the Tuerto and Ancha

Formations (Stearns, 1953; Koning et al., 2002; and Connell et al., 2002). The Ortiz paleosurface was extended across the Albuquerque Basin and onto eastern flank of the Colorado Plateau and was correlated to the Llano de Albuquerque (Bryan and McCann, 1938; Wright, 1946; Kelley, 1977; and Stearns, 1979).

Bachman and Mehnert (1978) recognized the compound (and allostratigraphic) character of the Ortiz paleosurface, but restricted it to the upper aggradational surface on the Tuerto Formation, in the Hagan embayment (Koning et al., 2001), and on the Ancha Formation in the adjacent Española Basin (Koning et al., 2002). This division was challenged by Stearns (1979) who considered the lower surface to be more useful as a boundary between tilted Miocene rocks and the overlying subhorizontally bedded Plio-Pleistocene sediment. We also consider the erosional aspect of the lower paleosurface to have regional importance and correlate it to the Rincones paleosurface; however, we assign the relict depositional top of the Ceja Formation to the younger Llano de Albuquerque surface (see below).

Figure 2.29 (following page). Chronostratigraphic diagram depicting major stratigraphic units, bounding surfaces, and fault zones across the southeastern margin of the Colorado Plateau, Albuquerque Basin, and Hagan embayment, including the Ceja del Rio Puerco (CDRP), Rio Puerco Valley (RPV), and Rio Grande Valley. The global polarity timescale (GPTS) is shown for reference. Thick vertical lines schematically denote major fault zones, and vertical hachures denote stratigraphic lacunae. Short hachured lines denote petrocalcic paleosols developed on bounding surfaces; roman numerals denote maximum pedogenic carbonate morphologic stage. Unit symbols defined on Figure 2.5. Abbreviations refer to volcanic units: Cat Mesa flow (CM), Cerro Colorado dacite (CCD), La Mesita Negra flow (LMN), older Los Lunas volcano (LLVo), a lava from San Felipe volcanic field (SFV), and Wind Mesa volcano (WM). Younger deposits (Qa) include a suite of terraces of the Rio Grande (chronology from Connell et al., 2007a), and alluvial, colluvial, and eolian deposits. Miocene units are shaded gray; light-gray shading denotes eroded deposits. Black rectangles denote lava flows. The “plus” and “circle-in-circle” symbols denote primary and recycled volcanic materials, respectively. Numbers refer to age determinations (in Ma) from Tables 2.1-2.3 and other studies (Bachman and Mehnert, 1978; Izett and Wilcox, 1982; Drake et al., 1991; Hallett et al., 1997; Connell et al., 1999 & 2002; Connell, 2008a & b; and Maldonado et al., 2006 & 2007).



The Rincones and lower Ortiz paleosurfaces are recognized along the flanks of the Albuquerque Basin, and represent the same lacuna (Fig. 2.29). The character of these paleosurfaces in depocentral areas is not clear. Drill-hole data indicate that the stratigraphic correlatives to the Rincones paleosurface in depocentral areas form a rather sharp boundary (Connell et al., 1998; and Stone et al., 1998). This boundary in the drill-holes supports an abrupt change in environmental conditions or a disconformity; however, major stratal discontinuities were not recognized in the exposed piedmont succession along the eastern margin of the basin (Fig. 2.23; Kelley, 1982; Cather and Connell, 1998; and Connell, 2008b), suggesting that deposition may have continued with little or no interruption within the deepest parts of the basin.

The Llano de Albuquerque surface represents the depositional top of the Ceja Formation (Machette, 1985). The Llano de Albuquerque landform is a 106-km long, south-sloping tableland between the Rio Grande and Rio Puerco valleys that is 110 to 494 m above the Rio Grande. Petrocalcic paleosols developed on this relict depositional surface commonly possess stage III+ to IV pedogenic carbonate morphology and are thicker than those developed on the Sierra Ladrones Formation (Machette, 1985; Connell, 2008a; and Connell and Wells, 1999). The sharp contact between the Sierra Ladrones and Ceja Formations exposed along the eastern flank of the Rio Grande Valley likely represents an eroded remnant of this surface (Fig. 2.25).

The Cañada Colorada, Las Huertas, Sunport, and Llano de Manzano geomorphic surfaces define local tops of the Sierra Ladrones Formation and parts of the younger piedmont alluvium (Lambert, 1968; Machette, 1985; Maldonado et al., 1999; Connell and Wells, 1999; and Connell, 2004). The Cañada Colorada surface developed on a

faulted block on the northern Hubbell bench (Maldonado et al., 1999). The other surfaces are 95 to 120 m above the Rio Grande and serve as useful stratigraphic datum planes to correlate depositional tops of the Sierra Ladrones Formation.

Petrocalcic paleosols on the Cañada Colorada surface (stage III+ to V; Connell et al., 2001c) are more strongly developed than those on the Las Huertas, Llano de Manzano, and Sunport surfaces (stage III+; Machette, 1985; and Connell and Wells, 1999), suggesting that it may be much older than these other surfaces. Isolated, high-level, relict surfaces are preserved on remnants of locally derived alluvium on the northern flank of the Sandia Mountains (Connell and Wells, 1999; and Connell, 2008b). These surfaces have erosionally modified petrocalcic soils (Stage IV+ pedogenic carbonate morphology) and may represent older surfaces of the Tuerto Formation.

Alluvial Sequences

The Ceja and Sierra Ladrones Formations comprise a basin-wide, nonmarine depositional sequence that is defined by distinct sets of bounding surfaces (Fig. 2.29). The lower bounding surface, defined by the Rincones and lower Ortiz paleosurfaces, contain strongly developed paleosols that indicate that large parts of the basin was subjected to prolonged periods of landscape stability ($10^5 - 10^6$ years, Machette, 1985) before being buried by the Ceja Formation during late Pliocene time. Although these paleosurfaces are areally extensive, the lack of an obvious unconformable boundary in the piedmont succession near the basin master fault (along the northern flank of the Sandia Mountains) suggests that sedimentation continued essentially uninterrupted in the deeper parts of the basin.

The upper boundaries of this alluvial sequence are defined by a suite of relict depositional surfaces (i.e., Cañada Colorada, Llano de Albuquerque, Las Huertas, Sunport, and Llano de Manzano) that contain strongly developed paleosols. Depositional onlap and intrabasinal faulting increased the duration of stratigraphic lacunae towards the basin margins (Fig. 2.29). Deep incision by younger alluvium associated with episodic cutting by the Rio Grande (and major tributaries) also defines the upper boundary of this sequence.

Miocene Sedimentation

Middle to upper Miocene strata exposed in the northern part of the Albuquerque Basin are dominated by fluvial and eolian deposits of the Cerro Conejo Formation (Fig. 2.30A). The eastward (basinward) slope of the Rincones paleosurface, generally consistent eastward to southeastward stratal tilt directions, eastward thickening of the basin fill, southeast-directed paleoflow directions, and western-margin (Colorado Plateau-Sierra Nacimiento) gravel provenance (Brandes, 2002; Connell, 2004; and Connell et al., 2008a & b) all indicate that the study area has been dominated by generally eastward basin subsidence, and has not been subjected to any major changes in the direction of basin tilting since early Miocene time (*cf.* Ingersoll, 2001).

Movement along the basin-master fault system increased after about 9 Ma, resulting in continued eastward tilting and thickening of the Arroyo Ojito Formation (Fig. 2.30B). The northern part of the Albuquerque Basin received extrabasinal sediments as early 7 Ma, but the southern part of the basin was dominated by internal surface drainage until early Pliocene time (Fig. 2.30B-C). Deposition of the Arroyo Ojito

Formation ceased shortly after about 6.3 Ma with the development of the Rincones paleosurface (Fig. 2.30B). During late Miocene time, the underlying fluvial succession was subjected to approximately 0.5 km of erosion along the western (up-dip) margin of the basin (Fig. 2.30B-C).

Workers in the adjacent Socorro and Española basins reported an overall reduction in the rate of deformation after about 10 Ma (Cather et al., 1994; and Koning et al., *in press*). Geochronologically calibrated deformational indicators (e.g., stratal-tilt data) are not well established in the Albuquerque Basin, but they suggest a slight decrease in stratal tilt across the Rincones paleosurface (Connell, 2008b). This change in tilting in the underlying Miocene strata suggest that the Rincones and lower Ortiz paleosurfaces were cut following major deformation and support a reduction in tectonism after about 6 Ma.

Plio-Pleistocene Sedimentation and Axial-drainage Development

The relatively long Miocene phase of internal surface drainage gave way to through-going drainage of the ancestral Rio Grande into southern New Mexico by early Pliocene time (Fig. 2.30B-C; Leeder et al., 1996; Mack et al., 2002 & 2006). Interbasinal integration of surface drainage may have occurred through the burial of low-lying structural zones (Jackson and Leeder, 1994) between the Albuquerque and Socorro basins. The integration of ancestral Rio Grande drainage into southern New Mexico could have been a consequence of progressive onlap of Pliocene sediments over low-lying structural culminations between these basins (Cather et al., 1994).

The Rincones and lower Ortiz paleosurfaces became progressively buried by the Ceja, Sierra Ladrones, and Tuerto Formations between about 2.8 and 2.6 Ma (Figs. 2.29 & 2.30C). The Ceja succession began to coarsen slightly in the Los Lunas section (LLV) after 3.6 Ma, but did not become dominated by coarse-grained detritus until after about 2.6 Ma. Widespread burial of the Rincones paleosurface occurred after about 3.0 Ma. Coarsening of the Ceja Formation culminated with the deposition of areally extensive sheets of pebble- to boulder-bearing sand that extended across much of the basin and east of the present Rio Grande Valley after about 1.8 Ma.

The overall lack of mud and clay in the upper part of the Ceja Formation indicates that most of the finer-grained sediment was transported out of the basin during this time. This coarsening of the Ceja Formation occurred after integration of the ancestral Rio Grande into southern New Mexico and western Texas (Connell et al., 2005) and was not directly related to base-level lowering of the axial river by drainage capture. Coarsening of the Ceja Formation ended with the development of the Llano de Albuquerque surface during (or shortly after) the 1.9-1.8 Ma Olduvai subchron (Figs. 2.29 & 2.30D).

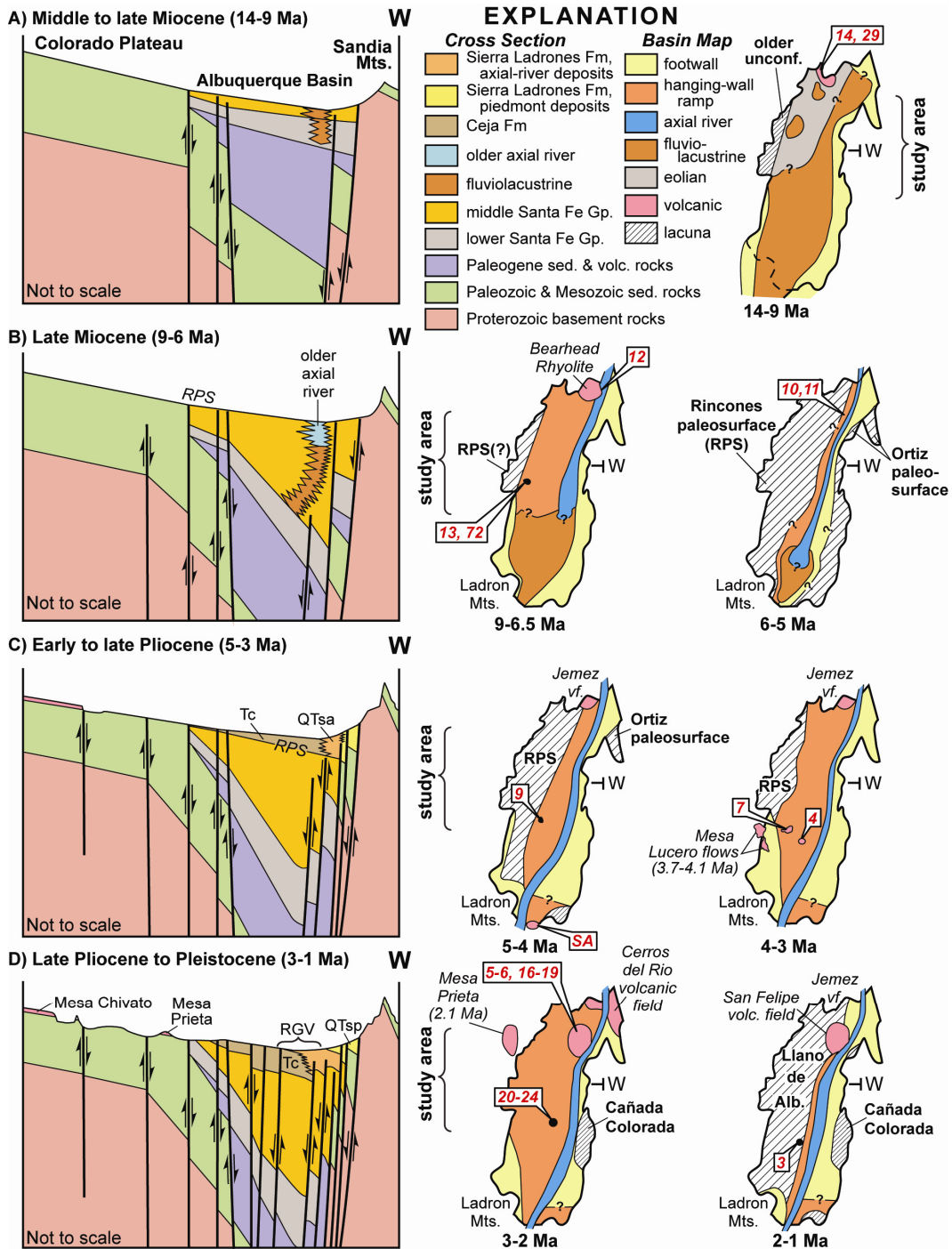


Figure 2.30. Schematic cross sections (left) and paleogeographic diagrams (right) illustrating the history of subsidence and sedimentation in the Albuquerque Basin since middle Miocene time (14-1 Ma): middle to late Miocene (A), late Miocene (B), Early to late Pliocene (C), and late Pliocene to early Pleistocene (D). The Rincones paleosurface is denoted by RPS. Red numbers denote age determinations (Tables 2.1-2.3). Other K-Ar and $^{40}\text{Ar}/^{39}\text{Ar}$ age determinations for lava flows on Mesa Lucero and Mesa Prieta are from Baldrige et al. (1980 & 1987) and Hallett et al. (1997), respectively.

After 1.8 Ma, sedimentation was largely restricted to the eastern part of the basin, where the course of the ancestral Rio Grande (Sierra Ladrones Formation) was within 5 km of the basin-boundary fault system. Also after 1.8 Ma, the Sierra Ladrones Formation lapped westward onto the abandoned top of the Ceja Formation and graded towards the Llano de Albuquerque surface. The presence of the Olduvai subchron in the Ceja and Sierra Ladrones Formations demonstrates contemporaneous sedimentation for these units and precludes incision of an earlier paleovalley of the ancestral Rio Grande (*cf.* Cole et al., 2001 & 2007). Like the Ceja Formation, gravel in the axial-fluvial member of the Sierra Ladrones Formation increased in size and abundance after 2.6 Ma, but the piedmont member deposits only prograded away from the master fault after about 1.8 to 1.6 Ma (Figs. 2.28C & 2.30C). Deposition of the Sierra Ladrones Formation continued for another 1 Ma until entrenchment of the Rio Grande Valley began shortly after 0.8 Ma.

Depositional Patterns

The stratigraphy of the Albuquerque Basin generally follows a progression of drainage development and sedimentation patterns that are similar to other continental rifts (e.g., Lambiase and Bosworth, 1995; Contreras et al., 1997; and Olsen, 1997). The basins initially become dominated by internal surface drainage as subsidence exceeds sedimentation. This results in an underfilled condition that persists until sediment discharge exceeds the volume of basin formed by subsidence. The basin then becomes overfilled, leading to the topographic and hydrologic connection with adjoining, lower-lying basins. At higher rates of strain, topographic closure of the basin would be

maintained, even with increasing contributions of sediment (e.g., Contreras et al., 1997). It is possible that the stratigraphic progression in the Albuquerque Basin may reflect an evolutionary phase in the development of rift-basin alluvial sequences, where climatically induced increases in sediment delivery, rather than tectonism, dominate the Plio-Pleistocene stratigraphic architecture (see below).

The asynchronous progradation of fluvial deposits derived from opposing basin flanks, and the development of diachronous relict (depositional) tops on the Plio-Pleistocene alluvial succession may be a geometric consequence of asymmetrical basin subsidence where basinward tilting of the hanging-wall ramp promotes extensive sediment bypass near the basin flanks (Figs. 2.29 & 2.30; Connell et al., 2001a; and Smith et al., 2001). The distal hanging-wall ramp has a fore-tilted basin geometry that allows potential accommodation to increase down the structural dip towards the master fault. Back-tilted basin geometry dominates near the structural footwall cutoff, where accommodation decreases away from the master fault. Because of this fore-tilted geometry, drainages would be more sensitive to changes in subsidence than near the (back-tilted) footwall block. Thus, decreases in basin subsidence could drive the progradation (offlap) of coarse-grained sediment off of the distal hanging-wall ramp, which would promote sediment bypass and the eventual cessation of deposition as accommodation decreased marginward. Intrabasinal (normal) faulting of the hanging-wall ramp would accentuate erosion and sediment bypass on the upthrown block (Fig. 2.29).

This asynchronous depositional pattern seems to support numerical models of basin filling that suggest progradation of these opposing marginal wedges could be

driven by changes in subsidence rate (e.g., Paola et al., 1992; and Travis and Nunn, 1994). Attributing this progradational couplet to changing subsidence rates is not likely here because it would require an unreasonably short pulse in tectonism (after 2.6 Ma), followed by a rapid decrease after 1.8 Ma. Long-term (average) sediment accumulation rates for the Ch5 well are slightly higher than those determined for the Gauss-aged part of the Atrisco Member that is exposed near the basin flanks (Fig. 2.28A). The higher average accumulation rate for Ch5 well suggests that basin subsidence did not significantly diminish in depocentral areas. Thus, the overall decrease in sediment accumulation in the measured sections may be the result of decreased accommodation towards the basin margins.

Synchronous progradation of basin-flanking deposits would be expected if sediment flux increased in similarly sized tributary catchments; however, hanging-wall catchments are typically much larger than those on the footwall (Leeder and Jackson, 1994). Larger hanging-wall catchments should respond to climatic changes with greater magnitude than the smaller footwall catchments. For example, the present Rio Puerco drainage basin (a tributary to the Rio Grande) covers nearly 19,000 km² of the southeastern Colorado Plateau and northwestern Albuquerque Basin (Love and Connell, 2005) and is more than 12 times larger than the combined drainage area of the eastern mountain fronts south of the Hagan embayment (1573 km² in Anderholm, 2001).

The coarsening of the uppermost Ceja succession and formation of the Llano de Albuquerque geomorphic surface, before the onset of regional fluvial entrenchment, suggests that incision of the paleo-Rio Puerco drainage system may have begun earlier along the structurally higher western flank of the basin. It is not clear whether the

remnants of such an early paleovalley existed, but such a paleovalley could have graded into a conformable stratigraphic succession toward the southern end of the basin where basin tilting shifted to the west (Russell and Snelson, 1994). If this were the case, the southward course of the present Rio Puerco drainage would be antecedent and controlled by sediment bypass during the final stages of deposition of the Rio Puerco Member. It is possible that the depositional top of the Ceja Formation remained active as a thin, transport-dominated surface until the Rio Grande began to incise during early Pleistocene time. This is unlikely because of the thickness and degree of pedogenic development on the Llano de Albuquerque surface supports a greater age of formation than for the younger geomorphic surfaces on the Sierra Ladrones Formation.

Climatic Implications

Rates of sediment accumulation, reported from numerous globally distributed settings, increased by a factor of two to ten over the last 4 Ma (e.g., Zhang et al., 2001). This globally recognized increase in sediment flux is thought to represent a depositional response to increased climatic variability and magnitude (Molnar, 2004). The late Miocene was a period extreme aridity that was followed by periods of increased sediment discharge and greater seasonal climate variability (e.g., Axelrod, 1981; Smith, 1994; Webb and Opdyke, 1995; and Chapin, 2008).

Alluvial successions in the semi-arid southwestern regions of North America may record the effects of Pliocene and Pleistocene climatic change on both tectonically active and quiescent basins. Studies of Plio-Pleistocene fluviolacustrine and fluvial deposits (St. David Formation) in the tectonically quiescent San Pedro Valley of

southeastern Arizona (Fig. 2.2) indicate an increase in sheet channels and sand-to-mud ratios and a reduction in sediment accumulation rates after the Gauss-Matuyama chron boundary at 2.58 Ma (Smith, 1994). These sedimentologic changes coincided with climate changes inferred from the stable-isotopic composition of pedogenic carbonate in paleosols (Smith et al., 1993). A similar correspondence between basin sedimentation and climate was also reported for Plio-Pleistocene fluvial deposits of the Palomas and Camp Rice Formations in the tectonically active Rio Grande rift in southern New Mexico (Mack et al., 1993 & 1994).

The Plio-Pleistocene alluvial succession in the Albuquerque Basin is interpreted to reflect the effects of long-term aggradation within a basin that has been subjected to either constant or decreasing rates of tectonic subsidence since late Miocene time. During late Miocene through early Pliocene time, subsidence would continue to deform the basin flanks as sediment discharges diminished to a level where basin depocenters would receive less sediment. Later increases in discharge would strip the uplifted basin flanks and surrounding upland regions and provide more sediment for the basin. Although subsidence controls cannot be completely ruled out, the overall upward coarsening of this alluvial succession and increase in gravel size supports augmentation of sediment discharge in the sediment delivery system, rather than solely due to a reduction in tectonic subsidence.

Sediment accumulation rates diminished after 3.0 Ma and coarsening of the Ceja and Sierra Ladrones Formations became widespread after about 2.6 Ma. Changes in sedimentation may have been driven by expansion of hinterland drainage area (Fraser and DeCelles, 1990), late Cenozoic climatic variability (Zhang et al., 2001; and Chapin,

2008), or diminished basin subsidence (e.g., Mack and Seager, 1990). The present limits of the major western tributaries to the Albuquerque Basin were probably established by late Pliocene time (Love and Connell, 2005). Studies of the Arroyo Ojito and Ceja Formations indicate that crystalline basement rock was probably exposed by late Miocene time (Connell et al., 1999), so durable basement rocks would have already been exposed in hinterland catchment regions before the Ceja stream transported coarse-grained deposits.

Amalgamated coarse-grained channel deposits in the Ceja, Sierra Ladrones, and Tuerto Formations occurred after sediment-accumulation rates decreased on the distal hanging-wall ramp (Fig. 2.28B & D), suggesting that the basin may have filled to a level that promoted extensive sediment bypass through the basin. Although a decrease in sedimentation rate and overall coarsening of the Ceja section during late Pliocene time may suggest a decrease in subsidence rate, it seems unlikely that diminished subsidence can solely account for the relatively sudden introduction of coarse-grained clastic detritus into the basin following a decrease in sediment-accumulation rate. The approximately coeval depositional responses in the Albuquerque Basin and the tectonically quiescent San Pedro Valley of Arizona (Smith, 1994) suggest that climate may play an important role in the development of sedimentary sequences in slowly subsiding basins.

The 0.8-Ma onset of valley cutting coincides with the start of eccentricity-driven climate cycles (e.g., Zachos et al., 2001) and is within the chronological resolution reported for the cutting of the Rio Grande Valley in southern New Mexico (Mack et al., 2006) and in southeastern Arizona (Smith, 1994). The transition from basin filling to

valley cutting also agrees with other studies that document the onset of major regional incision before 0.6 Ma (e.g., Dethier, 2001). The timing of onset of incision and the approximate number (and age) of inset terrace deposits supports the importance of regional climatic controls, rather than tectonic changes, to base level (Gile et al., 1981; Connell et al., 2007a; and Leeder and Mack, 2007).

Valley incision in central and southern New Mexico may be slightly older than the 0.44 Ma age of overflow that Machette et al. (2007) postulated for their Lake Alamosa in the upper Rio Grande drainage, which is about 240 km north of Albuquerque and near the Colorado-New Mexico state line (Fig. 2.2). If this age of upper-basin drainage integration is correct, then a nearly 0.3 Ma lag exists between the initial cutting of the Rio Grande Valley in the Albuquerque Basin and integration of the headwaters in southern Colorado. Such a lag would not support capture of the upper Rio Grande as the principal driver of downstream valley incision in central and southern New Mexico (Wells et al., 1987). It is possible that Pleistocene drainage integration of the upper Rio Grande might have been promoted by filling of the southern San Luis Basin by sediment in response to climatically induced increases in discharge.

Chapter Summary and Conclusions

We utilized combined geochronologic, sequence-stratigraphic, sedimentologic, and geomorphologic approaches to interpreting the development of a Plio-Pleistocene alluvial sequence in the Albuquerque Basin of the Rio Grande rift in north-central New Mexico. Seventy-eight new and previously published age determinations refine the ages of Miocene through lower Pleistocene basin fill of the synrift Santa Fe Group. These

geochronologic data permitted the development of a robust magnetic-polarity stratigraphy for the Plio-Pleistocene part of the basin-fill succession.

The Ceja and Sierra Ladrones Formations comprise a nonmarine depositional sequence that is bounded by distinct sets of erosional and depositional surfaces. Deposition of upper Miocene strata in the Albuquerque Basin ceased shortly after 6.3 Ma and is marked by widespread erosion of the basin flanks and development of the Rincones and lower Ortiz paleosurfaces. The upper boundaries of this alluvial sequence are defined by a suite of relict depositional surfaces that include the Cañada Colorada, Llano de Albuquerque, Las Huertas, Sunport, and Llano de Manzano surfaces.

Integration of axial-river drainage (by an ancestral Rio Grande) through the Albuquerque Basin occurred by 4.8 Ma, probably as a result of increased sedimentation that began to bury these areally extensive upper Miocene unconformities, eventually burying low-lying structural culminations that divided the southern Albuquerque and Socorro basins. Progressive, marginward onlap of the Ceja and Tuerto Formations eventually buried the Rincones and lower Ortiz paleosurfaces between 2.8 and 2.6 Ma. Later stages of paleosurface burial corresponded to a coarsening of the Ceja succession, and culminated with the development of the Llano de Albuquerque surface shortly after 1.8 Ma. Deposition of the Sierra Ladrones Formation continued for another million years until cutting of the Rio Grande Valley initiated shortly after 0.8 Ma. Progradation of Sierra Ladrones piedmont deposits away from the master fault began after about 1.8 to 1.6 Ma. Cutting of the Rio Grande Valley (south of the Española Basin) coincided with increased global climatic variability, and may have occurred before entrenchment of the headwaters region of the Rio Grande in southern Colorado.

The asynchronous progradation of margin-sourced deposits in this stratigraphic succession probably reflects a geometric response to decreasing accommodation up the hanging-wall ramp. The fore-tilted geometry of the hanging-wall promoted progradation of amalgamated channels that formed broad sheets across the distal hanging-wall ramp as sediment bypassed the basin margins. Reduced sediment accumulation rates after 3.0 Ma may represent extensive sediment bypass. Although active tectonism is clearly of first-order importance in the formation of sedimentary successions, the development of an Plio-Pleistocene alluvial sequence in the Albuquerque Basin may reflect the importance of climate on basin filling in relatively slowly subsiding basins.

Chapter Acknowledgments

This contribution was supported by the National Science Foundation (EAR-0344146) and the New Mexico Bureau of Geology and Mineral Resources (Peter A. Scholle, Director). The $^{40}\text{Ar}/^{39}\text{Ar}$ dating and geologic mapping was supported by the New Mexico Statemap Program component of the National Cooperative Geologic Mapping Act of 1992. The Pueblos of Cochiti, Isleta, Jemez, Sandia, San Felipe, Santo Domingo, and Zia graciously provided access to tribal lands. Ivan Benavidez, Westland Corporation, and the King Brothers Ranch kindly provided access to much of the land along the Ceja del Rio Puerco. The New Mexico State Land Office also kindly provided rights of access to parts of Tijeras Arroyo. Teresa and Kathleen Connell, Holly Buehler, Linda Donohoo-Hurley, Dan Koning, Travis Naibert, Scott Muggleton, Mitchell Reese, and Kate Zeigler assisted with the acquisition, preparation, and analysis of more than 1400 paleomagnetic specimens. Steve Cather, Richard Chamberlin, Nelia Dunbar, and

Dave Love kindly provided some of the geochronologic data presented here. This paper benefited from conversations with Steve Cather, Richard Chamberlin, John Hawley, Dan Koning, and Dave Love. Reviews by Brian Horton, Mark Hudson, and Mike Leeder improved the paper and are gratefully acknowledged.

Chapter References

- Anderholm, S.K., 2001, Mountain-front recharge along the east side of the Albuquerque Basin, central New Mexico (revised): U.S. Geological Survey, Water-Resources Investigations Report 00-4010, 36 p.
- Angevine, C.L., Heller, P.L., and Paola, C., 1990, Quantitative sedimentary basin modeling: American Association of Petroleum Geologists, Continuing Education Course Note Series 32, 247 p.
- Axelrod, D.L., 1981, Role of volcanism in climate and evolution: Geological Society of America Special Paper 185, 59 p.
- Bachman, G.O., and Mehnert, H.H., 1978, New K-Ar dates and the late Pliocene to Holocene geomorphic history of the central Rio Grande region, New Mexico: Geological Society of America Bulletin, v. 89, p. 283-292.
- Baldrige, W.S., Damon, P.E., Shafiqullah, M., and Bridwell, R.J., 1980, Evolution of the central Rio Grande rift, New Mexico: New Potassium-argon ages: Earth and Planetary Sciences Letters, v. 51, n. 2, p. 309-321.
- Baldrige, W.S., Perry, F.V., and Shafiqullah, M., 1987, Late Cenozoic volcanism of the southeastern Colorado Plateau: I. Volcanic geology of the Lucero area, New Mexico: Geological Society of America Bulletin, v. 99, n. 10, p. 463-470.
- Bartolino, D.P., and Cole, J.C., 2002, Ground-water resources of the middle Rio Grande basin, New Mexico: U.S. Geological Survey, Circular 1222, 132 p.
- Bell, C.J., Lundelius, E.L., Jr., Barnosky, A.D., Graham, R.W., Lindsay, E.H., Ruez, D.R., Semken, H.A, Jr., Webb, S.D., and Zakrezewski, R.J., 2004, The Blancan, Irvingtonian, and Rancholabrean Mammal Ages, *in* Woodburne, M.O., ed., Late Cretaceous and Cenozoic Mammals of North America: biostratigraphy and geochronology: New York, Columbia University Press, p. 232-314.
- Birkeland, P.W., 1999, Soils and geomorphology: New York, Oxford University Press, 3rd edition, 430 p.

- Blair, T.C., and Bilodeau, W.L., 1988, Development of tectonic cyclothems in rift, pull-aparts, and foreland basins: sedimentary response to episodic tectonism: *Geology*, v. 16, n. 6, p. 517-520.
- Blum, M.D., and Törnqvist, T.E., 2000, Fluvial responses to climate and sea-level change; a review and look forward: *Sedimentology*, v. 47, Suppl. 1, p. 2-48.
- Brandes, N.N., 2002, Lithostratigraphy and petrography of upper Santa Fe Group deposits in the northern Albuquerque Basin, New Mexico [M.S. thesis]: Socorro, New Mexico Institute of Mining and Technology, 208 p.
- Bridge, J.S., and Leeder, M.R., 1981, A simulation model of alluvial stratigraphy: *Sedimentology*, v. 26, n. 5, p. 617-644.
- Bridge, J.S., and Mackey, S.D., 1993, A revised alluvial stratigraphy model, *in* Marzo, M., and Puigdefábregas, C., eds., *Alluvial sedimentation: International Association of Sedimentologists Special Publication 17*, p. 319-336.
- Broxton, D., WoldeGabriel, G., Peters, L., Budahn, J., and Luedemann, G., 2007, Pleistocene volcanic rocks of the Tschicoma Formation, east-central Jemez volcanic field: chemistry, petrography, and age constraints, *in* Kues, B.S., Kelley, S.A., and Lueth, V.W., eds., *Geology of the Jemez Region II: New Mexico Geological Society, Guidebook 58*, p. 284-295.
- Bryan, K., 1938, Geology and ground-water conditions of the Rio Grande depression in Colorado and New Mexico: Washington, Regional Planning, pt. 6, Rio Grande Joint Investigation, Upper Rio Grande Basin, Natural Resources Committee, v. 1, p. 2, sec. 1, p. 197-225.
- Bryan, K., and McCann, F.T., 1938, The Ceja del Rio Puerco-a border feature of the Basin and Range province in New Mexico, part II, geomorphology: *Journal of Geology*, v. 45, p. 1-16.
- Cather, S.M., and Connell, S.D., 1998, Geology of the San Felipe Pueblo 7.5-minute quadrangle, Sandoval County, New Mexico: New Mexico Bureau of Mines and Mineral Resources, Open-file Geologic Map 19, scale 1:24,000.
- Cather, S.M., Chamberlin, R.M., Chapin, C.E., and McIntosh, W.C., 1994, Stratigraphic consequences of episodic extension in the Lemitar Mountains, central Rio Grande rift: Geological Society of America, Special Paper 291, p. 157-170.
- Chamberlin, R.M., and McIntosh, W.C., 2007, Geochronology and structural control of late Cenozoic volcanism in the Loma Creston quadrangle, southern Jemez Mountains, New Mexico, *in* Kues, B.S., Kelley, S.A., and Lueth, V.W., eds.,

- Geology of the Jemez Mountains Region II: New Mexico Geological Society, Guidebook 58, p. 248-261.
- Chamberlin, R.M., Cather, S.M., Nyman, M.W., and McLemore, V.T., 2001, Preliminary geologic map of the Lemitar 7.5-minute quadrangle, Socorro County, New Mexico: New Mexico Bureau of Mines and Mineral Resources, Open-file Geologic Map 38, scale 1:24,000, 29 p.
- Chapin, C.E., 1971, The Rio Grande rift, part 1: modifications and additions: New Mexico Geological Society Guidebook 22, p. 191-201.
- Chapin, C.E., 2008, Interplay of oceanographic and paleoclimate events with tectonism during middle to late Miocene sedimentation across the southwestern USA: *Geosphere*, v. 4, n. 6, p. 976-991, doi: 10.1130/GES00171.1.
- Chapin, C.E., and Cather, S.M., 1994, Tectonic setting of the axial basins of the northern and central Rio Grande rift: Geological Society of America, Special Paper 291, p. 5-25.
- Cole, J.C., Stone, B.D., Shroba, R.R., and Dethier, D.P., 2001, Pliocene incision of the Rio Grande in northern New Mexico [abstract]: Geological Society of America Abstracts with Programs, v. 33, n. 5, p. A-48.
- Cole, J.C., Mahan, S.A., Stone, B.D., and Shroba, R.R., 2007, Ages of Quaternary Rio Grande terrace-fill deposits, Albuquerque area, New Mexico: *New Mexico Geology*, v. 29, n. 4, p. 123-132.
- Connell, S.D., 2004, Geology of the Albuquerque Basin and tectonic development of the Rio Grande rift in north-central New Mexico, *in* Mack, G.H., and Giles, K.A., eds., *The Geology of New Mexico: A Geologic History*: New Mexico Geological Society, Special Publication 11, p. 359-388.
- Connell, S.D., 2006, Preliminary geologic map of the Albuquerque-Rio Rancho metropolitan area, Bernalillo and Sandoval County, New Mexico: New Mexico Bureau of Geology and Mineral Resources, Open-file Report 496, version 2.0, scale 1:50,000.
- Connell, S.D., 2008a, Refinements to the stratigraphic nomenclature of the Santa Fe Group, northwestern Albuquerque Basin, New Mexico: *New Mexico Geology*, v. 30, n. 1, p. 14-35.
- Connell, S.D., 2008b, Geologic map of the Albuquerque-Rio Rancho metropolitan area, Bernalillo and Sandoval County, New Mexico: New Mexico Bureau of Geology and Mineral Resources, Geologic Map GM-78, scale 1:50,000, 2 pls.

- Connell, S.D., and Wells, S.G., 1999, Pliocene and Quaternary stratigraphy, soils, and tectonic geomorphology of the northern flank of the Sandia Mountains, New Mexico: implications for the tectonic evolution of the Albuquerque Basin, *in* Pazzaglia, F.J., and Lucas, S.G., eds., *Albuquerque Geology: New Mexico Geological Society, Guidebook 50*, p. 379-391.
- Connell, S.D., Allen, B.D., and Hawley, J.W., 1998, Subsurface stratigraphy of the Santa Fe Group from borehole geophysical logs, Albuquerque area, New Mexico: *New Mexico Geology*, v. 20, n. 1, p. 2-7.
- Connell, S.D., Koning, D.J., and Cather, S.M., 1999, Revisions to the stratigraphic nomenclature of the Santa Fe Group, northwestern Albuquerque Basin, New Mexico, *in* Pazzaglia, F.J., and Lucas, S.G., eds., *Albuquerque Geology: New Mexico Geological Society, Guidebook 50*, p. 337-353.
- Connell, S.D., Love, D.W., Maldonado, F., Jackson, P.B., McIntosh, W.C., and Eppes, M.C., 2000, Is the top of the Santa Fe Group diachronous in the Albuquerque Basin? [abstract]: U.S. Geological Survey Open-file Report 00-488, p. 18-20.
- Connell, S.D., Love, D.W., Cather, S.M., Smith, G.A., Lucas, S.G., 2001a, Tectonics, climate, and the transition from aggradation to incision of the upper Santa Fe Group, Albuquerque Basin, central New Mexico: Geological Society of America, *Abstracts with Programs*, v. 33, n. 5, p. A-48.
- Connell, S.D., Lucas, S.G., Koning, D.J., Maynard, S.R., and Derrick, N.N., 2001b, First-day, Santo Domingo sub-basin: Hagan Embayment and northern flank of the Sandia Mountains, *in* Connell, S.D., Love, D.W., Lucas, S.G., Koning, D.J., Derrick, N.N., Maynard, S.R., Morgan, G.S., Jackson-Paul, P.B., and Chamberlin, R., trip leaders., *Stratigraphy and tectonic development of the Albuquerque Basin, central Rio Grande rift, field trip guidebook: Albuquerque, New Mexico, Geological Society of America, Rocky Mountain-South Central Section Meeting: New Mexico Bureau of Geology and Mineral Resources, Open-file report 454A*, p. 1-15.
- Connell, S.D., Love, D.W., and Sorrell, J.D., 2001c, Geology of the Isleta Reservation, First-day road log, October 12, 2001, *in* Connell, S.D., Love, D.W., Sorrell, J.D., and Harrison, J.B.J., trip leaders., *Plio-Pleistocene stratigraphy and geomorphology of the central part of the Albuquerque Basin: Friends of the Pleistocene, Rocky Mountain Cell, Field-trip guidebook: New Mexico Bureau of Geology and Mineral Resources, Open-file report 454C*, p. 1-1 to 1-28.
- Connell, S.D., Love, D.W., and Sorrell, J.D., 2001d, Geology of southern Albuquerque and Tijeras Arroyo, Second-day road log, October 13, 2001, *in* Connell, S.D., Love, D.W., Sorrell, J.D., and Harrison, J.B.J., trip leaders., *Plio-Pleistocene stratigraphy and geomorphology of the central part of the Albuquerque Basin: Friends of the Pleistocene, Rocky Mountain Cell, Field-trip guidebook: New Mexico Bureau of Geology and Mineral Resources, Open-file report 454C*, p. 2-1 to 2-23.

- Connell, S.D., Cather, S.M., Dunbar, N., McIntosh, W.C., and Peters, L., 2002, Stratigraphy of the Tanos and Blackshare Formations (lower Santa Fe Group), Hagan embayment, Rio Grande rift, New Mexico: *New Mexico Geology*, v. 24, n. 4, p. 107-119.
- Connell, S.D., Hawley, J.W., and Love D.W., 2005, Late Cenozoic drainage development in the southeastern Basin and Range of New Mexico, southeasternmost Arizona, and western Texas, *in* Lucas, S.G., Morgan, G.S., and Ziegler, K.E., eds., *New Mexico's Ice Ages: New Mexico Museum of Natural History and Science Bulletin 28*, p. 125-150.
- Connell, S.D., Love D.W., and Dunbar, N.W., 2007a, Geomorphology and stratigraphy of inset fluvial deposits along the Rio Grande valley in the central Albuquerque Basin, New Mexico: *New Mexico Geology*, v. 29, n. 1, p. 13-31.
- Connell, S.D., Koning, D.J., Kelley, S.A., and Brandes, N.N., 2007b, Oligocene-Miocene sedimentation in the southwestern Jemez Mountains and northwestern Albuquerque basin, New Mexico, *in* Kues, B.S., Kelley, S.A., and Lueth, V.W., eds., *Geology of the Jemez Region II: New Mexico Geological Society, Guidebook 58*. p. 195-208.
- Connell, S.D., Smith, G.S., Geissman, J.W., and McIntosh, W.C., *in press*, Climatic controls on nonmarine depositional sequences in the Albuquerque Basin, Rio Grande rift, north-central New Mexico, *in* Hudson, M.R., and Grauch, V.J.S., eds., *New Perspectives on the Rio Grande rift: from tectonics to groundwater: Geological Society of America, Special Publication*.
- Contreras, J., Scholz, C.H., and King, G.C.P., 1997, A model of rift basin evolution constrained by first-order stratigraphic observations: *Journal of Geophysical Research*, v. 102, n. B4, p. 7673-7690.
- Dart, C., Cohen, H.A., Akyüz, H.S., Barka, A., 1995, Basinward migration of rift-border faults: Implications for facies distribution and preservation potential: *Geology*, v. 23, n. 1, p. 69-72.
- Deino, A., and Potts, R., 1992, Age-probability spectra from examination of single-crystal $^{40}\text{Ar}/^{39}\text{Ar}$ dating results: Examples from Ologesailie, Southern Kenya Rift: *Quaternary International*, v. 13/14, p. 47-53.
- Dethier, D.P., 2001, Pleistocene incision rates in the Western United States calibrated using Lava Creek B Tephra: *Geology*, v. 29, n. 9, p. 783-786.
- Drake, P.G., Harrington, C.D., Wells, S.G., Perry, F.V., and Laughlin, A.W., 1991, Late Cenozoic geomorphic and tectonic evolution of the Rio San Jose and tributary drainages within the Basin and Range/Colorado Plateau transition zone in west-

- central New Mexico, *in* Julian B., and Zidek, J., eds., Field guide to geologic excursions in New Mexico and adjacent areas of Texas and Colorado: New Mexico Bureau of Mines and Mineral Resources Bulletin 137, p. 149-157.
- Dunbar, N.W., McIntosh, W.C., and Love, D.W., 2001, Dating basalts using the $^{40}\text{Ar}/^{39}\text{Ar}$ method—Improvements based on electron microprobe evaluation of samples [abstract]: EOS, Transactions of the American Geophysical Union, v. 82, p. F1321.
- Fisher, R.A., 1953, Dispersion on a sphere: Proceedings of the Royal Society, London, v. A217, p. 295-305.
- Fraser, G.S., and DeCelles, P.G., 1992, Geomorphic controls on sediment accumulation at margins of foreland basins: Basin Research, v. 4, p. 233-252.
- Frostick, L.E., and Reid, I., 1989, Is structure the main control of river drainage and sedimentation in rifts?: Journal of African Earth Sciences, v. 11, p. 165-182.
- Gawthorpe, R.L., and Hurst, J.M., 1993, Transfer zones in extensional basins: Their structural style and influence on drainage development and stratigraphy: Journal of the Geological Society of London, v. 150, p. 1137-1152.
- Gawthorpe, R.L., and Leeder, M.R., 2000, Tectono-sedimentary evolution of active extensional basins: Basin Research, v. 12, p. 195-218.
- Gile, L.H., Hawley, J.W., and Grossman, R.B., 1981, Soils and geomorphology in the Basin and Range area of southern New Mexico—Guidebook to the Desert Project: New Mexico Bureau of Mines and Mineral Resources, Memoir 39, 222 p.
- Gile, L. H., Hawley, J. W., Grossman, R. B., Monger, H. C., Montoya, C. E., and Mack, G. H., 1995, Supplement to the Desert Project Guidebook, with emphasis on soil micromorphology: New Mexico Bureau of Mines and Mineral Resources, Bulletin 142, 96 p.
- Goff, F., and Gardner, J., 2004, La Cenozoic geochronology of volcanism and mineralization in the Jemez Mountains and Valles Caldera, north central New Mexico, *in* Mack, G.H., and Giles, K.A., eds., The Geology of New Mexico: A Geologic History: New Mexico Geological Society, Special Publication 11, p. 295-312.
- Gradstein, F., Ogg, J. and Smith, A., 2005, A Geologic Time Scale 2005: Cambridge University Press, 589 p.
- Grauch, V.J.S., Keller, G.R., and Gillespie, C.L., 1999, Discussion of new gravity maps for the Albuquerque Basin area *in* Pazzaglia, F.J., and Lucas, S.G., eds., Albuquerque Geology: New Mexico Geological Society, Guidebook 50, p. 119-124.

- Hallett, R.B., Kyle, P.R., and McIntosh, W.C., 1997, Paleomagnetic and $^{40}\text{Ar}/^{39}\text{Ar}$ age constraints on the chronologic evolution of the Rio Puerco volcanic necks and Mesa Prieta, west-central New Mexico; implications for transition zone magmatism: Geological Society of America Bulletin, v. 109, n. 1, p. 95-106.
- Haneberg, W.C., 1995, Depth-porosity relationships and virgin specific storage estimates for the upper Santa Fe Group aquifer system, central Albuquerque basin, New Mexico: New Mexico Geology, v. 17, n. 4, p. 62-71.
- Hawley, J.W., ed., 1978, Guidebook to Rio Grande rift in New Mexico and Colorado: New Mexico Bureau of Mines and Mineral Resources, Circular 163, 241 p.
- Hawley, J. W., 1996, Hydrogeologic framework of potential recharge areas in the Albuquerque Basin, central New Mexico: New Mexico Bureau of Mines and Mineral Resources, Open-file report 402 D, Chapter 1, 68 p.
- Hawley, J.W., and Haase, C.S. (compilers), 1992, Hydrogeologic framework of the northern Albuquerque basin: New Mexico Bureau of Mines and Mineral Resources, Open-file Report 387, 165 p. 7 plates.
- Hawley, J.W., Haase, C.S., Lozinsky, R.P., 1995, An underground view of the Albuquerque Basin: New Mexico Water Resources Research Institute, Report 290, p. 27-55.
- Heller, P.L., and Paola, C., 1992, The large-scale dynamics of grain-size variation in alluvial basins, 2: Application to syntectonic conglomerate: Basin Research, v. 4, p. 94-102.
- Hudson, M.R., Mikolas, M., Geissman, J.W., and Allen, B.D., 1999, Paleomagnetic and rock magnetic properties of Santa Fe Group sediments in the 98th Street core hole and correlative surface exposures, Albuquerque basin, New Mexico, *in* Pazzaglia, F.J., and Lucas, S.G., eds., Albuquerque Geology: New Mexico Geological Society, Guidebook 50, p. 355-361.
- Hudson, M.R., Grauch, V.J.S., and Minor, S.A., 2008, Rock magnetic characterization of faulted sediments with associated magnetic anomalies in the Albuquerque Basin, Rio Grande rift, New Mexico: Geological Society of America Bulletin, v. 120, n. 5/6, p. 641-658, doi: 10.1130/B26213.1.
- Ingersoll, R.V., 2001, Structural and stratigraphic evolution of the Rio Grande rift, northern New Mexico and southern Colorado: International Geology Review, v. 43, p. 867-891.
- Izett, G.A., and Wilcox, R.E., 1982, Map showing localities and inferred distributions of the Huckleberry Ridge, Mesa Falls, and Lava Creek ash beds (Pearlette family ash

- beds) of Pliocene and Pleistocene age in the western United States and southern Canada: U.S. Geological Survey, Miscellaneous Investigation Series Map I-1325.
- Izett, G.A., and Obradovich, J.D., 1994, $^{40}\text{Ar}/^{39}\text{Ar}$ age constraints for the Jaramillo normal subchron and the Matuyama-Brunhes geomagnetic boundary: *Journal of Geophysical Research*, v. 99, n. B2, p. 2925-2934.
- Jackson, J.A., and Leeder, M.R., 1994, Drainage systems and the development of normal faults: an example from Pleasant Valley, Nevada. *Journal of Structural Geology*, v. 16, p. 1041-1059.
- Johnson, N.M., Opdyke, N.D., and Lindsay, E.H., 1975, Magnetic polarity stratigraphy of Pliocene–Pleistocene terrestrial deposits and vertebrate faunas, San Pedro Valley, Arizona, *Geologic Society of America Bulletin*, v. 86, n. 1, p. 5-12.
- Johnson, N.M., Opdyke, N.D., Woodward, G.D., Lindsay, E.H., and Tehirkheli, R.A.K., 1982, Magnetic polarity stratigraphy and ages of Siwalik Group rocks of the Potwar Plateau, Pakistan: *Palaeogeography, Palaeoclimatology, Palaeoecology*, v. 37, n. 1, p. 14-42.
- Jones, C. H., 2002, User-driven Integrated Software Lives: “PaleoMag” Paleomagnetism Analysis on the Macintosh, *Computers and Geosciences*, v. 28, n. 10, p. 1145-1151.
- Justet, L., and Spell, T.L., 2001, Effusive eruptions from a large silicic magma chamber: the Bearhead Rhyolite, Jemez volcanic field, NM: *Journal of Volcanology and Geothermal Research*, v. 107, n. 4, p. 241-264.
- Kelley, V.C., 1952, Tectonics of the Rio Grande depression of central New Mexico: *New Mexico Geological Society Guidebook 3*, p. 93-105.
- Kelley, V.C., 1977, *Geology of the Albuquerque basin, New Mexico*: New Mexico Bureau of Mines and Mineral Resources, Memoir 33, 60 p.
- Kelley, V.C., 1979, Tectonics, middle Rio Grande rift, New Mexico *in* Riecker, R.E., ed., *Rio Grande rift: Tectonics and magmatism*: American Geophysical Union, p. 57-70.
- Kelley, V.C., 1982, The right-relayed Rio Grande rift, Taos to Hatch, New Mexico: *New Mexico Geological Society, Guidebook 33*, p.147-151.
- Kelley, V. C. and Kudo, A. M., 1978, *Volcanoes and related basaltic rocks of the Albuquerque-Belen Basin, New Mexico*: New Mexico Bureau Mines Mineral Resources, Circular 156, 30 p.

- Kirschvink, J.L., 1980, The least squares line and plane and the analysis of paleomagnetic data: *Geophysical Journal of the Royal Astronomical Society*, v. 62, p. 699-718.
- Koning, D.J., Grauch, V.J.S., Connell, S.D., Ferguson, J., McIntosh, W., Slate, J., Wan, E., and Baldrige, W.S., *in press*, Structure and tectonic evolution of the eastern Española Basin, Rio Grande rift, north-central New Mexico, *in* Hudson, M.R., and Grauch, V.J.S., eds., *New Perspectives on the Rio Grande rift: from tectonics to groundwater*: Geological Society of America, Special Publication.
- Koning, D.J., and Personius, S.F., 2002, Preliminary geologic map of the Bernalillo NW quadrangle, Sandoval County: U.S. Geological Survey, Miscellaneous Field Investigations Map, MF-2404, scale 1:24,000.
- Koning, D.J., Connell, S.D., Pazzaglia, F.J., and McIntosh, W.C., 2001, Stratigraphy of the Tuerto and Ancha formations (upper Santa Fe Group), Hagan and Santa Fe embayments, north-central New Mexico, *in* Connell, S.D., Lucas, S.G., and Love, D.W., eds., *Stratigraphy and tectonic development of the Albuquerque Basin, central Rio Grande rift, mini-papers for field trip guidebook*: Albuquerque, New Mexico: Geological Society of America, Rocky Mountain-South Central Section Meeting: New Mexico Bureau of Geology and Mineral Resources, Open-file report 454B, p. I57-I66.
- Koning, D.J., Connell, S.D., Pazzaglia, F.J., and McIntosh, W.C., 2002, Redefinition of the Ancha Formation and Pliocene-Pleistocene deposition in the Santa Fe embayment, north-central New Mexico: *New Mexico Geology*, v. 24, n. 3, p. 75-87.
- Lambert, P.W., 1968, Quaternary stratigraphy of the Albuquerque area, New Mexico [Ph.D. Thesis]: Albuquerque, University of New Mexico, 329 p.
- Lambiase, J.J., and Bosworth, W., 1995, Structural controls on sedimentation in continental rifts, *in* Lambiase, J.J., ed., *Hydrocarbon habitat in rift basins*: Geological Society Special Publication No. 80, p. 117-144.
- Lanphere, M.A., Champion, D.E., Christiansen, R.L., Izett, G.A., Obradovich, J.D., 2002, Revised ages for tuffs of the Yellowstone Plateau volcanic field: assignment of the Huckleberry Ridge Tuff to a new geomagnetic polarity event: *Geological Society of America Bulletin*, v. 114, n. 5, p. 559-568.
- Leeder, M.R., and Gawthorpe, R.L., 1987, Sedimentary models for extensional tilt block/half-graben basins, *in* Coward, M.P., Dewey, J.F., and Hancock, P.L., eds., *Continental extensional tectonics*: Geological Society of London Special Publication 28, p. 139-152.

- Leeder, M. R., and Jackson, J. A., 1993, The interaction between normal faulting and drainage in active extensional basins, with examples from the western United States and central Greece: *Basin Research*, v. 5, n. 2, p. 79-102.
- Leeder, M.R., and Mack, G.H., 2001, Lateral erosion (“toe cutting”) of alluvial fans by axial rivers: implications for basin analysis and architecture: *Journal of the Geological Society of London*, v. 158, 885-893.
- Leeder, M.R., and Mack, G.H., 2007, Basin-fill incision, Rio Grande and Gulf of Corinth rifts: convergent response to climatic and tectonic drivers, *in* Nichols, G., Williams E., and Paola, C eds., *Sedimentary processes, Environments and basins: A Tribute to Peter Friend: International Association of Sedimentologists Special Publication 38*, 9-28. 2007.
- Leeder, M.R., Mack, G.H., and Salyards, S.L., 1996, Axial-transverse fluvial interactions in half-graben: Plio-Pleistocene Palomas Basin, southern Rio Grande rift, New Mexico, USA: *Basin Research*, v. 8, n. 3, p. 225-241.
- Lindsay, E. H., Johnson, N. M., Opdyke, N. D., and Butler, R. F., 1987, Mammalian chronology and the magnetic polarity time scale, *in* Woodburne, M. O., ed., *Cenozoic mammals of North America, geochronology and biostratigraphy*: Berkeley, University of California Press, p. 269–284.
- Liu, Q., Bloemendal, J., Torrent, J. and Deng, C., 2006, Contrasting behavior of hematite and goethite within paleosol S5 of the Luochuan profile, Chinese Loess Profile: *Geophysical Research Letters*, v. 33, L20301.
- Love D.W., and Connell, S.D., 2005, Late Neogene drainage developments on the southeastern Colorado Plateau, New Mexico, *in* Lucas, S.G., Morgan, G.S., and Ziegler, K.E., eds., *New Mexico’s Ice Ages: New Mexico Museum of Natural History and Science Bulletin 28*, p. 151-169.
- Love, D.W., Maldonado, F., Hallett, B., Panter, K., Reynolds, C., McIntosh, W., Dunbar, N., 1998, *Geology of the Dalies 7.5-minute quadrangle: New Mexico Bureau of Geology, Open-file Geologic Map 21*, scale 1:24,000.
- Love, D.W., Connell, S.D., Chamberlin, R.M., Cather, S.M., McIntosh, W.C., Dunbar, N., Smith, G.A., Lucas, S.G., 2001a, Constraints on the age of extensive fluvial facies of the upper Santa Fe Group, Albuquerque and Socorro basins, central New Mexico [abstract]: *Geological Society of America, Abstracts with Programs*, v. 33, n. 5, p. A-48.
- Love, D.W., Connell, S.D., Lucas, S.G., Morgan, G.S., Derrick, N.N., Jackson-Paul, P.B., and Chamberlin, R., 2001b, Third-day, Belen sub-basin: Belen, Sevilleta National Wildlife Refuge, and northern Socorro Basin, *in* Connell, S.D., Love, D.W., Lucas, S.G., Koning, D.J., Derrick, N.N., Maynard, S.R., Morgan, G.S., Jackson-

- Paul, P.B., and Chamberlin, R., trip leaders., Stratigraphy and tectonic development of the Albuquerque Basin, central Rio Grande rift, field trip guidebook: Albuquerque, New Mexico, Geological Society of America, Rocky Mountain-South Central Section Meeting: New Mexico Bureau of Geology and Mineral Resources, Open-file report 454A, p. 27-53.
- Love, D.W., Connell, S.D., Lucas, S.G., Morgan, G.S., Derrick, N.N., Jackson-Paul, P.B., and Chamberlin, R., 2001c, Third-day road log: Geology of Los Lunas volcano, *in* Connell, S.D., Love, D.W., Sorrell, J.D., and Harrison, J.B.J., trip leaders., Plio-Pleistocene stratigraphy and geomorphology of the central part of the Albuquerque Basin: New Mexico Bureau of Geology and Mineral Resources, Open-file report 454C, p. 3-1 to 3-13.
- Lowrie, W., 1990, Identification of ferromagnetic minerals in a rock by coercivity and unblocking temperature properties: *Geophysical Research Letters*, v. 17, p. 159-162.
- Lozinsky, R.P., 1994, Cenozoic stratigraphy, sandstone petrology, and depositional history of the Albuquerque basin, central New Mexico: Geological Society of America, Special Paper 291, p. 73-82.
- Lozinsky, R.P., and Tedford, R.H., 1991, Geology and paleontology of the Santa Fe Group, southwestern Albuquerque Basin, Valencia County, New Mexico: New Mexico Bureau of Mines and Mineral Resources, Bulletin 132, 35 p.
- Lucas, S.G., Williamson, T.E., and Sobus, J., 1993, Plio-Pleistocene stratigraphy, paleoecology, and mammalian biochronology, Tijeras Arroyo, Albuquerque area, New Mexico: *New Mexico Geology*, v. 15, n. 1, p. 1-8.
- Machette, M.N., 1978, Geologic map of the San Acacia Quadrangle, Socorro County, New Mexico: U.S. Geological Survey, Geologic Quadrangle Map GQ-1415, scale 1:24,000.
- Machette, M.N., 1985, Calcic soils of the southwestern United States: Geological Society of America, Special Paper 203, p. 1-42.
- Machette, M.N., Personius, S.F., Kelson, K.I., Haller, K.M., and Dart, R.L., 1998, Map and data for Quaternary faults and folds in New Mexico: U.S. Geological Survey Open-file report 98-821, 443 p., 1 pl.
- Machette, M.N., Marchetti, D.W., and Thompson, R., 2007, Ancient Lake Alamosa and the Pliocene to middle Pleistocene evolution of the Rio Grande, *in* Machette, M.N., Coates, M.M., and Johnson, M.L., eds., 2007 Rocky Mountain Section Friends of the Pleistocene Field Trip—Quaternary Geology of the San Luis Basin of Colorado and New Mexico, September 7-9, 2007: U.S. Geological Survey Open-file report 2007-1193, p. 157-167.

- Mack, G.H. and Seager, W.R., 1990, Tectonic controls on facies distribution of the Camp Rice and Palomas Formations (Pliocene-Pleistocene) in the southern Rio Grande rift: *Geological Society of America Bulletin*, v. 102, p. 45-53.
- Mack, G.H., Salyards, S.L., and James, W.C., 1993, Magnetostratigraphy of the Plio-Pleistocene Camp Rice and Palomas Formations in the Rio Grande rift of southern New Mexico: *American Journal of Science*, v. 293, p. 47-77.
- Mack, G.H., Cole, D.R., James, W.C., and Giordano, T.H., and Salyards, S.L., 1994, Stable oxygen and carbon isotopes of pedogenic carbonate as indicators of Plio-Pleistocene paleoclimate in the southern Rio Grande rift, south-central New Mexico: *American Journal of Science*, . 294, p. 621-640.
- Mack, G.H., McIntosh, W.C., Leeder, M.R., and Monger, H.C., 1996, Plio-Pleistocene pumice floods in the ancestral Rio Grande, southern Rio Grande rift, New Mexico, USA: *Sedimentary Geology*, v. 103, p. 1-8.
- Mack, G.H., Leeder, M., and Salyards, S.L., 2002, Temporal and spatial variability of alluvial-fan and axial-fluvial sedimentation in the Plio-Pleistocene Palomas half graben, southern Rio Grande rift, New Mexico, USA, *in* Renaut, R.W., and Ashley, G.M., eds., *Sedimentation in continental rifts: SEPM (Society for Sedimentary Geology) Special Publication No. 73*, p. 165-177.
- Mack, G.H., Seager, W.R., Leeder, M.R., Perea-Arlucea, M., and Salyards, S.L., 2006, Pliocene and Quaternary history of the Rio Grande, the axial river of the southern Rio Grande rift, New Mexico, USA: *Earth-Science Reviews*, v. 79, p. 141-162.
- Maldonado, F., Connell, S.D., Love, D.W., Grauch, V.J.S., Slate, J.L., McIntosh, W.C., Jackson, P.B., and Byers, F.M., Jr., 1999, Neogene geology of the Isleta Reservation and vicinity, Albuquerque Basin, New Mexico: *New Mexico Geological Society Guidebook 50*, p. 175-188.
- Maldonado, F., Budahn, J.R., Peters, L., and Unruh, D.M., 2006, Geology, geochronology, and geochemistry of basaltic flows of the Cat Hills, Cat Mesa, Wind Mesa, Cerro Verde, and Mesita Negra, central New Mexico: *Canadian Journal of Earth Sciences*, v. 43, n. 9, p. 1251-1268.
- Maldonado, F., Slate, J.L., Love, D.W., Connell, S.D., Cole, J.C., and Karlstrom, K.E., 2007, Geologic map of the Pueblo of Isleta tribal lands and vicinity, Bernalillo, Torrance, and Valencia Counties, central New Mexico: U.S. Geological Survey Scientific Investigations Map 2913, 35-p. 1 pamphlet, 1 pl, scale 1:50,000.
- Marr, J.G., Swenson, J.B., Paola, C., and Voller, V.R., 2000, A two-dimensional model of fluvial stratigraphy in closed depositional basins: *Basin Research*, v. 12, p. 381-398.

- May, J.S., Kelley, S.A., and Russell, L.R., 1994, Footwall unloading and rift shoulder uplifts in the Albuquerque Basin: their relation to syn-rift fanglomerates and apatite fission-track ages: Geological Society of America, Special Paper 291, p. 125-134.
- McAda, D.P., and Barroll, P., 2002, Simulation of ground-water flow in the middle Rio Grande Basin between Cochiti and San Acacia, New Mexico: U.S. Geological Survey, Water-Resources Investigations Report 02-4200, 81 p.
- McIntosh, W.C., and Quade, J., 1995, $^{40}\text{Ar}/^{39}\text{Ar}$ geochronology of tephra layers in the Santa Fe Group, Española Basin, New Mexico, *in* Bauer, P.W., Kues, B.S., Dunbar, N.W., Karlstrom, K.E., and Harrison, B., eds., *Geology of the Santa Fe region: New Mexico Geological Society, Guidebook 46*, p. 279-287.
- Molnar, P., 2004, Late Cenozoic increase in accumulation rates of terrestrial sediment: How might climate change have affected erosion rates?: *Annual Review of Earth and Planetary Sciences*, v. 32, p. 67-89.
- Morgan G.S., and Lucas, S.G., 2003, Mammalian biochronology of Blancan and Irvingtonian (Pliocene and early Pleistocene) faunas from New Mexico: *American Museum of Natural History Bulletin*, v. 13, n. 279, p. 269-320.
- NOAA (National Oceanic and Atmospheric Agency) Geophysical Data Center, 2005, <http://www.ngdc.noaa.gov/geomag/>, accessed May 2008.
- Olsen, P.E., 1997, Stratigraphic record of the early Mesozoic breakup of Pangea in the Laurasia-Gondwana rift system: *Annual Review of Earth and Planetary Science*, v. 25, p. 337-401.
- Opdyke, N.D., Lindsay, E.H., Johnson, N.M., and Downs, T., 1977, The paleomagnetism and magnetic polarity stratigraphy of the mammal-bearing section of Anza Borrego State Park, California: *Quaternary Research*, v. 7, n. 3, p. 316-329.
- Paola, C., 2000, Quantitative models of sedimentary basin filling: *Sedimentology*, v. 47, p. 121-178.
- Paola, C., Heller, P.L., and Angevine, C.L., 1992, The large-scale dynamics of grain-size variation in alluvial basins, 1: Theory: *Basin Research*, v. 4, p. 73-90.
- Pazzaglia, F.J., Pederson, J.L., Garcia, A.F., Koning, D.J., Formento-Trigilio, M.L., and Toya, C., 1998, *Geology of the Jemez Pueblo 7.5-minute quadrangle: New Mexico Bureau of Mines and Mineral Resources Open-file Geologic Map 14*, scale 1:24,000.
- Peakall, J., 1998, Axial river evolution in response to half-graben faulting, Carson River, Nevada: *Journal of Sedimentary Research*, v. 68, n. 5, p. 788-799.

- Peakall, J., Leeder, M., Best, J., and Ashworth, P., 2000, River responses to lateral ground tilting: a synthesis and some important implications for the modeling of alluvial architecture in extensional basins: *Basin Research*, v. 12, p. 413-424.
- Phillips, E.H., Goff, F., Kyle, P.R., McIntosh, W.C., Dunbar, N.W., and Gardner, J.N., 2007, The $^{40}\text{Ar}/^{39}\text{Ar}$ age constraints on the duration of resurgence at the Valles caldera, New Mexico: *Journal of Geophysical Research*, v. 112, n. B8, B08201, doi: 10.1029/2006JB004511
- Reheis, M.C., Sarna-Wojcicki, A.M., Burbank, D.M., and Meyer, C.E., 1991, The late Cenozoic section at Willow Wash, west-central California: a tephrochronological Rosetta Stone, *in* Reheis, M.C., Slate, J.L., Sawyer, T.L., Sarna-Wojcicki, A.M., Harden, J.W., Pendall, E.G., Gillespie, A.R., and Burbank, D.M., eds., *Pacific Cell, Friends of the Pleistocene guidebook for field trip to Fish Lake Valley, California-Nevada*: U.S. Geological Survey, Open-file report 91-290, p. 46-66.
- Reneau, S.L., and Dethier, D.P., 1996, Late Pleistocene landslide-dammed lakes of the Rio Grande, White Rock Canyon, New Mexico: *Geological Society of America, Bulletin*, v. 108, n. 11, p. 1492-1507.
- Renne, P.R., Swisher, C.C., W.D., Deino, Karner, D.B., Owens, T.L., and DePaolo, D.J., 1998, Intercalibration of standards, absolute ages and uncertainties in $^{40}\text{Ar}/^{39}\text{Ar}$ dating: *Chemical Geology*, v. 145, p. 117-152.
- Russell, L.R., and Snelson, S., 1994, Structure and tectonic of the Albuquerque Basin segment of the Rio Grande rift: Insights from reflection seismic data: *Geological Society of America, Special Paper 291*, p. 83-112.
- Sadler, P. M. 1981. Sediment accumulation rates and the completeness of stratigraphic sections: *Journal of Geology*, v. 89, p. 569-584.
- Samson, S. D., and Alexander, E. C., Jr., 1987, Calibration of the interlaboratory $^{40}\text{Ar}/^{39}\text{Ar}$ dating standard, Mmhb1: *Chemical Geology*, v. 66, n. 1-2, p. 27-34.
- Sarna-Wojcicki, A.M., Lajoie, K.R., Meyer, C.E., and Adam, D.P., 1991, Tephrochronologic correlation of upper Neogene sediments along the Pacific margin, conterminous United States, *in* Morrison, R.B., ed., *Quaternary nonglacial geology, conterminous U.S.*: Geological Society of America, *The Geology of North America*, v. K-2, p. 117-140.
- Schlische, R.W., 1991, Half-graben basin filling models: New constraints on continental extensional basin development: *Basin Research*, v. 3, p. 123-141.
- Schlische, R.W., 1995, Geometry and origin of fault-related folds in extensional settings: *American Association of Petroleum Geologists Bulletin*, v. 79, n. 11, p. 1661-1678.

- Smith, G.A., 2001, Development of a pyroclastic apron adjacent to rhyolite domes in a subsiding basin: upper Miocene Peralta Tuff, Jemez Mountains, New Mexico, *in* Crumpler, L.S., and Lucas, S.G., eds., *Volcanology in New Mexico: New Mexico Museum of Natural History and Science, Bulletin 18*, p. 85-96.
- Smith, G.A., Wang, Y., Cerling, T.E., and Geissman, J.W., 1993, Comparison of a paleosol-carbonate isotope record to other records of Pliocene-early Pleistocene climate in the western United States: *Geology*, v. 21, n. 8, p. 691-694.
- Smith, G.A., and Lavine, A., 1996, What is the Cochiti Formation?, *in* Goff, F., Kues, B.S., Rogers, M.A., McFadden, L.D., and Gardner, J.N., eds., *The Jemez Mountains Region: New Mexico Geological Society Guidebook 47*, p. 219-224.
- Smith, G.A., McIntosh, W.C., and Kuhle, A.J., 2001, Sedimentologic and geomorphic evidence for sea-saw subsidence of the Santo Domingo accommodation-zone basin, Rio Grande rift, New Mexico: *Geological Society of America, Bulletin*, v. 113, n. 5, p. 561-574.
- Smith, R.L., Bailey, R.A., and Ross, C.S., 1970, Geologic map of the Jemez Mountains, New Mexico: U.S. Geological Survey, *Miscellaneous Geological Investigations*, I-571, scale 1:125,000.
- Spell, T.L., Harrison, T.M., and Wolff, J.A., 1990, $^{40}\text{Ar}/^{39}\text{Ar}$ dating of the Bandelier Tuff and San Diego Canyon ignimbrites, Jemez Mountains, New Mexico: *Journal of Geophysical Research*, v. 98, n. B3, p. 8031-8051.
- Spell, T.L., McDougall, I., and Doulgeris, A.P., 1996, Cerro Toledo rhyolite, Jemez Volcanic Field, New Mexico: $^{40}\text{Ar}/^{39}\text{Ar}$ geochronology of eruptions between two caldera-forming events: *Geological Society of America*, v. 108, p. 1549-156.
- Spiegel, Z., and Baldwin, B., 1963, Geology and water resources of the Santa Fe area, New Mexico: U.S. Geological Survey, *Water-Supply Paper 1525*, 258 p, 7 pls.
- Stearns, C.E., 1953, Tertiary geology of the Galisteo-Tonque area, New Mexico: *Geological Society of America Bulletin*, v. 64, p. 459-508.
- Stearns, C.E., 1979, New K-Ar dates and the late Pliocene to Holocene geomorphic history of the central Rio Grande region, New Mexico: *Discussion: Geological Society of America, Bulletin*, v. 90, n. 8, p. 799-800.
- Steiger, R. H., and Jäger, E., 1977, Subcommittee on geochronology—convention on the use of decay constants in geo- and cosmo-chronology: *Earth and Planetary Science Letters*, v. 36, p. 359–362.
- Stone, B.D., Allen, B.D., Mikolas, M., Hawley, J.W., Haneberg, W.C., Johnson, P.S., Allred, B., and Thorn, C.R., 1998, Preliminary lithostratigraphy, interpreted

- geophysical logs, and hydrogeologic characteristics of the 98th Street core hole, Albuquerque, New Mexico: US Geological Survey, Open-file Report 98-0210, 82 p.
- Sun, W.W., and Kodama, K.P., 1992, Magnetic anisotropy, scanning electron microscopy, and X-ray pole figure goniometry study of inclination shallowing in a compacting clay-rich sediment: *Journal of Geophysical Research*, V. 97, n. B13, p. 19,599-19,615.
- Tedford, R.H., and Barghoorn, S., 1999, Santa Fe Group (Neogene), Ceja del Rio Puerco, northwestern Albuquerque Basin, Sandoval County, New Mexico: *New Mexico Geological Society, Guidebook 50*, p. 327-335.
- Tedford, R.H., Albright, L.B., III, Barnosky, A.D., Ferrusquia-Villafranca, I., Hunt, R.M., Jr., Storer, J.E., Swisher, C.C., III, Voorhies, M.R., Webb, S.D., and Whistler, D.P., 2004, Mammalian biochronology of the Arikarean through Hemphillian interval (late Oligocene through early Pleistocene epochs), *in* Woodburne, M.O., ed., *Late Cretaceous and Cenozoic Mammals of North America: biostratigraphy and geochronology*: New York, Columbia University Press, p. 169-231.
- Thorn, C.R., McAda, D.P., and Kernodle, J.M., 1993, Geohydrologic framework and hydrologic conditions in the Albuquerque basin, central New Mexico: U.S. Geological Survey, Water-resources Investigations Report 93-4149, 106 p.
- Travis, C.J., and Nunn, J.A., 1994, Stratigraphic architecture of extensional basins: Insights from a numerical model of sedimentation in evolving half grabens: *Journal of Geophysical Research*, v. 99, n. B8, p. 15,653-15,666.
- Van Hinte, J.E., 1978, Geohistory analysis—Application of micropaleontology in exploration geology: *American Association of Petroleum Geologists Bulletin*, v. 62, n. 2, p. 201-222.
- Webb, S.D., and Opdyke, N.D., 1995, Global climatic influences on Cenozoic land mammal faunas, *in* Stanley, S.M., chairperson, *Effects of past global change on life*: Washington D.C., National Academy Press, p. 184-208.
- Wells, S.G., Kelson, K.I., and Menges, C.M., 1987, Quaternary evolution of fluvial systems in the northern Rio Grande rift, New Mexico and Colorado: implications for entrenchment and integration of drainage systems, *in* Menges, C.M., Enzel, Y., and Harrison, J.B.J., eds., *Quaternary tectonics, landform evolution, soil chronologies, and glacial deposits: northern Rio Grande rift of New Mexico*: Friends of the Pleistocene-Rocky Mountain Cell Guidebook, p. 55-69.
- Williams, P.L., and Cole, J.C., 2007, Geologic map of the Albuquerque 30' x 60' quadrangle, north-central New Mexico: U.S. Geological Survey, Scientific Investigations Map 2946, 31 p., scale 1:100,000.

- Wright, H.E., 1946, Tertiary and Quaternary geology of the lower Rio Puerco area, New Mexico: Geological Society of America Bulletin, v. 57, n. 5, p. 383-456.
- Xiao, H., and Suppe, J., 1992, Origin of rollover: American Association of Petroleum Geologists Bulletin, v. 76, n. 4, p. 509-529.
- Zachos, J., Pagani, M., Sloan, L., Thomas, E., Billups, K., 2001, Trends, rhythms, and aberrations in global climate 65 Ma to present: Science, v. 292, p. 686-693.
- Zhang, P., Molnar, P., and Downs, W.R., 2001, Increased sedimentation rates and grain sizes 2-4 Myr ago due to the influence of climate change on erosion rates: Nature, v. 410, p. 891-897.
- Zijderveld, J.D.A., 1967, A.C. demagnetization of rocks: Analysis of results, *in* D.W. Collinson, K.M. Creer, and S.K. Runcorn, eds., Methods of Paleomagnetism: Elsevier, p. 254-286.

CHAPTER 3. EXPERIMENTAL STUDY OF INTERACTING DRAINAGES IN A SEDIMENTARY BASIN: SURFACE MORPHOLOGY

Sean D. Connell^{1,2}, Wonsuck Kim³, Chris Paola⁴, and Gary A. Smith¹

¹*Department of Earth and Planetary Sciences, MSC03 2040, University of New Mexico, Albuquerque, New Mexico 87131 USA*

²*New Mexico Bureau of Geology and Mineral Resources-Albuquerque Office, New Mexico Institute of Mining and Technology, 2808 Central Ave., SE, Albuquerque, New Mexico 87106 USA*

³*Department of Geological Sciences, University of Texas at Austin, 1 University Station, Austin, Texas 78712 USA*

⁴*Department of Geology and Geophysics and St. Anthony Falls Laboratory, University of Minnesota, Minneapolis, Minnesota 55414 USA*

Chapter Abstract

A fundamental distinction in the stratigraphic architecture of intracontinental rift basins is that between depositional belts associated with the basin axis versus flanking tributary streams on the piedmonts. Spatiotemporal distributions of these component facies associations are sensitive to a variety of factors, including basin geometry, subsidence rate, and sediment discharge; however, most studies focused on only one or two components of the rift-basin succession. A new perspective on how these depositional belts evolve under steady subsidence and (sediment and water) discharge conditions and respond to allogenic forcing can be derived from experimental stratigraphy, which offers a unique view of how sedimentary systems evolve under controlled conditions.

The Experimental EarthScape 2006 run (XES06) focused on the geomorphic evolution of multiple sedimentary successions within an asymmetrically subsiding basin based on the form of a simple half graben. Four interacting supply points of sediment and water produced an axial fan and channel that was flanked on either side by transverse fan systems that defined the edges of the axial system. Imposition of various combinations of lateral and axial sediment flux showed that the locations and widths of the axial and transverse systems were controlled by relative sediment fluxes (“flux steering”) and not by the location of the subsidence maximum. Footwall fans persisted even under conditions of very large axial sediment discharge, aided by topographic inheritance caused by the steeper depositional slopes, even in the face of frequent toe cutting by the axial drainage system. Steeper surface slopes also help maintain radial symmetry relative to the shallowly sloping axial drainage. Transverse deposit slopes tended toward an oblique orientation relative to the axial drainage. We found a good correspondence between fan morphology and the mapped extent of axial sediment in the deposits, indicating that the preserved depositional belts provide reasonable approximations of the sizes of the associated morphologic systems. The axial drainage system tended to be dominated by transversely sourced sediment (except during the highest axial sediment discharges) derived from the transverse drainages through toe cutting.

Introduction

Rift basins are important tectonic elements in continental regions subject to crustal extension. The stratigraphic architecture of intracontinental rift basins is defined by three depositional belts associated with the basin floor and two sets of flanking piedmonts that have drainages oriented generally perpendicular to the basin edges (Fig. 3.1). The positions of these belts are thought to be sensitive to subsidence and sediment delivery rate, effective moisture, catchment morphology and size, and rock type (e.g., Gawthorpe and Leeder, 2000, and references therein). The development of alluvial successions within rift basins has been examined through numerous field-based studies and numerical simulations (Bridge and Leeder, 1979; Leeder and Gawthorpe, 1987; Blair and Bilodeau, 1988; Mack and Seager, 1990; Heller and Paola, 1992; Paola et al., 1992; Bridge and MacKay, 1993; Leeder et al., 1996a & b; Gawthorpe and Leeder, 2000; Peakall, 1998; Marr et al., 2000; Leeder and Mack, 2001; Smith, 1994; and Smith et al., 2001). Most of these studies focused on only one or two depositional components, and not the entire basin-fill succession. Numerical simulations typically treat basin filling from a single sediment source (e.g., Marr et al., 2000). They do not account for transport by longitudinal drainages that occur in large intracontinental rift systems, such as the Cenozoic Rio Grande rift of North America (Chapin and Cather, 1994; Connell et al., 2005; and Mack et al., 2006) and rift valleys of East Africa (Lambiase and Bosworth, 1995; and Frostick, 1997), or the Triassic rift valleys of Pangaea in eastern North America (LeTourneau and Olsen, 2003).

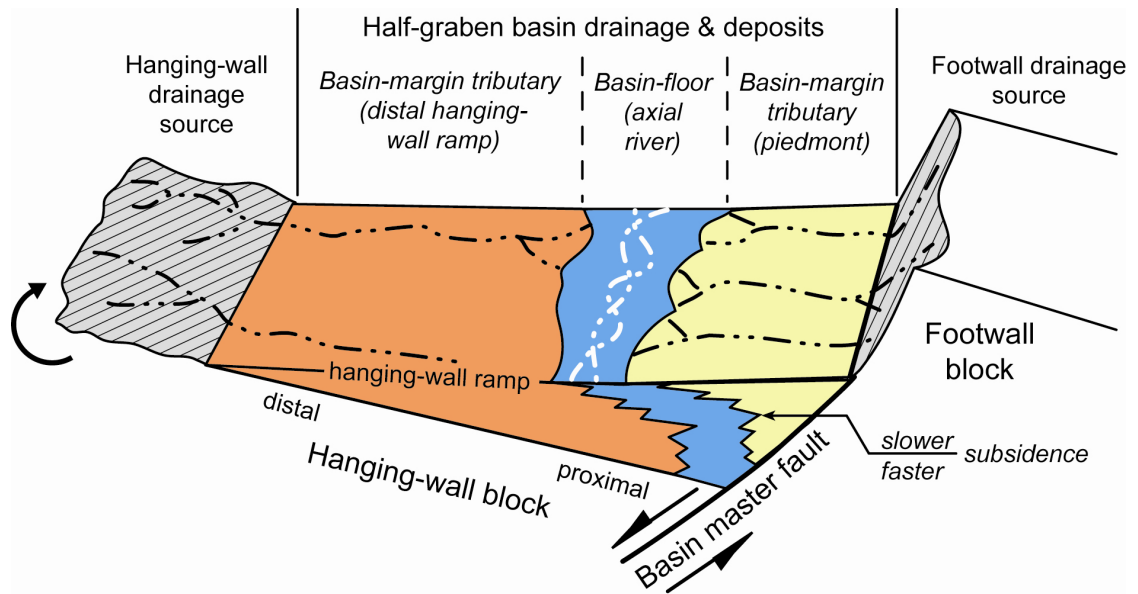


Figure 3.1. Diagram illustrating major depositional belts in a fluvially integrated half-graben basin containing tributary drainages adjacent to the uplifting footwall block and on the subsiding hanging-wall block (modified from Mack and Seager, 1990).

Models of basin filling deal with the timing and partitioning of sediment into stratigraphic sequences (Schlische and Olsen, 1990; Kendall et al., 1991; Lawrence, 1994; and Shanley and McCabe, 1994). Quantification of how sediments are distributed within a basin would aid in understanding how depositional belts develop and respond to allogenic forcing. Experimental approaches can also explore and quantify linkages between surface processes and sedimentary architecture that are largely unavailable in field-based studies (Paola, 2000).

Experimentation is a forward approach to physical modeling that offers a unique view of how sedimentary systems change under well-controlled boundary conditions and carefully monitored surface topography (Paola et al., 2001; Van Heijst and Postma, 2001; Sheets et al., 2002; Hickson et al., 2005; and Martin et al., 2009). Because there are no practical ways to scale certain physical aspects of basin filling, such as grain size

and fluid viscosity (e.g., Peakall et al., 1996; and Paola, 2000), the value of the experimental approach relies on the similarity of processes that establish topography and distribute sediment. For instance, experiments create landscapes that bear remarkable similarity to natural environments (Hasbargen and Paola, 2000). Braided channel networks are easily created and maintained in experimental basins, exhibit similar geometry over many spatial scales, and have similar spatial organization relative to natural distributary networks (Sapazhnikov and Fofoula-Georgiou, 1996; Fofoula-Georgiou and Sapazhnikov, 1998 & 2001; and Edmonds et al., 2007).

This contribution presents the results of a series of experiments that examined the development of sedimentary successions within an asymmetrically subsiding basin containing multiple interacting sediment sources. These experiments were motivated by a desire to understand how the three depositional belts respond to changes in subsidence and sediment supply. Specifically, we examined how tributary piedmont drainage influences the position of the longitudinal (axial) river, and how the axial river transferred sediment through the basin. The ability of the axial drainage system to move sediment was examined using a simple sediment mass-balance model and comparing it to the total sediment input and mapped depositional belts. The distribution of the component depositional belts is important because their contrasting three-dimensional facies-stacking arrangements broadly define reservoir (or aquifer) anisotropy, heterogeneity, and permeability (e.g., Davis et al., 1993; Bryant et al., 1995; Heller and Paola, 1996; and Smith, 2000). This paper examines the development of surface morphology of depositional belts. A companion paper examines the distribution of sediment and stratigraphic architecture from these experiments (Chapter 4).

Methods

Experimental EarthScape Facility

The Experimental EarthScape (XES) facility at Saint Anthony Falls Laboratory (University of Minnesota) is an experimental basin built to examine sedimentation under conditions of programmable differential subsidence (Paola et al., 2001). Other controllable variables include base level, sediment and water supply, and sediment size, sorting and composition. The XES facility is approximately 85 m² in area (13.0 m x 6.5 m); however, only a quarter of the subsidence cells beneath 17.5 m² of the basin (5.82 m x 3.01 m) were utilized in this experiment (Fig. 3.2).

Subsidence allows for the accumulation and preservation of sediment by lowering deposits below the effects of surface erosion. Subsidence is achieved in the XES basin by removing well-sorted, pea-sized gravel from the base of 108 subsidence cells underneath a flexible rubber membrane that acts as an impermeable basement. This basement can be programmed to subside in nearly any spatial pattern, provided the slope does not exceed the angle of internal friction of the underlying gravel. Subsidence was monitored every 240 seconds by manometers assigned for each active cell. The smallest subsidence increment is 0.12 mm, and as much as 1.3 m of sediment can be accommodated in the basin (Paola et al., 2001).

Base level is set by a lake whose elevation is controlled independently of subsidence, and sediment and water supply through a computer-driven siphon system. Sediment and water inputs can be controlled individually and delivered at arbitrary locations along the basin margins. Sediment is treated with titanium-dioxide (TiO₂)

powder and water is injected with non-toxic blue dye to create semi-opaque water to aid in the mapping of submerged regions.

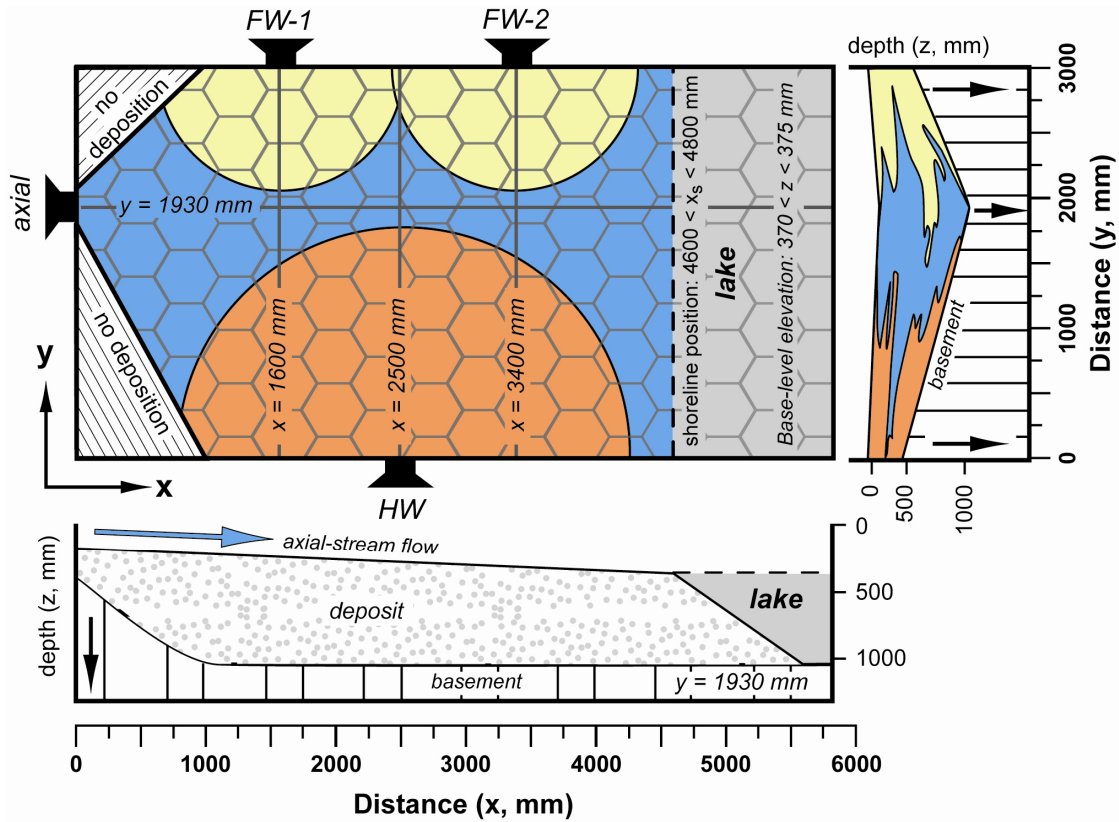


Figure 3.2. Schematic plan-view map and cross sections of the experimental setup, depicting dimensions of the tank and locations of sediment input points. Schematic cross sections illustrate geometry of basin subsidence. The four sediment feed points are analogous to the axial, hanging-wall (HW), and footwall sources in half-graben basins. The footwall contains upstream (FW-1) and downstream (FW-2) inputs. The honeycomb pattern represents the active subsidence cells that control basin subsidence. The light-gray shading denotes standing water (a lake) that controls base level.

Surface morphology is recorded through repeated surveys of topography, bathymetry, and high-resolution digital photography. Topography is scanned using a laser sheet system having 0.1-mm vertical resolution. Scans of subaqueous bathymetry in the terminal lake are done using an ultrasonic transducer having 1-mm vertical

resolution. The subaerial surface is photographed every 10 seconds with a high-resolution digital camera. These images are orthorectified at 60-second intervals for use in surface mapping and to create time-lapse movies of surface fluvial processes. After the run is complete the deposit is dissected and examined using a semi-automated slicing and imaging system that produces composite images of the deposit cross section (Mullin and Ellis, 2008).

Experimental Design

The experimental apparatus was modified to deliver multiple, independent sources of sediment and water (Fig. 3.2). Discharge controls are emphasized in the experiments (henceforth XES06) in order to better understand upstream controls on fluvial geomorphology and sedimentation (Blum and Törnqvist, 2000). A set of experiments that examined all possible sedimentary responses would result in more than 18 different permutations (and even more if variable discharge, subsidence, and base-level were included). This experiment tests the most relevant sediment discharge and subsidence scenarios in five sequential stages. The sediment-to-water ratio and base-level elevation were held constant in order to reduce the number of experimental variables. Variable subsidence and base-level effects can be introduced into future experiments.

The design for XES06 imposed a simple, double-hinge-type asymmetrical subsidence pattern with the axis of maximum subsidence located about two-thirds of the distance across the shorter side of the basin (Fig. 3.2). Subsidence rates increased linearly toward the subsidence maximum (rather than along the margin of the tank)

because of mechanical limitations of the basement membrane. The subsidence pattern resembles those of simple half-graben basins (e.g., Leeder and Gawthorpe, 1987; and Mack and Seager, 1990), where the master fault is along one side, although the degree of subsidence asymmetry is lower in the experiment than in half-grabens in the field. In this sense, the imposed subsidence pattern resembles those of basins formed by low-angle normal faults (e.g., Wernicke, 1981; and Schlische and Olsen, 1990).

This experimental configuration included four separate sediment-input points (Fig. 3.2) that provided three compositionally distinct sediment sources that could vary in discharge and sediment concentration (Fig. 3.3). A single supply point at the upper end of the basin served as the source of longitudinal drainage (analogous to the axial river in half-graben basins) and was placed at the upper end of the basin (Fig. 3.2). Catchments on the distal hanging-wall ramp of half-graben basins tend to be much larger and more widely spaced than their footwall-derived counterparts (e.g., Leeder and Jackson, 1993), so the analogous transverse inputs were placed in positions that were reasonably similar to those found in extensional basins. A single input on the river-right side of the basin served as the source of the analogous hanging-wall ramp fan (HW). At the opposite side, two inputs for the analogous footwall sources were equally divided into up-basin (FW-1) and down-basin (FW-2) inputs based on the observation of smaller and more numerous footwall fans in half-graben basins (e.g., Gawthorpe and Leeder, 2000).

The relative supplies of water and sediment to the axial and transverse fans were determined in part from field observations. Fans derived from the footwall tend to have smaller areas and steeper depositional slopes compared to the much broader and

shallowly sloping fans on the hanging wall (Leeder and Jackson, 1993). Slopes on axial rivers, such as the Rio Grande in New Mexico, tend to be less than 0.02 (vert./horiz.), whereas the slopes of tributary drainages can be as high as 0.15 near the mountain fronts (Gile et al., 1981, p. 26-29; Leeder et al., 1996b).

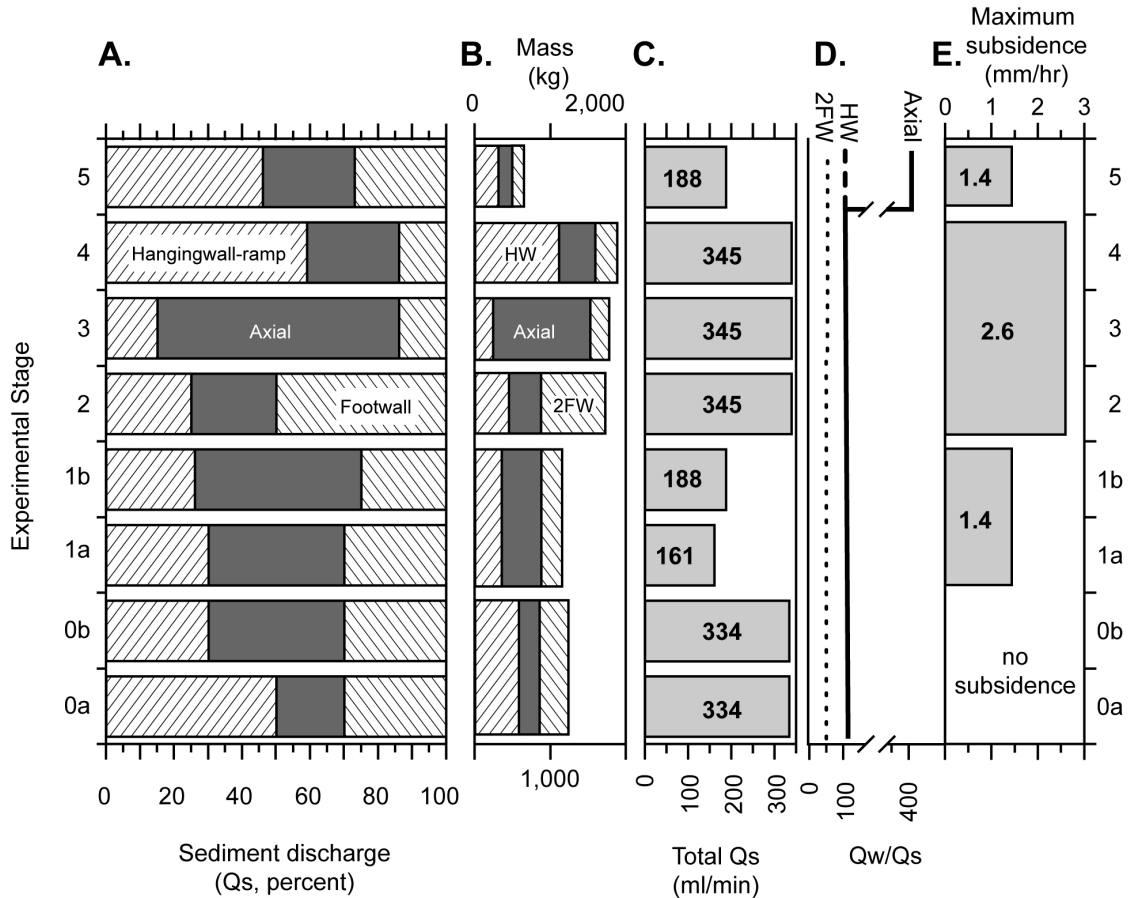


Figure 3.3. Variables for XES06 stages and substages (Table 3.1). A: sediment discharge for each input (in cumulative percent); B: cumulative sediment mass for each input (in kg; 2FW is the combined sediment discharge for FW-1 and FW-2); C: total sediment discharge rate (ml/min); D: ratio of water to sediment (Q_w/Q_s); and E: maximum subsidence rate (mm/hr) along the axis of maximum subsidence (Fig. 3.2).

The alluvial slope is proportional to the ratio of sediment discharge (Q_s) to water discharge (Q_w ; Lane, 1955; Blum and Törnqvist, 2000; and Paola, 2000). Thus, the

gradients of the alluvial profiles were steepened or reduced by altering this ratio. To achieve lower gradients for the axial drainage and the hanging-wall fan, Q_s/Q_w was set to 0.01, and was increased to 0.02 for the footwall fans (Table 3.1).

The volume of sediment delivered to the basin was less than the volume created by subsidence, resulting in an under-filled condition, with a terminal lake filling the remaining basin volume. This was done to avoid contact between the delta toe and the distal basin wall. The total sediment supplied from multiple sources was matched to total basin accommodation to achieve a nearly constant shoreline position ($460 < x_s < 480$ cm) at the lower end of the basin with a fixed base-level elevation (z) of 375 mm below the top of the tank (Fig. 3.2). Maintaining the ratio of subsidence to aggradation near unity minimizes variations in the axial-drainage length that would otherwise exert unwanted, local base-level controls (i.e., overall axial channel aggradation and degradation) on the transverse deposits.

Table 3.1. Summary of XES06 discharge parameters.

Experimental Stage		Proportion (percent)	Qs (ml/min)	Qw (ml/min)	Qw/Qs
Stage 0*	<i>HW</i>	47	156	15,583	100
	<i>Axial</i>	23	78	7,817	100
	<i>2FW</i>	30	100	5,000	50
Stage 0a	<i>HW</i>	50	167	16,700	100
	<i>Axial</i>	20	67	6,700	100
	<i>2FW</i>	30	100	5,000	50
Stage 0b	<i>HW</i>	30	100	10,000	100
	<i>Axial</i>	40	134	13,400	100
	<i>2FW</i>	30	100	5,000	50
Stage 1*	<i>HW</i>	28	48	4,800	100
	<i>Axial</i>	44	75	7,547	100
	<i>2FW</i>	28	48	2,400	50
Stage 1a	<i>HW</i>	28	48	4,800	100
	<i>Axial</i>	40	65	6,500	100
	<i>2FW</i>	30	48	2,400	50
Stage 1b	<i>HW</i>	26	48	4,800	100
	<i>Axial</i>	49	92	9,292	101
	<i>2FW</i>	25	48	2,400	50
Stage 2	<i>HW</i>	25	88	8,800	100
	<i>Axial</i>	25	85	8,840	104
	<i>2FW</i>	50	172	8,600	50
Stage 3	<i>HW</i>	14	49	4,900	100
	<i>Axial</i>	71	246	25,830	105
	<i>2FW</i>	14	50	2,700	54
Stage 4	<i>HW</i>	62	203	20,300	100
	<i>Axial</i>	23	92	9,650	105
	<i>2FW</i>	16	50	2,700	54
Stage 5*	<i>HW</i>	47	88	8,800	100
	<i>Axial</i>	27	50	22,556	451
	<i>2FW</i>	26	50	2,700	54
Stage 5a	<i>HW</i>	47	88	8,800	100
	<i>Axial</i>	27	50	9,650	193
	<i>2FW</i>	26	50	2,700	54
Stage 5b	<i>HW</i>	47	88	8,800	100
	<i>Axial</i>	27	50	20,820	416
	<i>2FW</i>	26	50	2,700	54

Note: *Asterisk denotes time-weighted arithmetic mean for the entire stage.

Sediment

Sediment and water were mixed outside of the basin and fed through pipes to input points along the tank boundary (Fig. 3.2). The sediment is a volumetric mixture of 70 percent, moderately well-sorted, fine-grained ($178 \pm 121 \mu\text{m}$) white silica sand, and 30 percent, moderately sorted, medium-grained, crushed anthracite coal ($368 \pm 264 \mu\text{m}$). The (pre-depositional) bulk density of this sediment mixture is 1.61 kg/liter. Compaction effects are considered negligible because of the relatively thin overburden (thickness, $\theta < 1.3 \text{ m}$) in the experimental apparatus. The specific gravity of the crushed coal ($sg = 1.3$) is nearly half of the sand ($sg = 2.65$), making it a reasonable hydraulic surrogate for the finer-grained and more mobile sediment fraction (Paola et al., 2001).

Substitution of 7 percent painted quartz sand grains provided colored tracers that aided deposit mapping. Green sand tracers were included for all sediment sources in stage 0. The remaining stages used three sand tracers for the analogous inputs: footwall-sourced sediment contained yellow grains, axially sourced sand contained blue grains, and hanging-wall sourced sediment contained red grains.

Experimental Stages

XES06 progressed through six stages, designated stage 0 to stage 5 (Table 3.1). Stage 0 established the initial topography with no subsidence. Five subsequent stages were designed to explore combinations of sediment discharge for the three depositional belts using two different overall subsidence rates (Fig. 3.3). The overall goal of these experiments was to measure how changes in the relative sediment supply rates among the three source types would be manifested in surface morphology and stratigraphy.

Changes in subsidence and sediment discharge at stage boundaries were abrupt. This was done to produce clearly defined stratigraphic boundaries in the deposit. Total sediment discharge was maintained between 161 and 188 ml per minute (0.0027 and 0.0031 L/s, respectively) during the slowly subsiding stages (1 and 5), and increased to 345 ml/minute (0.0058 L/s) during rapid subsidence in stages 2 through 4. The Q_s/Q_w ratio for the axial input was increased to 0.0024 (1:416) during stage 5 in an attempt to decrease axial-channel slopes. Isolation of the different depositional morphologies (i.e., axial, hanging-wall, and footwall) was done using overhead imagery to clip out areas of interest for analysis.

Stage 1 emphasized axially dominated sedimentation under low rates of subsidence (max. rate = 1.4 mm/hr, or 0.0004 mm/s), where axial sediment discharge amounted to slightly less than half of the total basin sediment discharge (Fig. 3.3, Table 3.1). Subsidence during stages 2 through 4 increased to nearly twice (max. rate = 2.6 mm/hr, or 0.0007 mm/s) that of stages 1 and 5. Stage 2 emphasized footwall-dominated sedimentation, where axial sediment discharge was reduced to 25 percent of the total sediment discharge. All inputs had equivalent sediment discharge during this stage, and the two footwall inputs delivered half of the total sediment (Fig. 3.3). Stage 3 emphasized axially dominated sedimentation, where axial sediment discharge increased to 71 percent of the total sediment discharge in the basin. Stage 4 emphasized hanging-wall dominated sedimentation, where the axial sediment discharge was reduced to about a quarter of the total sediment discharge in the basin. Hanging-wall sources accounted for 62 percent of the total sediment discharge; footwall sources were 16 percent. Stage 5 subsidence rates decreased to the levels of stage 1 and sediment discharges were reduced

accordingly to match the diminished subsidence (Fig. 3.3). The relative proportions of sediment discharge remained the same as stage 4; however, the axial-water discharge was incrementally increased over a period of 18 hours to 1249 liters per hour (0.347 L/s) in an attempt to lower the slope of the axial drainage.

Data Collection

Deposit-surface morphology was documented using repeat surveys of elevation and overhead imagery (Fig. 3.4). Data processing was done using Adobe Systems Photoshop™ (CS3 Extended, <http://www.adobe.com/>) and Mathworks Matlab™ (version 7.1 with image analysis tool box, <http://www.mathworks.com/>). Data related to XES06 (including time-lapse movies) are available in Appendix D-I. All data associated with XES06 are available through the National Center for Earth-Surface Dynamics (NCED) repository at the University of Minnesota (<https://repository.nced.umn.edu/>).

Over the 300-hour experiment, 63 scans of subaerial topography were collected at intervals ranging from 2 to 5 hours; 8 scans of subaerial topography were collected at 2- to 7-hr intervals during stage 0. Twenty scans of subaqueous bathymetry in the terminal lake were collected at 20-hour intervals. Digital elevation models (DEMs) of the deposit surface were made by interpolating bathymetric scans to the topographic-scan intervals and merging them with the topographic data using a simple linear interpolation. The topographic and bathymetric data were initially gridded with a cell spacing of 50 cm in the long (*x-axis*) direction and 10 cm in the short (*y-axis*) direction of the basin and edited to remove spurious data. The final DEMs were created by re-

gridding the data into 1-cm² cells and extrapolating elevations to the edges of the experimental basin.

DEMs of basement subsidence were created by gridding elevation data collected by manometers on the 108 active subsidence cells and extrapolating this surface to the edges of the basin. The subsidence DEMs were used to stratigraphically migrate the topographic DEMs in order to account for the total subsidence between elevation scan-times and the end of the experiment. These stratigraphically migrated DEMs were clipped to account for post-depositional erosion by comparing them to later migrated elevations at each grid point. Where a subsequent elevation was lower than the reference scan, the reference elevation was replaced with the value on the later scan. These migrated datasets represent isochronous surfaces that were used to resolve sediment volumes and to correlate deposits.

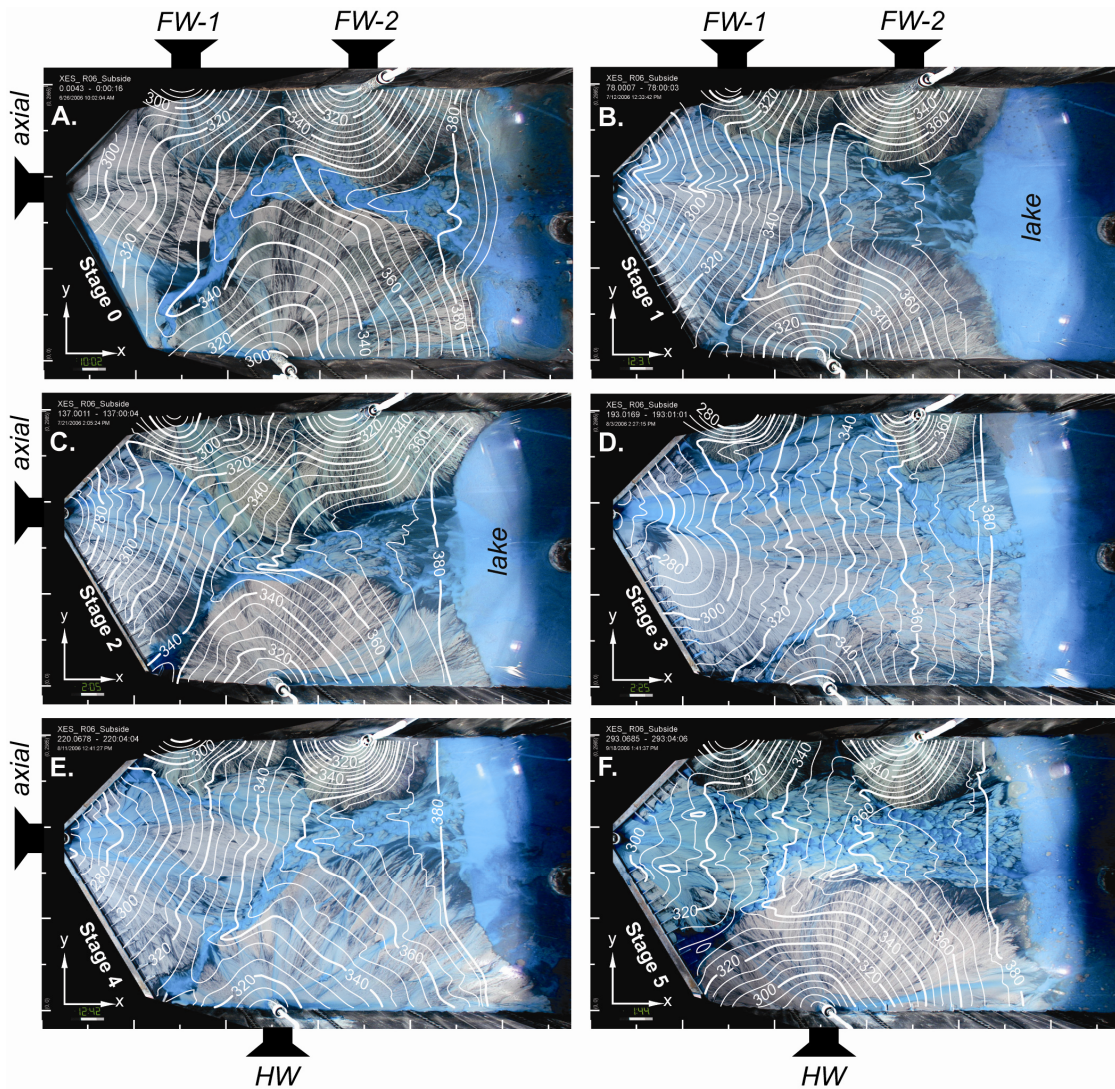


Figure 3.4. Orthorectified overhead photographic images illustrating the axial river, hanging-wall (HW) fan, and the upstream (FW-1) and downstream (FW-2) footwall fans during the experiment. The images are overlain by topographic contours (Toposcan, contour interval of 5 mm) that denote depths below the top of the tank. A: Axial river and transverse fans mark the beginning of stage 1 (runtime = 0 hrs, Toposcan = 0 hrs), where nearly all of the axially sourced sediment was sequestered up-basin. The greenish tint is from colored tracer sand. B: Development of broad axial river near end of stage 1 (runtime = 78 hours, Toposcan = 80 hrs). Axially sourced sediments moved farther downstream than at the beginning of stage 1. C: Progradation of footwall fans during stage 2 (runtime = 137 hrs, Toposcan = 130 hrs). D: Development of wide axial river and retreat of transverse fans during stage 3 (runtime = 193 hrs, Toposcan = 190 hrs). E: Oblique progradation of hanging-wall sourced fan during stage 4 (runtime = 220 hrs, Toposcan = 220 hrs). F: Development of deep axial river system during stage 5 (runtime = 293 hrs, Toposcan = 290 hrs).

We examined the development of surface morphology using topographic maps generated from the DEMs and overhead imagery at 5-hour intervals. Mean areas for each depositional belt was established using the harmonic mean of the 5-hour mapped fan-edge positions. The harmonic mean is used here because it is less sensitive (than arithmetic and geometric means) to infrequent but large deviations in fan-edge position and planform area. Overhead digital photographic images were corrected for radial distortion and perspective view for every 60 seconds of experimental runtime. These orthorectified images have a resolution of 1164 x 677 pixels (JPEG format having a pixel area of 0.25 mm²) and were compared to the topographic DEMs in order to map the areal extent of the footwall and hanging-wall fans, axial drainage, shoreline, and to determine deposit slopes and the orientations of active drainages.

Surface Morphology

The experiment began as an open basin with four sources supplying sediment to a shallow lake (Figs. 3.4A & 3.5). Initial conditions were established when fluvial deposits filled the tank to a position near $x = 4200 \text{ mm}$ (Fig. 3.6). Minor adjustments to the total sediment discharge were made in stage 1b in order to maintain the area of the fluvial surface and reverse a slight retreat in the shoreline observed earlier in that stage. Twenty acrylic roughness elements were inserted at the upper end of the basin after 65 hours of runtime in an attempt to keep the upper part of the axial drainage course positioned away from the upper edges of the basin (Fig. 3.4B-F).

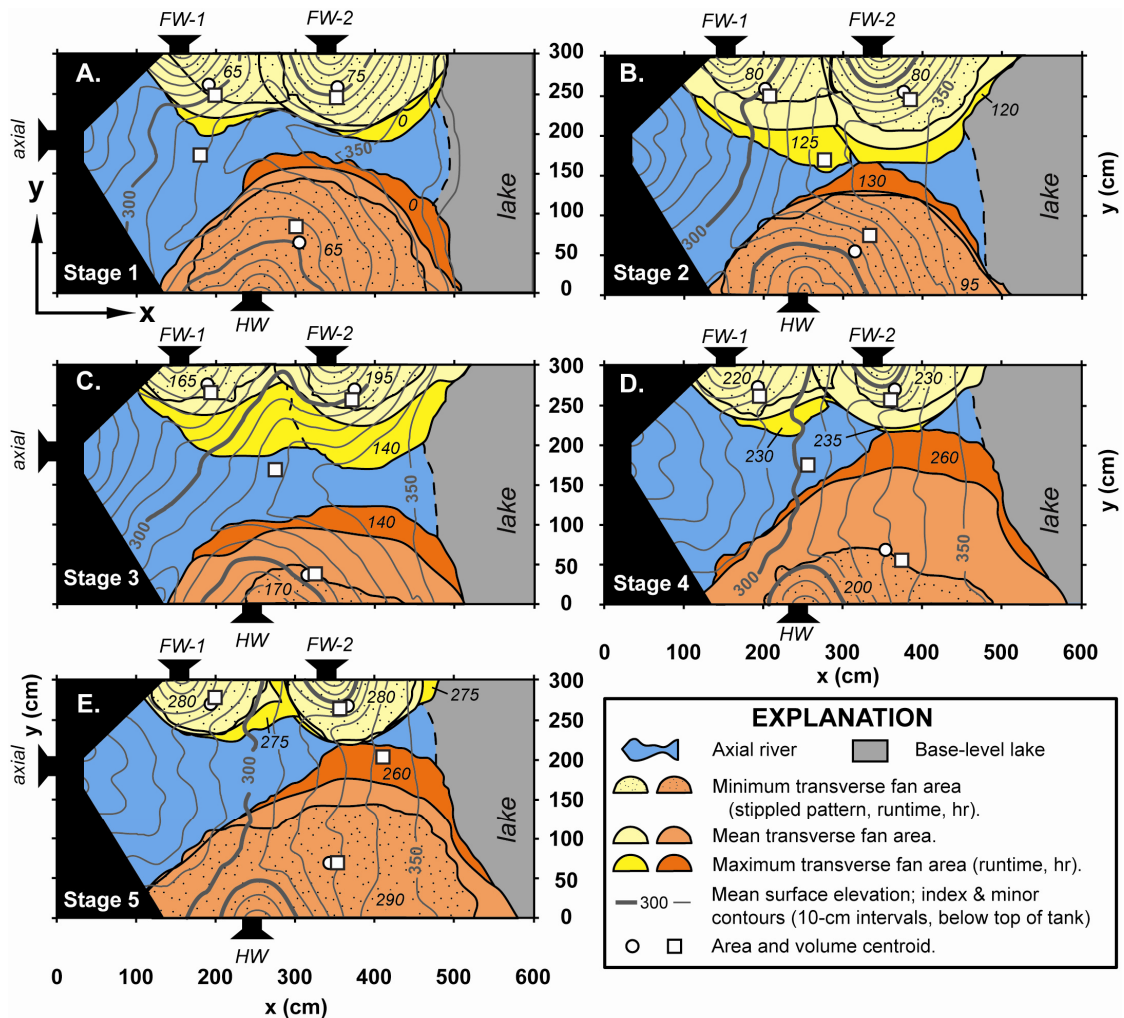


Figure 3.5. Harmonic-mean positions of the transverse hanging-wall and footwall fans and approximate shoreline position determined using overhead imagery and topographic scans (A-E). Gray lines denote the (arithmetic) mean elevation of the deposit surface for each stage relative to the top of the tank (Stage 1, $N = 17$; Stages 2-4, $N=13$ each; Stage 5, $N = 9$). Lake elevation is around 375 mm below the top of the tank. Sediment inputs are diagrammatically shown: axial river, hanging-wall (HW), and upper (FW-1) and lower (FW-2) footwall inputs.

Other than placing the sources (Fig. 3.2), setting the supply rates of water and sediment (Fig. 3.3, Table 3.1), and (after the initial fluvial build-out period) imposing the spatial subsidence pattern (Fig. 3.7), we did nothing to prescribe any particular morphologic pattern on the experiment. Thus, the first and most important result is that under the imposed conditions, the experimental system organized itself into the general

pattern observed in half-graben systems in the field (e.g., Fig. 1). The deposits formed fan-shaped masses of sediment that were centered on each input (Fig. 3.4). Beyond an initial, up-basin axial-fan zone, the axial drainage system evolved to a broad, low-gradient channel flanked by steeper and more radial transverse fans (Fig. 3.5). In the field, semi-radial alluvial fans tend to form in piedmont settings where confined, upland drainage gives way to unconfined channel conditions that promote expansion of flow (e.g., Bull, 1977; Blair and McPherson, 1994; and Smith, 2000). Fan-shaped deposits can also form through the development of a distributary channel network, through nodal avulsions, or through radially migrating channels emanating from the structural margin of the basin or mountain front (e.g., Wells and Dorr, 1987; Stanistreet and McCarthy, 1993; Galloway and Hobday, 1996; Mack et al., 1997; and Weissman et al., 2005 and 2007).

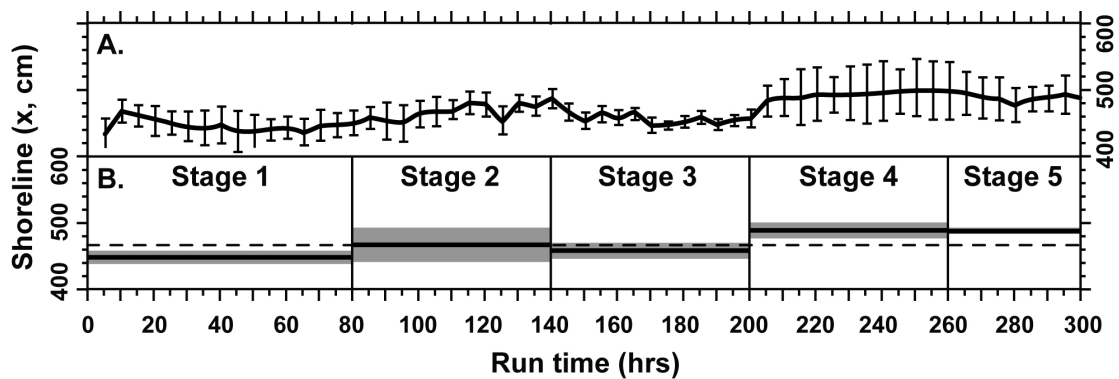


Figure 3.6. Harmonic-mean positions of the shoreline during XES06. A: Mean position of the shoreline ($\pm 2\sigma$) determined every 5 hours. B: Mean position of shoreline for entire stage (black line) $\pm 2\sigma$ (gray bar) in Table 3.2. The dotted line is the mean shoreline position for the entire experimental run.

Table 3.2. Summary of XES06 results.

	Stage 1	Stage 2	Stage 3	Stage 4	Stage 5	Total Mean
<u>Sediment mass (kg)</u>						
HW	356	451	239	1109	312	3049*
Axial	524	426	1285	481	183	3169*
2FW	273	847	250	292	155	2199*
<u>Mean slope (%)</u>						
HW	4.7 ± 2.6	4.7 ± 2.6	4.1 ± 3.3	3.7 ± 2.4	4.5 ± 3.0	4.3 ± 1.0
Axial	3.7 ± 3.4	3.6 ± 3.1	3.2 ± 2.3	3.3 ± 2.9	3.2 ± 3.1	3.5 ± 0.6
2FW	8.4 ± 5.2	6.4 ± 4.2	8.8 ± 5.8	9.3 ± 7.3	9.1 ± 6.7	8.3 ± 2.3
<u>Max. slope (%)</u>						
HW	9 ± 1	10 ± 2	10 ± 1	11 ± 4	14 ± 12	10 ± 10
Axial	11 ± 2	10 ± 2	13 ± 3	14 ± 5	19 ± 8	13 ± 10
2FW	15 ± 1	23 ± 9	17 ± 3	19 ± 1	26 ± 11	19 ± 13
<u>Flow occupation (%)</u>						
HW	33 ± 36	42 ± 33	57 ± 37	76 ± 21	79 ± 26	na
Axial	85 ± 16	88 ± 17	91 ± 16	92 ± 15	91 ± 19	na
2FW	10 ± 32	20 ± 41	17 ± 38	23 ± 46	19 ± 44	na
<u>Mean shoreline (x) (cm)</u>						
	448 ± 5	466 ± 13	458 ± 12	489 ± 12	488 ± 5	467 ± 20

Notes: HW–“hanging-wall” input; 2FW–both “footwall” inputs. Not applicable (na).

*Total sediment mass (8417 kg) includes Stage 0 (HW = 582 kg, Axial = 270 kg, 2FW = 382 kg). Deposit bulk density is 1487 kg/m³.

Deposit surface slopes (arithmetic mean ± 2σ and maximum slope) determined from topographic grids at 5-hour intervals: Stage 1 (n = 17), Stage 2-4 (n = 12), and Stage 5 (n = 8). 2FW is the sum of FW1 and FW2 values. Stage 0 areas are: 4.78 (HW), 4.63 (Axial), 1.33 (FW1), and 1.92 (FW2) m².

Shoreline distance (harmonic mean ± 1σ, relative to x-axis) determined from shoreline mapped at 5-hr intervals.

As is typical in small-scale experiments, deposit slopes (Table 3.2) were much higher than those of field-scale alluvial fans and rivers (e.g., Gile et al., 1981; and Blair and McPherson, 1994). The desired differences in slopes were achieved, where the transverse fans were steeper than the axial drainage (Fig. 3.8A). Slopes of the axial fluvial surface ranged from 0.05 at the upper end of the drainage (where fan-forms dominate) and declined to less than 0.01 at the lake shore. Slopes on the hanging-wall deposit surface ranged from about 0.03 to 0.06. Footwall deposit-surface slopes were consistently higher (ranging from 0.03 to 0.14) than the axial and hanging-wall deposit surfaces (Fig. 3.8A-B). Slopes of the hanging-wall deposit surface approached those of the axial drainage during stage 4, suggesting that differences in deposit slopes between

the flanking tributary fans and axial rivers may not be very large (*cf.* Blair and McPherson, 1994). Slopes of the mapped footwall deposits decreased with increasing area and (sediment and water) discharge (Fig. 3.8B-D). The axial region showed a weak, negative correlation between area and slope, and the slope-area relationship for the hanging-wall fan was essentially invariant (Fig. 3.8B). The hanging-wall and axial deposit slopes increased with increased sediment and water discharge (Fig. 3.8C-D).

The abrupt changes in subsidence rate imposed for stages 2 and 5 resulted in no obvious change in deposit slope between the slow and rapid subsidence stages (Fig. 3.8A). Slopes developed on the axial-fluvial surface descended nearly parallel to the long axis of the tank. Hanging-wall fan slopes increased slightly with increased axial slopes, and footwall fan slopes decreased with increased axial slopes (Fig. 3.8F).

Local deviations between the programmed subsidence and monitored basement elevations resulted in the formation of broad undulating arches and troughs near the basin edges and along the axis of maximum subsidence (Fig. 3.7). Isochronous surfaces derived from the basement-migrated topography likewise deviated from the stage boundaries that were mapped from the scanned deposit cross sections (Chapter 4). This unanticipated subsidence behavior resulted in basement slopes that were locally steeper than programmed along the analogous footwall margin.

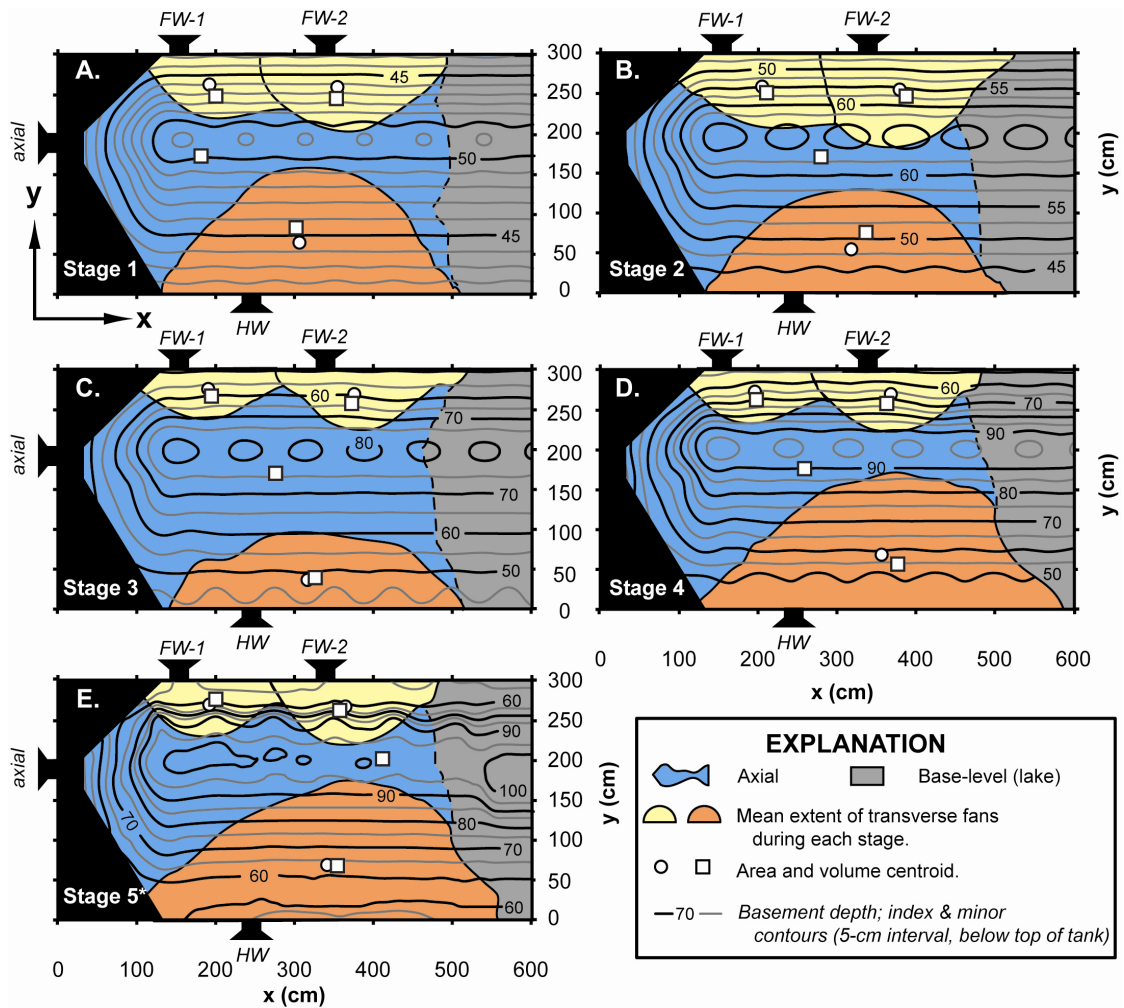


Figure 3.7. Mean fan areas and centroid locations (from Figure 3.5), and contour maps of basement depth at the end of each experimental stage; stages 1-4 measured using manometers. The depth of stage 5* was determined using imaged cross sections of the deposit. A: Basement elevation at the end of stage 1 ($t = 80$ hrs). B: Basement elevation at end of stage 2 ($t = 140$ hrs). C: Basement elevation at end of stage 3 ($t = 200$ hrs). D: Basement elevation at end of stage 4 ($t = 260$ hrs). E: Basement elevation at end of experiment (stage 5, $t = 300$ hrs). Contour intervals: stage 1 = 10 mm; stage 2 = 25 mm; stage 3 through stage 5 = 50 mm. Dome-shaped contours denote regions where deviations from the simple hinge-type subsidence occurred during the experiment.

Axial and transverse deposits were morphologically distinct and were delineated using overhead images through differences in channel orientation, surface slope and aspect, bed forms, and sand color (Fig. 3.4). The dyed sand used to mark sediment provenance is visible in Figure 3.4, where hanging-wall-sourced fan sand is pale pink,

and footwall sands are greenish yellow. Axial surface morphology was dominated by numerous broad sandy, longitudinal bed forms and black, coal-filled channel scours (Figs. 3.4 & 3.10) that developed under conditions of relatively deep, uniform water flow. Tributary drainages formed prominent fans through nodal avulsion and radial migration of channels, leaving much of the transverse fan surface dry at any given time (Fig. 3.9). Nodal avulsion and flow-expansion events left broad, sandy fans that were commonly covered by scattered coal grains. Flow was commonly confined within fan-head trenches and valleys that formed on the proximal parts of the transverse fans. Distributary channel networks also developed, but these were typically less common and occurred prior to stream capture events or during channel avulsions.

Axial Drainage

The axial stream formed a braided fan up-basin of the upper footwall fan (FW-1) that persisted throughout most of the experiment (Fig. 3.4). Water and sediment delivered by the axial fan collected downstream to form a relatively narrow trunk drainage consisting of a single channel or multiple subparallel channels that were confined by the opposing transverse fans, about 0.2 m down the long axis of the basin. A surprising result of the experiment is that much of the sediment incorporated into the axial drainage appeared to be derived from transverse sources (Fig. 3.10A). Under conditions of relatively low axial sediment discharge, the axially sourced sediment was preferentially stored in the proximal (upstream) fan.

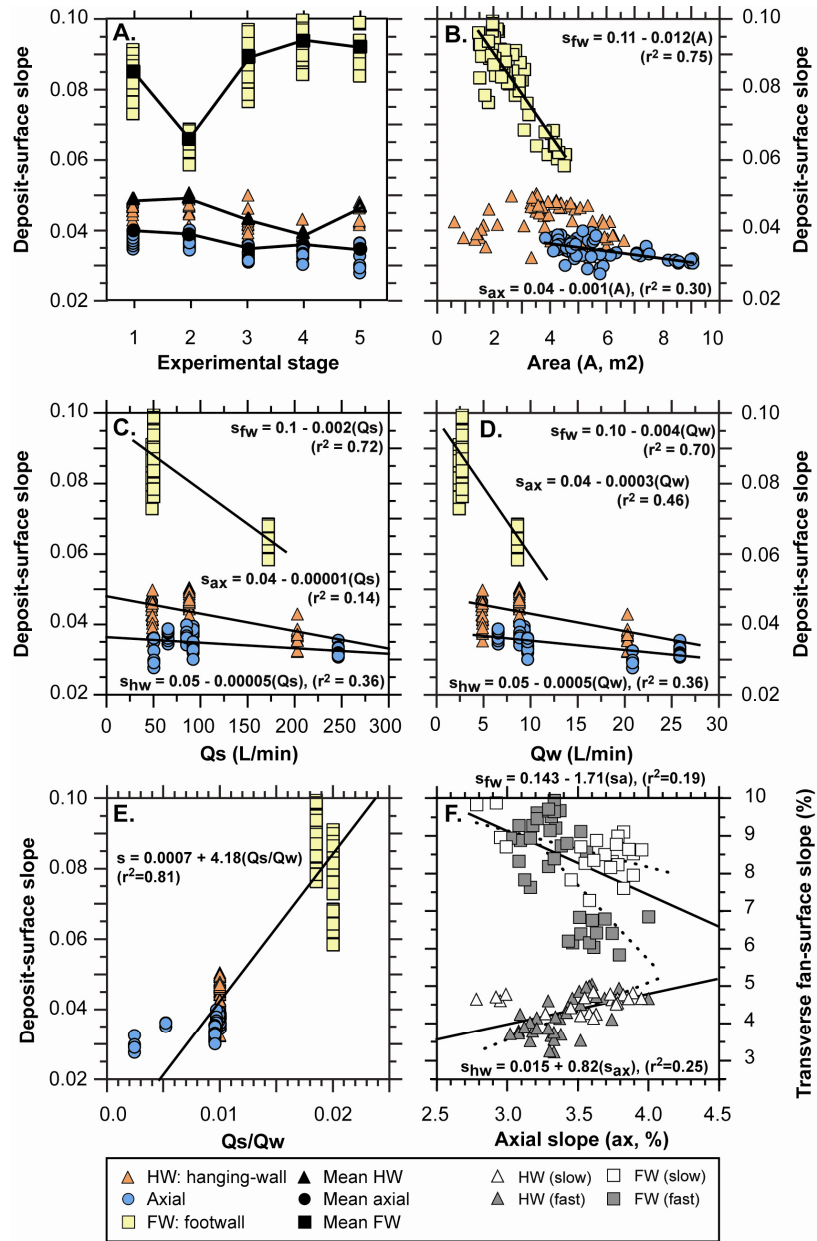


Figure 3.8. Plots of dimensionless deposit-surface slope (vertical/horizontal) versus deposit area and sediment discharge determined from topographic scans at 5 hour intervals. Best-fit lines (and equations) for axial (s_{ax}), footwall (s_{fw}), and hanging-wall (s_{hw}) are shown where appropriate. Number of measurements: stage 1 ($n = 17$); stage 2 ($n = 12$), stage 3 ($n = 12$), stage 4 ($n = 12$), and stage 5 ($n = 8$). A: Fan-surface slopes and stage-mean fan slope (black) for experimental stages. B: Plot of deposit-surface slope versus fan area determined from overhead imagery. C: Deposit-surface slope versus sediment discharge. D: Deposit-surface slope versus water discharge. E: Deposit-surface slope and ratio of sediment to water discharge (Q_s/Q_w). F: Plot of transverse-surface slopes (HW and FW) versus axial-deposit surface slope at slow and fast subsidence rates.

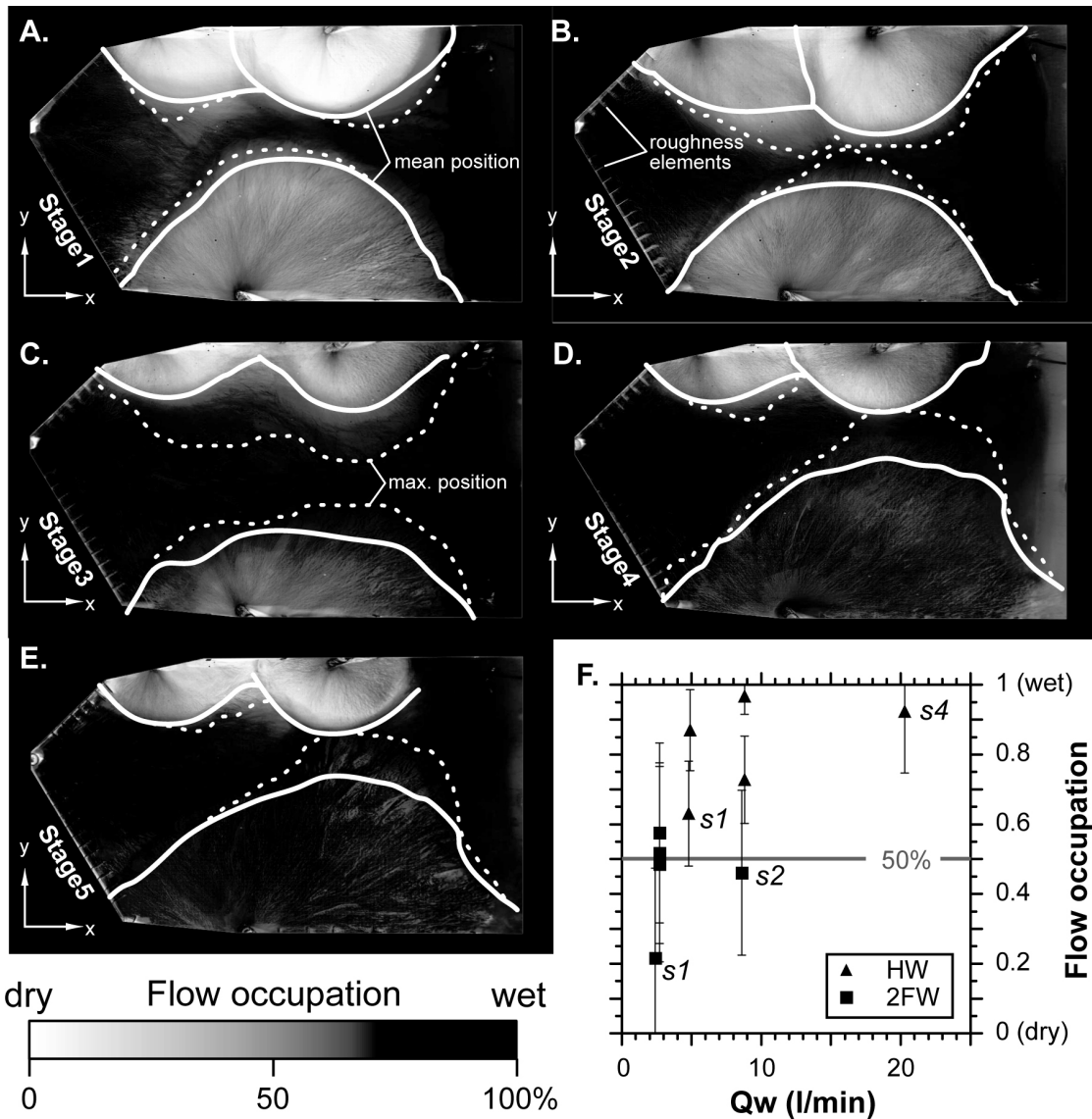


Figure 3.9. Maps of (arithmetic) mean flow occupation (A-E). Flow occupation was determined by setting thresholds for blue water for 1-minute overhead imagery and averaging wetted areas for the entire stage. The number of measurements per stage is: Stage 1 ($N = 4800$); stages 2-4 ($N = 3600$ each); and stage 5 ($N = 2400$). White lines denote mean boundary of transverse fans; dotted lines denote the maximum mapped extents of the transverse fans. The axial river was almost entirely occupied by flow during the experiment. F: plot of mean flow occupation ($\pm 1\sigma$) versus water discharge (in liters per minute) for hanging-wall (HW) and both footwall (2FW) fans during each stage. During stage 1, the hanging-wall fan was occupied by flow 63% of the time, whereas the two footwall fans were occupied 22% of the time. For the remaining stages, the hanging-wall fan surfaces were occupied by flow 73-97% of the time, and the footwall fan surfaces were occupied 46-58% of the time.

Downstream of the axial fan, channels remained almost entirely submerged and contained numerous downstream-migrating arcuate bed forms and coal-filled scours (Figs. 3.4 & 3.10). A deep channel frequently formed along the interface between the hanging-wall fan and the axial fan (Fig. 3.4E) because of the combined water discharges originally apportioned their respective inputs. Axial drainage expanded during stage 3 to form a broad braided channel system that occupied nearly the entire width of the basin (Fig. 3.4D). The combination of relatively high water discharge and confinement by the transverse fans led to subcritical flow in the axial channel, a relatively rare condition for self-formed experimental fluvial channels.

Axial drainage flowed down-basin (Fig. 3.11) and occupied the central portion of the tank (Fig. 3.4), except during stage 3, where it encountered the basin edges (Fig. 3.4D). At higher axial-sediment discharges (stage 3), a broad braided channel complex migrated across the basin (Fig. 3.4D). Footwall fans occupied the areas where basement slopes were steepest and extended across the subsidence-maximum position during the highest footwall sediment discharges in stage 2 (Figs. 3.5 & 3.7). The hanging-wall fan reached the subsidence-maximum position during its highest sediment discharge in stage 4.

Transverse Drainage

Transverse drainages created fan-shaped deposits through multiple processes. In strong contrast to the axial river, which was relatively deep and dominated by subcritical-flow bed forms, the transverse fans exhibited steep, shallow, unstable supercritical flows. Transverse fan deposition was dominated by nodal avulsion and flow

expansion downstream of fan-head trenches (Fig. 3.10D). Active distributary channel networks were also more common on footwall fans. Transverse drainage tended to favor an oblique orientation relative to the axial stream course (Fig. 3.11), rather than the transverse-sloping deposits found in half-graben basins (e.g., Gawthorpe and Leeder, 2000). This radial asymmetry of the planform fan geometry was enhanced for the hanging-wall fan during stage 4 (Fig. 3.4E), where sediment discharge was greatest.

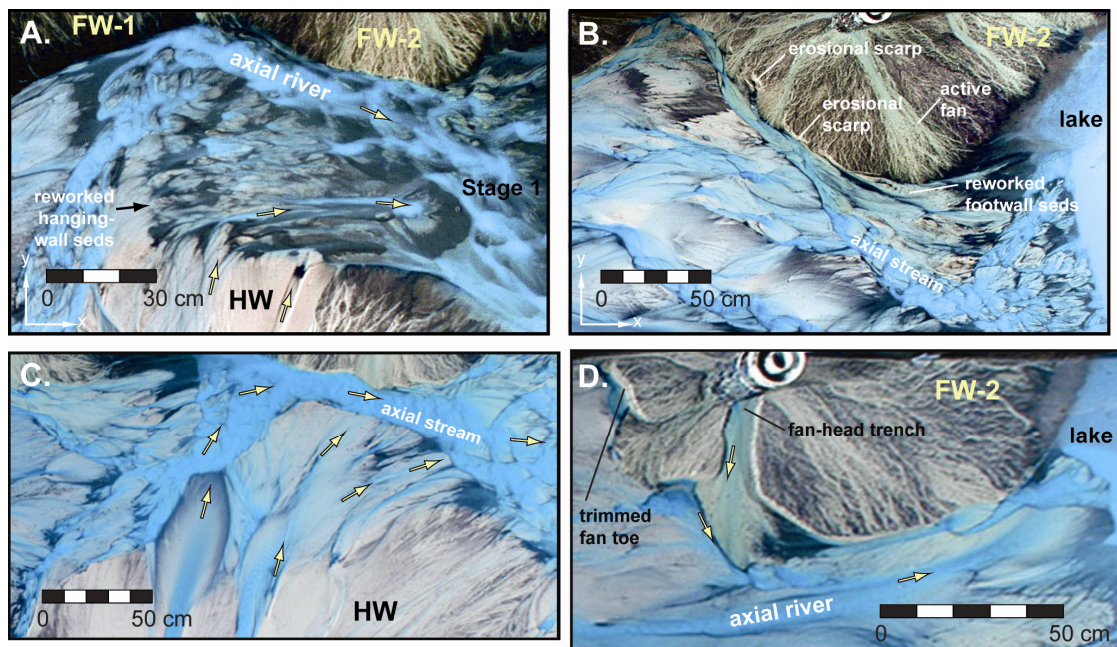


Figure 3.10. Overhead photographic images illustrating the axial river, hanging-wall (HW) fan, and the upstream (FW-1) and downstream (FW-2) footwall fans during the experiment. Arrows denote channel flow direction based on channel forms and bed-form orientations. A: Image illustrating reworking HW sediment into axial river during stage 1 (runtime = 55 hrs). Boundary between axial and HW fan is difficult to distinguish because of shallow water depths and abundant fines at contact. B: Image illustrating partial burial of earlier toe cutting of FW-2 during stage 3 (runtime = 156 hrs). The colors in (A) and (B) were modified to enhance differences among deposits. C: Orientation of channels in hanging-wall deposit locally mimic the direction of axial stream flow (Stage 4, $t = 246.2$ hrs). D: At least two generations of fan-head trenching and inset fans illustrated during Stage 3 (runtime $t = 181.6$ hrs).

Footwall-fan slopes declined as axial slopes increased under the imposed subsidence and sediment-discharge scenarios (Fig. 3.8F). Mean slopes on the hanging-wall deposit surface (0.037) approached those of the axial deposit surface (0.033) during stage 4 (Fig. 3.8A). Slopes of the hanging-wall fan increased with increased axial slope for all subsidence and sediment-discharge scenarios. The difference in the behavior of the hanging-wall and footwall deposit slopes, relative to the axial slope, may be related to the higher sensitivity of the footwall slopes relative to their smaller depositional areas.

Overall, the mapped positions of the transverse fans remained within 0.5 m of their mean fan-edge position during each stage (Fig. 3.5). Larger variations in the position of the hanging-wall fan occurred during stages 3, 4 and 5, mainly because of the large lateral expansion of the transverse fans as they first adjusted to the different sediment discharges imposed across the stage boundaries. Large lateral variations in footwall-fan areas occurred in stage 2, where they experienced their maximum sediment discharge. The amount of erosion of the lower footwall fan (FW-2) appeared to be far less extensive than on the hanging-wall and upper footwall fans (FW-1). The most obvious visible mechanism for erosion on the transverse fans was episodic formation of deep (centimeter-scale) fan-head trenches that delivered transverse-sourced sediment into the axial system (Fig. 3.10).

The center of each depositional body was approximated by its centroid, which is defined as the position where a solid body of arbitrary shape is in gravitational balance. Area centroids were determined by finding the center of the mean-stage fan areas (Fig. 3.5). Centroids of fan volume (or mass) were determined by finding the center of mass for each deposit body using isopach maps of the stage volume (see below). Centroids of

fan area and deposit volume both occupied similar positions in the basin, suggesting that the fan areas roughly match those of the fan depocenter. The volume centroids are typically located slightly basin-ward of the fan-area centroid because the subsidence profile promotes the preservation of thicker deposits towards the axis of maximum subsidence (Fig. 3.7).

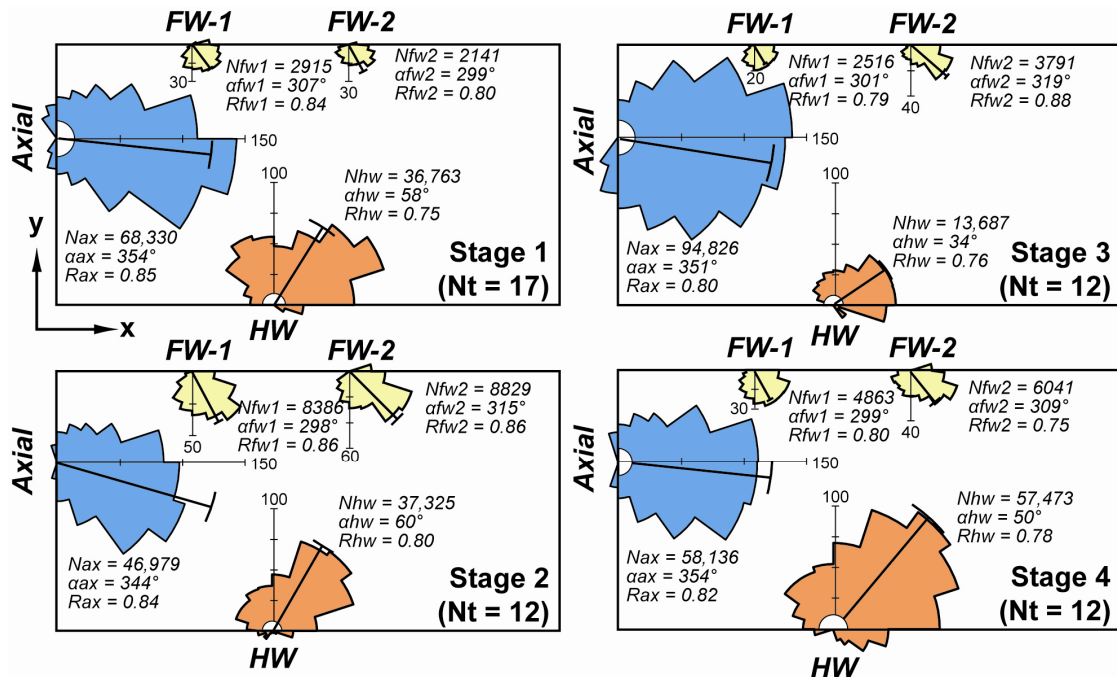


Figure 3.11. Circular histograms (rose diagrams) of mean flow-directions for deposits in stages 1 through 4. Flow directions were determined by clipping wetted areas (using overhead images) onto maps of slope aspect derived from topography at 5-hr intervals; Nt represents the total number of 5-hr intervals in a given stage. The outer 15-cm of the tank edges were removed to minimize flow effects induced along tank margins. Aspect data represents 11 mm² of the deposit surface. Number of measurements (N), mean directions (α), and resultant lengths (R) for axial, hanging-wall, and upper and lower footwall drainages are denoted by *ax*, *hw*, *fw1*, and *fw2*, respectively.

In most stages, the semi-conical shape and size of the lower footwall fan (FW-2) remained relatively stable and was not obliterated by the axial drainage, even when axial channels impinged upon the basin margins between the upper (FW-1) and lower (FW-2)

footwall fans during stage 3 (Fig. 3.4D & G). FW-1 maintained its semi-conical form during maximum sediment discharge (stage 1) and maximum axial-water discharge (stage 5), but was greatly modified by axial drainage during the other stages. FW-1 tended to be more frequently and extensively altered by the axial drainage than FW-2.

The footwall fans prograded beyond the axis of maximum subsidence during stage 2, displacing the axial channel toward the hanging-wall fan (Figs. 3.4, 3.5 & 3.7). The steeper footwall-fan slopes likely maintained their radial symmetry because fan area is very sensitive to slope (Fig. 3.8B-D). The influence of the footwall fans on the position of the axial drainage course is interesting, particularly because they carry less water. With the exception of stage 2, the axial drainage system typically delivered 3 to 10 times more water than the combined sediment discharges from the footwall. Could the footwall fans deliver enough sediment to the fan surface to influence the course of the axial river?

One way to quantify the effects of fluvial activity on deposit morphology is to determine how much of the surface is occupied by flow at a given time (e.g., Cazanacli et al., 2002). To do this, maps of time-integrated mean flow-occupation were made by setting thresholds of wet and dry areas using the blue-dyed water on the overhead imagery at 1-minute intervals and averaging them for each experimental stage (Fig. 3.9). Areas of high flow occupation tended to occur in areas of persistent channelized flow (Sheets et al., 2002) and provide an estimate of channel mobility on the fluvial surface. The average flow occupancy for the axial drainage was 85 and 91 percent for stages 1 and 5, respectively, and 88-92 percent for stages 2-4. The axial surface, as expected, was wet virtually all of the time because it conveyed nearly all of the basin water to the lake.

The high flow-occupancy for the axial drainage illustrates the abundance of active and highly mobile channels (Figs. 3.9 & 3.10) as well as confinement by the transverse fans. The average flow occupancy for hanging-wall fans was 33 and 79 percent for stages 1 and 5, respectively, and 42-76 percent for stages 2-4. The average flow occupancy for footwall fans was 10 and 19 percent for stages 1 and 5, respectively, and 17 to 23 percent for stages 2 through 3. Flow occupied the surface of footwall fans about half as often as on the hanging-wall fan because the footwall flows conveyed half of the water per grain of sediment as the other drainages.

Axial-Transverse Drainage Interactions

An important element of self organization in the experiment was the boundary between the transverse and axial systems down-basin of the axial fan. The axial-transverse border was a fully dynamic boundary that migrated over most of the available width of the basin through the course of the experiment. The key dynamical element in setting the boundary location was the transfer of sediment between the axial and transverse systems. Our observations indicate that this transfer was exclusively one-way, from the transverse systems to the axial. At the same time, the width of the axial system, and hence its capacity for sediment transport, was determined by the lengths of the transverse fans.

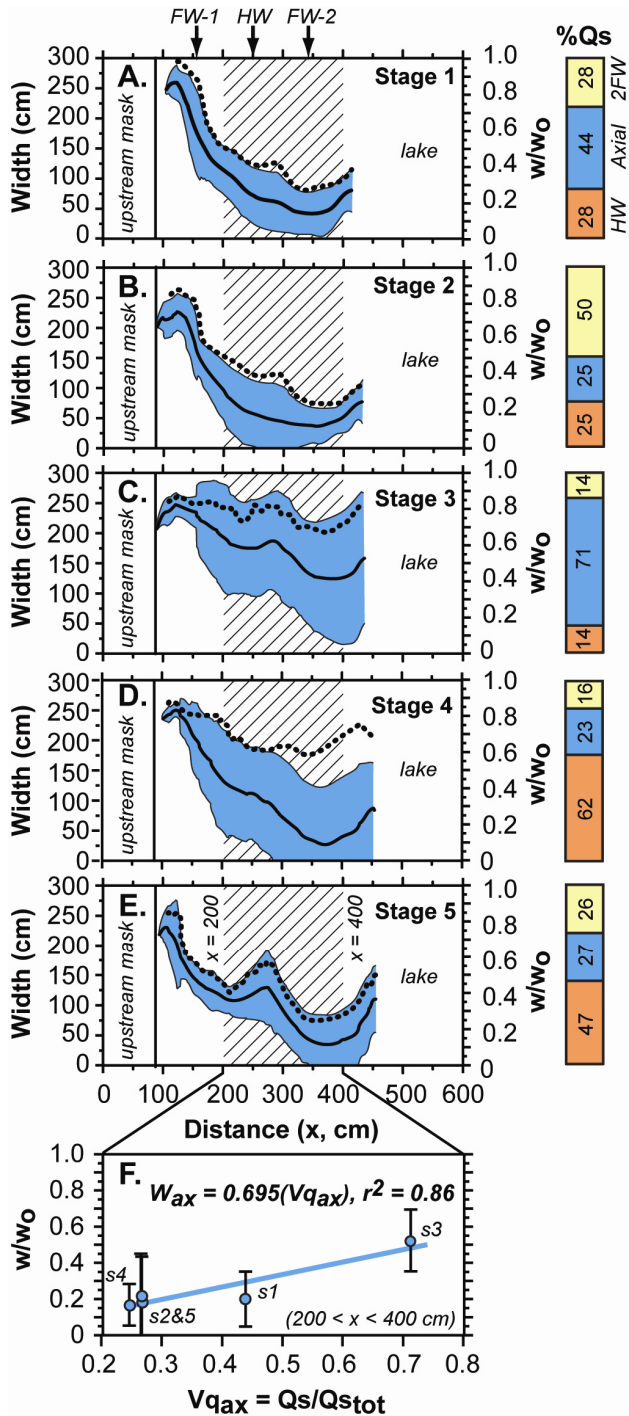


Figure 3.12. Plots of mean width (solid line) $\pm 2\sigma$ (blue shading) and maximum width (dotted line) of the axial river versus basin distance ($90 < x < 450 \text{ cm}$); dimensionless width ($w_0 = \text{total width}$) shown on right-hand side of plots A-E. Stacked columns denote sediment discharge for both footwalls (2FW), axial, and hanging-wall (HW) inputs, in percent. A-E: Width of axial river, illustrating an overall downstream increase in width. The cross-hatched area denotes part of the basin ($200 < x < 400 \text{ cm}$) where the axial drainage resembled a trunk stream. This area was used to remove the influence of the upstream axial fan and downstream delta. F: Plot of dimensionless harmonic mean of axial-river width ($\pm 2\sigma$) showing a slightly positive correlation between axial width (w_{ax}) and axial-sediment discharge (Vq_{ax}).

The transfer of transverse sediment into the axial drainage system was accomplished through two processes. As the axial drainage migrated across the basin, it trimmed the toes of transverse fans, leaving steep erosional scarps that became quickly buried by prograding transverse fans (Fig. 3.4E-F). Erosion of fan toes contributed transversely-sourced sediment directly into the axial stream (Fig. 3.10B). Hanging-wall fans also directly contributed sediment into the axial drainage as plumes that were re-oriented to the axial drainage course (Fig. 3.10A & C).

The position and width of the axial system is sensitive to sediment discharges imposed on the entire basin and reflect the relative strengths of tributary sediment discharges (Fig. 3.12). For a given subsidence profile, the primary control on axial width is the ratio of the axial sediment discharge to the sum of the transverse (tributary) sediment discharges, while the primary control on axial location is the ratio of sediment discharge among the transverse sources (i.e., on one side of the basin versus the other). Water discharge played a lesser role.

The width of the axial drainage was variable, but it generally widened down-basin. Down-basin widening of the axial drainage is expected because it collects nearly all of the water delivered by the transverse fans. Drainage across the downbasin-facing portions of the lower footwall-fan and hanging-wall fans runs directly into the terminal lake. However, most of the water supplied to the transverse systems reached the lake via the axial drainage. The up-basin axial fan, and down-basin delta, areas were not typical of rift-basin axial rivers (e.g., Mack and Seager, 1990), so the effects of these two areas were removed to examine the relationship between axial sediment discharge and axial channel width. Figure 3.12F shows a strong positive correlation between mean axial

drainage width and sediment discharge for the portion of the basin containing a single axial stream. Downstream of FW-1, the width of the axial drainage course increased almost three fold (2.8) with increasing sediment discharge, indicating the strong control on width of the axial channel belt by axial sediment discharge (relative to the total supply to the transverse systems).

Sediment Mass Balance

As stated above, an important aspect of the experiment was the evolution of the dynamic boundaries between the three main morphologic elements: the axial, hanging-wall, and footwall transport systems. These boundaries control the surface morphology as well as the stratigraphy of the basin. A simple geometric model of sediment mass balance provides a quantitative basis for the physical experiments. The main objective of this model is to examine how sediment may be partitioned among these depositional elements.

This sediment mass balance allows sediment to enter the basin and form fans along the margin (Fig. 3.13). Semi-conical fans should emerge where there is little or no interference among other deposits and sediment discharge is constant. A mass balance can be estimated by integrating the subsidence rate over the area beneath a theoretical semi-conical fan. It is assumed that the geometric parameters for the model depositional system do not change with time and all of the sediment supplied is preserved in the depositional system.

Theoretical estimates of deposit area and volume were made by transforming known mass inputs using the bulk density estimated from the experimental deposit. The total mass of sediment was 8417 kg. Deposit volume, estimated by subtracting DEMs of migrated topography for the deposit top and bottom, yielded 5660 liters. Thus, the bulk density was 1.487 kg/liter, which is 92 percent of the original density of the sediment mixture (see above). This reduction in bulk density was likely due to increased porosity caused by compaction.

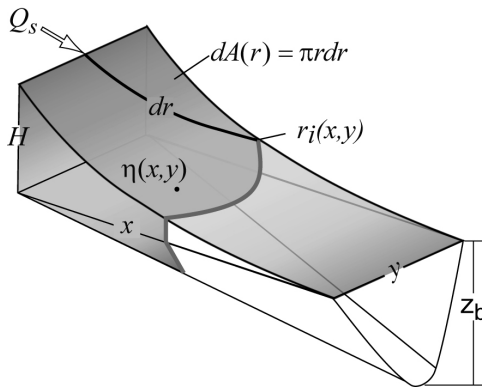


Figure 3.13. Definition diagram of circular fan boundary used to determine fan area and sediment volume (see text for definitions). Sediment enters the basin at the arrow point. The areal extent of the deposit surface is defined by the xy reference plane. The deposit depth below the reference plane is defined by the variable z_b ; H is the deposit height above the reference plane. The surface elevation of the deposit is denoted by the symbol η . The light shading denotes the deposit surface, and the darker shading denotes the area and volume of the theoretical fan.

A mass balance was estimated by assuming a perfectly semi-circular fan shape in plan-view (xy -plane) area (Fig. 3.13). Deposit volume can be established from sediment discharge Q_s , measured as volume sediment delivered per time [L^3T^{-1}]. The volume of sediment introduced into the basin during a stage of duration Δt is $V = Q_s\Delta t$. The height

of the deposit surface (η) and basin depth (z_b) are related to basin position (x, y). The rate of change of surface elevation ($\dot{\eta}$) at a point is expressed as:

$$\dot{\eta}(x, y) = \dot{\eta}(r) = \frac{d\eta}{dt}, \quad (1)$$

and the subsidence rate (σ) at a point is:

$$\sigma(x, y) = \frac{dz_b}{dt}. \quad (2)$$

Combining the equation of the area of a semi-circle ($A = 0.5\pi r^2$, radius of r) with the top and bottom of the deposit yields an expression for the fan area, assuming that all the supplied sediment is retained in the fan:

$$Q_s = \int_0^A (\sigma(A)dA + \dot{\eta}(A)dA), \quad (3)$$

where $dA = \pi r dr$. Solving for volume and integrating with respect to radius, and again with respect to time yields

$$V = \int_0^{\Delta t} Q_s dt = \int_0^{\Delta t} \int_0^r \pi (\sigma(r) + \dot{\eta}(r)) r dr dt. \quad (4)$$

Substituting η and σ from equations 2 and 3 into equation 4 yields an incremental version suitable for numerical integration:

$$dV = \pi \int_0^r (dz_b(r) + d\eta(r)) r dr. \quad (5)$$

We solved equation 5 numerically using a spline-type interpolator that approximates the volume of sediment beneath the area of sequentially increasing parametric semi-circles that are centered about each sediment input. A solution is obtained when the semi-circular volume approaches 99 percent of the volume of sediment contributed during a given experimental stage (Fig. 3.14, Table 3.2). For the

steady-state solution, the surface elevation is constant (i.e., $\dot{\eta} = 0$). The overlap of transverse-fan areas for stages 2 and 4 (Fig. 3.14B, D & G) is not realistic, but it illustrates the importance of sediment redistribution by the axial drainage.

Model Results

Examination of deposit areas is described below, and the examination of deposit volumes is investigated in a companion paper (Chapter 4). The areas of the mapped axial drainages were consistently higher than predicted by the model; transverse-fan areas were consistently smaller (Fig. 3.15A & Table 3.3). Although attempts to maintain a stable shoreline were generally successful, it varied throughout the experimental runs (Table 3.2). These changes in shoreline position could lead to important differences in comparing the areas of the depositional belts. In order to minimize the influence of shoreline position for these comparisons, the deposit areas were normalized to the total mean fluvial area of each experimental stage (Fig. 3.15B). Normalizing these areas resulted in better fits between the model and sediment mass balance, and retained the differences among the axial and transverse depositional systems (Fig. 3.15A). These differences in deposit areas occurred because the sediment mass balance model assumes no mixing. The area of the mapped axial deposits increased because it was able to widen downstream as it collected (water and sediment) discharges from the transverse fans.

Table 3.3. Summary of XES06 deposit areas.

	Stage 1	Stage 2	Stage 3	Stage 4	Stage 5
<i>Mapped Area (m²)</i>					
HW	3.95 ± 0.46	3.59 ± 0.17	1.50 ± 0.83	4.33 ± 1.47	5.45 ± 0.61
Axial	4.67 ± 0.55	4.47 ± 0.48	7.75 ± 1.19	5.35 ± 1.19	5.18 ± 0.52
FW1	1.10 ± 0.19	1.72 ± 0.39	0.86 ± 0.34	0.97 ± 0.13	0.94 ± 0.10
FW2	1.62 ± 0.14	2.03 ± 0.27	0.93 ± 0.44	1.08 ± 0.16	1.04 ± 0.03
<i>Model Area (m²)</i>					
HW	5.08	5.07	2.87	7.00	8.79
Axial	2.99	4.03	8.17	3.60	1.94
FW1	1.73	1.95	1.32	1.32	1.52
FW2	1.96	1.98	1.42	1.42	1.69

Notes: HW–“hanging-wall” input; FW-1 and FW-2 are the upper and lower basin “footwall” inputs. Harmonic mean of deposit area ($\pm 1\sigma$) for each experimental stage determined from overhead mapping at 5-hr intervals.

Model areas determined from the iterative solution to the spline-interpolated sediment mass balance described in text. Stage 0 deposit areas are: 6.44 (HW), 1.97 (Axial), 1.95 (FW1), and 2.27 (FW2) m².

The expansion of axial-drainage area for a given sediment discharge, corresponds to a concomitant loss of transverse area and to the volume of sediment delivered to the basin (Fig. 3.15C). For a given sediment discharge (between 20-60% of the total), the axial-deposit area was about 2.5 to 3.0 times larger than the footwall fans and about 1.4 times the hanging-wall fan. The mapped footwall fan areas were consistently smaller than the model area, indicating the axial stream removes more of its original area than the hanging-wall fan.

These increases in axial sedimentation were accomplished by cutting of the transverse-fan toes by the axial channel, as recognized from the overhead images described above (Figs. 3.4 & 3.10). The linear trends of sediment discharge to mapped deposit area and similar best-fit slopes (0.34-0.66) on Figure 3.15C imply no other major feedbacks affecting the increase of the axial sediment discharge, and that the axial system dominates basin sedimentation. Mapped axial areas approach model areas under high axial-sediment discharge conditions, whereas the mapped hanging-wall fan areas diverge from the model area (Fig. 3.15B).

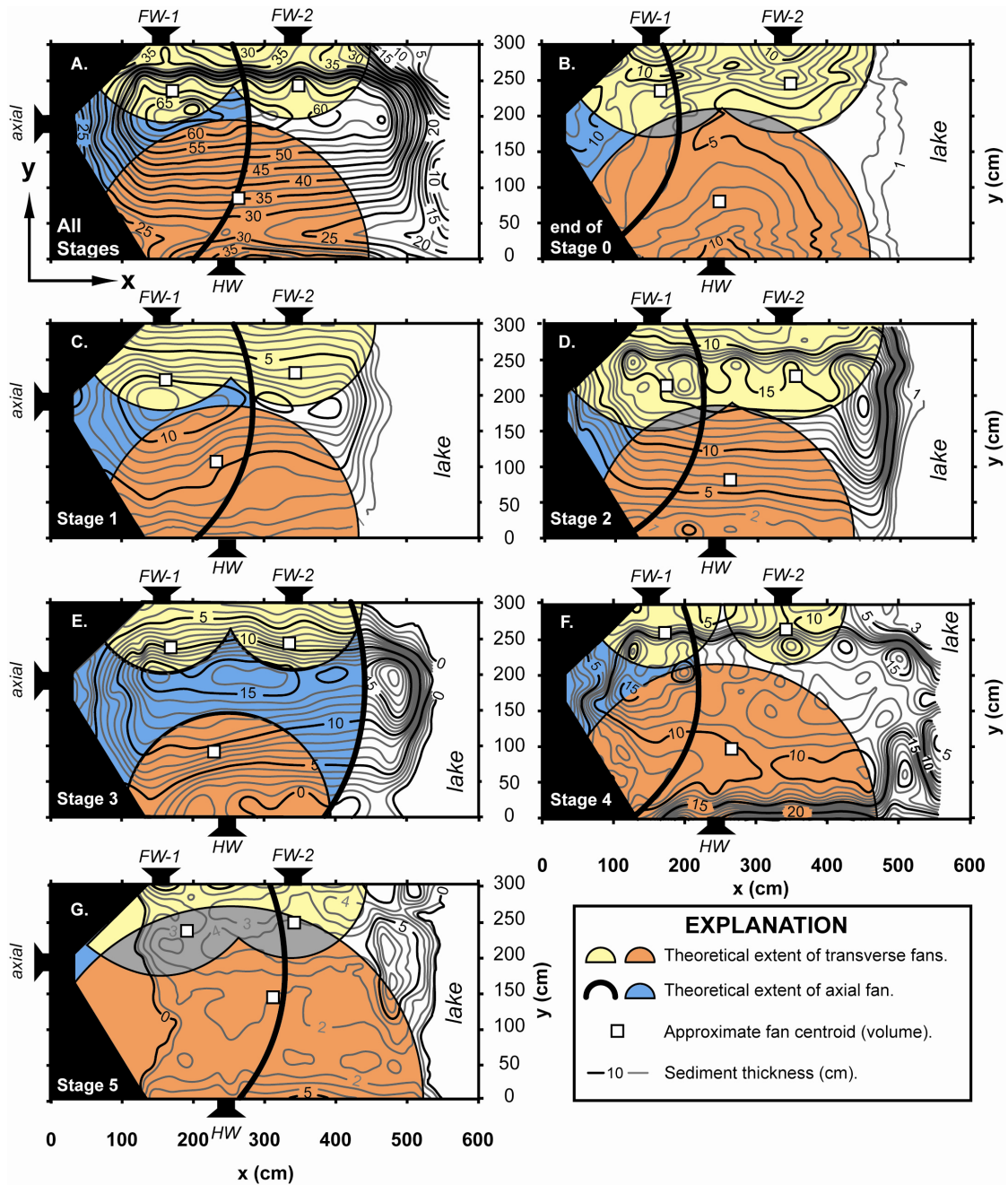


Figure 3.14. Spline-interpolated circular areas modeled for hypothetical semi-circular fans entering the basin at the sediment input points. Darker shading denotes regions of overlapping fans, and the bold curved line depicts the approximate down-stream position of an axial fan assuming no interference from the transverse fans. Model fan areas assume a perfectly radial distribution of sediment with no interference from the other sources of sediment or transport by the axial river. Contours denote sediment thickness determined from stage volumes. A: Total sediment accumulation for all stages and model fan areas. B: Sediment thickness and model fan areas at end of initial stage (stage 0). C-G: Sediment thickness and model fan areas during stages 1-5, respectively.

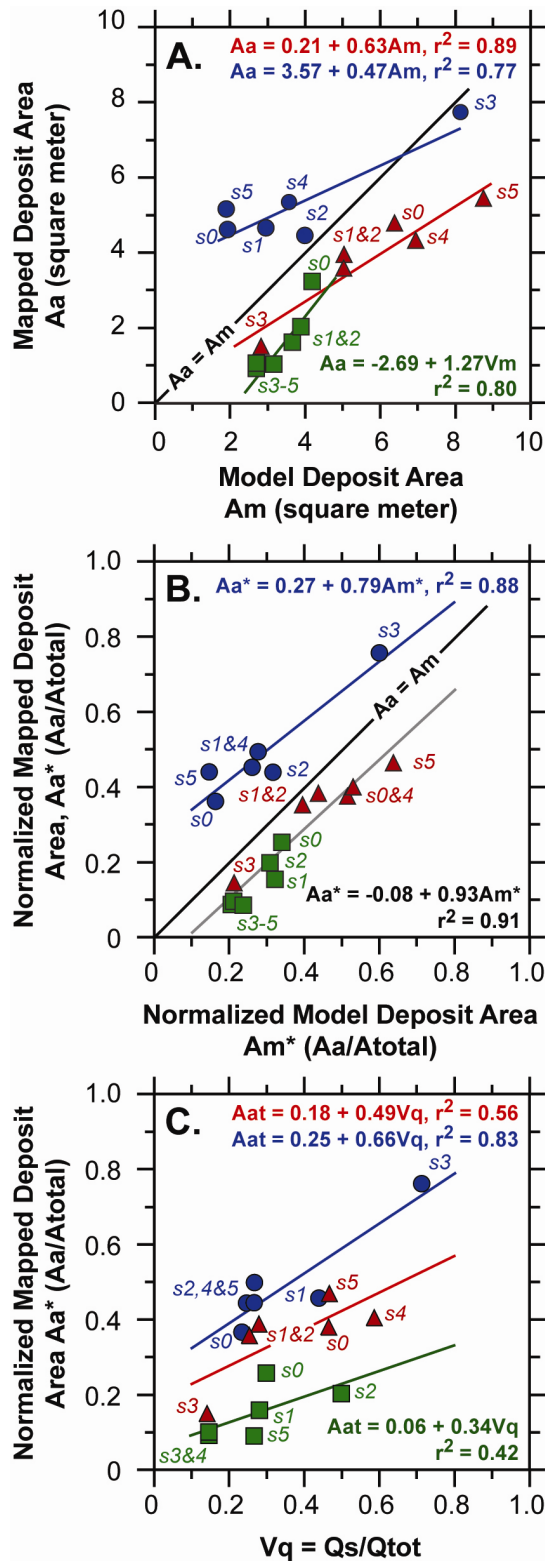


Figure 3.15. Plots illustrating mapped and model deposit areas and sediment discharge. Blue circles denote axial data, red triangles denote hanging-wall (HW), and green squares denote both footwall fans (2FW). Linear best-fit curves and r^2 values are also shown. Discharge-normalized volume (Vq) is sediment discharge (Qs) normalized to total sediment discharge. A: Deposit model area (Aa) versus mapped area (Am), in square meters. B: Areas normalized to the mapped fluvial area. Dimensionless model area (Aa^*) versus mapped area (Am^*). The gray line illustrates best-fit curve for transverse fans has a slope near unity (0.93 , $r^2 = 0.91$). C: Normalized mapped area (Aa^*) versus sediment-discharge-normalized volume (Vq), indicating linear relationships between deposit area and sediment discharge.

Discussion

Axial-Drainage Morphology

At the start of the experiment, the emergence of an axially aligned drainage depended on the toes of the transverse fans to define its edges. Without these flanking fans, a large axial fan would only form at the upper region of the experimental basin. A field example of such fan forms are recognized on the upper Rio Grande of southern Colorado (Fig. 3.16), where a large fluvial fan developed at the transition between the San Juan Mountains and San Luis Basin of the Rio Grande rift (Galloway and Hobday, 1996). The upper Rio Grande fan developed as a nodally avulsing channel where it emerges from the mountain front. Longitudinal drainage only develops about 30 km downstream where the river encounters tributary fans and is cut into resistant volcanic rock of the San Luis Hills. Internally drained basins, such as those containing the Rio Mimbres in southern New Mexico (Love and Seager, 1996; and Mack et al., 1997), or the Okavango fan in Botswana (Stanistreet and McCarthy, 1993) also formed broad fluvial fans where not impinged by tributary fans.

The location of the axial river is thought to be sensitive to the tilting of the basin floor imposed by the basin master fault (e.g., Peakall et al., 2000; and Smith et al., 2001). A result of basin tilting is to concentrate channel bodies as close to the axis of maximum subsidence as the transverse fans will allow (Leeder and Gawthorpe, 1987). The experiments showed that sediment discharges from the footwall catchments can easily steer the axial river away from the subsidence maximum.

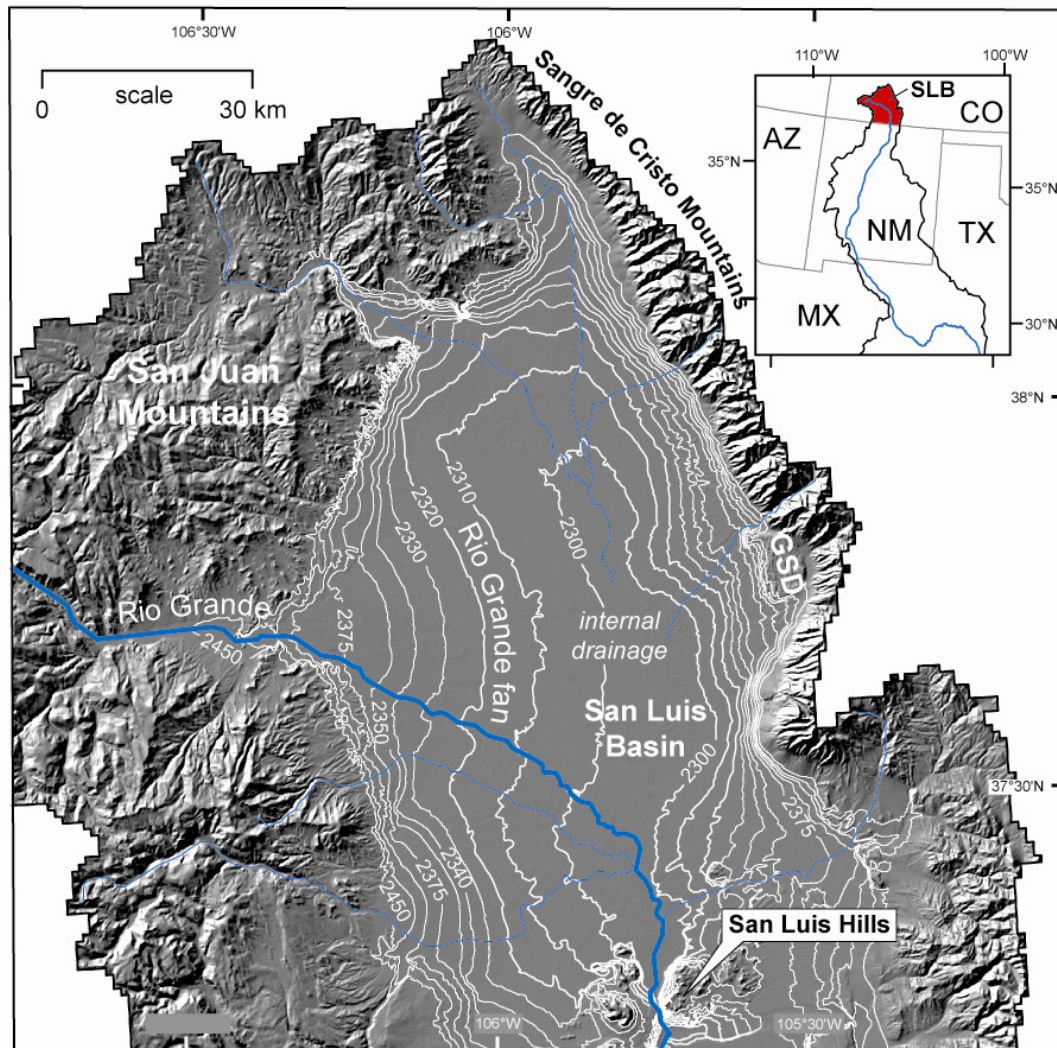


Figure 3.16. Shaded-relief map of upper Rio Grande drainage in southern Colorado, illustrating the large fluvial fan formed by the Rio Grande as it enters the San Luis Basin (from USGS 30-m DEM data). White contours are of elevation (in feet above mean sea level): contour intervals are 10 ft (3 m) between 2300 and 2350 ft, and 25 ft (7.6 m) between 2350 and 2450 ft elevation. GSD denotes the location of Great Sand Dunes National Monument.

A field example of “flux steering” of the axial drainage course by tributary fans is in the Basin and Range of southeastern Arizona (Smith, 1994) and in the Rio Grande rift of New Mexico (Leeder et al., 1996b). Migration of the axial belt through nontectonic flux steering by the footwall fans demonstrates the importance that tributary inputs can have on the position of the axial depositional belt. Under conditions of relatively slow subsidence, shifts in the position of this belt could result from the expansion of hinterland drainage area or stream capture events, rather than changes in basin subsidence.

Another field example of subsidence and sediment-discharge controls on location of an axial-river comes from the Rio Grande rift in New Mexico (Fig. 3.17). There, a perennial axial river (i.e., the Rio Grande) has been flowing through the Albuquerque Basin since early Pliocene time (see Chapter 2). The axial drainage course in the Rio Grande Valley also tends to be deflected by larger middle Holocene tributary fans (Gile et al., 1981; Connell et al., 2007; and Connell, 2008a), indicating that transverse fans can locally influence the position of the axial river. About half of the basin once contained deposits associated with large hanging-wall-derived drainages and fluvial fans. The remaining portion of the Plio-Pleistocene basin-fill succession consists of axial-river, and flanking piedmont deposits (Connell, 2004 and 2008a). Areas of axial-river deposition constituted about 22 percent of the basin area; footwall-fans occupied about 28 percent. The areas of the footwall fans were close to those of the experiments (both FW = 18%), but the axial deposit areas were about a third of the experimental area, suggesting that the ancestral Rio Grande was less capable of transporting sediment than in the experimental case.

The structure of the Albuquerque Basin also provides an opportunity to examine structural and sediment-discharge controls on depositional patterns. The axial river crosses strain-accommodation zones that divide the basin into distinct structural domains based on tilting (Russell and Snelson, 1994). This structural segmentation is useful in comparing depositional and subsidence patterns with the experimental results (Russell and Snelson, 1994; Connell, 2004, 2008a & b; Connell et al., 2001a & b; Grauch et al., 1999 & 2007; and Maldonado et al., 2007). Although the boundaries of the strain accommodation zones are controversial, the northern part of the basin contains predominantly east-tilted strata and the southern part is predominantly west tilted (*cf.* Russell and Snelson, 1994; Grauch et al., 2007; and Maldonado et al., 1999).

To the north, the axial-river flowed near the eastern margin and migrated toward the western structural margin at the southern end of the basin (Fig. 3.17). The southwestern portion of the basin contains the remains of large southeast-flowing drainages (of the ancestral Rio Puerco and Rio San Jose; Love and Connell, 2005). These deposits dominated the western part of the basin on the distal hanging-wall ramp, and flowed across a zone of strain accommodation into the southern end of the basin where strata tilt towards the western rift flank uplifts of the Ladron Mountains. The ancestral Rio Grande initially flowed along the structural margin of the Ladron Mountains (Machette, 1978). Later development of large obliquely-flowing, hanging-wall-sourced drainages prevented the ancestral Rio Grande from maintaining this margin-ward position through late Pliocene and early Pleistocene time, despite the continued locus of subsidence near the southwestern margin of the basin.

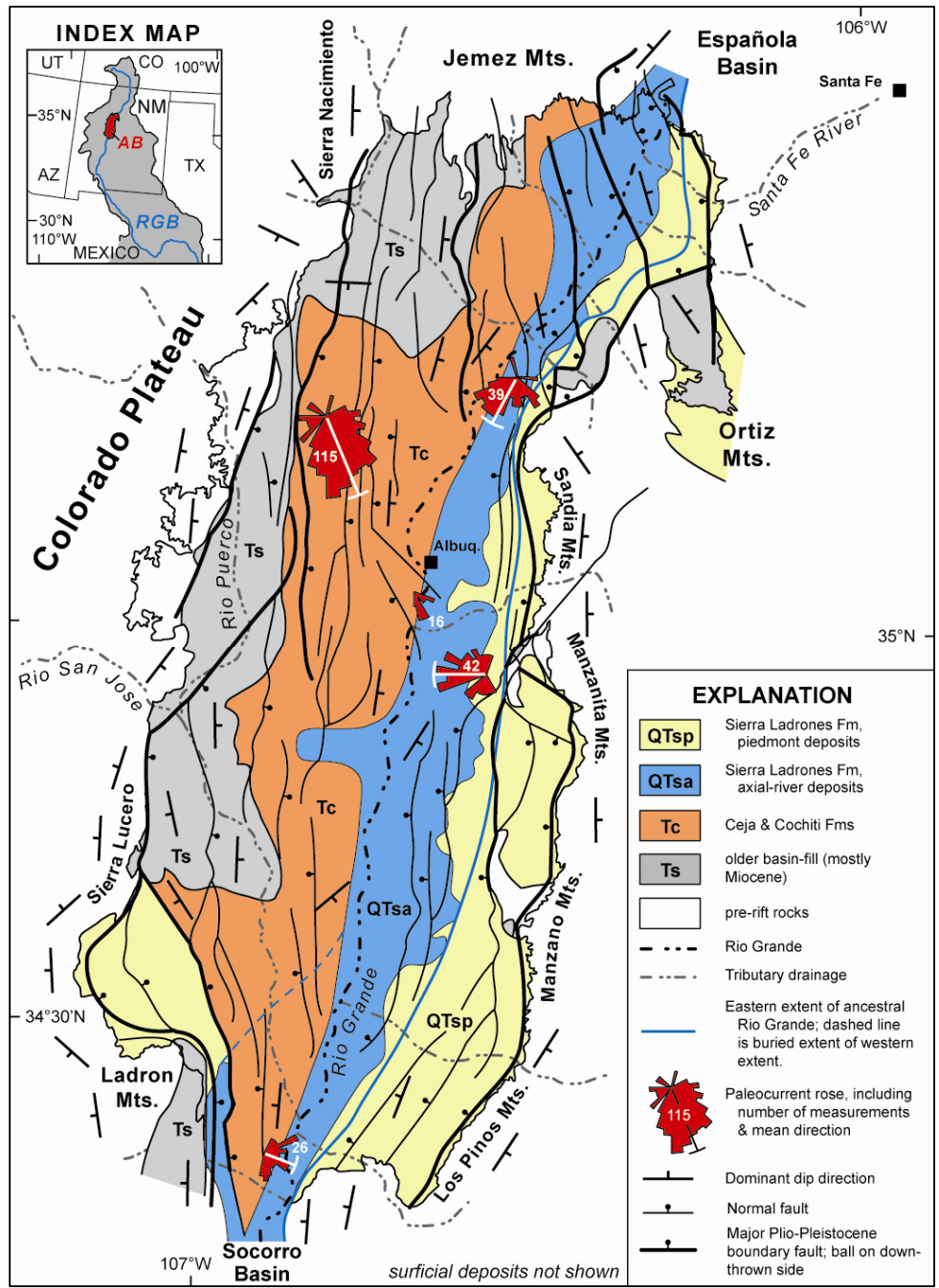


Figure 3.17. Simplified geologic map of the Albuquerque Basin (AB) of the Rio Grande basin (RGB) in southwestern North America, illustrating major Plio-Pleistocene depositional units, paleocurrent roses, strike and dip of inclined bedding, and inferred sub-basin boundaries (modified from Kelley, 1977; Osburn, 1983; Connell, 2004; 2008; Connell et al., 2001a, b; Brandes, 2002; Maldonado et al., 2007; Russell and Snelson, 1994; and Grauch et al., 1999 & 2007). Geologic structures are highly simplified and surficial deposits are not shown. The northern and central portions of the basin tilt to the east, and the southern part tilts to the west, near the Socorro Basin.

Transverse-Fan Morphology

The sizes of transverse fans enlarged with increasing sediment discharge. Deposit areas were sensitive to slope, which is controlled by the ratio of water to sediment discharge (Fig. 3.8). The lower flow-occupation and slower channel-response times on the footwall fans (Fig. 3.9) implies a timescale mismatch with the larger and highly mobile axial drainage. However, even with this potential impediment, the footwall fans maintained their form and size against the larger and more mobile axial drainage system. The steeper slopes of the footwall fans play a crucial role both in confining the axial stream, and help to maintain their radial symmetry.

Depositional slopes decreased with increasing (sediment and water) discharge, as in previous studies (e.g. Whipple et al., 1998), and the slopes of the transverse fans approached those of the axial drainage course (Fig. 3.8C & D). The slopes on footwall fans decreased with increasing axial slope, whereas sloped of the hanging-wall deposits increased slightly with increasing axial slope (Fig. 3.8B). All deposit slopes increased with increasing Q_s/Q_w (Fig. 3.8E), indicating that the higher slopes of the footwall fans are a consequence of doubling the sediment supply relative to water discharge. Thus, the differences between the footwall and hanging-wall fans may represent different terrestrial diffusion rates or topographic inheritance that cause the axial drainage to flow around these steeper obstacles rather than completely obliterating them through toe cutting.

The positive correspondence between the hanging-wall and axial slopes indicates that the morphology and stratigraphy of these two systems respond similarly to changes in sediment discharge. They are both quite large and have much lower slopes relative to

the footwall fans. The inverse correlation of footwall to axial slope implies the presence of a threshold between slope and sediment discharge. This threshold may be approximated by projecting the best-fit lines for the transverse fans on Figure 3.8F, which cross the axial slopes at 0.051. Such high axial slopes were not observed during the experiment and would require having sediment-to-water ratios approaching those of the transverse fans.

Transverse flows tended toward an oblique orientation relative to the longitudinal (axial) drainage. Channels on the distal parts of the hanging-wall fan frequently became oriented towards the axial-stream direction (Fig. 3.10), making differentiation of drainage sources ambiguous using only flow direction as an indicator. This oblique orientation is atypical of tributary fans in the field, which normally contain drainages that are oriented perpendicular to the flanking uplifts (e.g., Leeder and Jackson, 1993; and Blair, 1999). However, unusual flow orientations have been documented in basins of the Rio Grande rift. A field-based example of obliquely oriented tributary drainage comes from the Albuquerque Basin, where a large Pliocene tributary to the axial Rio Grande flowed to the southeast in a direction that was clearly oblique to the southerly trend of the axial river and long axis of the basin (Fig. 3.18; Connell et al., 2001a & b; and Brandes, 2002). The drainage catchment is one of the largest of the Rio Grande tributaries (Love and Connell, 2005), implying that tributary-drainage obliquity may be a consequence of large tributary sediment discharge.

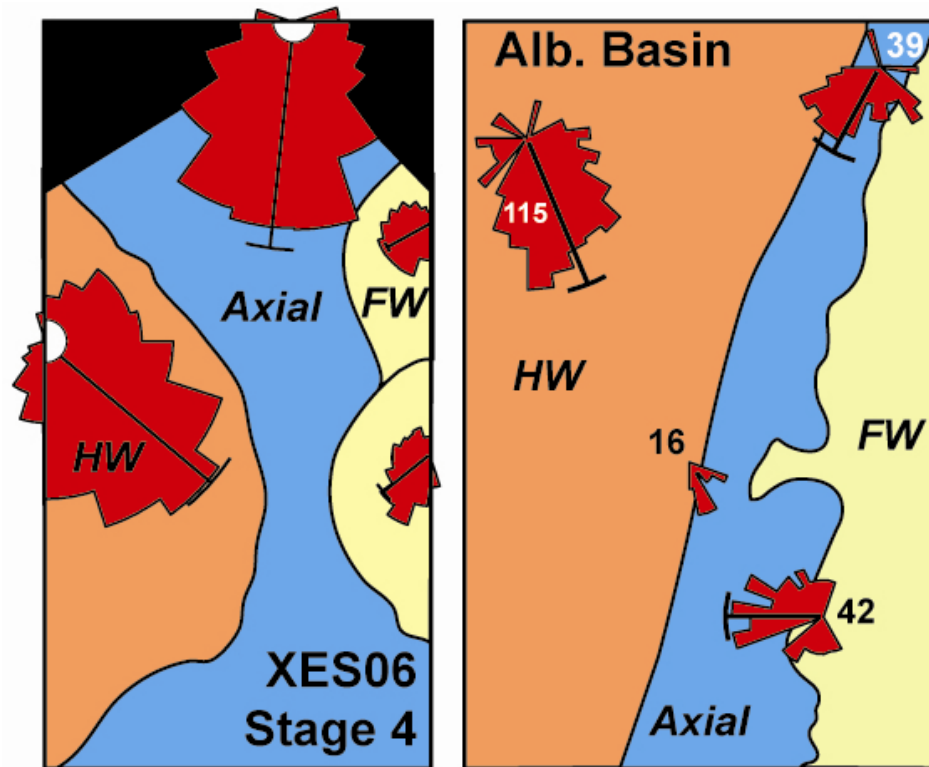


Figure 3.18. Circular histograms (rose diagrams, in red) comparing mean flow directions (black line) during stage 4 of XES06 (left) and field data collected in the Albuquerque Basin (right); N refers to number of observations (data from Connell et al., 2001a, b; and Brandes, 2002). Colors denote analogous sediment sources: hanging wall (orange), axial (blue), and footwall (yellow).

The development of this oblique drainage pattern may be the result of lengthening the radial fan distance relative to the axial drainage course. The emergence of strong drainage obliquity in the transverse fans during high sediment-discharge regimes could result from the lengthening of stream courses that preferentially would lower deposit slopes towards the axial drainage. As tributary sediment discharge approached that of the axial river, their morphology would resemble that of the axial drainage system. It is also possible that the slope of the axial drainage is high enough to make the downstream side of the hanging-wall fan lower than the upstream side. This

would make the hanging-wall fan shape an artifact of relatively high experimental river slopes.

Larger catchments can also develop along major fault segment boundaries and across accommodation and transfer zones (e.g., Gawthorpe and Hurst, 1993). Structural transfer zones tend to dip into the basin at oblique angles relative to the long axis of the basin, which would enhance the tendency of large tributary drainages to flow oblique to the basin axis. Thus, this drainage obliquity could also be the result of southeastern basement slopes imposed by a set of relay-ramps that accommodate an eastward step in the structural margin of the basin (Kelley, 1982).

Drainage Interactions

The observed fluvial responses reflect self-organization of the depositional system because the boundary conditions remained constant (i.e., sediment supply, subsidence, and base level) during each experimental stage. The relative consistency in the fraction of transverse fan area and volume extracted by the axial drainage system suggests that the dynamic axial-transverse boundary remained consistent over a wide range of sediment discharges (Fig. 3.15). Large-scale autogenic processes in fluviodeltaic systems are an expression of the nature of the moving boundaries of the system and include the shoreline, the delta toe, and the alluvium-basement transition at the upstream end of the alluvial river (Paola et al., 1992; and Swenson et al., 2000). Results of these experiments suggest a dynamic boundary between the axial and transverse depositional systems that may be analogous to the fluviodeltaic boundary in coastal settings.

The volume of sediment delivered to the experimental basin compares favorably to the mean areas of the mapped fluvial surfaces, implying a reasonable correspondence between sediment discharge and fan morphology. Increased sediment discharge in the axial and footwall drainages are marked by abrupt increases in deposit area. Small episodic swings in deposit area are recognized in nearly all stages and probably represent a stratigraphic manifestation of autogenic processes, such as river avulsion or fan-lobe switching (e.g., Miall, 1996; and Kim and Jerolmack, 2008).

Although much of the axial sediment remained in the upstream fan region, the axial-drainage system was clearly capable of transferring transverse sediment through the basin. Tributaries that carried larger sediment discharges tended to contribute slightly more sediment into the axial system (Fig. 3.15). The expansion of axial-deposit area was matched by a nearly concomitant decrease in the volume of the transverse deposits, suggesting that the axial river provides a record of the relative sediment discharges of upstream drainage sources. Under conditions of high axial sediment discharge, the axial river dominated the basin subsidence and indicates that reconstruction of the width of the axial depositional belt would be a useful approximation of sediment discharge in the axial belt.

Chapter Conclusions

Experimental EarthScape run in 2006 (XES06) examined fluvial sedimentation in a basin that used a simple, laterally asymmetric subsidence pattern and four point sources of sediment and water (one axial and three transverse) to simulate sedimentation in a simple half-graben basin. Results of this study provide additional insights regarding

allogenic drivers of the geomorphic and architectural evolution of fluvial basins. Although many details differ, the overall geometry is similar to that in field-scale asymmetric rifts.

Deposits formed in the experimental basin organized itself to a low-gradient, subcritical axial stream flanked and bounded by three steep, transverse fans. The main control on the lateral position and width of the experimental axial stream was the ratio of the sediment discharges relative to the discharge in the transverse systems. The location of the lateral subsidence maximum did not exert a strong control on the location of the axial system, but was strongly influenced by the relative strengths of the tributary drainages that resulted in “flux steering” of the axial stream.

The observed self-organization of the fluvial depositional system is autogenic because the boundary conditions of sediment supply, subsidence, and base level remained constant during each experimental stage. The relative consistency in the fraction of the transverse fans extracted by the axial drainage system suggests that the axial-transverse boundary is also autogenic in nature. Results of these experiments suggest the presence of a moving boundary between the axial and transverse depositional systems that may be analogous to the fluviodeltaic boundary in coastal settings. The distal toes of the transverse fans are modified by a sort of along-basin axial transport analogous to long-shore drift. Without this boundary, the surface morphology of the axial drainage system would resemble those of the transverse fans.

Chapter Acknowledgements

This work was supported by the National Science Foundation (EAR-0344146), the New Mexico Bureau of Geology and Mineral Resources (P.A. Scholle, Director), and the St. Anthony Falls Industrial Consortium, including Chevron, Conoco-Phillips, Exxon-Mobil Upstream Research Corporation, Japan Oil, Gas and Metals National Corporation (JOGMEC), and Royal-Dutch Shell Corporation. We are indebted to the engineers and technical staff at Saint Anthony Falls Laboratory, most notably Jim Mullin, Chris Ellis, and Dick Christopher, for their help with the design, execution, and data collection for this set of experiments.

Chapter References

- Blair, T.C., 1999, Sedimentology of the debris-flow dominated Warm Spring Canyon alluvial fan, Death Valley, California: *Sedimentology*, v. 46, p. 941-965.
- Blair, T.C., and Bilodeau, W.L., 1988, Development of tectonic cyclothems in rift, pull-aparts, and foreland basins: sedimentary response to episodic tectonism: *Geology*, v. 16, p. 517-520.
- Blair, T.C., and McPherson, J.G., 1994, Alluvial fans and their natural distinction from rivers based on geomorphology, hydraulic processes, sedimentary processes, and facies assemblages: *Journal of Sedimentary Research*, v. A64, n. 3, p. 450-489.
- Blum, M.D., and Törnqvist, T.E., 2000, Fluvial responses to climate and sea-level change; a review and look forward: *Sedimentology*, v. 47, Suppl. 1, p. 2-48.
- Brandes, N.N., 2002, Lithostratigraphy and petrography of upper Santa Fe Group deposits in the northern Albuquerque Basin, New Mexico [M.S. thesis]: Socorro, New Mexico Institute of Mining and Technology, 208 p.
- Bridge, J.S., and Leeder, M.R., 1979, A simulation model of alluvial stratigraphy: *Sedimentology*, v. 26, p. 617-644.
- Bridge, J.S., and MacKey, S.D., 1993, A revised alluvial stratigraphy model, *in* Marzo, M., and Puigdefabregas, C., eds., *Alluvial Sedimentation: International Association of Sedimentologists, Special Publication 17*, p. 319-336.

- Bryant, M., Falk, P., and Paola, C., 1995, Experimental study of avulsion frequency and rate of deposition: *Geology*, v. 23, p. 365-368.
- Bull, W.B., 1977, The alluvial-fan environment: *Progress in Physical Geography*, v. 1, p. 222-270.
- Cazanacli, D., Paola, C., and Parker, G., 2002, Experimental steep, braided flow: application to flooding risk on fans: *Journal of Hydraulic Engineering*, v. 128, p. 322-330.
- Chapin, C.E., and Cather, S.M., 1994, Tectonic setting of the axial basins of the northern and central Rio Grande rift: *Geological Society of America, Special Paper 291*, p. 5-25.
- Connell, S.D., 2004, Geology of the Albuquerque Basin and tectonic development of the Rio Grande rift, north-central New Mexico, *in* Mack, G.H., and Giles, K.J., eds., *The Geology of New Mexico, A geologic history*: New Mexico: New Mexico Geological Society, Special Publication 11, p. 359-388.
- Connell, S.D., 2008a, Geologic map of the Albuquerque-Rio Rancho metropolitan area, Bernalillo and Sandoval County, New Mexico: New Mexico Bureau of Geology and Mineral Resources, Geologic Map GM-78, scale 1:50,000, 2 pls.
- Connell, S.D., 2008b, Refinements to the stratigraphic nomenclature of the Santa Fe Group, northwestern Albuquerque Basin, New Mexico: *New Mexico Geology*, v. 30, n. 1, p. 14-35.
- Connell, S.D., Lucas, S.G., Koning, D.J., Maynard, S.R., and Derrick, N.N., 2001a, First-day, Santo Domingo sub-basin: Hagan Embayment and northern flank of the Sandia Mountains, *in* Connell, S.D., Love, D.W., Lucas, S.G., Koning, D.J., Derrick, N.N., Maynard, S.R., Morgan, G.S., Jackson-Paul, P.B., and Chamberlin, R., trip leaders., *Stratigraphy and tectonic development of the Albuquerque Basin, central Rio Grande rift, field trip guidebook*: Albuquerque, New Mexico, Geological Society of America, Rocky Mountain-South Central Section Meeting: New Mexico Bureau of Geology and Mineral Resources, Open-file report 454A, p. 1-15.
- Connell, S.D., Love, D.W., and Sorrell, J.D., 2001b, Geology of southern Albuquerque and Tijeras Arroyo, Second-day road log, October 13, 2001, *in* Connell, S.D., Love, D.W., Sorrell, J.D., and Harrison, J.B.J., trip leaders., *Plio-Pleistocene stratigraphy and geomorphology of the central part of the Albuquerque Basin: Friends of the Pleistocene, Rocky Mountain Cell, Field-trip guidebook*: New Mexico Bureau of Geology and Mineral Resources, Open-file report 454C, p. 2-1 to 2-23.
- Connell, S.D., Hawley, J.W., and Love, D.W., 2005, Late Cenozoic drainage development in the southeastern Basin and Range of New Mexico, southeasternmost

- Arizona, and western Texas, *in* Lucas, S.G., Morgan, G.S., and Zeigler, K.E., eds., New Mexico's Ice Ages: New Mexico Museum of Natural History and Science, Bulletin No. 28, p. 125-150.
- Connell, S.D., Love D.W., and Dunbar, N.W., 2007, Geomorphology and stratigraphy of inset fluvial deposits along the Rio Grande valley in the central Albuquerque Basin, New Mexico: *New Mexico Geology*, v. 29, n. 1, p. 13-31.
- Davis, J. M., Lohmann, R. C., Phillips, F. M., Wilson, J. L., and Love, D. W., 1993, Architecture of the Sierra Ladrones Formation, central New Mexico: Depositional controls on the permeability correlation structure: *Geological Society of America Bulletin*, v. 105, p. 998-1007.
- Edmonds, D.A., Hoyal, D.C., Sheets, B., and Bloch, R.B., 2007, On the nature of delta distributary fill (abstract): *American Association of Petroleum Geologists, Annual Meeting Abstracts*, v. 16, p. 40.
- Foufoula-Georgiou, E., and V. B. Sapazhnikov, 1998, Anisotropic scaling in braided rivers: An integrated theoretical framework and results from application to an experimental river: *Water Resources Research*, v. 34, p. 863–867, doi: 10.1029/98WR00216.
- Foufoula-Georgiou, E., and V. B. Sapazhnikov, 2001, Scale invariances in the morphology and evolution of braided rivers: *Mathematical Geology*, v. 33, p. 273–291, doi: 10.1023/A:1007682005786.
- Frostick, L.E., 1997, The East African Rift basins, *in* Selley, R.C., ed., *African Basins: Sedimentary basins of the world*, v. 3: Amsterdam, Elsevier Science, p. 187-209.
- Galloway, W.E., and Hobday, D.K., 1996, *Terrigenous clastic depositional systems; applications to fossil fuels and groundwater resources*: Berlin, Springer-Verlag, second edition, 489 p.
- Gawthorpe, R.L., and Hurst, J.M., 1993, Transfer zones in extensional basins: their structural style and influence on drainage development and stratigraphy: *Journal of the Geological Society*, v. 150, p. 1137-1152.
- Gawthorpe, R.L., and Leeder, M.R., 2000, Tectono-sedimentary evolution of active extensional basins: *Basin Research*, v. 12, p. 195-218.
- Gile, L.H., Hawley, J.W., and Grossman, R.B., 1981, Soils and geomorphology in the Basin and Range area of southern New Mexico-Guidebook to the Desert Project: New Mexico Bureau of Mines and Mineral Resources, Memoir 39, 222 p.

- Grauch, V.J.S., Keller, G.R., and Gillespie, C.L., 1999, Discussion of new gravity maps for the Albuquerque Basin area: New Mexico Geological Society, Guidebook 50, 119-124.
- Grauch, V.J.S., Connell, S.D., and Sawyer, D.A., 2007, Rethinking an archetype of rift half-graben formation; a revised model of basin geometry for the Albuquerque segment of the Rio Grande Rift, New Mexico [abstract]: Geological Society of America, Abstracts with Programs, v. 39, n. 6, p. 364.
- Hasbargen, L.E., and Paola, C., 2000, Landscape instability in an experimental drainage basin: *Geology*, v. 28, n. 12, p. 1067-1070.
- Heller, P.L., and Paola, C., 1992, The large-scale dynamics of grain-size variation in alluvial basins, 2: application to syntectonic conglomerate: *Basin Research*, v. 4, p. 91-102.
- Heller, P.L., and Paola, C., 1996, Downstream changes in alluvial architecture: An exploration of controls on channel-stacking patterns, *Journal of Sedimentary Research*, v. 66, 297-306.
- Hickson, T. A., B. A. Sheets, C. Paola, and M. Kelberer, 2005, Experimental test of tectonic controls on three-dimensional alluvial facies architecture: *Journal of Sedimentary Research*, v. 75, p. 710–722, doi: 10.2110/jsr.2005.057.
- Kelley, V.C., 1977, Geology of the Albuquerque basin, New Mexico: New Mexico Bureau of Mines and Mineral Resources, Memoir 33, 60 p.
- Kelley, V.C., 1982, The right-relayed Rio Grande rift, Taos to Hatch, New Mexico: New Mexico Geological Society, Guidebook 33, p.147-151.
- Kendall, C.G. St. C., Strobel, J., Cannon, R., Bezdek, J., and Biswas, G., 1991, The simulation of the sedimentary fill of basins: *Journal of Geophysical Research*, v. 96, p. 6911-6929.
- Kim, W., and Jerolmack, D.J., 2008, The pulse of calm fan deltas: *Journal of Geology*, v. 116, n. 4, p. 315-330.
- Lambiase, J.J., and Bosworth, W., 1995, Structural controls on sedimentation in continental rifts, *in* Lambiase, J.J., ed., Hydrocarbon habitat in rift basins: Geological Society Special Publication No. 80, p. 117-144.
- Lane, E.W., 1955, The importance of fluvial morphology in hydraulic engineering: American Society of Civil Engineers, Proceedings, v. 81, n. 745, p. 1-17.
- Lawrence, D.T., 1994, Evaluation of eustasy, subsidence, and sediment input as controls on depositional sequence geometries and the synchronicity of sequence boundaries, *in*

- Weimer, P., and Posamentier, H.W., eds., Siliclastic sequence stratigraphy; recent developments and applications: American Association of Petroleum Geologists Memoir 58, p. 337-367.
- Leeder, M.R., and Gawthorpe, R.L., 1987, Sedimentary models for extensional tilt block/half graben basins, *in* Coward, M.P., Dewey, J.F., and Hancock, P.L., eds., Continental Extensional Tectonics, Geological Society of London Special Publication 28, p.139-152.
- Leeder, M. R., and Jackson, J. A., 1993, The interaction between normal faulting and drainage in active extensional basins, with examples from the western United States and central Greece: *Basin Research*, v. 5, n. 2, p. 79-102.
- Leeder, M.R., and Mack G.H., 2001, Lateral erosion (“toe cutting”) of alluvial fans by axial rivers; implications for basin analysis and architecture: *Journal of the Geological Society of London*, v. 158, n. 6, p. 885-893.
- Leeder, M.R., Mack, G.H., Peakall, J., and Salyards, S.L., 1996a, First quantitative test of alluvial stratigraphic models: Southern Rio Grande rift, New Mexico: *Geology*, v. 24, n. 1, p. 87-90.
- Leeder, M.R., Mack, G.H., and Salyards, S.L., 1996b, Axial-transverse fluvial interactions in half-graben: Plio-Pleistocene Palomas Basin, southern Rio Grande rift, New Mexico, USA: *Basin Research*, v. 8, n. 3, p. 225-241.
- LeTourneau, P.M., and Olsen, P.E., eds., 2003, The great rift valleys of Pangea in eastern North America: Volume 2, Sedimentology, stratigraphy, and paleontology: Columbia University Press, 384 p.
- Love, D.W., and Seager, W.R., 1996, Fluvial fans and related basin deposits of the Mimbres drainage: *New Mexico Geology*, v. 18, n. 4, p. 81-92.
- Love D.W., and Connell, S.D., 2005, Late Neogene drainage developments on the southeastern Colorado Plateau, New Mexico, *in* Lucas, S.G., Morgan, G.S., and Ziegler, K.E., eds., *New Mexico’s Ice Ages: New Mexico Museum of Natural History and Science Bulletin 28*, p. 151-169.
- Machette, M.N., 1978, Geologic map of the San Acacia Quadrangle, Socorro County, New Mexico: U.S. Geological Survey, Geologic Quadrangle Map GQ-1415, scale 1:24,000.
- Mack, G.H. and Seager, W.R., 1990, Tectonic controls on facies distribution of the Camp Rice and Palomas Formations (Pliocene-Pleistocene) in the southern Rio Grande rift: *Geological Society of America Bulletin*, v. 102, p. 45-53.

- Mack, G.H., Love, D.W., and Seager, W.R., 1997, Spillover models for axial rivers in regions of continental extension; the Rio Mimbres and Rio Grande in the southern Rio Grande Rift, USA: *Sedimentology*, v. 44, n. 4, p. 637-652.
- Mack, G.H., Seager, W.R., Leeder, M.R., Parea-Arlucea, M., and Salyards, S.L., 2006, Pliocene and Quaternary history of the Rio Grande, the axial river of the southern Rio Grande rift, New Mexico, USA: *Earth-Science Reviews*, v. 79, p. 141-162.
- Maldonado, F., Connell, S.D., Love, D.W., Grauch, V.J.S., Slate, J.L., McIntosh, W.C., Jackson, P.B., and Byers, F.M., Jr., 1999, Neogene geology of the Isleta Reservation and vicinity, Albuquerque Basin, New Mexico: *New Mexico Geological Society Guidebook 50*, p. 175-188.
- Maldonado, F., Slate, J.L., Love, D.W., Connell, S.D., Cole, J.C., and Karlstrom, K.E., 2007, Geologic map of the Pueblo of Isleta tribal lands and vicinity, Bernalillo, Torrance, and Valencia Counties, central New Mexico: U.S. Geological Survey Scientific Investigations Map 2913, 35-p. pamphlet, 1 plate, scale 1:50,000.
- Marr, J.G., Swenson, J.B., Paola, C., and Voller, V.R., 2000, A two-dimensional model of fluvial stratigraphy in closed depositional basins: *Basin Research*, v. 12, p. 381-398.
- Martin, J., Paola, C., Abreu, V., Neal, J., and Sheets, B., 2009, Sequence stratigraphy of experimental strata under known conditions of differential subsidence and variable base level: *American Association of Petroleum Geologists Bulletin*, v. 93, n. 4, p. 503-533.
- Miall, A.D., 1996, *The geology of fluvial deposits*: Berlin, Springer-Verlag, 582 p.
- Mullin, J., and Ellis, C., 2008, Method to produce grain-scale digital images of large experimental sedimentary deposits and other imperfectly flat stratigraphy: *Journal of Sedimentary Research*, v. 78, n. 3, p.239-244.
- Osburn, G.R., 1983, Socorro County geologic map: New Mexico Bureau of Mines and Mineral Resources, Open-file report 238, 14 p., 1 pl. scale 1:200,000.
- Paola, C., 2000, Quantitative models of sedimentary basin filling: *Sedimentology*, v. 47, p. 121-178.
- Paola, C., Heller, P.L., and Angevine, C.L., 1992, The large-scale dynamics of grain-size variation in alluvial basins, 1: Theory: *Basin Research*, v. 4, p. 73-90.
- Paola, C., Mullin, J., Ellis, C., Mohrig, D.C., Swenson, J.B., Parker, G., Hickson, T., Heller, P.L., Pratson, L., Syvitski, J., Sheets, B., and Strong, N., 2001, Experimental Stratigraphy: *GSA Today*, v. 11, p. 4-9.

- Peakall, J., 1998, Axial river evolution in response to half-graben faulting, Carson River, Nevada, U.S.A.: *Journal of Sedimentary Research*, v. 68, n. 5, p. 788-799.
- Peakall, J., Ashworth, P.J., and Best, J.L., 1996, Physical modeling in fluvial geomorphology: principals, applications and unresolved issues, *in* Rhodes, B.L., and Thorn, C.E., eds., *The scientific geomorphology: 27th Binghamton symposium in Geomorphology*, Proceedings of the Annual Geomorphology Symposia Series, Binghamton, New York, p. 221-253.
- Peakall, J., Leeder, M., Best, J., and Ashworth, P., 2000, River responses to lateral ground tilting: a synthesis and some important implications for the modeling of alluvial architecture in extensional basins: *Basin Research*, v. 12, p. 413-424.
- Russell, L.R., and Snelson, S., 1994, Structure and tectonic of the Albuquerque Basin segment of the Rio Grande rift: Insights from reflection seismic data: *Geological Society of America*, Special Paper 291, p. 83-112.
- Sapozhnikov, V. B., and E. Fofoula-Georgiou, 1996, Self affinity in braided rivers: *Water Resources Research*, v. 32, p. 1429-1439, doi: 10.1029/96WR00490.
- Schlische, R.W., and Olsen, P.E., 1990, Quantitative filling model for continental extensional basins with applications to early Mesozoic rifts of eastern North America: *The Journal of Geology*, v. 98, n. 3, p. 135-155.
- Shanley, K.W., and McCabe, P.J., 1994, Perspectives on the sequence stratigraphy of continental strata: *American Association of Petroleum Geologists Bulletin*, v. 78, p. 544-568.
- Sheets, B., T. Hickson, and C. Paola, 2002, Assembling the stratigraphic record: Depositional patterns and timescales in an experimental alluvial basin: *Basin Research*, v.14, p. 287-301, doi: 10.1046/j.1365-2117.2002.00185.x.
- Smith, G.A., 1994, Climatic influences on continental deposition during late-stage filling of an extensional basin, southeastern Arizona: *Geological Society of America Bulletin*, v. 106, n. 8, p. 1212-1228.
- Smith, G.A., 2000, Recognition and significance of streamflow-dominated piedmont facies in extensional basins: *Basin Research*, v. 12, p. 399-411.
- Smith, G.A., McIntosh, W.C., and Kuhle, A.J., 2001, Sedimentologic and geomorphic evidence for sea-saw subsidence of the Santo Domingo accommodation-zone basin, Rio Grande rift, New Mexico: *Geological Society of America*, *Bulletin*, v. 113, n. 5, p. 561-574.
- Stanistreet, I.G., and McCarthy, T.S., 1993, The Okavango Fan and the classification of subaerial fan systems: *Sedimentary Geology*, v. 85, p. 115-133.

- Swenson, J.B., Voller, V.R., Paola, C., Parker, G., and Marr, J.G., 2000, Fluvio-deltaic sedimentation: A generalized Stefan problem: *European Journal of Applied Mathematics*, v. 11, p. 433-452.
- Van Heijst, M. W. I. M., and G. Postma, 2001, Fluvial response to sea-level changes: A quantitative analog, experimental approach: *Basin Research*, v. 13, p. 269–292, doi: 10.1046/j.1365-2117.2001.00149.x.
- Wernicke, B., 1981, Low-angle normal faults and seismicity; a review: *Journal of Geophysical Research*, v. 100, n. 20, p. 20,159-20,174.
- Weissman, G.S., Hartley, A.J., and Nichols, G., 2007, A new view of fluvial facies models aggradational distributary networks [abstract]: *Geological Society of America, Abstracts with Programs*, v. 39, n. 6, p. 629.
- Weissmann, G. S., Bennett, G.L., and Lansdale, A.L., 2005, Factors controlling sequence development on Quaternary fluvial fans, San Joaquin Basin, California, USA, *in* Harvey, A.M., Mather, A.E., and Stokes, M. eds., *Alluvial Fans: Geomorphology, Sedimentology, Dynamics*: Geological Society, London, Special Publication, v. 251, p. 169-186.
- Wells, N.A., and Dorr, J.A., Jr., 1987, A reconnaissance of sedimentation on the Kosi alluvial fan of India, *in* Flores, R.M., and Harvey, M.D., eds., *Recent developments in fluvial sedimentology*: Society of Economic Paleontologists and Mineralogists, Special Publication No. 39, p. 51-62.
- Whipple, K., Parker, G., Paola, C., Mohrig, D., 1998, Channel dynamics, sediment transport, and the slope of alluvial fans: experimental study: *Journal of Geology*, v. 106, p. 677-693.

**CHAPTER 4. EXPERIMENTAL STUDY OF INTERACTING DRAINAGES IN A
SEDIMENTARY BASIN: STRATIGRAPHIC ARCHITECTURE AND
SEDIMENT TRANSPORT**

Sean D. Connell^{1,2}, Wonsuck Kim³, Gary A. Smith¹, and Chris Paola⁴

¹*Department of Earth and Planetary Sciences, MSC03 2040, University of New Mexico, Albuquerque, New Mexico 87131 USA*

²*New Mexico Bureau of Geology and Mineral Resources, New Mexico Institute of Mining and Technology, 2808 Central Ave., SE, Albuquerque, New Mexico 87106 USA*

³*Department of Geological Sciences, University of Texas at Austin, 1 University Station, Austin, Texas 78712 USA*

⁴*Department of Geology and Geophysics and St. Anthony Falls Laboratory, University of Minnesota, Minneapolis, Minnesota 55414 USA*

Chapter Abstract

The stratigraphic architecture of intracontinental rift basins is defined by a dynamic relationship between depositional belts associated with the basin floor and flanking piedmont tributary streams. The depositional history of these belts is sensitive to a variety of factors, including basin geometry, subsidence rate, and sediment discharge. Experimental studies aid in the understanding of how these deposits respond to allogenic forcing. The Experimental EarthScape run in 2006 (XES06) explored the evolution of surface morphology and stratigraphic architecture in a fluvial basin based on the form of a simple half graben. This companion paper to Chapter 3 examines relationships among stratigraphic architecture and sediment composition and transport.

Depositional patterns were examined using sequential maps of deposit volume using cross-sectional slices and overhead imagery acquired during the experiment. A

sediment mass balance was compared to the distribution of dyed tracer sand in order to understand how the axial drainage can remove sediment from the basin. The axial drainage system primarily transported sediment provided by the transverse (piedmont) streams, except during the highest axial sediment discharges where axially-sourced sediment was transported to the delta. Sediment from the transverse drainages was introduced into the axial stream through toe cutting or re-alignment of transverse drainages to the prevailing axial-flow direction. Changes in sediment discharge were generally well expressed by scours that served as recognizable stratigraphic discontinuities. The hanging-wall fan recorded stage-bounding stratigraphic lacunae more reliably than its footwall counterparts.

Introduction

The stratigraphic architecture of intracontinental rift basins is defined by three depositional belts associated with the basin floor and two flanking piedmonts. The locations of these depositional belts are sensitive to subsidence, sediment delivery rate, effective moisture, catchment morphology, and rock type (e.g., Gawthorpe and Leeder, 2000, and references therein). The development of alluvial successions in rifted basins have been examined through numerous field-based studies and numerical simulations (Bridge and Leeder, 1979; Leeder and Gawthorpe, 1987; Blair and Bilodeau, 1988; Mack and Seager, 1990; Heller and Paola, 1992; Paola et al., 1992; Bridge and MacKay, 1993; Leeder et al., 1996a & b; Gawthorpe and Leeder, 2000; Peakall, 1998; Marr et al., 2000; Paola, 2000; Leeder and Mack, 2001; Smith, 1994; and Smith et al., 2001). Most of these studies focused on only one or two components of the rift-basin succession and

did not fully account for extrabasinal sediment transport by longitudinal drainages that are common in large intracontinental rift systems (Chapin and Cather, 1994; Lambiase and Bosworth, 1995; Frostick, 1997; LeTourneau and Olsen, 2003; Connell et al., 2005; and Mack et al., 2006).

Models of basin filling deal with the timing and apportioning of sediment into stratigraphic sequences (Schlische and Olsen, 1990; Kendall et al., 1991; Lawrence, 1994; and Shanley and McCabe, 1994). Quantification of how sediment is deposited in a basin would aid in better understanding how the three depositional belts in fluvially dominated half-graben basins respond to allogenic forcing. In this study, the ability of the axial drainage to remove sediment from the basin was examined using a simple sediment mass-balance model and comparing it to the total sediment input and mapped depositional belts. Sediment transport can also be quantified by an analysis of sediment composition through tracking of distinctive grains (e.g., Dickinson, 1988). A major motivation for the experiments reported here was to understand how tributary drainages influence the position, size, and composition of axial-river deposits in rift basins. We examined the development of sedimentary successions within an asymmetrically subsiding basin containing multiply interacting sediment sources. This paper is a companion to a study of surface morphology produced by these experiments (see Chapter 3).

Methods

Experimental EarthScape Facility

The Experimental EarthScape (XES) facility at Saint Anthony Falls Laboratory (University of Minnesota) is an experimental basin built to examine basin filling under conditions of programmable differential subsidence (Paola et al., 2001). The experiment reported here (henceforth XES06) was described in Chapter 3, and the experimental setup is briefly summarized below. XES06 examined surface morphology and stratigraphic architecture created by multiple, multidirectional sources that filled an actively subsiding basin (Fig. 4.1). The active portion of XES06 utilized a simple asymmetrical subsidence pattern over a 5.8 m x 3.0 m area, where subsidence was monitored every 240 seconds by manometers assigned to 108 active subsidence cells. Sedimentation patterns were documented by orthorectified digital images taken at 60-second intervals. Deposit topography and bathymetry were acquired at vertical resolutions of 0.1 mm and 1 mm, respectively. These datasets were merged into digital elevation models (DEM) having an areal resolution of 1 cm². Deposit topography was stratigraphically migrated using DEMs of the basement topography to create isochronous surfaces that were used to correlate deposits. The deposit was sliced and digitally imaged to form a high-resolution, three-dimensional record of the subsurface architecture and sediment distribution.

Experimental Design and Data Collection

The stages of XES06 were designed to explore relationships between subsidence and sediment flux (Table 4.1). Initial conditions (established after 42 hours of runtime in

stage 0) were followed by five stages (300 hours of runtime) with two subsidence rates (slow, 1.4 mm/hr; fast, 2.6 mm/hr) and varying sediment and water discharges (Fig. 4.2). Data related to XES06 (including time-lapse movies) are available in Appendix D through I. These data are also available through the National Center for Earth-Surface Dynamics (NCED) data repository at the University of Minnesota (<https://repository.nced.umn.edu/>).

The XES06 setup contained four separate sediment-input points that provided three compositionally distinct sediment sources (Fig. 4.1). The subsidence pattern resembles a simple half-graben basin with sediment inputs that are broadly analogous to those in half-graben basins. A single supply point at the upper end of the basin served as the source of longitudinal drainage analogous to the axial river. A single input on the river-right side of the basin served as the source of the analogous hanging-wall ramp fan (HW). At the opposite side of the basin, the footwall sources were equally divided into up-basin (FW-1) and down-basin (FW-2) inputs in an attempt to imitate the smaller and more numerous footwall fans in half-graben basins (e.g., Leeder and Jackson, 1993). Slopes were set by altering the ratio of sediment discharge (Q_s) to water discharge (Q_w). The analogous axial and hanging-wall drainages had Q_s/Q_w set to 0.01; footwall fans were set to 0.02 (Table 4.1).

Table 4.1. Summary of XES06 experimental parameters.

Stage	Dur. (hrs)	Max. Subs. (mm/hr)	Hanging-wall input			Axial-stream input			Footwall input*		
			Qs (ml/min)	Qs (%)	Qw/ Qs	Qs (ml/min)	Qs (%)	Qw/ Qs	Qs (ml/min)	Qs (%)	Qw/ Qs
1	80	1.4	48	28	100	75	44	100	48	28	50
2	60	2.6	88	25	100	85	25	104	172	50	50
3	60	2.6	49	14	100	246	71	105	50	14	54
4	60	2.6	203	62	100	92	23	105	50	16	54
5	40	1.4	88	47	100	50	27	416	50	26	54

Note: Weighted means of sediment discharge values listed for stage 1 and 5; maximum axial (Qs) sediment discharge listed for stage 5.

*Footwall input was divided equally between two sources.

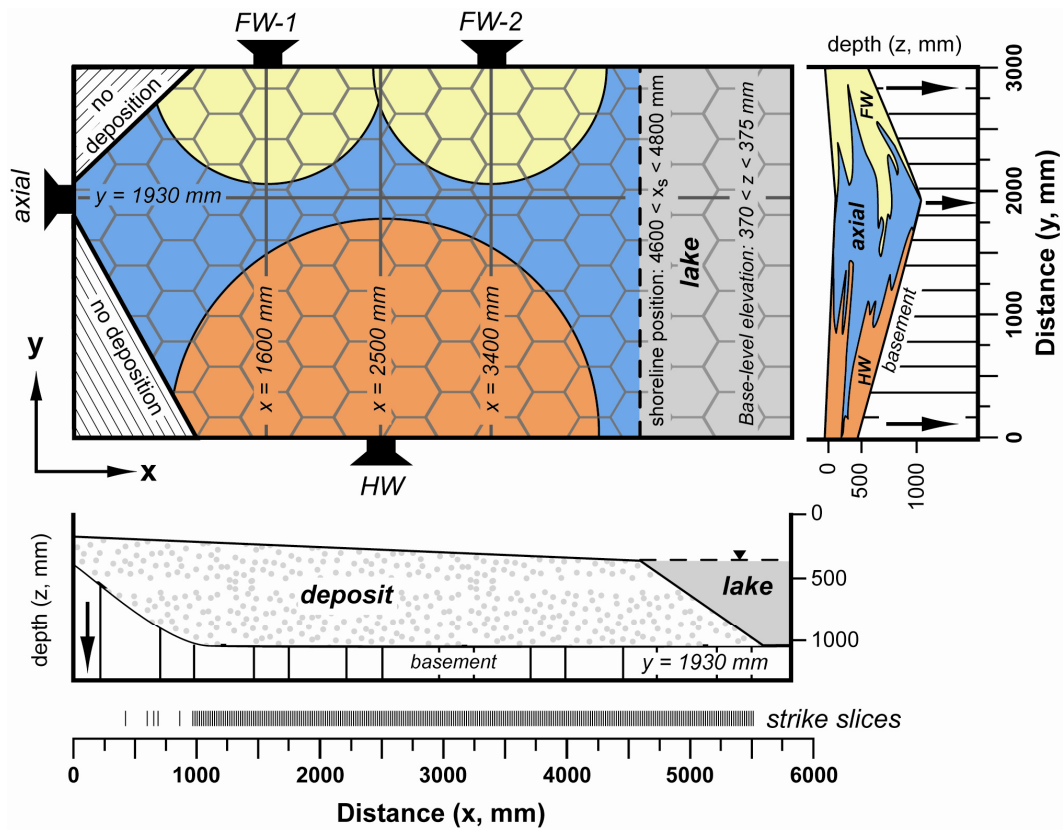


Figure 4.1. Schematic plan-view map and cross sections of the setup for XE06, depicting tank dimensions (and coordinates), sediment input points, and schematic cross sections of the basin subsidence pattern. The four sediment feed points are analogous to the axial, hanging-wall (HW), and two footwall sources (FW-1 and FW-2) in half-graben basins. The honeycomb pattern represents the active subsidence cells that control basin subsidence. The light-gray shading denotes a lake that controls base level. Approximately 4.6 m of the deposit was documented through 465 consecutive strike slices between $x = 870$ mm and $x = 5510$ mm; four additional slices ($x = 420$, 605 , 655 , and 695 mm, black horizontal bar) document the uppermost part of the basin.

Sediment supply was matched to the rate of creation of basin accommodation in order to achieve a nearly constant shoreline position at the lower end of the basin, which terminated in still water analogous to a lake. The volume of sediment delivered into the basin was less than the volume created by subsidence, resulting in an under-filled condition that minimized contact between the delta toe and basin wall at the end of the lake.

Sediment was treated with titanium-dioxide (TiO_2) powder and water was injected with non-toxic blue dye to create semi-opaque water to aid in the mapping of submerged regions (i.e., the active channels). The sediment used in this experiment contained a volumetric mixture of 70 percent, moderately well-sorted, fine-grained, white silica sand, and 30 percent, moderately sorted, medium-grained, crushed anthracite coal (Table 4.2). The bulk density of the deposit at the end of the experiment was 1.487 kg/liter. The specific gravity of the black crushed coal ($sg = 1.3$) is nearly half of the white sand ($sg = 2.65$), making it a reasonable hydraulic surrogate for the finer-grained and more mobile sediment fraction (Paola et al., 2001). The coal-sand mixture also has the benefit of providing high optical contrast that aided in the interpretation of the stratigraphic architecture.

Substitution of 7 percent painted quartz sand grains provided colored tracers that allowed for construction of a source-specific sediment mass balance. Green sand tracers were used in stage 0. In the remaining stages footwall-sourced sediment contained yellow grains; axially sourced sand contained blue grains; and hanging-wall sourced sediment contained red grains.

Table 4.2. Descriptive statistics of sediment size.

Sediment type	Mean $\pm 2\sigma$ (μm)	Median (μm)	Mode (μm)	Sediment size
Coal (PC6)	368 \pm 264	283	262	Medium-grained sand
Sand (F110)	177 \pm 126	137	133	Fine-grained sand
Red sand	184 \pm 75	167	175	Fine-grained sand
Weighted-mean sand	178 \pm 121	137	137	Fine-grained sand

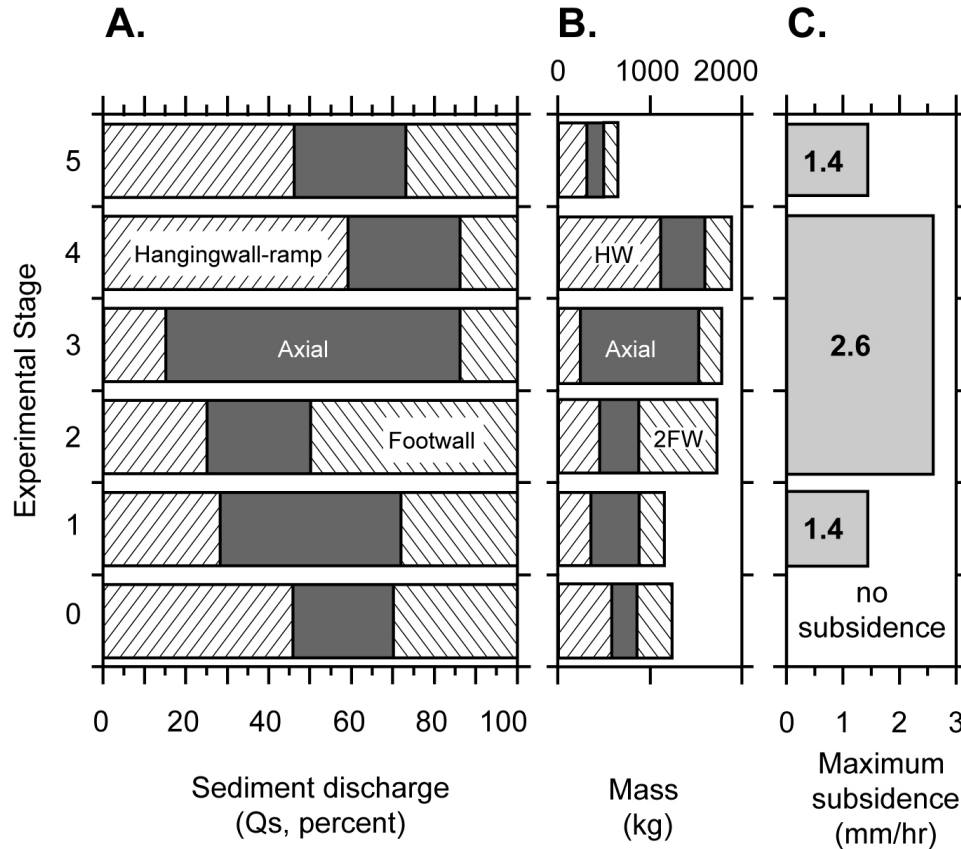


Figure 4.2. Parameters used for XES06 experimental stages. A: volume-normalized sediment discharge for each sediment source (in cumulative percent); B: cumulative sediment mass for each sediment source (2FW is the combined sediment discharge for FW-1 and FW-2); and C: maximum basement subsidence rate, in mm/hr.

An advantage of experimental stratigraphy is that the deposit can be sectioned at sufficiently close spacing to reconstruct a reasonably complete view of the three-dimensional sedimentary architecture. To do this, the deposit was sliced and scanned in the cross-stream direction (relative to the axial drainage) every 1 cm into a series of 465

consecutive parallel faces that were scanned using a telecentric lens system coupled to a digital camera (Mullin and Ellis, 2008). Four additional slices were taken at the up-basin end. These images have a resolution of 5 pixels per square millimeter ($0.04 \text{ mm}^2/\text{pxl}$). Synthetic dip-sections (oriented orthogonally to the strike slices) were interpolated at 1-cm intervals using the scanned strike sections. These images cover about 80 percent of the basin.

Image Analysis

Cross-sectional deposit imagery was digitally acquired in Red-Green-Blue (RGB) color space. RGB colors were not used in mapping the grain composition because the relationships between hue, saturation, and value are not linear and could not be used to adequately isolate the colored sand tracers. Grain-composition maps were created after transforming the original RGB images into $L^*a^*b^*$ color space using Adobe Systems Photoshop™ (CS3 Extended, <http://www.adobe.com>). $L^*a^*b^*$ color space, defined by the Commission Internationale d'Eclairage (CIE), is useful in delineating colors because it is device independent, perceptually uniform, and approximates human vision (Russ, 1995).

The $L^*a^*b^*$ color space is a three-component system, where L^* represents luminosity, and a^* and b^* represent opponent colors. Luminosity (or lightness) is represented by a scale where black is zero and white is 100. The two remaining channels (a^* and b^*) are color opponents that represent magenta versus green (where $a^* < 0$ is green and $a^* > 0$ is magenta) and yellow versus blue (where $b^* < 0$ is blue and $b^* > 0$ is yellow). Because $L^*a^*b^*$ treats luminosity (L^*) as a separate channel, it can easily

distinguish the darker coal from the lighter colored sand. The color opponents were used to differentiate the red, blue, and yellow tracer sands. Green tracer sand was only used in stage 0 and was not analyzed. The images were separated into three, 8-bit grayscale channels, where integer values range between 0 and 255. In this configuration, L^* varies between 0 (for black) and 255 (for white). The origins for both a^* and b^* channels were set to 128, the center of the 8-bit grayscale range of 256 units.

The scanned deposit slices lacked regions containing pure dyed-sand tracers, so reference grain colors were established by calculating image histograms for sample windows (400 pxl wide by 100 pxl high). The mean values of 500 sample windows were measured on five strike slices ($x = 1600, 2500, 3400, 4100, \text{ and } 4500 \text{ mm}$) in regions where the deposit provenance was unambiguous. Reference samples were rejected where the standard deviation varied by more than 20 percent of the mean luminosity, and more than 5 percent in the color opponents. To match the integer values of the grayscale channels, the decimal part of the lower color ranges were truncated to the nearest integer, and the upper color ranges were rounded up to the nearest integer.

Estimating the numbers of sampled grains for a given cross section depends on the resolution of the scanned image and sediment size. Assuming roughly spherical grains, the cross-sectional area is about 0.0246 mm^2 for the sand, and 0.578 mm^2 for the coal. Thus, the cross-section images can resolve 1.61 sand grains per pixel (0.62 pixels per grain), and 0.38 coal grains per pixel (2.66 pxl/grain). The imaged cross section surfaces are relatively smooth and flat; however, grain stacking arrangements and deposit porosity could introduce errors in grain estimation on the image plane. Dried deposit porosity was about 8 percent (see Chapter 3). Assuming a uniform distribution of

colored grains across a given cross section, grains occupying interstitial regions could over-estimate the dyed tracers by about 2 percent.

Stratigraphy

Topographic conditions for the start of XES06 were set during stage 0 in an open basin containing four sources that supplied sediment and water to a shallow lake with a constant base level and no subsidence. Initial conditions were established when fluvial deposits filled the tank to a position near $x = 4200 \text{ mm}$ (Fig. 4.1). This was followed by a series of five experimental stages that were completed under varying subsidence and supply rates (Fig. 4.2 & Table 4.1). Other than the placement of the sediment and water sources, setting the supply rates, and imposing the spatial subsidence pattern, we did nothing to prescribe any particular morphologic pattern on the experiment. The deposits formed fan-shaped masses of sediment that were centered on each sediment input (Fig. 4.3). Downstream of the near-source axial fan zone, the axial drainage system evolved into a broad, low-gradient subcritical axial stream flanked by steeper, radial transverse fans. The axial drainage system and down-basin parts of the hanging-wall and lower footwall fans fed directly into a delta at the lake shore.

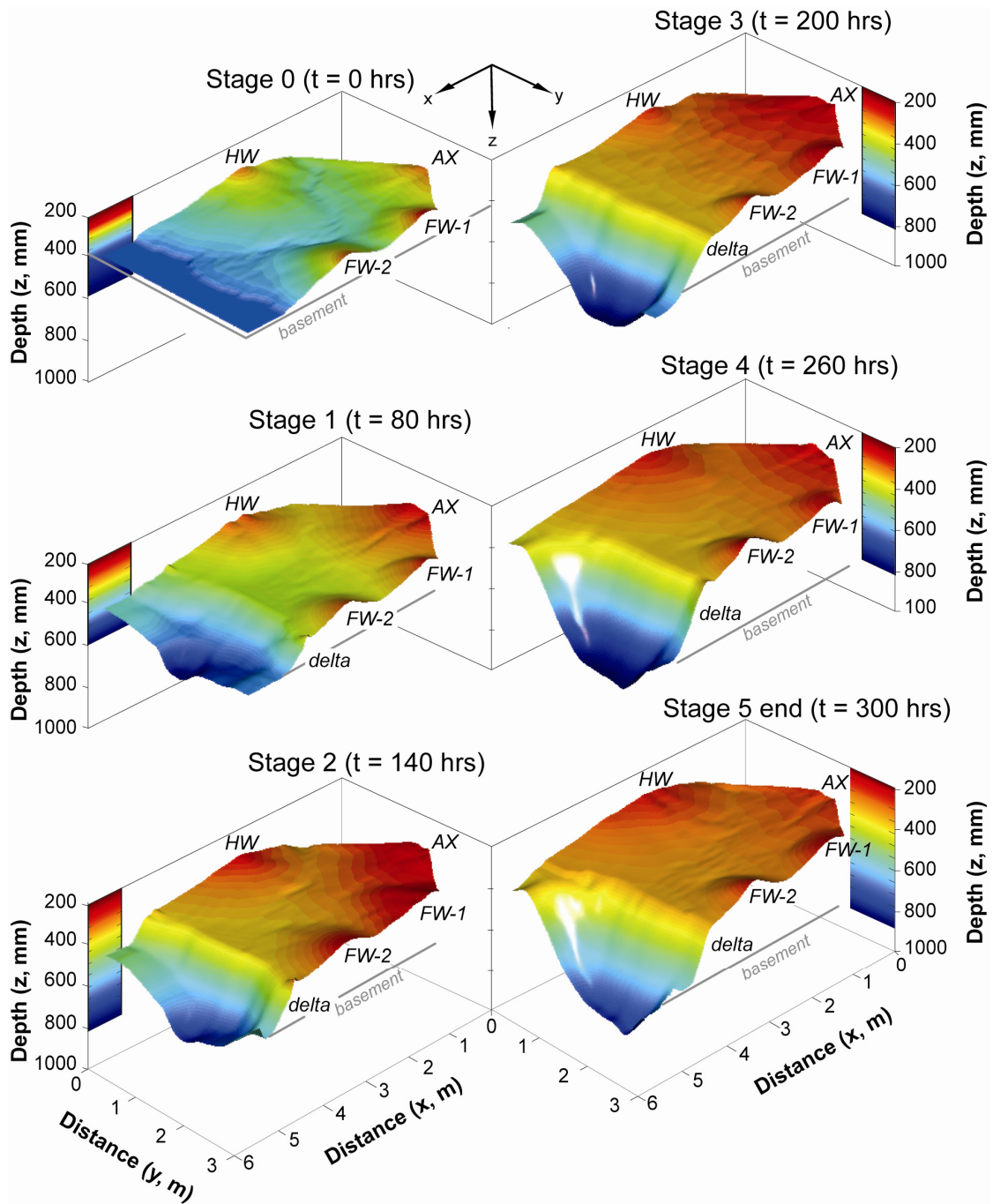


Figure 4.3. Shaded-relief block diagrams illustrating topography and bathymetry of the deposit surface at the beginning of each stage and at the end of the experiment ($t =$ subsidence runtime). Sediment inputs include the axial river (AX), hanging-wall (HW) fan, and the upstream (FW-1) and downstream (FW-2) fans. The downstream end (at the toe of the delta) approximates the maximum depth of the subsiding basement (gray line).

The stratigraphy of XES06 was characterized using a series of cross sections (Figs. 4.4-4.6) and isopach maps (Fig. 4.7). Although the basin can accommodate 1.3 m of sediment, the drainage slopes and base-level position created a deposit that was no more than about 0.7-m thick (Fig. 4.7A). Axial sediments were delineated using bed-form morphology and sediment color (Figs. 4.4 & 4.5). Mapping deposits was very labor-intensive, so a limited number of cross-section slices were used to delineate the axial depositional belt (Fig. 4.6). Four slices were mapped across the tank at the sediment input locations ($x = 1600, 2500, 3400 \text{ mm}$, and $y = 2000 \text{ mm}$). The volume of mapped sediment (between $x = 300$ and $x = 5500 \text{ mm}$) was approximated through numerical integration of twelve additional slices ($x = 650, 1000, 1270, 1400, 1800, 2000, 3000, 4000, 4500, 4750, 5000$, and 5250 mm).

Cross-sectional mapping (see below) showed that experimental-stage boundaries were expressed by mostly continuous, unconformable contacts that were relatively easy to delineate (Fig. 4.4). Unconformities were well expressed towards the hanging-wall side of the tank because the asymmetric subsidence pattern used in the experiments restricted the preservation of sediment along the margins. Delineation of stage boundaries was locally ambiguous within the thickest part of the basin, and stratigraphic discontinuities in part of the footwall succession were not clear for all stage boundaries.

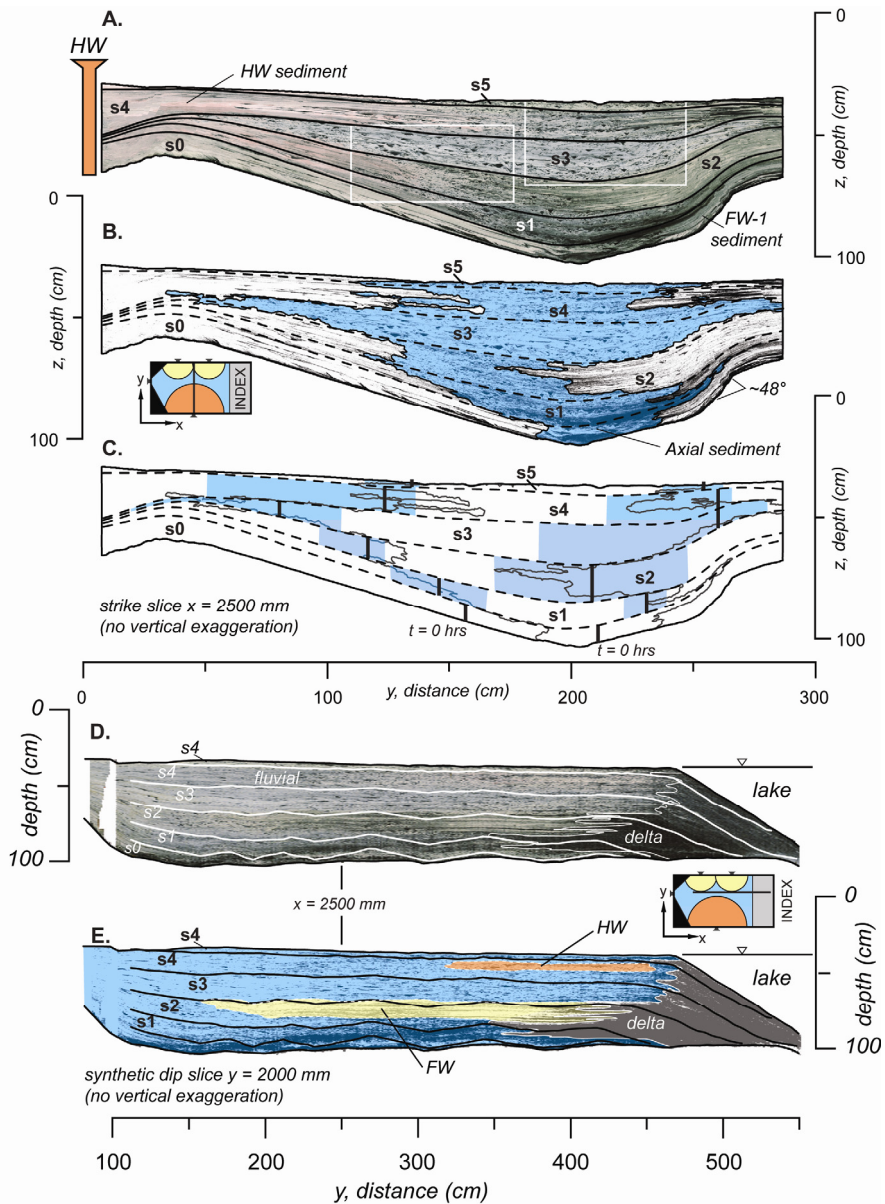


Figure 4.4. Images of strike slice ($x = 2500 \text{ mm}$), synthetic dip slice ($y = 2000 \text{ mm}$), and index map. A: natural-color image of strike section with superimposed stage boundaries (s0-s5). White rectangles denote areas mapped in Figure 4.5. Sediments derived from the hanging-wall input have a pinkish hue; sediments in the axial river have bluish hues; footwall sediments have yellowish hues. B: Interpreted image of mapped edges of axial deposits (light-blue color) over image of coal-bearing sediments. The higher proportion of coal along the footwall side of the tank is due to the position of the cross section between the two footwall fan inputs. C: Outline of axial deposit, illustrating stage boundaries and the (harmonic) mean positions of transverse fans (black vertical line) and minimum and maximum ranges (light-blue shade) derived from overhead imagery (Chapter 3). D: natural-color image of dip section with superimposed stage boundaries. E: Interpreted image of mapped hanging-wall (pink), footwall (yellow), and deltaic sediments (black) over image of coal-bearing sediments.

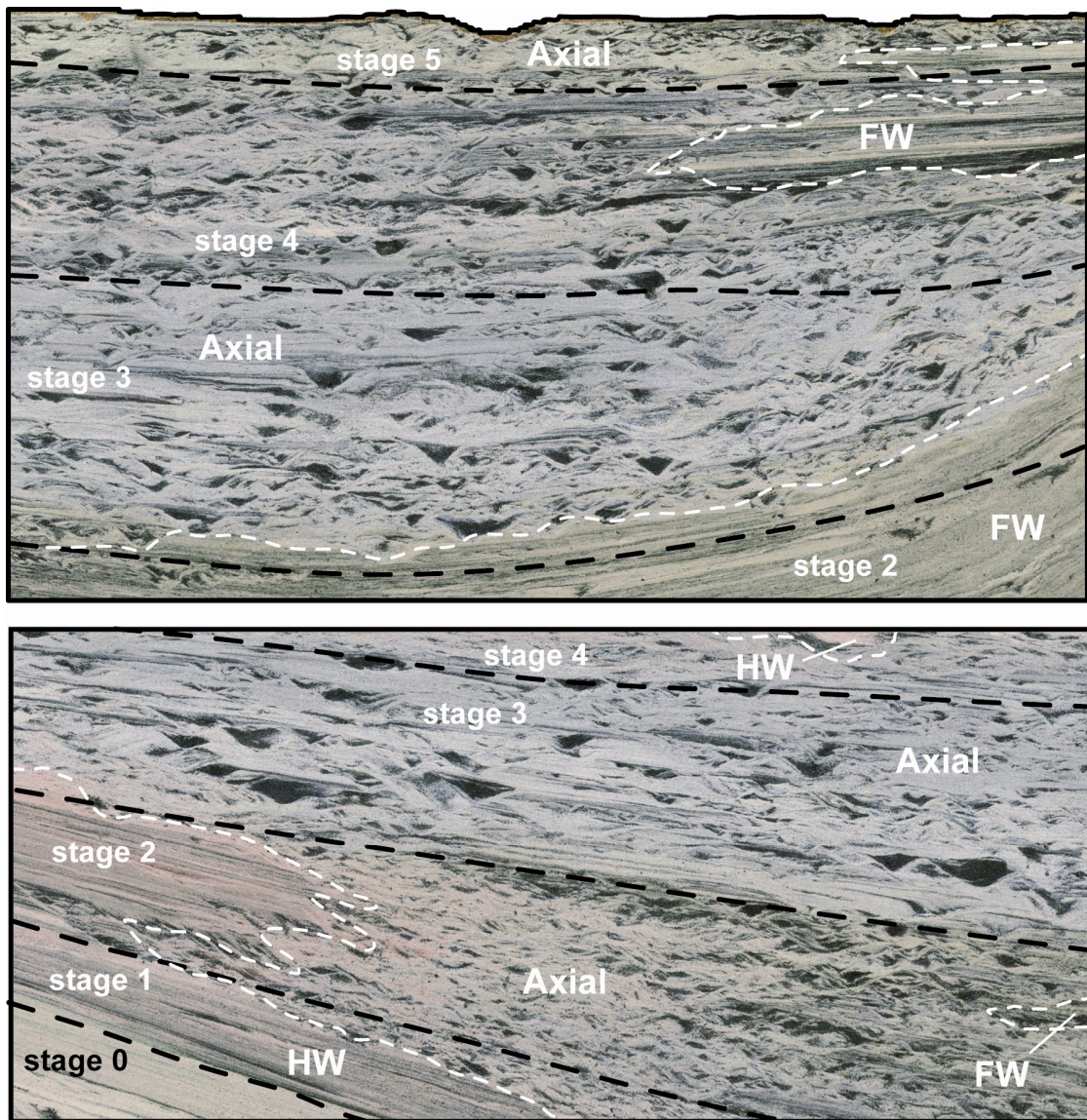


Figure 4.5. Natural-color images of two regions of strike slice $x = 2500 \text{ mm}$ in Figure 4.4, illustrating stage boundaries (black dashed line) and approximate contacts (white dashed line) between hanging-wall (HW), axial, and footwall (FW) deposits. The top image shows the axial-FW boundary. The bottom image spans part of the axial-HW boundary in stages 1 and 2.

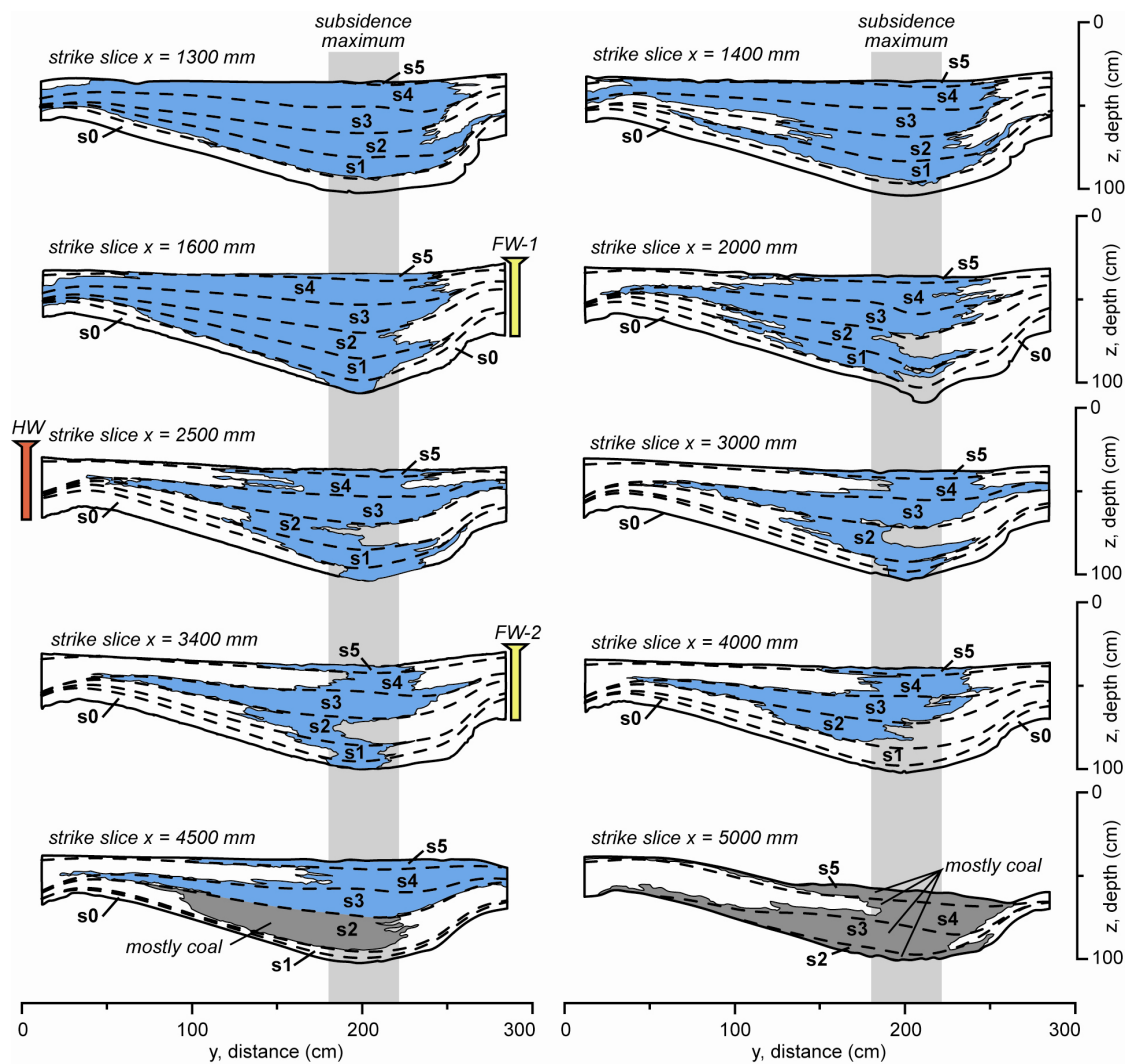


Figure 4.6. Outlines of strike sections down-basin (x -axis), illustrating mapped boundaries of the axial river (blue) during each stage as determined from cross section imagery. Light-gray vertical bars denote the approximate location of the maximum subsidence cell for XES06. The cross-sectional extent of the axial deposits were mapped for 16 slices, 9 of which are shown above ($x = 1300, 1400, 1600, 2000, 3000, 3400, 4000, 4500$ & 5000 mm). Coal sediment (moderate gray shading) dominated the lower two slices ($x = 4500$ and 5000 mm). Stages 0-2 were not present at $x = 5000$ mm.

Differences in bed forms associated with transverse and axial drainage suggest that sedimentary structures would be useful in distinguishing deposits in cross section (see Chapter 3). Mapping the depositional units in cross sections was initially done without the aid of stage-bounding isochrons (see below) so that stratigraphic contacts would not be biased during mapping. Bed forms partly reflect the orientation of the transverse and longitudinal cross-sections relative to the dominant flow direction (Fig. 4.4). Bed forms in the axial and transverse deposits should also differ because of the discharge conditions that prevailed during deposition. Bed forms in the axial channel formed under deeper and more uniform flow, whereas those of the transverse fans formed in shallow channels under less uniform flow conditions (see Chapter 3). Figure 4.4 illustrates examples of deposit mapping for strike and synthetic-dip sections imaged across the basin. Down-dip views of the deposit illustrate an overall increase in fine-grained (coal) sediment and a decrease in the amount of axial sediment at the delta front (Fig. 4.4D-E).

Axial deposits contain blue-dyed sand and are dominated by interleaving lenticular coal-filled channels and dune troughs (Fig. 4.5) that resemble stacked multistoried channel sand bodies recognized in fluvial deposits in the field (e.g., Leeder et al., 1996b). Axial channels are much shallower in stage 2 than in stage 3 (Fig. 4.5) because most of the sediment was delivered through the axial input during stage 3. The shallower axial channels in stage 2 suggest that the axial drainage received less sediment than during stage 3 at $x = 2500 \text{ mm}$. The distribution of axial deposits mapped on cross sections compare favorably to the mean position of the axial river determined from the overhead image sequences (Fig. 4.4B-C). Axial deposits locally contain large volumes

of transverse sediments that obscure axial-sourced sediments (Fig. 4.5), which made interpretation of the depositional belts using only the dyed tracer sand ambiguous.

Bed forms in the transverse deposits developed in shallow channels under non-uniform flow conditions that were punctuated flow-expansion events that left alternating light and dark tabular bands of sediment (Fig. 4.4). The tops of these flow-expansion events commonly contain scattered coal-filled lenses (Fig. 4.5). Transverse deposits were relatively easy to differentiate in cross section because they retained their dyed marker sands. Hanging-wall-sourced sediment was clearly recognizable by a pinkish hue, and yellowish-grains of the footwall had a greenish-yellow hue (Figs. 4.4 & 4.5). The elliptical channel shapes in the transverse deposits were probably caused by the oblique intersection of radial drainages with the strike panels.

Isochrons

In order to examine the spatiotemporal evolution of the basin stratigraphy, it was necessary to develop a temporal framework for deposit correlation. To do this, isochronous surfaces were derived from the basement-migrated topography and interpolated onto the imaged cross-section panels at 5-hour intervals. Isochronous surfaces locally deviated from the programmed subsidence pattern, forming broad arches along the sides of the tank and an undulating trough along the subsidence axis (Figs. 4.1 & 4.4); deviations were most pronounced in stage 4. Causes of these deviations are not clear, but they may be due to unexpected behavior in the gravel-extraction system employed by the XES (see Paola et al., 2001, for an explanation of the subsidence system). The steepest slopes in the basement are about 48 degrees from horizontal (Fig.

4.4A & B) and are close what would be expected from shallowly dipping normal faults in highly extended regions (e.g., Wernicke, 1981). Conjugate normal faults and high-angle reverse faults developed at inflections on the basement surface. These faults only locally obscured important stratigraphic boundaries and did not appreciably hamper mapping of the deposits.

The basement elevation was corrected for these local subsidence deviations by using the actual base of the deposit (as determined from the deposit slices) to adjust the isochrons. The mapped deposit base was used to migrate topography in stage 1. For stages 2 and 3, the hanging-wall ramp ($0 < y < 1930 \text{ mm}$) was corrected by fitting the mapped deposit basement to the subsidence elevation and using those results to migrate deposit-surface topography. Adjustments on the footwall ramp ($1930 < y < 3010 \text{ mm}$) used the monitored subsidence elevations from the manometers. Unreasonable mismatches between deposit-basement and manometer-basement migrated topography remained in stage 4, so isochrons were linearly interpolated between stage 3 and 4 (between runtimes of 200 and 260 hrs, respectively). These interpolated isochrons were reasonably close to the non-interpolated elevations near the deepest part of the basin and toward the footwall margin, but they deviated by more than half of the stage-4 thickness toward the hanging-wall edge. For stage 5, surface topography was migrated using the subsidence-cell manometer data. With the exception of the basin edges in stage 4, visual comparisons of stage bounding isochrons to the deposit slices were reasonably close to the mapped stage boundaries.

Depositional patterns

A useful product of experimental stratigraphic studies is the ability to explore linkages between surface morphology and sedimentary architecture. The stratigraphic architecture of the experimental basin was evaluated using sediment thickness and delineating discrete bodies of sediment in cross section. Sediment isopach maps can also reveal relationships between surface morphology and depositional patterns (Fig. 4.7). If fan morphology plays a large role in deposition, then the shape of the isopach contours should reflect the shapes of the original fans. If either subsidence or fluvial trimming of the transverse fans by axial drainage plays a major role in net deposition, then isopach contours should reflect subsidence or the course of the axial river.

Planimetric maps of mean-stage deposit areas (derived in Chapter 3) were overlain onto isopach maps in order to approximate deposit volumes (Fig. 4.7B-G & Table 4.3). At the end of stage 0, we see a clear correspondence between the mapped fan area and sediment thickness (Fig. 4.7B). This correspondence is not surprising because subsidence played no role in basin deposition during this stage. With the introduction of subsidence, relationships between fan morphology and deposit isopachs become less apparent (Fig. 4.7C-G). During slower subsidence (stages 1 and 5), a slight basinward bowing of the isopach contours for the hanging-wall fan (Fig. 4.7C) suggests that subsidence (or erosion by the axial river) did not strongly modify the morphology of the transverse fans. During faster subsidence (stages 2-4), isopach contours followed the imposed subsidence pattern (Fig. 4.7D-F). During the faster subsidence stages (2-4), the isopach contours generally followed the basin subsidence pattern; however, the expansion of footwall sediment across the subsidence maximum in stage 2 suggests that

footwall-fan morphology had a greater influence on stratigraphic architecture during periods of high transverse sediment discharge. Erosion dominated on the upstream axial fan during stage 5 (Fig. 4.7G) when axial water discharge was the greatest.

Sediment Mass Balance

The ability of the axial river to transport sediment through a basin was examined using a simple geometric sediment mass balance (see Chapter 3). Results (Table 4.3) indicate that the mapped transverse-fan areas were consistently larger than those predicted by the model (Fig. 4.8A). These differences occurred because the model assumes perfect radial fan-forms with no loss of sediment (see Chapter 3). The mapped transverse volumes were consistently lower than the model volume, and the axial volume was consistently higher than the model, having best-fit linear slopes (s_L) near unity (Fig. 4.8A, $0.88 \leq s_L \leq 1.09$, $r^2 = 0.96-0.98$). The eccentric shape of the hanging-wall fan (Fig. 4.7C-G) suggests that the sediment mass-balance model under-estimates its contribution. Comparing normalized sediment discharge (Vq) to the normalized model volume (Vmt) yielded a best-fit line with a slope of 0.83, indicating that the mass-balance model favorably corresponds to sediment discharge (Fig. 4.8B).

Axial volumes increased linearly with increasing sediment discharge at the expense of the transverse fans (Fig. 4.8B & C). These increases in axial-sediment volume were accomplished by toe-cutting of the transverse fans or through direct contribution of tributary sediment into the axial channel (see Chapter 3). This linear relationship between mapped sediment volume and sediment discharge suggests that few

(or no) additional feedbacks would control the size of the axial depositional belt at higher sediment discharges.

The upper part of the axial drainage system is fan-shaped and is not a part of an axial stream (*sensu stricto*). The volume of this persistent fan could bias the results towards larger axial deposit volumes. To minimize the influence of the upstream axial fan, comparisons of mapped sediment volume and sediment discharge for the portion of the basin dominated by an axial (trunk-stream) drainage were made (*Vat**, $2000 < x < 4000$ mm). Axial sediment in the proximal fan moved down-basin; however, the mean axial-deposit slopes did not appreciably decrease between stages 4 and 5 (see Chapter 3). Much of the differences between axial and transverse sediment volumes were removed; however, the axial volume remained the largest depositional component, if only by a few percent (Fig. 4.8D).

Table 4.3. Summary of mapped and model volume.

	Stage 0	Stage 1	Stage 2	Stage 3	Stage 4	Stage 5
<i>Actual volume (liter)</i>						
HW	259	126	146	97	601	107
Axial	427	427	706	952	815	178
FW1	93	46	189	41	53	23
FW2	100	66	290	46	73	30
Isopach total	762	664	1331	1136	1541	337
<i>Model volume (liter)</i>						
HW	395	245	317	169	770	217
Axial	93	186	441	759	542	78
FW1	167	131	295	111	123	54
FW2	133	106	301	99	111	56

Note: Sediment sources include hanging-wall (HW), axial, and upper (FW-1) and lower (FW-2) inputs. Total volume determined from deposit isopachs. Total volume = 5665 liters.

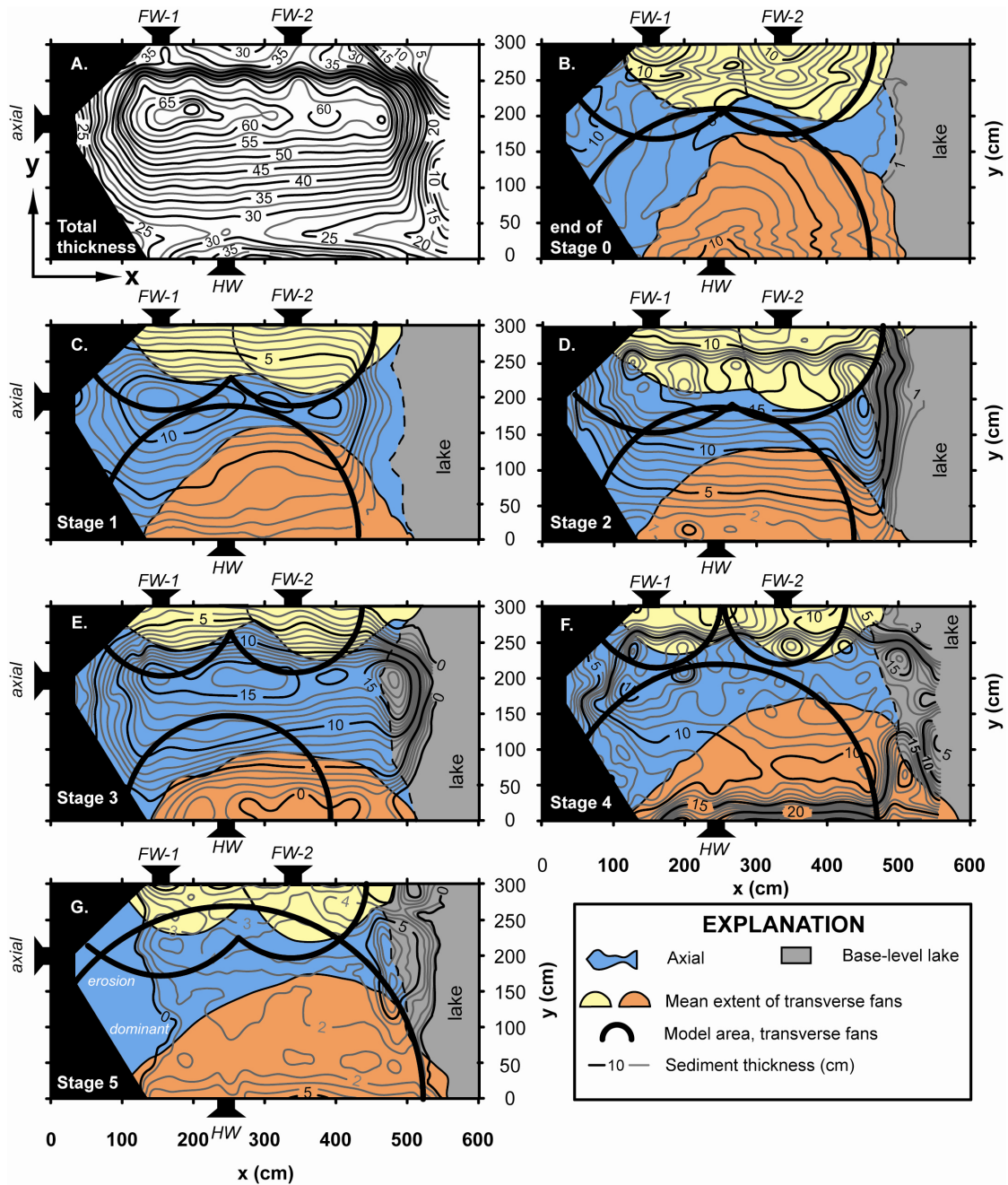


Figure 4.7. Harmonic mean positions of mapped hanging-wall and footwall fans overlain on isopach maps of sediment preserved at the end of each experimental stage. Bold lines denote areas of transverse fans from sediment mass balance. A: Total thickness of the deposit (25-mm contour interval). B: Thickness of deposit at end of initial stage. C-G: Deposit thickness and mean mapped fan boundaries for stages 1-5, respectively (1-cm contour interval).

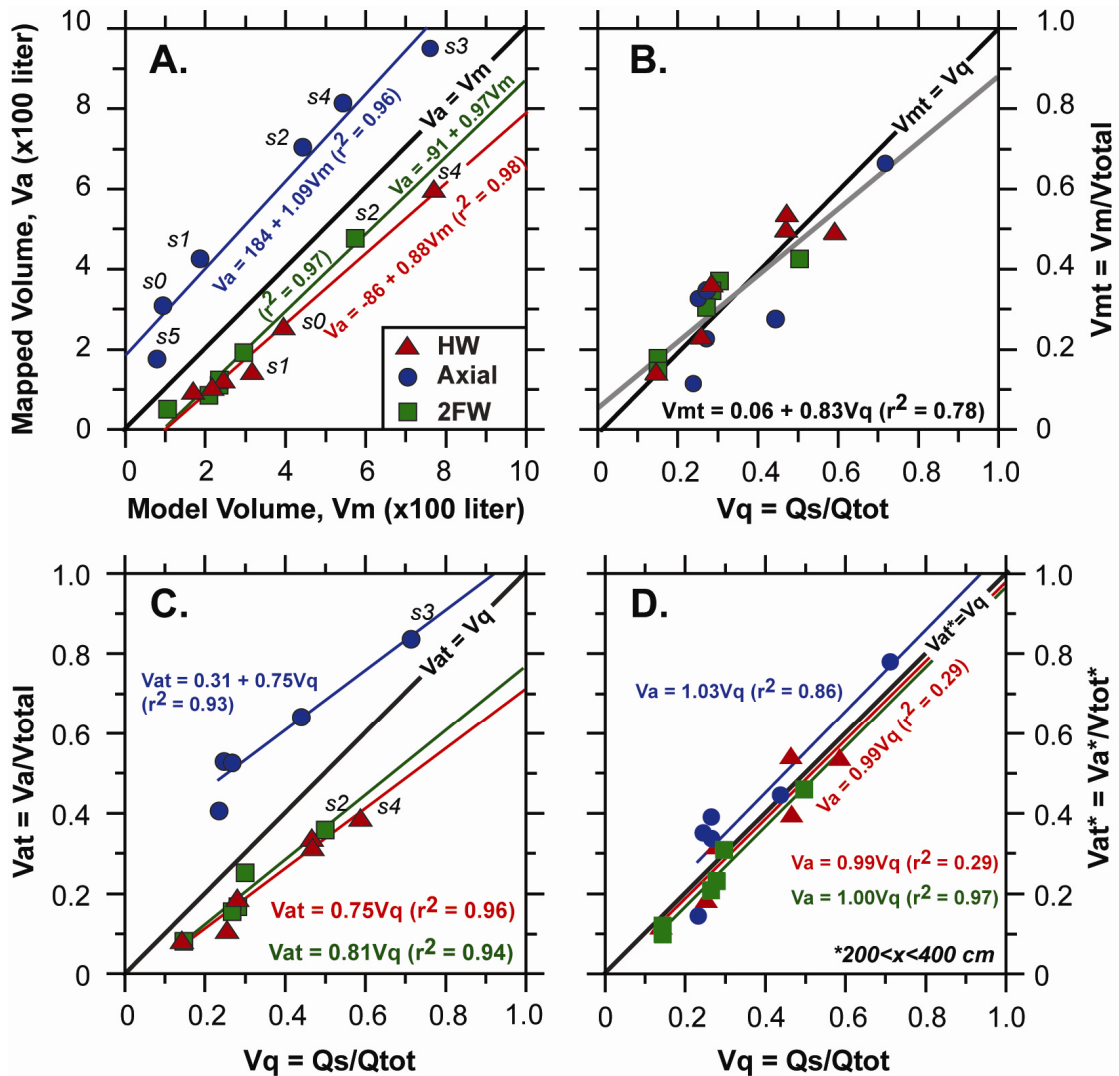


Figure 4.8. Summary plots of sediment volume and sediment discharge. Circles denote axial data, triangles denote hanging-wall (HW), and squares denote both footwall fans (2FW). Observed volume (V_a , mapped) and model volume (V_m) in hectoliters. Approximate sediment volume (V_q) is sediment discharge (Q_s) normalized to total sediment discharge. Linear best-fit curves and regression coefficients (r^2); y-intercepts of the best-fit lines were rounded to zero where less than 0.04. A: Plot of mapped volume (V_a) versus model volume (V_m). B: Model volume (V_{mt}) normalized to model fluvial volumes versus sediment volume (V_q). C: Mapped volume (V_{at}) normalized to mapped fluvial volumes versus sediment volume. D: Dimensionless mapped volume versus sediment volume determined along portion of tank downstream of the axial fan and upstream of the terminal lake ($2000 < x < 4000 \text{ mm}$).

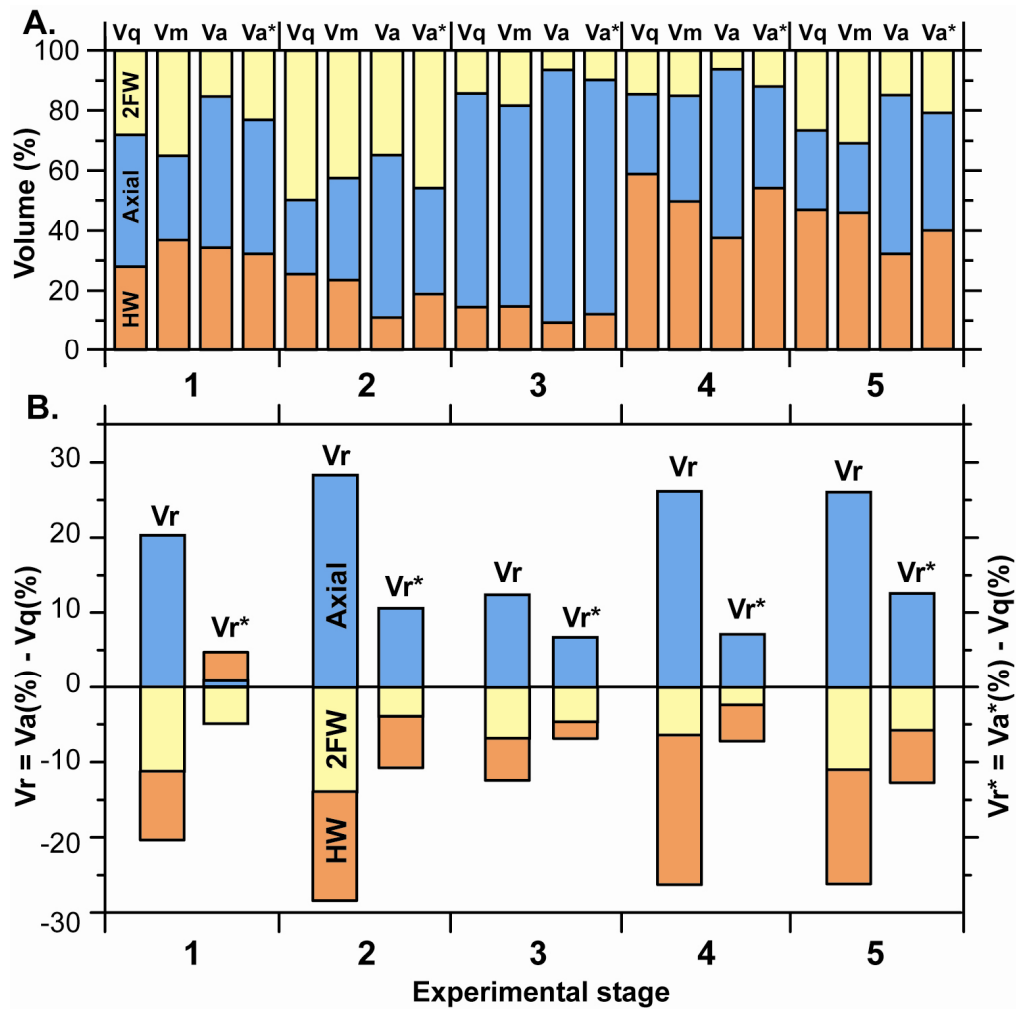


Figure 4.9. Bar graphs illustrating sediment volume and experimental stage. Sediment sources include: axial, hanging-wall (HW), and both footwall (2FW). Sediment volume includes sediment-discharge-derived (Vq), model (Vm), and mapped (Va) values. Asterisk denotes volumes determined from a shorter part of the tank that exhibits axial drainage ($200 < x < 400$ cm). A: Comparison of modeled, mapped, and discharge-derived sediment volume. B: Residual of mapped volume to sediment-discharge volume ($Vr = Va - Vq$). Positive residual values denote increased axial-river volume; negative residuals denote decreased transverse-fan volumes.

Quantifying the amounts of transverse sediment incorporated into the axial drainage system was done by comparing volumes for the entire basin (Vq , Va and Vm) and for the portion of the basin downstream of the axial fan (Va^* , Fig. 4.9A). The mapped deposit volumes generally corresponded to sediment discharge. The volume of axial sediment expanded by 5 percent to almost 30 percent, and was matched by a nearly concomitant decrease in the volume of transverse deposits (Fig. 4.9B). In stages 2 and 4, where the footwall and hanging-wall inputs contributed the largest proportion of basin sediment, transverse fans contributed a larger part of their sediment into the axial drainage system. These differences imply that the composition of the axial sediment records the relative strengths of sediment discharge from tributary drainages.

Intra-stage Variations

In order to better appreciate the formation of the experimental sedimentary succession in XES06, the volume of sediment delivered to the tank was divided into 5-hour intervals using stratigraphically migrated surface topography and areal mapping (Fig. 4.10). To do this, deposit volumes were estimated by superimposing mapped fan boundaries onto isopach maps in 5-hour runtime increments (Fig. 4.10A). Basinwide sediment volume was approximated by numerically integrating 16 mapped deposit slices across the basin (Fig. 4.10C). The evolution of depositional sequences was examined with chronostratigraphic diagrams (Wheeler, 1958) that were constructed by using the isochron data to transform the axial-transverse boundary into time (Fig. 4.11).

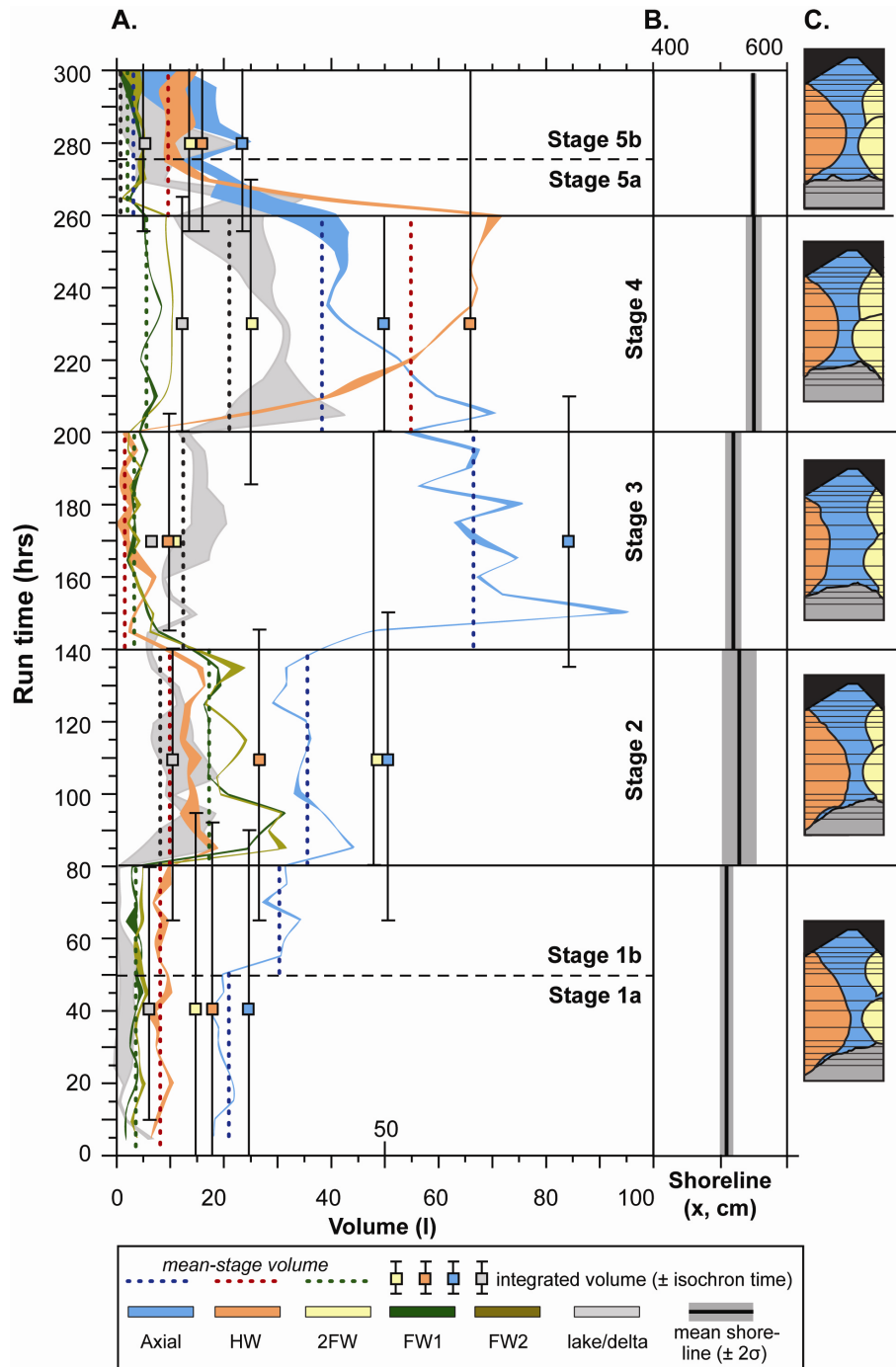


Figure 4.10. Intra-stage variations in sediment volume and shoreline. A: Volume for hanging-wall, axial, both footwall, and delta deposits in 5-hour increments using stratigraphically migrated topography (isochrons) and surface mapping. The lower volume curve is clipped to remove subsequent erosion. Harmonic mean sediment volume (dotted line) determined for each stage and substage. B: Harmonic-mean position of shoreline ($\pm 2\sigma$) of each stage. C: Mean mapped positions of deposits and lake, illustrating 16 cross sections (thin horizontal line) used in numeric integration of deposit volume and grain mapping.

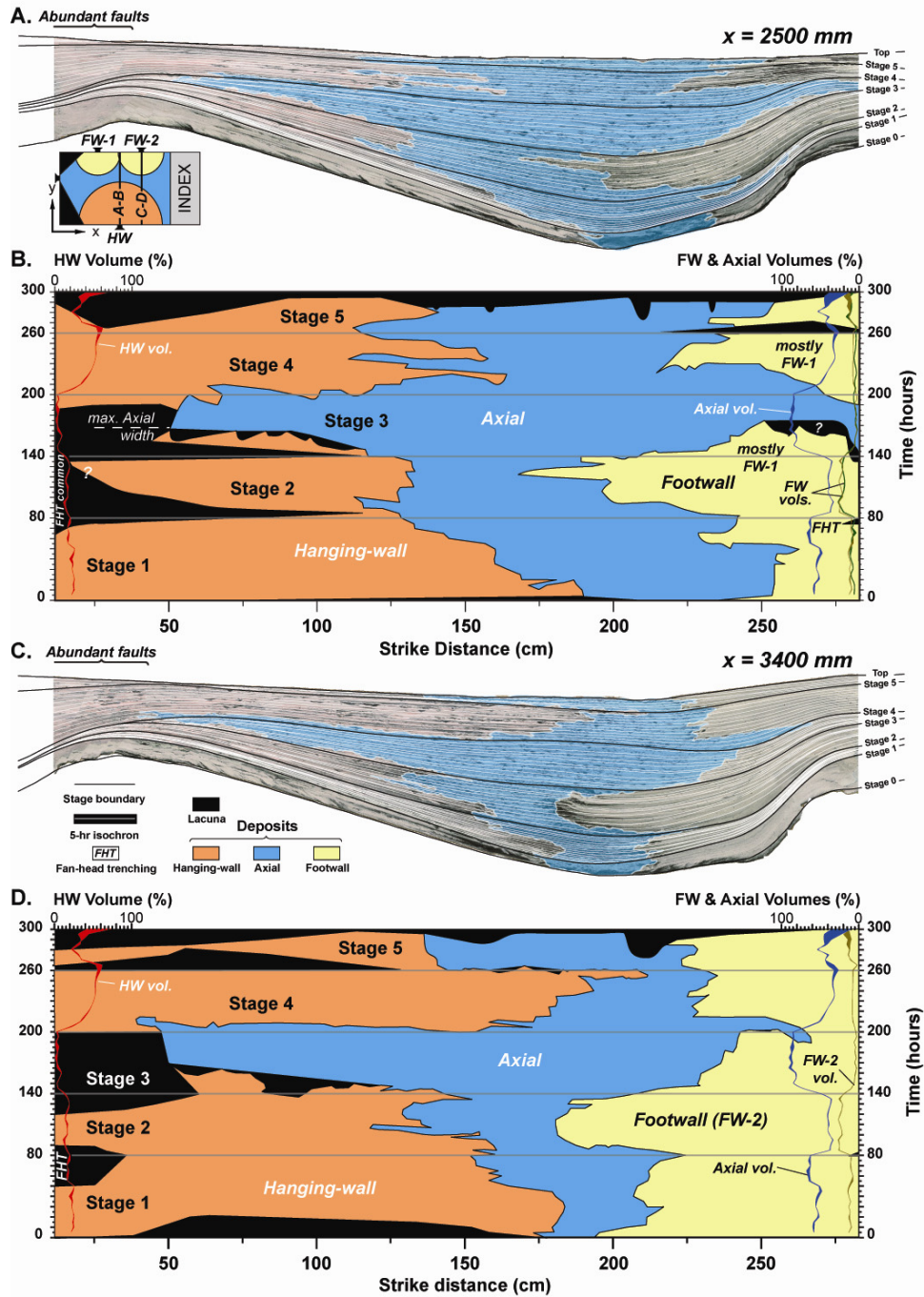


Figure 4.11. Axial-transverse boundaries (A and C) interpreted for two cross sections ($x = 2500$ and $x = 3400 \text{ mm}$, see inset map), and chronostratigraphic diagrams (C and D) derived from 5-hr isochrons, illustrating the development of the hanging-wall (orange), axial (blue), and footwall (yellow) deposits and lacunae (black) through time. The vertical graphs on the sides of the chronostratigraphic diagrams denote deposit volume (in 5-hr intervals), which have been normalized to the total fluvial deposit volume.

The position of the shoreline remained relatively steady, staying between $x = 4500$ and $x = 4890$ mm during most of the experiment (Fig. 4.10B and Fig. 3.6, Chapter 3), so base-level variation did not considerably influence deposition or erosion. The shoreline position, did however, move down basin in the last two experimental stages because the hanging-wall fan advanced into the lake during stage 4 (Fig. 4.7F & G). The maximum thickness of sediment preserved during fast subsidence stages (2-3) was 194 to 261 mm. The maximum thickness of sediment preserved during the slow subsidence stages was 129 mm for stage 1 and 90 mm for stage 5.

Lateral shifts in the deposit boundaries and volumes were relatively rapid (Figs. 4.10 and 4.11), and approached their mean-stage fan-positions within 5 to 15 hours of the start of a new stage (representing 8-25% of the stage duration). Overall, changes in deposit volume immediately followed stage boundaries and approached an average sediment volume within 10 hours of run time (13-17% of stage duration). During stage 1 (slow subsidence), this transition is roughly comparable to 15 to 20 mm of deposit thickness (representing 12-16% of maximum stage thickness). During stages 2 and 3 (fast subsidence), this transition occurred is roughly comparable to a deposit thickness of 30 to 45 mm (11-23% of maximum stage thickness).

Small episodic swings in sediment volume were present in nearly all of the experimental stages and diminished in amplitude as the stages progressed (Fig. 4.10A). These volumetric pulses are the result of autogenic processes, such as fan-lobe switching (Kim and Jerolmack, 2008), that were probably expressed as the interfingering of axial and transverse deposits (Fig. 4.11). There were no obvious trends in the magnitude of interfingering that directly corresponded with changes in deposit volume.

The correspondence between the lateral edges of the axial drainage belt and mapped deposit boundaries indicate that the preserved depositional belts provide reasonably good approximations of sediment discharge and drainage location (Fig. 4.11). With the exception of stage 4, the axial drainage provided the dominant sediment discharge, even when axially-derived sediment was mostly sequestered near the upper end of the basin (Fig. 4.10A). During stage 4, sediment volume derived from the hanging-wall input slowly increased over a period of 20 hours. This slower rate of change in both the axial and hanging-wall deposit volume may be a result of the sediment discharges imposed from stage 3 to 4, where the axial and hanging-wall deposits required more time to adjust to their rather large changes in sediment discharge. The continued expansion of the hanging-wall fan during stage 4 indicates that it responded gradually to changes in sediment discharge. Thus, the slower build up of the hanging-wall fan may reflect a longer response time for this larger fan to migrate about the basin.

The volume of footwall sediment, determined from integrating the mapped cross-sectional slices, was generally greater than the volumes established using the mean-stage isochrons (Fig. 4.10A). This over-estimation of footwall sediment volume mostly resulted from ambiguities in mapping boundaries across stages 2 and 3, where the transition was not obviously erosional everywhere (Fig. 4.11). Thus, without the stage-bounding isochron for reference, interpreting this important (stage-defining) stratigraphic boundary would be ambiguous.

The chronostratigraphic diagrams of Figure 4.11 also highlight important differences in the depositional response of the transverse deposits to changes in sediment

discharge. Stratigraphic lacunae, mostly caused by erosion and including locally deep fan-head trenching at the sediment sources, are more prominent on the hanging-wall side of the basin. The prominent lacuna on the footwall side during stage 3 was created when the axial river encountered the edge of the tank. The shorter and less extensive lacunae in the footwall succession were caused by local erosion by the axial river and fan-head trenching.

Grain Composition

Sediment dispersal patterns were documented through an examination of provenance using dyed tracer sands that were added to the sediment. These colored tracers were distinguished using L*a*b* color space (Fig. 4.12). Mapped sediments include coal and sand, as well as the dyed sand tracers added to the hanging-wall, axial, and footwall sediment supplies. The dyed sediments formed three distinct color-opponent clusters that were mapped using a range of colors that captured grains at the 99% significance level (Table 4.4). Ambiguous colors and the green marker sand in stage 0 were ignored.

Table 4.4. Descriptive statistics of deposit color.

Comp.	No.	L* ± 1σ	a* ± 1σ	b* ± 1σ	L*	a*	b*
Coal	50	45.5 ± 5.3	125.1 ± 0.9	131.1 ± 0.7	<110	--	--
Sand	450	174.1 ± 9.1	129.8 ± 3.5	131.7 ± 2.3	>111	--	--
HW	150	187.1 ± 11.1	139.1 ± 2.3	133.6 ± 1.2	--	>130	--
Axial	150	178.4 ± 13.0	125.9 ± 1.2	125.7 ± 1.6	--	<130	<130
2FW	150	156.7 ± 14.4	124.3 ± 1.6	135.7 ± 1.9	--	<130	>130

Note: Grain equivalents determined using 0.2 mm/pixel (0.04 mm²/pxl) image resolution mean coal and sand grain areas: Coal (11,815); Sand (113,622); tracer sands (37,874 each).

Sand values determined using combined HW, Axial, and 2FW values.

Italics denote upper and lower color ranges used to map grain composition at the 99% confidence level.

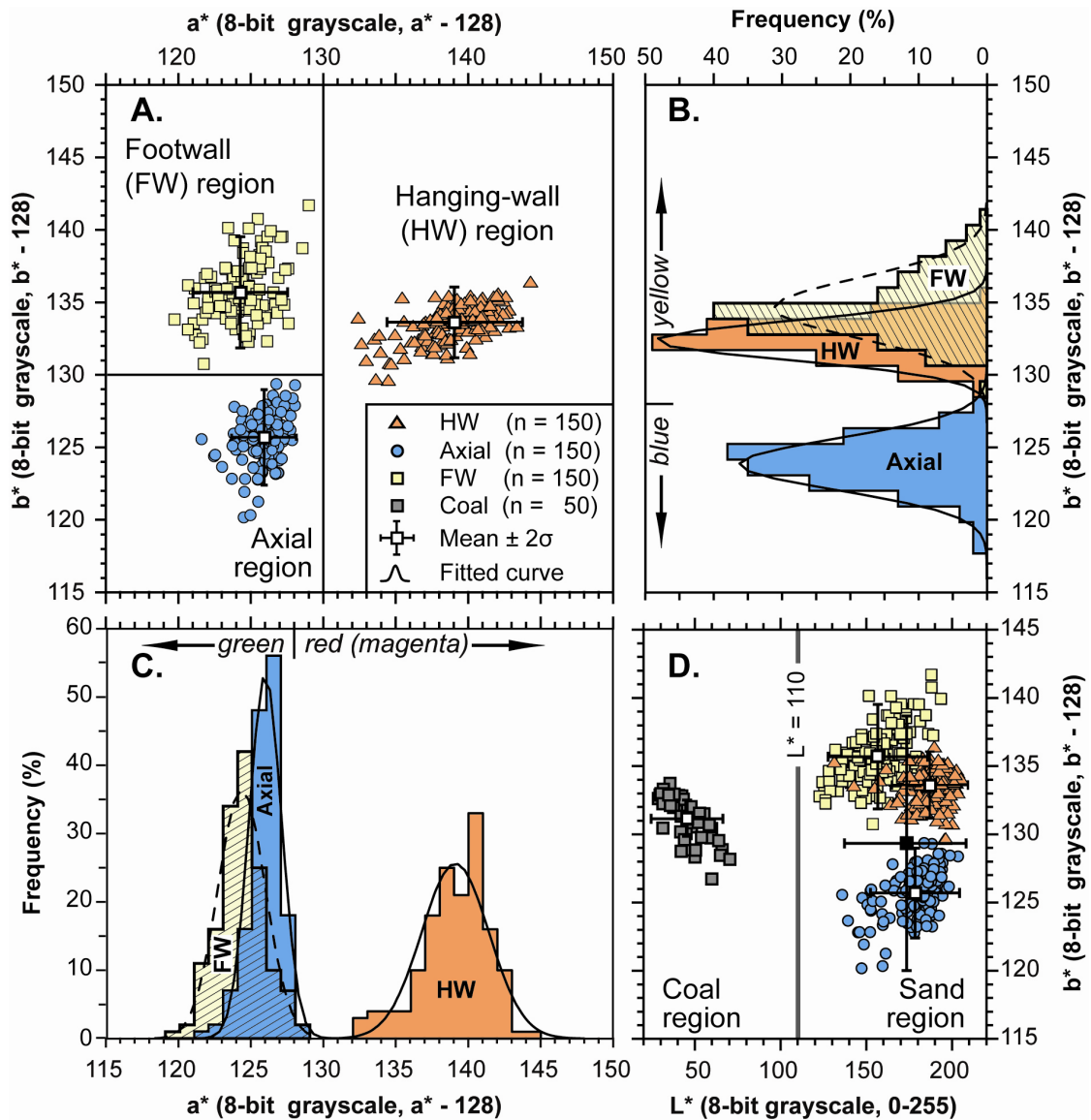


Figure 4.12. Color distribution of coal, sand, and color-coded sand assigned to HW, Axial and FW sources. Color channels are rounded to the nearest integer value. A: Plot of a^* and b^* slice images sampled from regions of unambiguous source area ($n = 150$ colored sand; $n = 50$ coal). White symbol denotes mean of each sample category. The gray boxes denote a^* and b^* ranges used to differentiate deposit sources. B: Histograms and fitted curves of the b^* color component. C: Histograms and fitted curves of the a^* color component. D: Plot of luminosity (L^*) and b^* color components, including the coal/sand cutoff value at $L^* = 110$ (vertical gray line) at the midline between the means of all colored sand ($n = 450$) and coal ($n = 50$).

A computerized algorithm was implemented to determine grain compositions for broadly-defined color ranges across a portion of the basin ($1600 < x < 3400 \text{ mm}$, Table 4.4). The luminosity (L^*) channel was used to distinguish coal from sand. Channel a^* was used to differentiate the pinkish hanging-wall (HW) sourced grains from the axial and footwall (FW) grains. Channel b^* was used to differentiate the blue-colored axial deposits from the transverse deposits.

Grain-selection results compared favorably to the original cross-section imagery and mapped axial belts (Fig. 4.13-4.16) and to the volume of sediment supplied to the tank (Fig. 4.17). Sand is dominant in the fluvial portion of the experimental basin, indicating that the axial drainage system is effective in transporting finer grained material through the basin and to the delta (Fig. 4.16).

Grain-color mapping overestimated the sand by about 136 percent relative to the original source (70%) and underestimated the coal by 15% relative to the original coal source (30%). Grain mapping also included about 2.5 to 3.7 more tracer-grains measured than in the original sediment supply (HW = 2.5; Axial = 3.7; and 2FW = 2.8). These discrepancies may be the result of processing artifacts or the grain-selection criteria. Although the pixel resolution is 40-60% of a single grain, the smoothing used in the compressed-image (JPEG) format may have led to a slight over-count of colored grains. Deposit porosity of 8 percent may also have led to an over-count of colored grains. It is likely that the overestimate resulted from the inclusion of similar-colored grains in the grain-selection algorithm.

Visual comparisons of the calculated colors with the natural color images did not show any noticeable discrepancies with the deposit mapping (Figs. 4.13-4.16).

Furthermore, reductions in the grain-selection thresholds for the color-selection algorithm did not appreciably change the relative proportions of selected grains. Thus, the grain-color maps are considered to represent reasonable estimates of grain distributions in the basin.

Axially sourced sediments clearly dominated the axial depositional belt in the upstream part of the basin (Fig. 4.16). The delta is recognized by an abrupt increase in coal near the shoreline (Fig. 4.17). The axial drainage contained bed forms indicating longitudinal flow (see Chapter 3), even though this axially transported sediment was derived almost entirely from transverse sources (Fig. 4.4E). Little axially-sourced sediment made it to the delta front, except during times of high axial sediment discharge (Figs. 4.16 & 4.17). The down-dip distribution of axial sediments roughly corresponds to the magnitude of axial-sediment discharge (Fig. 4.17). Footwall-derived sediment dominated stage 5, where the axial water discharge was greatest, but sediment discharge was rather low. This increase in footwall sediment may be the result of reworking of sediment in the upper footwall fan.

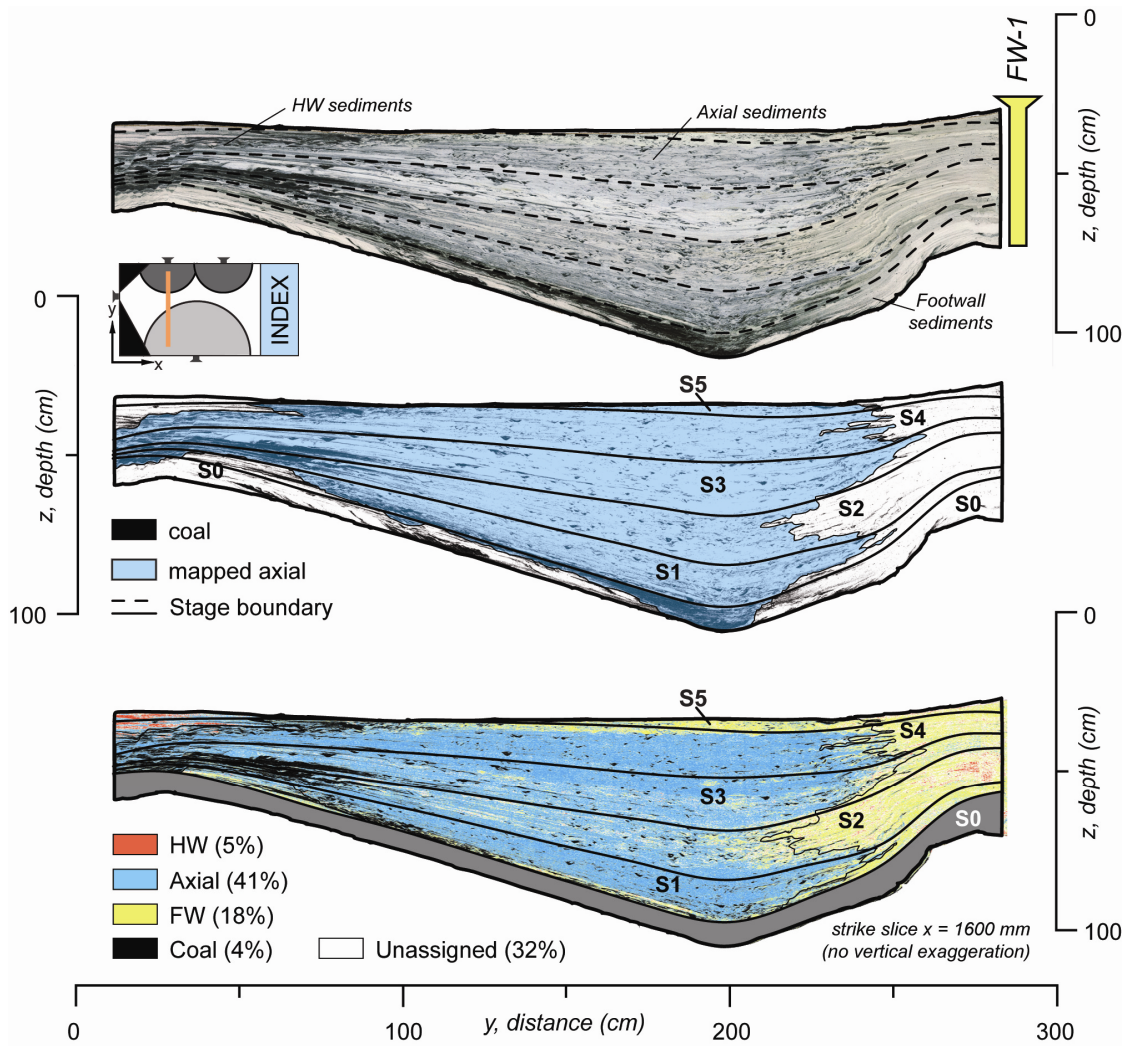


Figure 4.13. Images of strike section at $x = 1600 \text{ mm}$, illustrating stage boundaries, mapped axial deposits, and grain maps. Inset map denotes location of cross section. Top: natural-color image of deposit. Middle: interpreted image illustrating extent of mapped axial deposits and coal. Bottom: sediment composition, except for stage 0 (shown as dark-gray mask).

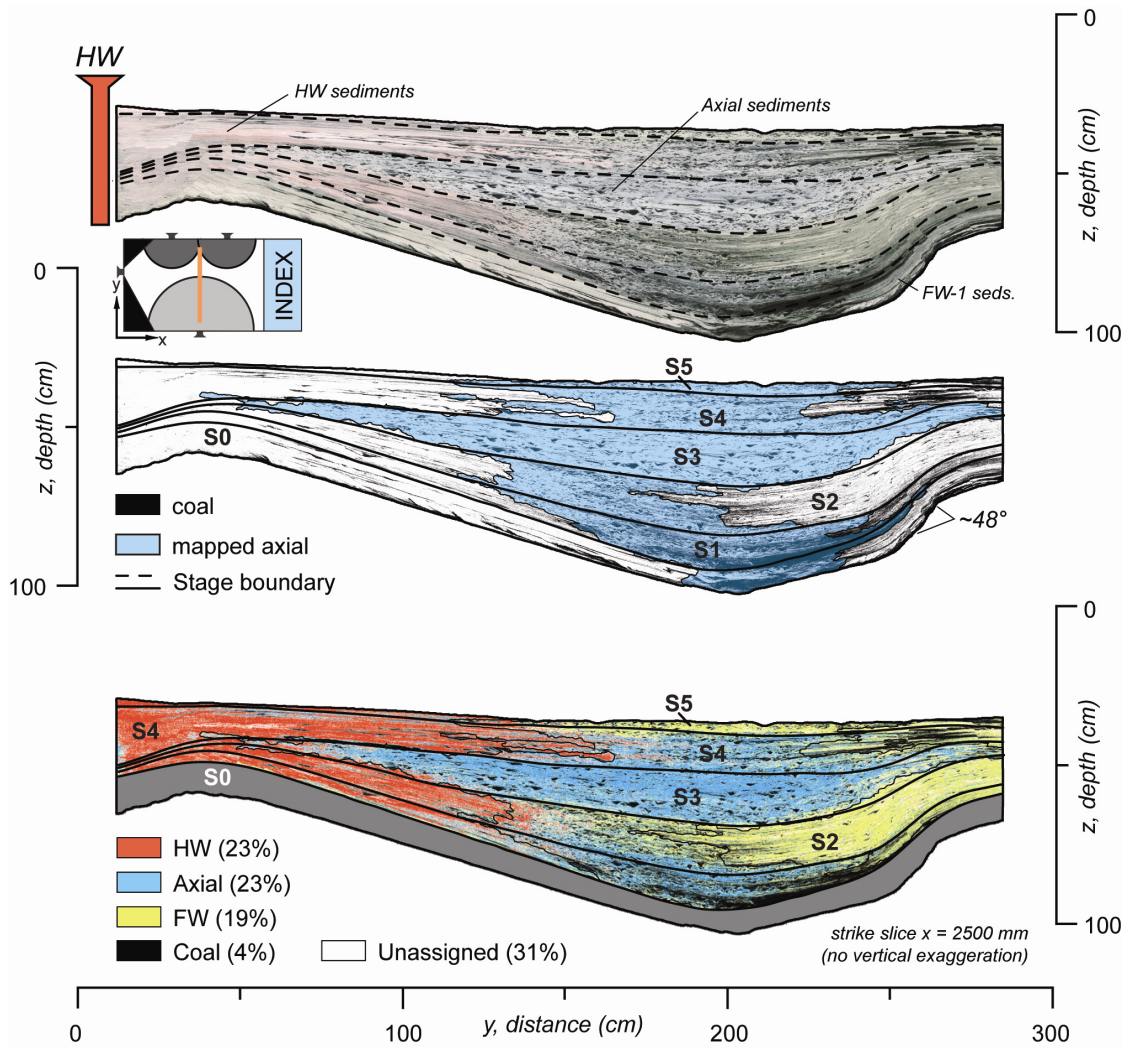


Figure 4.14. Images of strike section at $x = 2500 \text{ mm}$, illustrating stage boundaries, mapped axial deposits, and grain maps. Inset map denotes location of cross section. Top: natural-color image of deposit. Middle: interpreted image illustrating extent of mapped axial deposits and coal. Bottom: sediment composition, except for stage 0 (shown as dark-gray mask).

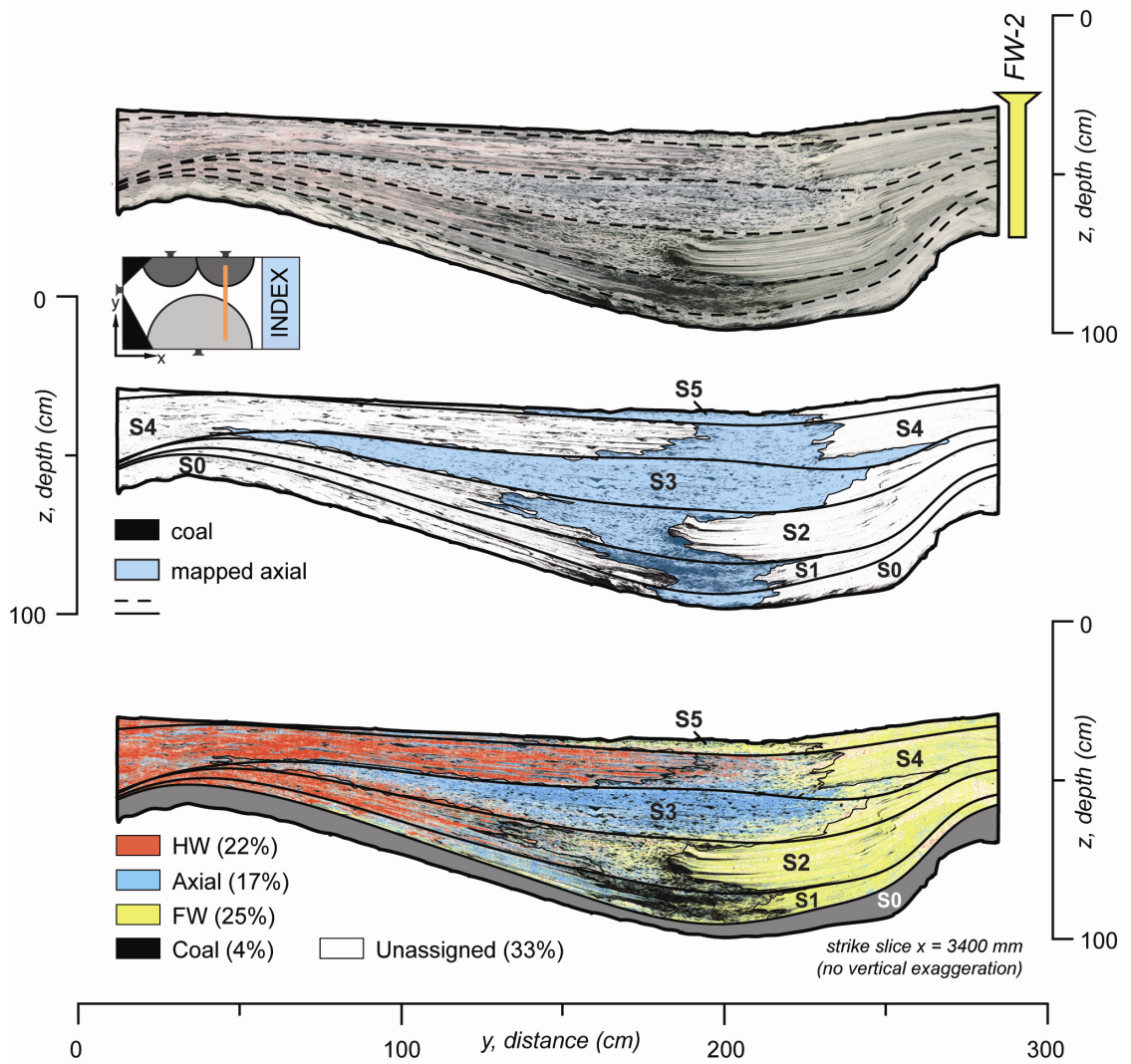


Figure 4.15. Images of strike section at $x = 3400 \text{ mm}$, illustrating stage boundaries, mapped axial deposits, and grain maps. Inset map denotes location of cross section. Top: natural-color image of deposit. Middle: interpreted image illustrating extent of mapped axial deposits and coal. Bottom: sediment composition, except for stage 0 (shown as dark-gray mask).

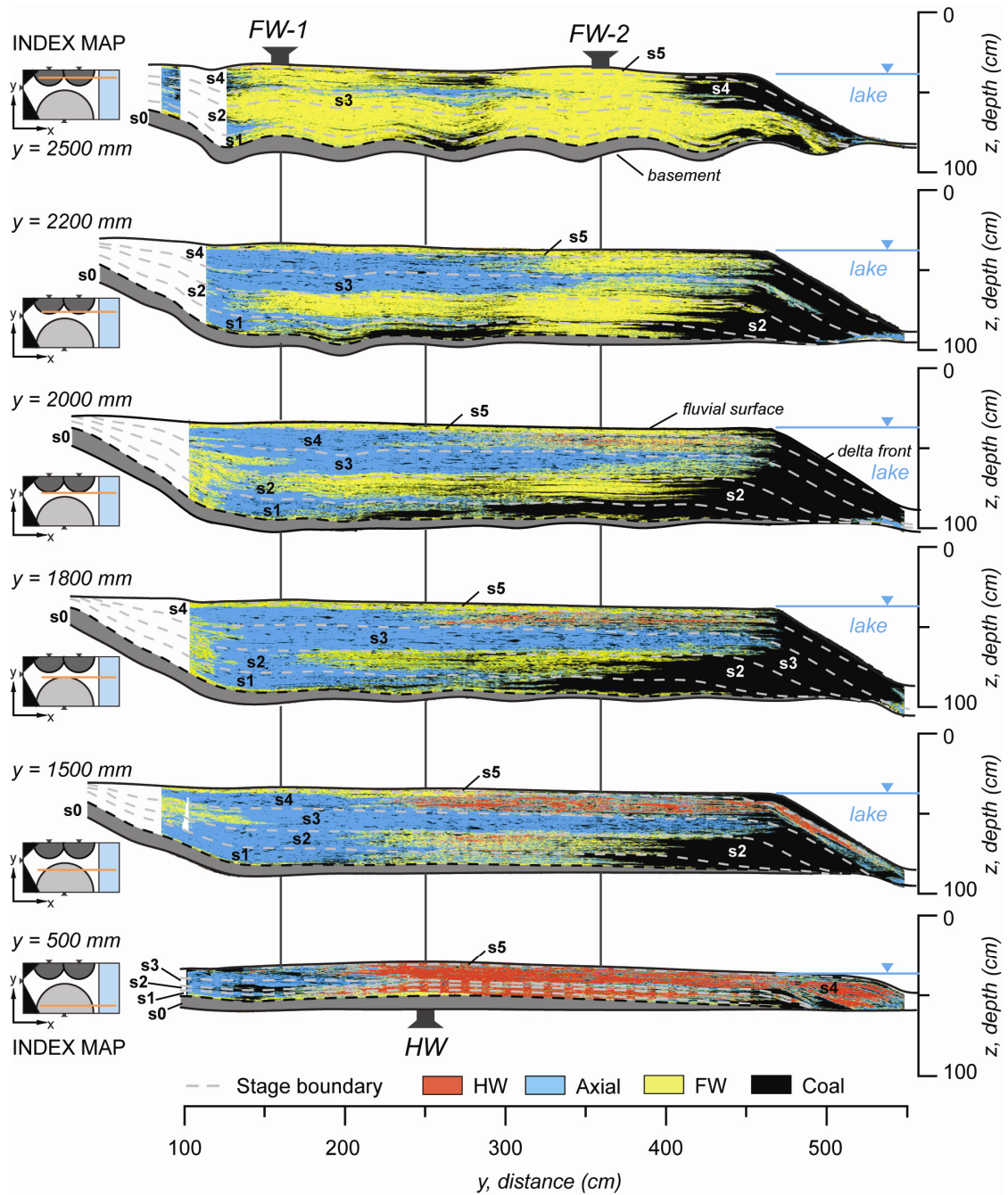


Figure 4.16. Color-enhanced images illustrating the sediment composition of 6 synthetic dip sections between $y = 500$ mm and $y = 2500$ mm showing stage boundaries, coal and sand composition. Index maps (to left) depict the locations of the synthetic dip sections.

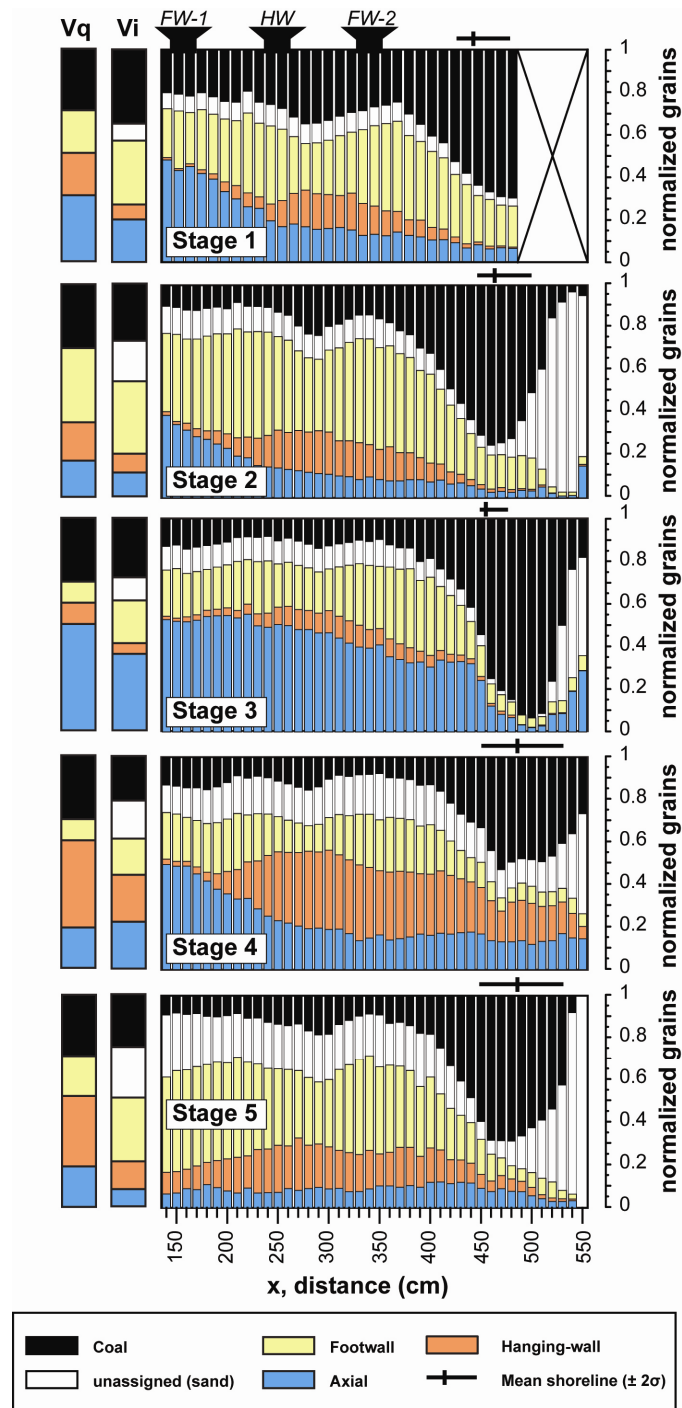


Figure 4.17. Stacked column plot of mapped coal, sand and colored sand determined from automated grain-color mapping for strike slices. The harmonic mean position of the shoreline ($\pm 2\sigma$) is also shown. Sediment-discharge-normalized volume (Vq) and slice-integrated volume (Vi) are shown by stacked columns on left-side of the figure.

Sediment mixing was examined by isolating grains in the mapped axial deposits in the above-mentioned sixteen cross sections (Figs. 4.6 & 4.18). The proportions of colored tracer sand were normalized to the total number of grains in the mapped axial-deposit in order to illustrate the down-basin variations in grain abundance (Fig. 4.18A). The basin length (L) was set to the mean shoreline position (L_o); deltaic deposition dominated where L/L_o exceeds unity. These data demonstrate a progressive downstream decrease in axial-grain abundance (Fig. 4.18B). Footwall sediment declined slightly down basin, whereas hanging-wall sediment was essentially invariant. Only under conditions of high axial-sediment discharge (71% of the total sediment discharge in stage 3) did axially-sourced sediment move through the basin. Continued delivery of axial sediment to the shoreline in stage 4 suggests that the basin may not have completely adjusted to the imposed conditions, which is supported by the reduction in hanging-wall fan areas throughout most of this stage. During stage 3, about 21 percent of the sediment in the axial depositional belt was axially sourced at the shoreline. These sediment-source trends suggest the presence of a threshold that limited the ability of the axial drainage to transport axially sourced sediment entirely through the basin.

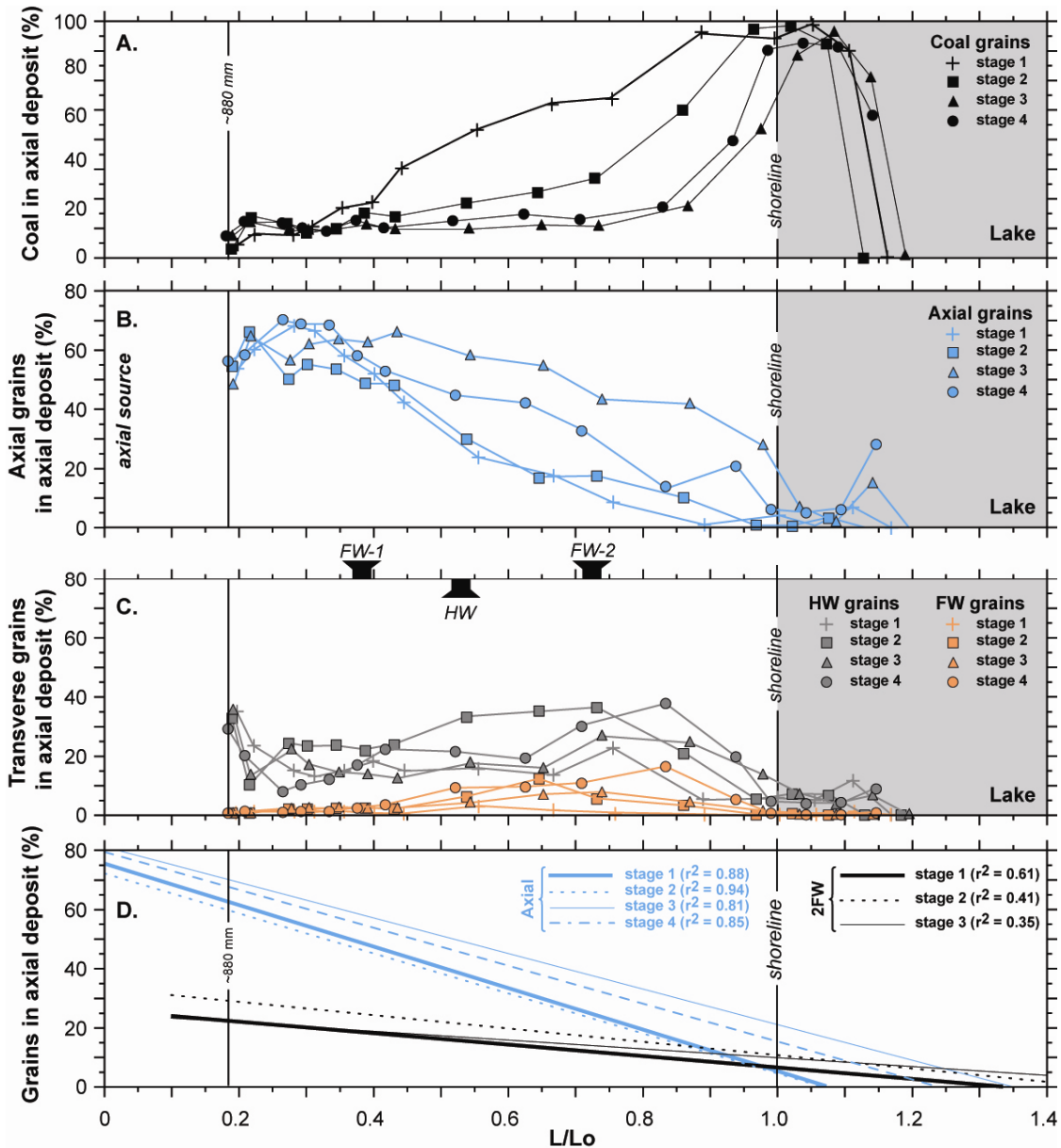


Figure 4.18. Axial- and transverse-sourced sediment normalized to total number of assigned grains in axial deposits mapped in 16 cross sections; unassigned sand grains are not shown. The down-basin distance (x -axis) is normalized to the mean shoreline position for stages 1-4, where deltaic environments dominate where $L/L_o > 1$ (shaded gray). A: Proportion of coal in mapped axial deposits. B: Proportion of axial marker grains in axial deposits. C: Proportion of hanging-wall (HW) and footwall (FW) marker grains in axial deposits. D: Best-fit lines for data points in B-C having regression coefficients (r^2) greater than 30%.

Discussion

The emergence of axially aligned drainage depended on the presence of the transverse fans, without which only an axial fan would form in the upper region of the experimental basin (see also Chapter 3). Thus, the boundaries between the axial and transverse depositional systems form important elements of self-organization in XES06. The key dynamical element in setting this boundary is the exclusively one-way transfer of sediment from the transverse to axial systems (Figs. 4.8 & 4.16). The axial drainage obtained additional sediment from the transverse fans through toe cutting. In natural systems, toe cutting is very effective at liberating piedmont sediment stored in the distal parts of the flanking transverse fans (e.g., Leeder and Mack, 2001).

The expansion of axial-sediment volume in XES06 was matched by a nearly concomitant decrease in the volume of transverse deposits (e.g., Fig. 4.9), and the volume of sediment delivered compared favorably to the mean areas of the mapped fluvial surfaces (see Chapter 3). These observations suggest a reasonable correspondence between sediment discharge and deposit size. The systematic increase of the axial-deposit volume with increasing sediment discharge implies that no other major feedbacks are present among these depositional belts (Fig. 4.8C). The relative consistency in the fraction of transverse fan sediment extracted by the axial drainage system indicates that the axial-transverse boundary remained steady over a wide range of tested sediment discharges. This consistency resembles the large-scale autogenic processes observed in the boundaries that define the morphology and stratigraphy of fluviodeltaic systems (Paola et al., 1992; and Swenson et al., 2000). The axial-transverse boundary in XES06 may be comparable to the fluviodeltaic boundary in coastal settings,

where the distal toes of the transverse fans become modified by down-basin axial transport analogous to longshore drift at the coastline. Without the imposition of this boundary, the axial drainage would resemble the transverse fans.

Much of the axially-sourced sediment remained in the upstream region (Figs. 4.17 & 4.18) until (axial-sediment) discharge increased to a level where it dominated sedimentation in the basin. Therefore, in natural systems, a lack of axially-sourced sediment in the axial drainage course may not require a lack of upstream drainage integration, but could be a result of preferential upstream sequestration of axial sediment. A threshold may be present in the experimental basin where axially sourced sediment is preferentially stored up-basin until the axial-sediment discharge exceeds a certain level (more than 44% or at least 71% in the experimental cases, Table 4.1).

The shifting of the axial channel in response to changing subsidence is an expected outcome of most basin sedimentation models (e.g., Smith et al., 2001); however, the location of the axial depositional belt in XES06 was not apparently sensitive to the location of the lateral subsidence maximum (e.g., Figs. 4.6 & 4.7). The position of the axial-river belt was instead mostly determined by the relative strengths of the tributary sediment inputs (see Chapter 3). This “flux steering” of the axial drainage by the tributary fans may have been enhanced by the imposed asymmetrical subsidence pattern. Sediment accumulation was matched to subsidence, so any localized increase in sediment delivery would be amplified as subsidence rates decreased towards the analogous piedmont margins.

If the location of the axial-river belt is mostly determined by piedmont sediment fluxes, then shifting of the axial belt would require alternating sediment discharge from

the hanging-wall and footwall systems. Syneruptive volcanoclastic fluxes, such as those from volcanic centers in continental rift settings (e.g., the Puyé Formation of New Mexico) may substantially increase the sizes of tributary fans (e.g., Waresback and Turbeville, 1990), and thus influence the position of the axial drainage.

Climatically induced changes in sediment and water delivery into the basin should be manifested regionally. Drainages on the hanging-wall are typically much larger than on the footwall (e.g., Leeder and Jackson, 1993; and Gawthorpe and Leeder, 2000), so climatically induced changes in sediment discharge may be amplified through the larger hanging-wall drainage systems. Expansion of hinterland drainage area through stream capture could enhance discharge from tributary catchments on either side of the basin (e.g., Fraser and DeCelles, 1992). Erosion, resulting in the unroofing of older and presumably less permeable rocks, would also alter catchment hydrology and sediment delivery in a tributary catchment. In slowly subsiding basins, sedimentation may overwhelm subsidence to a level where differences in tributary drainage could exert larger influences on the position of the axial drainage.

A field-based example of possible flux steering is in the Albuquerque Basin of New Mexico (see Chapter 2). For much of Pliocene time, the axial river remained near the basin master fault system. After 1.8 Ma, the axial river began migrating up-dip onto a recently abandoned depositional surface that formed by large hanging-wall tributaries (Ceja Fm), as tributary fans on the opposing (eastern) piedmont (Sierra Ladrones Fm) prograded basinward from the footwall uplift. It is not entirely clear whether the movement of the axial-footwall facies boundary was driven entirely by a decrease in basin subsidence or by an increase in sediment delivery (or both), but without a large

hanging-wall sediment source to the west, the axial river was no longer constrained to flow along the eastern structural margin of the basin.

The subsidence pattern used the experimental basin simulated a faulted footwall boundary that was shallower than typical of most half-graben basins (*cf.* Wernicke, 1981; and Mack and Seager, 1990). Although the basin geometry may resemble that associated with low-angle faults in highly extended terrains, it is the asymmetry of the basement that is important to consider in understanding the transverse-fan responses. The total sediment discharge in the basin was steady (relative to subsidence), thus the deeper basin volume along the analogous footwall (faulted) margin would be compensated by higher sediment supply rates for the footwall fans. The slopes of these fans may decline slightly, but their higher sediment-water ratios would maintain steeper depositional slopes.

Major stratigraphic boundaries may locally be difficult to delineate in the footwall succession (Fig. 4.11), especially in the case of the retreat of the footwall fan between stages 2 and 3 in XES06. The lack of obvious, basinwide stratigraphic discontinuities in the footwall succession indicates that important and widespread stratigraphic boundaries may not be well recorded in the area between the basin depocenter and the structural margin at the footwall. Failure to delineate such stratigraphic boundaries in the field would result in overestimation of the sediment volume delivered to the basin over a given time interval. Thus, deposits on the distal hanging-wall ramp of half-graben basins in the field may provide a better record of stratigraphically important unconformities in the basin-fill succession (see Chapter 2).

Geologic cross sections across the Albuquerque, Socorro and Palomas Basins, and the Hueco Bolson in the Rio Grande rift in New Mexico (Fig. 4.19) delineate major depositional belts associated with the axial river (ancestral Rio Grande) and tributary (transverse) fans that support experimental observations. Deposits on the distal hanging-wall ramp (analogous to the HW deposits in XES06) are the dominant basin-fill component in many of the Rio Grande basins in New Mexico. Differences in the thickness of basin fill among these cross sections are attributed to basin subsidence rate and the duration of occupancy by the axial river. Deposits of the ancestral Rio Grande are thicker in the Albuquerque Basin than in the south (Fig. 4.19), probably because basin subsidence may have been faster, and through-going axial-river drainage was established earlier here than in basins to the south (Smith et al., 2001; Connell et al., 2005; and Mack et al., 2006). The thinner Plio-Pleistocene basin fill in the Socorro and Palomas Basins may be a result of either slower subsidence or the younger age of the axial-fluvial system to the south. The northern part of the Hueco Bolson in southern New Mexico and northern Texas is unusual because it received axial-fluvial (ancestral Rio Grande) sediment during temporary drainage capture from the adjacent Mesilla Basin (e.g., Mack et al., 1997), so its greater thickness may be a result of faster subsidence.

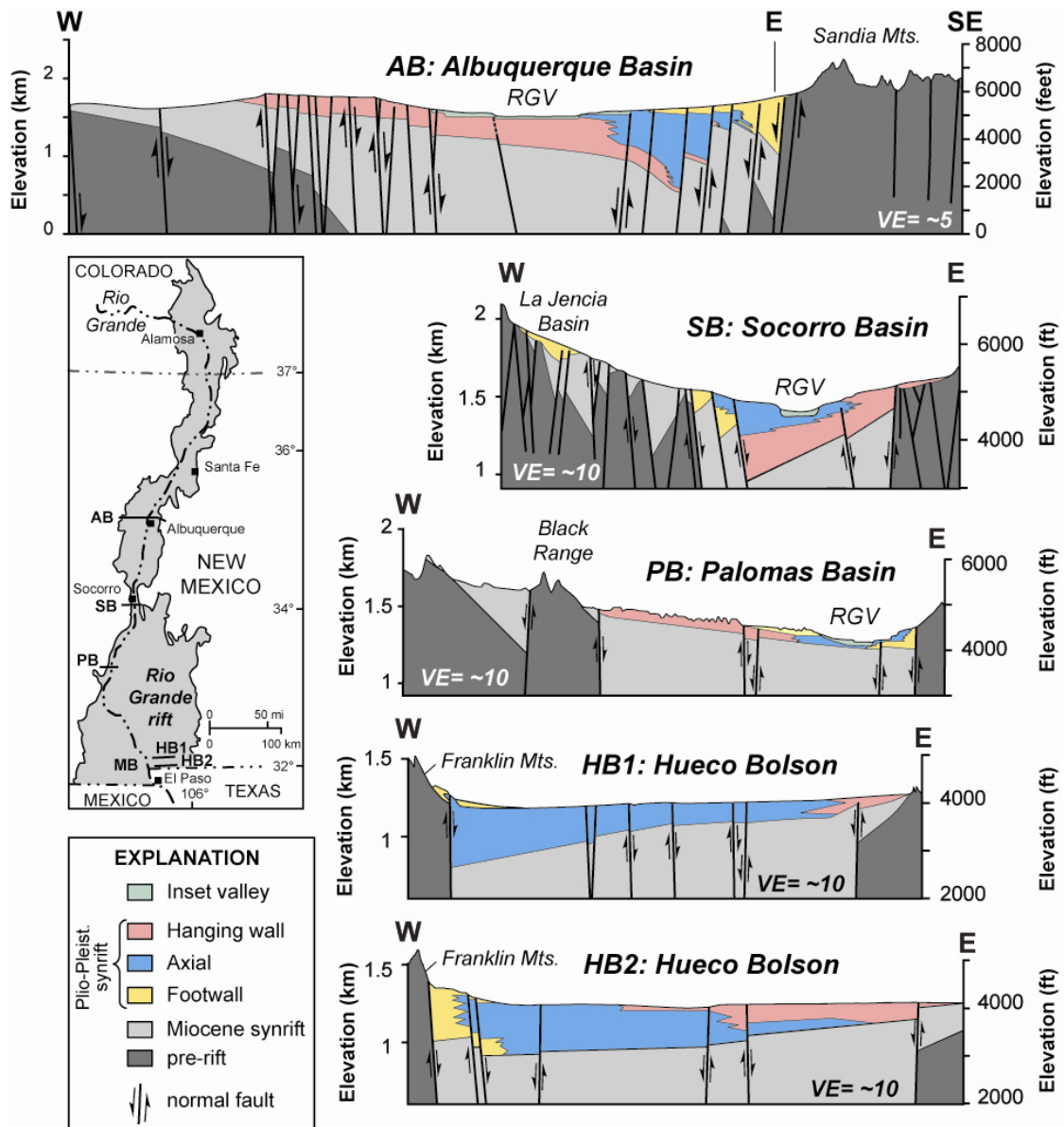


Figure 4.19. Generalized geologic cross sections illustrating selected fluvially dominated half-graben basins of the Rio Grande rift in New Mexico; VE = vertical exaggeration. Inset map shows boundary of rift (shaded gray) and approximate locations of cross section lines across the Albuquerque (AB), Socorro (SB), Palomas (PB), and Hueco (HB) basins. Other features include the Rio Grande Valley (RGV) and Mesilla Basin (MB). Plio-Pleistocene deposits overlie older (Oligocene to mostly Miocene) rift-basin fill, and are divided into hanging-wall ramp deposits, axial-river, and footwall deposits. AB: northern part of the Albuquerque Basin (simplified from Connell, 2008). SB: Socorro Basin (modified from McGrath and Hawley, 1987). PB: Palomas Basin (RA-RA' modified from Hawley and Kennedy, 2004). HB: northern Hueco Bolson (HB1 = C-C' & HB2 = B-B' modified from Hawley, et al., 2007).

The position of the axial river to the basin master fault tends to be influenced by the location of larger footwall-derived tributaries. The influence of tributary drainage on the position of the axial-fluvial belt is illustrated in the two cross sections across the Hueco Bolson on Figure 4.19. The northern section (HB-1) lies between major footwall drainages, so the axial-fluvial depositional belt is adjacent to basin-bordering faults that define the eastern side of the Franklin Mountains. To the south (HB-2), the axial belt lies to the east, presumably in response to the presence of larger footwall-derived fans draining the Franklin Mountains.

The downstream diminution of the axial-sediment load observed during the experiments (Fig. 4.18) suggests that petrographic indicators can be used to estimate the tributary flux into the axial depositional belt. The downstream reduction of axial sediment is supported by sparse petrographic measurements of synrift sediments (of the Santa Fe Group) in extensional basins of the Rio Grande in New Mexico. Compositional data from axial-river deposits in the Albuquerque Basin illustrate an overall decrease in well-rounded Proterozoic orthoquartzite pebbles and cobbles (derived from northern New Mexico) between sites in the northern part of the basin (33%, $n = 10$ sites, Brandes, 2002), and sites about 135 km downstream (22%, $n = 5$ sites, unpublished data used in Love et al., 2001).

Detrital sandstone compositions of similarly aged deposits from basins connected by the ancestral Rio Grande also show an overall downstream decrease in compositional maturity across a distance of about 300 km (Fig. 4.20; Mack, 1984; and Large and Ingersoll, 1997). A nearly 24 percent increase in lithic fragments in the synrift basin fill is attributed to volcanic sediment inputs as the Rio Grande flowed across the

eastern flank of the Oligocene Mogollon-Datil volcanic field between northern and southern New Mexico. Although more study would be required to quantify these downstream changes in the Rio Grande system, the differences in compositional maturity support experimental observations showing major contributions of tributary sediment to the axial-river system.

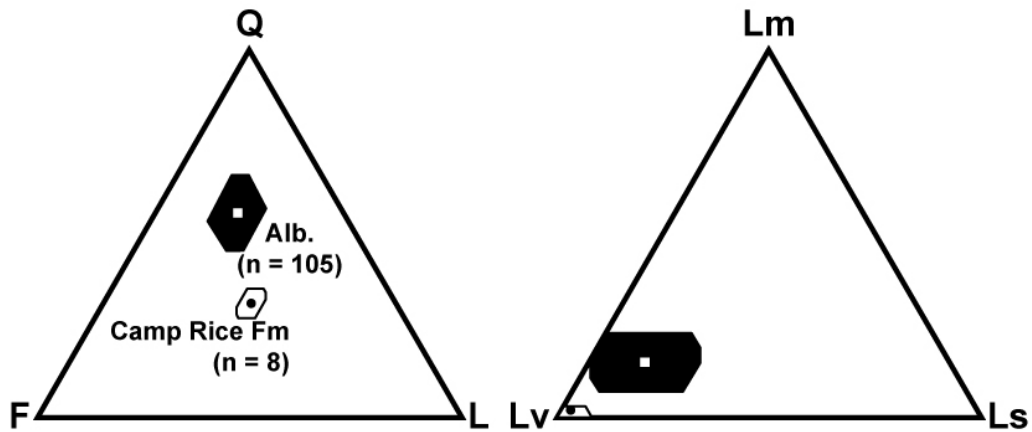


Figure 4.20. Detrital sandstone compositions (mean and standard deviation) in the synrift basin-fill of the Santa Fe Group in New Mexico, illustrating an overall decrease in compositional maturity between basins north of the Mogollon-Datil volcanic field (Albuquerque Basin, shaded black; Large and Ingersoll, 1997) and the Camp Rice Formation to the south (Mack, 1984). Albuquerque Basin QFL (in percent): $Q = 53 \pm 7$; $F = 26 \pm 5$; $L = 21 \pm 5$ ($n = 105$). Southern New Mexico QFL (in percent): $Q = 31 \pm 4$; $F = 35 \pm 3$; $L = 34 \pm 5$ ($n = 8$). Volcanic lithics (LvLmLs, in percent): $Lv = 72 \pm 7$ in Albuquerque Basin, and $Lv = 96 \pm 4$ in southern New Mexico.

During high axial sediment discharges in the experimental basin (i.e., stage 3), the axial drainage is capable of transporting axially sourced sediment through the basin. A field-based example of this behavior that supports experimental observations comes from Plio-Pleistocene flood deposits inferred in the Rio Grande system. Nearly pure beds of pumice-bearing pebbly sand and gravel have been documented in the Camp Rice Formation of southern New Mexico (Mack et al., 1996) that were interpreted to have

been laid down by floods that originated nearly 400 km upstream, where ignimbrites and landslides temporarily impounded the axial river (e.g., Reneau and Dethier, 1996).

Numerical models of sedimentation within simple, internally drained half-graben basins suggest that the location of the sediment input (relative to the master fault) controls the depositional response to subsidence rate and sediment flux (e.g., Paola et al., 1992; and Marr et al., 2000). For instance, diffusional models show that progradation of coarse-grained sediment delivered at the model fault (footwall) occurred during times of reduced basin subsidence or increased sediment flux and are in general agreement with field observations (e.g., Leeder and Gawthorpe, 1987; Blair and Bilodeau, 1988; and Mack and Seager, 1990).

These numerical simulations also suggest that progradation of coarse-grained sediment from opposing sides of a simple half-graben basin may be inversely correlated to subsidence (Paola et al., 1992). Although XES06 did not explore the development of depositional successions created by variable subsidence, changes in sediment discharge reflect variations in subsidence (independent of sediment flux) under constant basin accommodation. That is, an increase in sediment discharge would be similar to the effects of decreased subsidence. The volumes of the footwall fans seem to adjust more quickly to changes in sediment supply than the hanging-wall fan (Fig. 4.10A), suggesting the presence of a slight autogenic lag in the depositional response of the hanging-wall fans to changes in sedimentation rate. The slower volumetric expansion of the hanging-wall fan in XES06 suggests a slower response to reduced subsidence, rather than an increase in subsidence suggested by numerical models (Paola et al., 1992). A field-based example of asynchronous transverse-fan progradation was recognized in the

Albuquerque Basin, New Mexico, where sedimentation on the distal hanging-wall ramp coarsened up-section before the footwall deposits began to prograde towards the basin center (Chapter 2).

Chapter Conclusions

The Experimental EarthScape run in 2006 (XES06) provided new insights regarding autogenic fan responses and allogeonic drivers on the stratigraphic architecture and ability of the axial drainage to remove sediment from the basin in fluvially dominated half-graben basins. After setting the initial topographic conditions, where the sediment was supplied into an open, non-subsiding basin with four sources supplying sediment to a shallow lake, the basin fill organized itself to a low-gradient, subcritical, axial stream that was flanked and bounded by steep transverse fans. Axially-sourced sediment was mostly sequestered in an upstream axial fan. Only under conditions of high axial sediment discharge did the axial drainage contain appreciable quantities of axially-sourced sand. Although details differ, the overall geometry is similar to those of field-scale intracontinental rift basins.

The location of the axial depositional belt was not noticeably sensitive to the location of the lateral subsidence maximum. Thus, the location of this belt seemed to be mostly determined by the relative strengths of the tributary inputs (“flux steering”), rather than a response to changing subsidence. The supply of sediment to the experimental basin was sufficient to mask the influence of subsidence on stratigraphic architecture. The asymmetric subsidence pattern in half-graben basins also influences the preservation of sedimentary sequences, where major stratigraphic boundaries may be

easier to delineate in the on the distal hanging-wall ramp than on the footwall side of the basin.

Transverse sediment contributions to the axial system were almost equally apportioned by the axial stream through toe cutting of the distal transverse fans. The relative consistency in the fraction of transverse fan sediment extracted by the axial drainage system suggests that the axial-transverse boundary remained steady over a wide range of sediment discharges tested for XES06. The stability of the axial-transverse boundary resembles the large-scale autogenic processes observed in the moving boundaries that define the morphology and stratigraphy of fluviodeltaic systems, and may be comparable to the fluviodeltaic boundary in coastal settings. Without the imposition of this boundary, the experimental axial drainage resembled those of the transverse fans.

Chapter Acknowledgements

This study was supported by the National Science Foundation (EAR-0344146), the New Mexico Bureau of Geology and Mineral Resources (P.A. Scholle, Director), and the St. Anthony Falls Industrial Consortium, including Chevron, Conoco-Phillips, Exxon-Mobil Upstream Research Corporation, Japan Oil, Gas and Metals National Corporation (JOGMEC), and Royal-Dutch Shell Corporation. We thank Bill Haneberg for suggestions on automating grain-color mapping, and Jim Mullin, Chris Ellis, and Dick Christopher for help with the running of the XES and providing the sediment analyses.

Chapter References

- Blair, T.C., and Bilodeau, W.L., 1988, Development of tectonic cyclothems in rift, pull-aparts, and foreland basins: sedimentary response to episodic tectonism: *Geology*, v. 16, p. 517-520.
- Brandes, N.N., 2002, Lithostratigraphy and petrography of upper Santa Fe Group deposits in the northern Albuquerque Basin, New Mexico [M.S. thesis]: Socorro, New Mexico Institute of Mining and Technology, 208 p.
- Bridge, J.S., and Leeder, M.R., 1979, A simulation model of alluvial stratigraphy: *Sedimentology*, v. 26, p. 617-644.
- Bridge, J.S., and MacKey, S.D., 1993, A revised alluvial stratigraphy model, *in* Marzo, M., and Puigdefabregas, C., eds., *Alluvial Sedimentation: International Association of Sedimentologists, Special Publication 17*, p. 319-336.
- Chapin, C.E., and Cather, S.M., 1994, Tectonic setting of the axial basins of the northern and central Rio Grande rift: *Geological Society of America, Special Paper 291*, p. 5-25.
- Connell, S.D., 2008, Geologic map of the Albuquerque-Rio Rancho metropolitan area, Bernalillo and Sandoval County, New Mexico: New Mexico Bureau of Geology and Mineral Resources, Geologic Map GM-78, scale 1:50,000, 2 pls.
- Connell, S.D., Hawley, J.W., and Love, D.W., 2005, Late Cenozoic drainage development in the southeastern Basin and Range of New Mexico, southeasternmost Arizona, and western Texas, *in* Lucas, S.G., Morgan, G.S., and Zeigler, K.E., eds., *New Mexico's Ice Ages: New Mexico Museum of Natural History and Science, Bulletin No. 28*, p. 125-150.
- Dickinson, W.R., 1988, Provenance and sediment dispersal patterns in relation to paleotectonics and paleogeography of sedimentary basins, *in* Kleinspehn, K.L., and Paola, C., eds., *New Perspectives in Basin Analysis: New York, Springer-Verlag*, p. 3-26.
- Fraser, G.S., and DeCelles, P.G., 1992, Geomorphic controls on sediment accumulation at margins of foreland basins: *Basin Research*, v. 4, p. 233-252.
- Frostick, L.E., 1997, The East African Rift basins, *in* Selley, R.C., ed., *African Basins: Sedimentary basins of the world*, v. 3: Amsterdam, Elsevier Science, p. 187-209.
- Gawthorpe, R.L., and Leeder, M.R., 2000, Tectono-sedimentary evolution of active extensional basins: *Basin Research*, v. 12, p. 195-218.

- Hawley, J.W., and Kennedy, J.F., 2004, Creation of a digital hydrogeologic framework model of the Mesilla Basin and southern Jornada del Muerto Basin: Las Cruces, New Mexico State University, Water Resources Research Institute, Technical Completion Report No. 332, 105 p. 1 CD-ROM.
- Hawley, J.W., Kennedy, J. F., Granados-Olivas, A., and Ortiz, M.A., 2007, Hydrogeologic framework of the binational western Hueco Bolson-Paso del Norte area, Texas, New Mexico, and Chihuahua: Overview and progress report on digital model development; Chapter 1, *in* Hibbs, B.J., ed., Technical Completion Report prepared by CEA-CREST Center at California State University-Los Angeles, for U.S. Environmental Protection Agency Region VI, Interagency Contract no. X7-976401-01, 43 p., 3 tables, 10 figures, and 12 plates on CD-ROM.
- Heller, P.L., and Paola, C., 1992, The large-scale dynamics of grain-size variation in alluvial basins, 2: application to syntectonic conglomerate: *Basin Research*, v. 4, p. 91-102.
- Kendall, C.G. St. C., Strobel, J., Cannon, R., Bezdek, J., and Biswas, G., 1991, The simulation of the sedimentary fill of basins: *Journal of Geophysical Research*, v. 96, p. 6911-6929.
- Kim, W., and Jerolmack, D.J., 2008, The pulse of calm fan deltas: *Journal of Geology*, v. 116, n. 4, p. 315-330.
- Lambiase, J.J., and Bosworth, W., 1995, Structural controls on sedimentation in continental rifts, *in* Lambiase, J.J., ed., *Hydrocarbon habitat in rift basins: Geological Society Special Publication No. 80*, p. 117-144.
- Large, E., and Ingersoll, R.V., 1997, Miocene and Pliocene sandstone petrofacies of the northern Albuquerque Basin, New Mexico, and implications for evolution of the Rio Grande rift: *Journal of Sedimentary Research, Section A: Sedimentary Petrology and Processes*, v. 67, p. 462-468.
- Lawrence, D.T., 1994, Evaluation of eustasy, subsidence, and sediment input as controls on depositional sequence geometries and the synchronicity of sequence boundaries, *in* Weimer, P., and Posamentier, H.W., eds., *Siliclastic sequence stratigraphy; recent developments and applications: American Association of Petroleum Geologists Memoir 58*, p. 337-367.
- Leeder, M.R., and Gawthorpe, R.L., 1987, Sedimentary models for extensional tilt block/half graben basins, *in* Coward, M.P., Dewey, J.F., and Hancock, P.L., eds., *Continental Extensional Tectonics, Geological Society of London Special Publication 28*, p.139-152.

- Leeder, M. R., and Jackson, J. A., 1993, The interaction between normal faulting and drainage in active extensional basins, with examples from the western United States and central Greece: *Basin Research*, v. 5, n. 2, p. 79-102.
- Leeder, M.R., and Mack G.H., 2001, Lateral erosion (“toe cutting”) of alluvial fans by axial rivers; implications for basin analysis and architecture: *Journal of the Geological Society of London*, v. 158, n. 6, p. 885-893.
- Leeder, M.R., and Mack, G.H., 2007, Basin-fill incision, Rio Grande and Gulf of Corinth rifts: convergent response to climatic and tectonic drivers, *in* Nichols, G., Williams E., and Paola, C eds., *Sedimentary processes, Environments and basins: A Tribute to Peter Friend: International Association of Sedimentologists Special Publication 38*, 9-28. 2007.
- Leeder, M.R., Mack, G.H., Peakall, J., and Salyards, S.L., 1996a, First quantitative test of alluvial stratigraphic models: Southern Rio Grande rift, New Mexico: *Geology*, v. 24, n. 1, p. 87-90.
- Leeder, M.R., Mack, G.H., and Salyards, S.L., 1996b, Axial-transverse fluvial interactions in half-graben: Plio-Pleistocene Palomas Basin, southern Rio Grande rift, New Mexico, USA: *Basin Research*, v. 8, n. 3, p. 225-241.
- LeTourneau, P.M., and Olsen, P.E., eds., 2003, *The great rift valleys of Pangea in eastern North America: Volume 2, Sedimentology, stratigraphy, and paleontology: Columbia University Press*, 384 p.
- Love, D.W., Connell, S.D., Lucas, S.G., Morgan, G.S., Derrick, N.N., Jackson-Paul, P.B., and Chamberlin, R., 2001, Third-day, Belen sub-basin: Belen, Sevilleta National Wildlife Refuge, and northern Socorro Basin, *in* Connell, S.D., Love, D.W., Lucas, S.G., Koning, D.J., Derrick, N.N., Maynard, S.R., Morgan, G.S., Jackson-Paul, P.B., and Chamberlin, R., trip leaders., *Stratigraphy and tectonic development of the Albuquerque Basin, central Rio Grande rift, field trip guidebook: Albuquerque, New Mexico, Geological Society of America, Rocky Mountain-South Central Section Meeting: New Mexico Bureau of Geology and Mineral Resources, Open-file report 454A*, p. 27-53.
- Mack, G.H., 1984, Exceptions to the relationship between plate tectonics and sandstone composition: *Journal of Sedimentary Research*, v. 54, n. 1, p. 212-220.
- Mack, G.H. and Seager, W.R., 1990, Tectonic controls on facies distribution of the Camp Rice and Palomas Formations (Pliocene-Pleistocene) in the southern Rio Grande rift: *Geological Society of America Bulletin*, v. 102, p. 45-53.
- Mack, G.H., McIntosh, W.C., Leeder, M.R., and Monger, H.C., 1996, Plio-Pleistocene pumice floods in the ancestral Rio Grande, southern Rio Grande rift, New Mexico, USA: *Sedimentary Geology*, v. 103, p. 1-8.

- Mack, G.H., Love, D.W., and Seager, W.R., 1997, Spillover models for axial rivers in regions of continental extension: The Rio Mimbres and Rio Grande in the southern Rio Grande rift, USA: *Sedimentology*, v. 44, p. 637-652.
- Mack, G.H., Seager, W.R., Leeder, M.R., Parea-Arlucea, M., and Salyards, S.L., 2006, Pliocene and Quaternary history of the Rio Grande, the axial river of the southern Rio Grande rift, New Mexico, USA: *Earth-Science Reviews*, v. 79, p. 141-162.
- Marr, J.G., Swenson, J.B., Paola, C., and Voller, V.R., 2000, A two-dimensional model of fluvial stratigraphy in closed depositional basins: *Basin Research*, v. 12, p. 381-398.
- McGrath, D.B., and Hawley, J.W., 1987, Geomorphic evolution and soil-geomorphic relationships in the Socorro area, central New Mexico, *in* McLemore, V.T., and Bowie, M.R., compilers, *Guidebook to the Socorro area*, New Mexico: New Mexico Bureau of Mines and Mineral Resources, p. 55-67.
- Mullin, J., and Ellis, C., 2008, Method to produce grain-scale digital images of large experimental sedimentary deposits and other imperfectly flat stratigraphy: *Journal of Sedimentary Research*, v. 78, n. 3, p.239-244.
- Paola, C., 2000, Quantitative models of sedimentary basin filling: *Sedimentology*, v. 47, p. 121-178.
- Paola, C., Heller, P.L., and Angevine, C.L., 1992, The large-scale dynamics of grain-size variation in alluvial basins, 1: Theory: *Basin Research*, v. 4, p. 73-90.
- Paola, C., Mullin, J., Ellis, C., Mohrig, D.C., Swenson, J.B., Parker, G., Hickson, T., Heller, P.L., Pratson, L., Syvitski, J., Sheets, B., and Strong, N., 2001, Experimental Stratigraphy: *GSA Today*, v. 11, p. 4-9.
- Peakall, J., 1998, Axial river evolution in response to half-graben faulting, Carson River, Nevada, U.S.A.: *Journal of Sedimentary Research*, v. 68, n. 5, p. 788-799.
- Peakall, J., Leeder, M., Best, J., and Ashworth, P., 2000, River responses to lateral ground tilting: a synthesis and some important implications for the modeling of alluvial architecture in extensional basins: *Basin Research*, v. 12, p. 413-424.
- Reneau, S.L., and Dethier, D.P., 1996, Pliocene and Quaternary history of the Rio Grande, White Rock Canyon and vicinity, New Mexico: *New Mexico Geological Society Guidebook 47*, p. 317-324.
- Russ, J.C., 1995, *The image processing handbook*: Boca Raton, CRC Press, 2nd edition, 674 p.

- Schlische, R.W., and Olsen, P.E., 1990, Quantitative filling model for continental extensional basins with applications to early Mesozoic rifts of eastern North America: *The Journal of Geology*, v. 98, n. 3, p. 135-155.
- Shanley, K.W., and McCabe, P.J., 1994, Perspectives on the sequence stratigraphy of continental strata: *American Association of Petroleum Geologists Bulletin*, v. 78, p. 544-568.
- Smith, G.A., 1994, Climatic influences on continental deposition during late-stage filling of an extensional basin, southeastern Arizona: *Geological Society of America Bulletin*, v. 106, n. 8, p. 1212-1228.
- Smith, G.A., McIntosh, W.C., and Kuhle, A.J., 2001, Sedimentologic and geomorphic evidence for sea-saw subsidence of the Santo Domingo accommodation-zone basin, Rio Grande rift, New Mexico: *Geological Society of America Bulletin*, v. 113, n. 5, p. 561-574.
- Waresback, D.B., and Turbeville, B.N., 1990, Evolution of a Plio-Pleistocene volcanogenic-alluvial fan; the Puye Formation, Jemez Mountains, New Mexico: *Geological Society of America Bulletin*, v.102, n.3, p. 298-314.
- Wernicke, B., 1981, Low-angle normal faults and seismicity; a review: *Journal of Geophysical Research*, v. 100, n. 20, p. 20,159-20,174.
- Wheeler, H.E., 1958, Time-stratigraphy: *Bulletin of the American Association of Petroleum Geologists*, v. 42, n. 5, p. 1047-1063.

CHAPTER 5. CONCLUSIONS

Conclusions

The roles of spatially varying subsidence and sediment discharge on the fluvial components of half-graben basin fill were examined using field-based and experimental approaches. The studies reported in the previous chapters have important implications for the interpretation of facies patterns in fluvial dominated, continental rift basins, and provide examples of the usefulness of physical modeling of sedimentary processes in better understanding the surface processes responsible for developing fluvial successions.

In the actively aggrading depositional environment of the XES06 basin, the emergence of axially aligned drainage depended on the presence of the transverse tributary fans. This observed self-organization of the axial drainage was intrinsic to the depositional system, and without the influence of tributary drainage, fluvial fans would dominate the basin architecture. Thus, the geomorphic and stratigraphic boundaries between the axial and transverse depositional systems formed important elements of self-organization where the key dynamical element in setting this boundary was the exclusively one-way transfer of sediment from the transverse to axial systems.

A major component of sediment delivery to the axial stream was primarily through toe-cutting of the transverse fans, a process that is very effective at liberating sediment stored in the distal parts of the flanking transverse fans in natural systems. Determining the magnitude of this transfer is generally difficult to establish in field based studies, mostly because of the overall lack of exposure necessary to examine the contact between the axial and transverse deposits in alluvial basins. Estimates of this

sediment transfer can be readily obtained in experimental studies, which in this case showed that the transfer of transverse sediment to the axial drainage system was mostly independent of sediment discharge, and almost equally apportioned between the hanging-wall and footwall fans. The relative consistency in the fraction of transverse-fan sediment extracted by the axial drainage system suggests that the axial-transverse boundary remained steady over the wide range of sediment discharges that were tested in the experiments. This consistency resembles the large-scale autogenic processes observed in the moving boundaries that define the morphology and stratigraphy of fluviodeltaic systems, such as longshore drift (e.g., Ellis and Stone, 2006; Castelle et al., 2006; and Esteves et al., 2009).

The transfer of transverse and axial sediment through the basin has important implications regarding stratigraphic architecture and the reconstruction of catchment paleohydrology and basin paleogeography in ancient depositional systems. The overall lack of fine-grained sediments in the fluvial deposits and at the toes of the experimental fans and field examples demonstrate the effectiveness of long-basin sediment transport by the axial drainage system. Much of the axially-sourced sediment remained in the upstream region until axial-sediment discharge dominated the basin, which implies the presence of a threshold where the axial stream can move axially sourced sediment through the basin.

Sediment transport, reconstruction of basin geography and catchment hydrology is commonly estimated using sandstone petrography. The transfer of sediment through a basin can also be determined through experimentation. In the experimental cases, footwall-sourced sediment was preferentially transported through the basin. The

preferential sequestration of axially-sourced sediment in the experiment suggests that the axial-drainage can only transmit sediment through a basin under specific sediment-discharge conditions. Thus, in natural systems, a lack of axially-sourced sediment in the axial drainage course may not require a lack of upstream drainage integration, but could be a result of preferential upstream sequestration of axial sediment. Interpretations of depositional patterns using only petrography may underestimate the contributions from their respective depositional sources.

The shifting of the axial channel in response to changing subsidence is an expected outcome of most basin sedimentation models (e.g., Gawthorpe and Leeder, 1987; Peakall, 1998; and Smith et al., 2001). This idea was tested in the experimental basin, which showed that the position of the axial-channel was not particularly sensitive to the location of the basin subsidence maximum or the magnitude of subsidence. Instead, the location of the axial channel was mostly set by the relative strengths of the tributary inputs through “flux steering.” This flux steering of the axial-drainage course may be important in basins where the rates of subsidence and sediment delivery are nearly equal, such as in slowly subsiding or tectonically quiescent basins, where climatic influences on stratigraphic architecture are enhanced (e.g., Smith, 1994). Flux steering of the axial drainage by the tributary fans may also be enhanced by the imposed asymmetrical subsidence pattern, as suggested by the field study in the Albuquerque Basin of New Mexico.

Conceptual models of basin filling indicate that progradation of footwall-sourced piedmont deposits may be linked to diminished subsidence or increased sediment discharge (e.g., Gawthorpe and Leeder, 2000). These models are mostly based on studies

of footwall-sourced alluvial successions and the basin floor. Although little detailed work has been done on alluvial deposits on the distal hanging-wall ramp succession, results of the experiments and the Albuquerque Basin field study demonstrates the importance of considering all of the facies belts when interpreting the depositional history of a basin.

Numerical models of half-graben basin filling suggest that progradation of margin-sourced deposits are sensitive to basin position (Paola et al., 1992; and Marr et al., 2000), and imply that the progradation of coarse-grained sediment from opposite sides of the model basin respond differently to the same tectonic forcing. Comparing field and experimental results can help to better understand sedimentary responses to allogenic forcing. Results of the Albuquerque Basin field study suggest that the asynchronous progradation of opposing piedmont deposits may be more strongly controlled by the basin geometry, than by changes in subsidence rate. Basinward tilting of the hanging-wall likely promoted earlier progradation of coarse-grained amalgamated channels as sediment bypassed the basin margins. Later decreases in sediment accumulation on the distal hanging-wall ramp, and the nearly coincident upward coarsening of the hanging-wall succession suggest an overall decrease in sediment supply and removal of finer-grained sediment from the basin through sediment bypass.

Although XES06 was not specifically designed to examine the role of variable subsidence on morphology and architecture, the influence of subsidence-driven sedimentation can be inferred in the experimental basin because the amount of sediment extracted from transport by the fluvial system depends on both subsidence and sediment discharge rates. In XES06, basin subsidence could be considered an inverse case of

sediment discharge, where increased sediment supply would resemble a decrease in available basin volume created by diminished subsidence. The volumes of the experimental footwall fans tended to adjust more quickly to changes in sediment supply than did the hanging-wall fan, suggesting the presence of an autogenic lag in the depositional response of the hanging-wall fans to changes in sedimentation rate. The experimental observations suggest that the different sedimentary responses of the tributary fans to sediment discharge or subsidence stimuli may be influenced by the asymmetric subsidence geometry imposed on the basin. The Albuquerque Basin field study revealed examples of asynchronous progradation of the transverse deposits; however, the timing of progradation was opposite of the experimental cases. That is the deposits on the distal hanging-wall ramp prograded before those of associated with the footwall uplifts. The potential cause of this mismatch between experimental and field observation is not clear, but it may have to do with changes in sediment discharge driven by late Cenozoic climatic changes.

Research Directions

The results of research presented here focused on the depositional patterns in half-graben basins where subsidence and sedimentation rates were not significantly modified by base level changes. The imposition of steady base level is useful in understanding how the three component depositional belts interact without eustatic forcing. The stable base-level conditions imposed on the Experimental EarthScape run in 2006 (XES06) are not realistic for basins near the coast; however, they are relevant to basins located far upstream of the coastline. Subsidence and discharge variables were

limited because of the available space in the experimental apparatus. Future experiments could deal with more realistic basin-filling scenarios that include variable subsidence rates under variable (or oscillating) discharge. These conditions would create base-level variations that would strongly affect the length of the axial drainage and introduce more complicated and realistic feedback mechanisms, such as local incision and capture. Incorporation of these variables would also drive transgressions and regressions of the down-basin lake, which would be useful in understanding how structurally linked rift basins may eventually become hydrologically integrated.

The apportionment of transverse sediment into the axial system provides useful parameters for the development of new numerical models that can account for sediment flux throughout an entire sedimentary basin. The long-basin transport of sediment by the axial river could be compared with research on long-shore drift in order to better understand how sediment moves through a basin. Numerical models of basin sedimentation can now deal with the problems of multiply-moving boundary conditions (Swenson et al., 2000), so constraints on sediment movement from different sources in three spatial dimensions can provide useful parameters for future computational models.

The ability of the axial river to transport sediment through a basin was only incompletely tested. The available petrographic data suggest a link between transverse drainage sources and axial-sediment composition, but the data were not collected to address this question directly. A more robust test of the efficacy of axial-river transport could be conducted in the basins of the Rio Grande. Gravel compositions may be more reliable than sand for determining the changes in deposit composition. Studies of gravel

sampled from the similar-aged axial-river sediment in different basins would better quantify this change in composition.

Chapter References

- Castelle, B., Bonneton, P., Sénéchal, N., Dupuis, H., Buten, R., and Michel, D., 2006, Dynamics of wave-induced currents over an alongshore non-uniform multiple-barred sandy beach on the Aquitanian Coast, France: *Continental Shelf Research*, v. 26, p. 113-131.
- Ellis, J., and Stone, G.W., 2006, Numerical simulation of net longshore sediment transport and granulometry of surficial sediments along Chandeleur Island, Louisiana, USA: *Marine Geology*, v. 232, p. 115-129.
- Esteves, L., Williams, J.J., and Lisniowski, M.A., 2009, Measuring and modeling longshore sediment transport: *Estuarine, Coastal and Shelf Science*, v. 83, p. 47-59.
- Gawthorpe, R.L., and Leeder, M.R., 2000, Tectono-sedimentary evolution of active extensional basins: *Basin Research*, v. 12, p. 195-218.
- Leeder, M.R., and Gawthorpe, R.L., 1987, Sedimentary models for extensional tilt block/half graben basins, in Coward, M.P., Dewey, J.F., and Hancock, P.L., eds., *Continental Extensional Tectonics*, Geological Society of London Special Publication 28, p.139-152.
- Mack, G.H. and Seager, W.R., 1990, Tectonic controls on facies distribution of the Camp Rice and Palomas Formations (Pliocene-Pleistocene) in the southern Rio Grande rift: *Geological Society of America Bulletin*, v. 102, p. 45-53.
- Marr, J.G., Swenson, J.B., Paola, C., and Voller, V.R., 2000, A two-dimensional model of fluvial stratigraphy in closed depositional basins: *Basin Research*, v. 12, p. 381-398.
- Paola, C., Mullin, J., Ellis, C., Mohrig, D.C., Swenson, J.B., Parker, G., Hickson, T., Heller, P.L., Pratson, L., Syvitski, J., Sheets, B., and Strong, N., 2001, Experimental Stratigraphy: *GSA Today*, v. 11, p. 4-9.
- Paola, C., Heller, P.L., and Angevine, C.L., 1992, The large-scale dynamics of grain-size variation in alluvial basins, 1: Theory: *Basin Research*, v. 4, p. 73-90.
- Smith, G.A., McIntosh, W.C., and Kuhle, A.J., 2001, Sedimentologic and geomorphic evidence for sea-saw subsidence of the Santo Domingo accommodation-zone basin,

Rio Grande rift, New Mexico: Geological Society of America, Bulletin, v. 113, n. 5, p. 561-574.

Swenson, J.B., Voller, V.R., Paola, C., Parker, G., and Marr, J.G., 2000, Fluvio-deltaic sedimentation: A generalized Stefan problem: European Journal of Applied Mathematics, v. 11, p. 433-452.

APPENDIX

Appendix A. Rock-magnetic data for Chapter 2 (Supplementary files, 84 Mb).

Appendix B. Paleomagnetic site results for stratigraphic sections measured in Chapter 2 (Tables B1-B8).

Appendix C. Supplemental data for stratigraphic sections measured for the Ceja Formation in Chapter 2 (Tables C1 & C2).

Appendix D. Time-lapse movies of deposit surface and cross sections for XES06 (Supplementary files, 851 Mb).

Appendix E. Gridded elevation data of basement, deposit-surface, stratigraphically migrated topography (isochrons), deposit isopachs, and sediment mass balance model results for XES06 (Supplementary files, 80 Mb).

Appendix F. Areal extents of mapped fans from overhead images for XES06 (Supplementary files, 332 Mb).

Appendix G. Threshold images for flow-occupation maps for XES06 (Supplementary files, 2.5 Mb).

Appendix H. Images of deposit slices (strike sections) with stage boundaries from stratigraphically migrated topography, and deposit slices from grain mapping, including separate stages for XES06 (Supplementary files, 1.1 Gb).

Appendix I. Matlab™ computer application scripts used in analysis of data for XES06 (Supplementary files, 65 kb).

Appendix J. Graphical files for chapter figures (Supplementary files, 635 Mb).

Appendix B. Paleomagnetic Data Summary

Paleomagnetic site results for stratigraphic sections measured in Chapter 2 (Tables B1-B8). Location of sites (latitude and longitude, WGS84) and details are described at the bottom of each table.

Table B1. Summary of site results for stratigraphic section CDRP3.

Site	Unit	Z (m)	N/No	R	<i>k</i>	$\alpha 95$ (°)	Geo. Dec (°)	Geo. Inc (°)	Strat. Dec (°)	Srat. Inc (°)	VGP lat (°)	Class	Lith	Bedding
R01	Ton	1.6	4/6	3.89	27.1	18.0	343.6	57.7	345.2	57.7	77.1	I	ss	345/01
R02	Ton	2.2	6/6	5.55	11.2	20.9	211.9	72.6	209.7	73.3	7.13	II	ms	345/01
R03	Ton	10.8	7/7	6.89	56.3	8.1	14.2	48.1	15.2	47.6	75.7	I	ss	345/01
R04	Ton	19.2	6/6	5.90	48.6	9.7	351.6	35.7	352.3	35.6	73.3	I	ss	345/01
R04A	Ton	20.5	0/6	nd	nd	nd	nd	nd	nd	nd	nd	V	ss	345/01
R05	Tca	22.0	0/6	nd	nd	nd	nd	nd	nd	nd	nd	V	ss	345/01
R06	Tca	23.0	6/7	5.76	21.2	14.9	0.8	42.6	2.7	44.8	81.1	I	ms	345/01
R07	Tca	25.0	6/6	5.93	69.1	8.1	29.1	65.6	35.5	66.5	60.5	I	ms	050/03
R08	Tca	26.8	5/6	4.94	62.0	9.8	5.1	44.1	7.3	46.1	80.3	I	ms	050/03
R09	Tca	27.4	4/6	3.57	7.0	37.3	177.5	-43.6	179.3	-45.9	-82.3	II	ms	050/03
R10	Tca	28.0	4/6	3.13	3.4	58.6	159.5	-39.7	160.4	-42.5	-70.1	III	ss	050/03
R11	Tca	30.2	4/6	3.87	23.5	19.3	156.9	-63.3	158.9	-66.1	-69.3	I	ms	050/03
R12	Tca	31.2	4/6	3.86	22.1	20.0	197.1	-39.0	199.2	-40.6	-69.5	I	ss	050/03
R13	Tca	33.0	7/7	6.94	98.3	6.1	162.9	-18.5	163.3	-21.2	-61.6	I	ms	050/03
R14	Tca	35.4	6/6	5.93	73.7	7.9	162.9	-19.4	163.3	-22.2	-62.1	I	ss	050/03
R15	Tca	38.5	5/7	4.83	24.0	15.9	154.9	-61.1	156.5	-64.0	-69.2	I	ms	050/03
R16	Tca	39.8	4/7	3.94	49.4	13.2	210.2	-33.3	212.1	-34.3	-57.4	I	ms	050/03
R17	Tca	41.2	5/6	4.31	5.8	34.7	189.0	-46.3	191.5	-48.3	-78.7	II	ms	050/03
R18	Tca	44.4	0/6	nd	nd	nd	nd	nd	nd	nd	nd	V	ms	050/03
R19	Tcrp	46.4	7/7	6.96	148.0	5.0	350.6	57.9	350.6	57.9	81.7	I	ms	horiz.
R20	Tcrp	49.1	7/7	6.91	64.4	7.6	353.4	35.2	353.4	35.2	73.4	I	ss	horiz.
R21	Tcrp	51.2	8/9	7.75	28.0	10.7	330.7	46.9	330.7	46.9	64.2	I	ms	horiz.
R22	Tcrp	53.5	4/7	3.94	49.7	13.2	345.5	27.4	345.5	27.4	65.6	I	ss	horiz.

Notes: Top of CDRP3 section is 34.957°N, 106.893°W; Unit– Geologic unit; Z–height from base of measured section, in meters; N/No–number of sites accepted (N) and total number of sites (No); R–Fisher statistic; *k*–precision parameter; $\alpha 95$ –cone of confidence; Dec–declination; Inc–inclination. Geographic (Geo) and tilt-corrected (Strat) declination and inclinations shown; VGP lat–latitude of the virtual geomagnetic pole; Class–orientation and statistical data listed for class I, II, III, and IV sites; class V values not determined (nd); Lith–texture: mudstone (ms), sandstone (ss); Bedding–left-hand rule of azimuth/dip, in degrees.

Table B2. Summary of site results for stratigraphic section CDRP-CL.

Site	Unit	Z (m)	N/No	R	<i>k</i>	$\alpha 95$ (°)	Geo. Dec (°)	Geo. Inc (°)	Strat. Dec (°)	Srat. Inc (°)	VGP lat (°)	Class	Lith	Bedding
S01	Tca	1.3	6/6	5.86	34.4	11.6	12.6	22.0	14.6	23.5	63.5	I	ss	030/05
S02	Tca	2.0	5/7	4.86	29.0	14.5	8.2	58.5	16.2	60.0	76.1	I	ms	030/05
S03	Tca	3.3	7/7	6.84	36.6	10.1	11.8	37.5	15.5	38.9	71.0	I	ms	030/05
S04	Tca	3.9	6/11	5.95	108.6	6.5	276.3	58.0	265.5	62.2	20.5	I	ss	030/05
S05	Tca	5.2	5/7	4.78	18.3	25.4	276.3	32.1	276.3	36.7	16.6	II	ss	030/05
S06	Tca	5.5	3/3	2.97	75.3	14.3	15.3	19.1	17.0	20.3	60.8	I	ms	030/02
S07	Tca	6.5	0/7	nd	nd	nd	nd	nd	nd	nd	nd	V	ms	030/02
S08	Tca	8.5	6/8	5.72	18.1	16.2	31.7	31.7	9.1	33.6	71.3	I	ss	030/02
S09	Tca	9.5	9/9	8.70	26.5	10.2	13.2	33.6	16.5	34.9	68.4	I	ms	030/02
S10	Tca	11.5	4/4	3.88	24.7	18.9	5.9	14.5	6.4	15.3	62.0	I	ss	030/02
S11	Tca	13.2	4/5	3.93	44.3	14.0	196.9	29.8	195.8	29.3	-37.0	I	ss	030/02
S12	Tca	14.0	6/6	5.97	174.3	5.1	36.8	32.6	38.0	32.4	52.0	I	ms	030/02
S13	Tca	14.8	6/6	5.81	26.6	13.2	31.3	42.9	33.1	42.8	59.7	I	ss	030/02
S14	Tca	17.8	0/8	nd	nd	nd	nd	nd	nd	nd	nd	V	ss	030/02
S15	Tca	20.5	6/7	5.96	115.3	6.3	34.9	49.8	37.3	49.6	58.5	I	ms	030/02
S16	Tca	22.5	10/13	9.45	16.3	12.3	45.3	38.6	46.8	38.0	47.0	I	ms	030/02
S17	Tca	25.2	9/9	8.41	13.6	14.5	355.7	37.7	357.0	38.8	76.4	I	ms	030/02
S18	Tca	29.5	5/7	4.84	25.5	15.5	357.4	25.0	358.2	26.0	68.4	I	ms	030/02
S19	Tca	33.5	6/8	5.76	21.2	14.9	232.7	-11.8	233.1	-11.0	-33.0	I	ms	030/02
S20	Tcrp	35.5	5/10	4.76	16.7	19.3	339.3	17.9	339.3	21.8	59.6	I	ss	000/02
S21	Tcrp	40.5	9/9	8.03	8.3	19.0	352.5	15.8	353.1	16.1	62.3	I	ms	000/02
S22	Tcrp	42.2	6/9	5.83	29.8	12.5	29.0	38.0	32.9	37.9	58.0	I	ss	000/02
S23	Tcrp*	47.8	9/9	8.94	125.4	4.6	199.1	-36.9	200.5	-36.2	-66.5	I	ss	000/02
S24	Tcrp*	48.4	0/7	nd	nd	nd	nd	nd	nd	nd	nd	V	ss	000/02
S25	Tcrp*	50.6	10/12	9.04	9.4	16.7	208.6	29.5	207.6	30.5	-32.2	I	ss	000/02

Notes: Top of CDRP-CL section is 35.218°N, 106.862°W; Unit– Geologic unit; Z–height from base of measured section, in meters; N/No–number of sites accepted (N) and total number of sites (No); R–Fisher statistic; *k*–precision parameter; $\alpha 95$ –cone of confidence; Dec–declination; Inc–inclination. Geographic (Geo) and tilt-corrected (Strat) declination and inclinations shown; VGP lat–latitude of the virtual geomagnetic pole; Class–orientation and statistical data listed for class I, II, III, and IV sites; class V values not determined (nd); Lith–texture: mudstone (ms), sandstone (ss); Bedding–left-hand rule of azimuth/dip, in degrees.

Table B3. Summary of site results for stratigraphic section LLVN.

Site	Unit	Z (m)	N/No	R	<i>k</i>	$\alpha 95$ (°)	Geo. Dec (°)	Geo. Inc (°)	Strat. Dec (°)	Srat. Inc (°)	VGP lat (°)	Class	Lith	Bedding
N01	Tca	1.8	9/10	8.72	28.1	9.9	174.3	-50.9	177.0	-49.0	-49.0	I	ms	315/03
N09	Tca	3.4	6/8	5.71	17.3	16.5	144.0	-61.8	159.2	-63.4	-63.4	I	ss	315/03
N02	Tca	3.6	5/10	4.87	30.8	14.0	163.6	-53.1	166.9	-51.6	-51.6	I	ss	315/03
N03	Tca	7.2	5/8	4.91	43.5	11.7	195.7	-52.3	197.5	-49.7	-49.7	I	ms	315/03
N04	Tca	15.6	4/9	3.84	18.3	22.1	242.8	-51.6	241.7	-48.7	-38.4	II	ss	315/03
N05	Tca	20.8	3/6	2.97	61.4	15.9	221.8	-40.7	221.9	-37.8	-37.8	I	ss	315/03
N06	Tca	25.8	4/9	3.83	17.4	22.6	185.5	-62.4	188.9	-60.1	-80.7	II	ss	315/03
N07	Tca	26.2	4/6	3.97	87.3	9.9	1.0	21.7	1.8	19.6	19.6	I	ss	315/03
N07A	Tca	28.0	0/2	nd	nd	nd	nd	nd	nd	nd	nd	V	ss	315/03
N08A	Tca	30.2	0/9	nd	nd	nd	nd	nd	nd	nd	nd	V	ss	315/03
N08B	Tca	38.4	0/8	nd	nd	nd	nd	nd	nd	nd	nd	V	ss	343/08
N08	Tca	39.8	0/8	nd	nd	nd	nd	nd	nd	nd	nd	V	ss	343/08
N10	Tca	46.4	8/13	7.78	31.3	10.1	9.2	73.5	28.3	68.8	68.8	I	ms	343/08
N11	Tca	50.4	0/4	nd	nd	nd	nd	nd	nd	nd	nd	V	ss	343/08
N12	Tca	53.8	6/6	5.85	33.8	11.7	344.2	48.3	353.1	47.5	47.5	I	ms	343/08
N13A	Tca	60.2	6/17	5.88	43.0	10.3	335.0	35.9	340.9	36.6	36.6	I	ss	343/08
N14	Tca	68.8	5/10	3.93	40.1	14.7	1.0	54.3	10.8	51.2	51.2	I	ss	343/08
N15	Tca	72.0	0/8	nd	nd	nd	nd	nd	nd	nd	nd	V	ss	343/08
N16A	Tca	76.4	6/8	5.89	46.6	9.9	13.7	46.5	4.7	38.0	38.0	I	ss	343/08
N16	Tca	79.0	3/8	2.90	20.2	28.2	16.6	35.0	10.3	27.2	67.6	II	ss	343/08
N17	Tca	81.0	4/10	3.99	543.1	3.9	30.1	49.3	17.8	43.5	71.6	I	ms	230/13
N18	Tca	82.6	3/9	2.91	22.3	26.8	23.3	32.7	16.9	26.2	43.5	II	ms	230/13
N19	Tca	86.6	0/8	nd	nd	nd	nd	nd	nd	nd	nd	V	ms	225/15
N20	Tca	89.6	4/10	3.99	244.7	5.9	30.9	50.1	15.4	44.4	44.4	I	ss	225/15

Table B3 (continued).

Site	Unit	Z (m)	N/No	R	<i>k</i>	$\alpha 95$ (°)	Geo. Dec (°)	Geo. Inc (°)	Strat. Dec (°)	Srat. Inc (°)	VGP lat (°)	Class	Lith	Bedding
N21	Tca	92.2	10/10	9.80	45.9	7.2	9.4	33.4	2.9	23.9	23.9	I	ss	225/15
N22	Tca	96.4	0/8	nd	nd	nd	nd	nd	nd	nd	nd	V	ms	225/15
N22A	Tca	97.8	0/8	nd	nd	nd	nd	nd	nd	nd	nd	V	ms	225/15
N22E	Tca	98.4	4/9	3.87	22.3	19.9	204.7	-42.0	193.8	-35.4	-35.4	I	ss	225/15
N22D	Tca	99.4	0/8	nd	nd	nd	nd	nd	nd	nd	nd	V	ms	225/15
N22C	Tca	100.1	4/8	3.98	169.6	7.1	208.8	-33.5	200.3	-28.2	-28.2	I	ss	225/15
N22B	Tca	101.4	7/12	6.99	416.3	3.0	180.7	-71.8	161.1	-59.4	-59.4	I	ss	225/15
N23	Tca	103.9	4/10	3.89	28.2	17.6	169.1	-47.4	162.4	-34.5	-34.5	I	ms	225/15
N23A	Tca	105.0	4/8	3.95	58.5	12.1	161.0	-47.0	156.0	-33.2	-33.2	I	ms	225/15
N23B	Tca	107.0	0/4	nd	nd	nd	nd	nd	nd	nd	nd	V	ss	225/15
N24	Tca	109.0	6/8	5.87	39.5	10.8	30.1	51.1	14.5	45.2	45.2	I	ms	225/15
N25	Tca	111.0	7/8	6.92	77.8	6.9	23.7	66.5	359.6	58.0	58.0	I	ms	225/15
N26A	Tca	112.8	4/7	3.94	54.1	12.6	346.7	59.5	337.6	46.1	46.1	I	ss	225/15
N26	Tca	117.4	0/1	nd	nd	nd	nd	nd	nd	nd	nd	V	ss	225/15
N27	Tca	120.6	3/7	2.89	18.1	29.9	331.5	56.0	327.2	41.4	59.5	II	ss	225/15
N28	Tca	123.2	0/1	nd	nd	nd	nd	nd	nd	nd	nd	V	ms	225/15
N28A	Tca	124.8	6/8	5.96	112.1	6.4	28.0	49.8	13.4	43.5	43.5	I	ss	225/15
N29	Tca	127.0	7/8	6.94	94.1	6.3	7.5	61.4	351.8	50.6	50.6	I	ash	225/15
N30	Tca	130.3	0/8	nd	nd	nd	nd	nd	nd	nd	nd	V	ms	225/15

Table B3 (continued).

Site	Unit	Z (m)	N/No	R	k	α_{95} (°)	Geo. Dec (°)	Geo. Inc (°)	Strat. Dec (°)	Srat. Inc (°)	VGP lat (°)	Class	Lith	Bedding
N31	Tcrp	133.4	2/8	1.99	170.8	19.2	329.1	67.4	323.9	52.7	52.7	I	ss	225/15
N31A	Tcrp	135.4	0/8	nd	nd	nd	nd	nd	nd	nd	nd	V	ss	225/15
N32	Tcrp	140.0	3/6	2.99	169.7	9.5	184.4	-83.8	149.2	-70.4	-70.4	I	ms	225/15
N33	Tcrp	141.8	0/8	nd	nd	nd	nd	nd	nd	nd	nd	V	ss	225/15
N34	Tcrp	149.7	4/6	3.60	73.3	10.8	193.3	-66.4	172.7	-56.1	-56.1	I	ss	225/15
N35	Tcrp	158.2	0/6	nd	nd	nd	nd	nd	nd	nd	nd	V	ms	225/15
N36	Tcrp	159.4	8/8	7.84	42.5	8.6	195.3	-48.4	183.4	-39.6	-39.6	I	ss	225/15
N37	Tcrp	161.8	0/6	nd	nd	nd	nd	nd	nd	nd	nd	V	ss	225/15
N38	Tcrp	169.6	0/6	nd	nd	nd	nd	nd	nd	nd	nd	V	ss	225/15
N39	Qsc	170.4	4/6	3.95	58.0	12.2	158.4	-43.1	154.4	-29.1	-29.1	I	ms	225/15
N40	Qsc	172.5	5/6	4.92	51.9	10.7	210.5	-46.8	196.9	-41.3	-41.3	I	ms	225/15
N41	Qsc	173.6	0/3	nd	nd	nd	nd	nd	nd	nd	nd	V	ss	225/15

Notes: Top of LLVN section (LLVN-C) is 34.811°N, 106.804°W; Unit– Geologic unit; Z–height from base of measured section, in meters; N/No–number of sites accepted (N) and total number of sites (No); R–Fisher statistic; k–precision parameter; α_{95} –cone of confidence; Dec–declination; Inc–inclination. Geographic (Geo) and tilt-corrected (Strat) declination and inclinations shown; VGP lat–latitude of the virtual geomagnetic pole; Class–orientation and statistical data listed for class I, II, III, and IV sites; class V values not determined (nd); Lith–texture: mudstone (ms), sandstone (ss), volcanic ash (ash); Bedding–left-hand rule of azimuth/dip, in degrees.

Table B4. Summary of site results for stratigraphic section LLVS.

Site	Unit	Z (m)	N/No	R	<i>k</i>	α_{95} (°)	Geo. Dec (°)	Geo. Inc (°)	Strat. Dec (°)	Srat. Inc (°)	VGP lat (°)	Class	Lith	Bedding
S11	Tc	0.5	6/8	5.95	90.3	7.1	160.1	-44.8	160.1	-37.8	-67.9	I	ss	250/07
S10	Tc	4.5	7/7	6.96	153.4	4.9	164.4	-17.3	164.3	-10.4	-57.1	I	ms	250/07
S09	Tc	7.0	6/7	5.95	109.6	6.4	171.2	-46.9	170.0	-40.0	-75.1	I	ss	250/07
S08	Tc	9.5	6/7	5.94	77.4	7.7	175.3	-48.9	173.5	-42.1	-78.1	I	ss	250/07
S07	Tc	13.0	5/7	4.90	38.4	12.5	181.7	-37.0	180.0	-30.5	-71.6	I	ms	250/07
S06	Tc	15.2	5/6	4.83	23.6	16.1	167.9	-39.0	167.3	-32.0	-69.2	I	ms	250/07
S05	Tc	16.8	7/7	6.95	109.1	5.8	163.1	-23.2	163.0	-16.2	-59.2	I	ss	250/07
S04	Tc	18.2	7/7	6.85	40.1	9.6	183.0	-48.6	180.4	-42.1	-79.5	I	ss	250/07
S03	Tc	20.8	5/7	4.93	58.9	10.1	202.9	-27.4	200.8	-22.2	-60.0	I	ss	250/07
S02	Tc	22.6	6/7	5.95	106.0	6.5	181.3	-53.3	178.5	-46.7	-83.1	I	ms	250/07
S01	Tc	23.8	6/6	5.86	34.6	11.5	178.1	-43.5	176.3	-36.8	-75.4	I	ss	250/07

Notes: Top of LLVS section is 34.792°N, 106.803°W; Unit– Geologic unit; Z–height from base of measured section, in meters; N/No–number of sites accepted (N) and total number of sites (No); R–Fisher statistic; *k*–precision parameter; α_{95} –cone of confidence; Dec–declination; Inc–inclination. Geographic (Geo) and tilt-corrected (Strat) declination and inclinations shown. Class–orientation and statistical data listed for class I, II, III, and IV sites; class V values not determined (nd); Lith–texture: mudstone (ms), sandstone (ss); Bedding–left-hand rule of azimuth/dip, in degrees.

Table B5. Summary of site results for stratigraphic section CSA.

Site	Unit	Z* (m)	N/No	R	k	$\alpha 95$ (°)	Geo. Dec (°)	Geo. Inc (°)	Strat. Dec (°)	Srat. Inc (°)	VGP lat (°)	Class	Lith	Bedding
S01	Tca	0.2	6/18	5.82	28.1	12.9	355.9	56.0	357.6	52.2	87.1	I	ss	285/04
S01A	Tca	2.4	0/4	nd	nd	nd	nd	nd	nd	nd	nd	V	ms	285/04
S02A	Tca	3.0	0/18	nd	nd	nd	nd	nd	nd	nd	nd	V	ss	285/04
S02	Tca	6.5	3/3	2.91	23.1	26.3	7.1	78.8	9.1	74.8	62.8	II	ss	285/04
S03	Tca	10.5	4/10	3.95	62.4	11.7	336.7	60.1	340.6	56.9	74.2	I	ss	285/04
S04C	Tca	11.5	4/4	3.95	61.5	11.8	6.0	38.9	6.5	34.9	73.3	I	ms	285/04
S04D	Tca	12.8	5/7	4.93	58.6	10.1	349.3	37.5	350.5	33.9	70.7	I	ms	285/04
S04E	Tca	14.5	3/3	2.99	135.4	10.6	192.5	-61.9	192.8	-57.9	-79.1	I	ms	285/04
S04	Tca	16.0	1/1	nd	nd	3.6	317.6	45.4	320.9	43.2	nd	IV	ms	285/04
S04B	Tca	17.5	6/6	5.90	51.9	9.4	193.4	-41.4	193.5	-37.4	-71.7	I	ss	285/04
S05	Tca	18.8	12/13	11.94	185.2	3.2	346.4	37.1	347.7	33.6	70.2	I	ms	285/04
S06C	Tca	21.2	5/10	4.98	175.2	5.8	348.4	35.9	349.6	32.3	70.3	I	ss	285/04
S07	Tca	22.4	4/9	3.96	69.5	11.1	331.9	32.7	333.5	29.7	59.6	I	ms	285/04
S08A	Tcrp	29.4	4/6	3.79	14.5	25.0	191.2	-38.8	191.2	-38.8	77.1	II	ss	285/04
S08B	Tcrp	32.0	0/6	nd	nd	nd	nd	nd	nd	nd	nd	V	ss	horiz.
S09A	QTsa	42.2	5/11	4.97	114.2	7.2	291.6	32.7	294.1	32.1	29.4	I	ss	horiz.
S09	QTsa	47.6	9/22	2.98	112.2	11.7	150.8	-53.1	150.8	-53.1	-62.7	I	ss	horiz.

Notes: Top of CSA section is 34.926°N, 106.657°W; Unit– Geologic unit; Z–height from base of measured section, in meters; N/No–number of sites accepted (N) and total number of sites (No); R–Fisher statistic; k–precision parameter; $\alpha 95$ –cone of confidence; Dec–declination; Inc–inclination. Geographic (Geo) and tilt-corrected (Strat) declination and inclinations shown; VGP lat–latitude of the virtual geomagnetic pole; Class–orientation and statistical data listed for class I, II, III, and IV sites; class V values not determined (nd); Lith–texture: mudstone (ms), sandstone (ss), volcanic ash (ash); Bedding–left-hand rule of azimuth/dip, in degrees.

Table B6. Summary of site results for stratigraphic section PLU.

Site	Unit	Z* (m)	N/No	R	k	$\alpha 95$ (°)	Geo. Dec (°)	Geo. Inc (°)	Strat. Dec (°)	Srat. Inc (°)	VGP lat (°)	Class	Lith	Bedding
S09	Tcrp	33.5	9/22	6.94	92.2	6.3	171.2	-55.6	177.0	-55.3	-87.4	I	ss	horiz.
S10	Tcrp	34.0	0/6	nd	nd	nd	nd	nd	nd	nd	nd	V	ss	horiz.
S12	Tcrp	35.0	0/10	nd	nd	nd	nd	nd	nd	nd	nd	V	ss	horiz.
S01	Tcrp	36.0	4/8	3.99	397.3	4.6	178.7	-47.9	183.0	-47.2	-82.9	I	ss	horiz.
S02A	QTsa	40.8	10/10	9.86	64.1	6.1	172.3	-46.0	176.4	-45.7	-81.7	I	ss	horiz.
S03	QTsa	43.0	5/9	4.77	17.3	18.9	352.7	61.3	359.9	60.8	83.1	I	ss	horiz.
S04	QTsa	49.2	7/10	6.95	118.2	5.6	177.1	-51.3	182.0	-50.6	-86.1	I	ss	horiz.
S05	QTsa	55.0	6/6	5.97	141.7	5.6	14.6	67.9	22.9	66.0	68.4	I	ms	horiz.
S06	QTsa	55.5	6/6	4.43	3.2	44.9	12.4	75.3	24.9	73.4	60.8	II	ms	horiz.
S11	QTsa	56.8	9/9	7.96	155.3	4.5	44.7	66.1	49.2	62.7	51.5	I	ms	horiz.
S07	QTsa	57.8	3/3	2.98	102.8	12.2	336.2	38.0	336.2	38.0	65.1	I	ms	horiz.
S08	QTsa	59.4	0/4	nd	nd	nd	nd	nd	nd	nd	nd	V	ss	horiz.

Notes: Top of PLU section is 34.909°N, 106.659°W; Unit– Geologic unit; Z–height from base of measured section, in meters; N/No–number of sites accepted (N) and total number of sites (No); R–Fisher statistic; k–precision parameter; $\alpha 95$ –cone of confidence; Dec–declination; Inc–inclination. Geographic (Geo) and tilt-corrected (Strat) declination and inclinations shown; VGP lat–latitude of the virtual geomagnetic pole; Class–orientation and statistical data listed for class I, II, III, and IV sites; class V values not determined (nd); Lith–texture: mudstone (ms), sandstone (ss); Bedding–left-hand rule of azimuth/dip, in degrees.

Table B7. Summary of site results for stratigraphic-composite section TA2-TA4.

Site	Unit	Z* (m)	N/No	R	k	$\alpha 95$ (°)	Geo. Dec (°)	Geo. Inc (°)	Strat. Dec (°)	Srat. Inc (°)	VGP lat (°)	Class	Lith	Bedding
T09	QTsa	16.7	9/9	8.71	27.7	10.0	13.2	61.4	13.2	61.4	77.3	I	ss	horiz.
T10	QTsa	17.6	1/8	nd	nd	nd	33.8	36.9	33.8	36.9	nd	IV	ss	horiz.
T18	QTsa	18.8	0/8	nd	nd	nd	nd	nd	nd	nd	nd	V	ss	horiz.
T19	QTsa	21.2	4/8	3.93	44.6	13.9	175.1	-39.8	175.1	-39.8	-76.9	I	ss	horiz.
T11	QTsa	23.2	7/7	6.85	38.9	9.8	184.0	-35.5	184.0	-35.5	-74.2	I	ss	horiz.
T12	QTsa	24.8	0/4	nd	nd	nd	nd	nd	nd	nd	nd	V	ss	horiz.
T13	QTsa	25.6	5/5	4.98	226.7	5.1	174.1	-51.6	174.1	-51.6	-84.4	I	ash	horiz.
T14	QTsa	26.4	0/6	nd	nd	nd	nd	nd	nd	nd	nd	V	ms	horiz.
T20	QTsa	28.5	9/9	8.57	18.8	12.2	157.8	-47.8	157.8	-47.8	-70.2	I	ms	horiz.
T21	QTsa	35.0	5/9	2.39	1.5	77.7	306.0	30.6	306.0	30.6	38.6	V	ms	horiz.
T22	QTsa	35.0	0/9	nd	nd	nd	nd	nd	nd	nd	nd	V	ss	horiz.
T15	QTsa	36.4	0/6	nd	nd	nd	nd	nd	nd	nd	nd	V	ms	horiz.
T23p	QTsa	37.6	9/10	8.99	994.3	1.6	158.5	-44.3	158.5	-44.3	-69.5	I	ss	horiz.
T16	QTsa	38.0	0/1	nd	nd	nd	nd	nd	nd	nd	nd	V	ss	horiz.
T17	QTsa	40.0	0/4	nd	nd	nd	nd	nd	nd	nd	nd	V	ss	horiz.
T22	QTsa	41.0	0/9	nd	nd	nd	nd	nd	nd	nd	nd	V	ss	horiz.
T01	QTsp	42.4	7/7	6.70	19.8	13.9	65.4	42.4	65.4	42.4	33.3	I	ss	horiz.
T02	QTsp	44.0	0/7	nd	nd	nd	nd	nd	nd	nd	nd	V	ss	horiz.
T03	QTsp	45.2	4/6	3.80	14.7	24.8	2.8	36.0	2.8	36.0	74.7	II	ss	horiz.
T04	QTsp	46.0	5/6	4.94	67.8	9.4	6.3	57.7	6.3	57.7	84.0	I	ss	horiz.
T05	QTsp	49.0	3/5	2.83	11.9	37.4	167.7	52.5	167.7	52.5	-21.0	II	ms	horiz.
T06	QTsp	50.0	0/6	nd	nd	nd	nd	nd	nd	nd	nd	V	ss	horiz.

Notes: Top of TA2-TA3-TA4 composite section is 35.010°N, 106.596°W at TA4; Unit– Geologic unit; Z–height from base of measured section, in meters; N/No–number of sites accepted (N) and total number of sites (No); R–Fisher statistic; k–precision parameter; $\alpha 95$ –cone of confidence; Dec–declination; Inc–inclination. Geographic (Geo) and tilt-corrected (Strat) declination and inclinations shown; VGP lat–latitude of the virtual geomagnetic pole; Class–orientation and statistical data listed for class I, II, III, and IV sites; class V values not determined (nd); Lith–texture: mudstone (ms), sandstone (ss), volcanic ash (ash); Bedding–left-hand rule of azimuth/dip, in degrees.

Table B8. Summary of site results for stratigraphic section ZF.

Site	Unit	Z (m)	N/No	R	<i>k</i>	$\alpha 95$ (°)	Geo. Dec (°)	Geo. Inc (°)	Strat. Dec (°)	Srat. Inc (°)	VGP lat (°)	Class	Lith	Bedding
ZF01	Tc	18.8	4/6	3.91	34.6	15.8	15.6	38.5	17.9	39.1	70.0	I	ss	030/03
ZF02	Tc	27.8	3/5	2.86	14.0	34.2	81.2	74.4	87.0	72.0	29.9	II	ss	030/03
ZF03	Tc	28.3	0/7	nd	nd	nd	nd	nd	nd	nd	nd	V	ss	030/02
ZF04	Tc	30.4	6/7	5.86	35.2	11.5	227.5	-51.3	231.0	-50.3	-47.4	I	ash	030/03
ZF05	Tc	32.2	6/6	5.91	55.8	9.0	134.5	-74.6	137.8	-77.5	-50.0	I	ms	030/03
ZF06	Tc	33.8	3/6	2.94	31.8	22.2	175.7	-23.8	176.9	-25.4	-68.7	II	ms	030/03

Notes: Top of Zia fault (ZF) composite section is 35.403°N, 106.761°W; Unit– Geologic unit; Z–height from base of measured section, in meters; N/No–number of sites accepted (N) and total number of sites (No); R–Fisher statistic; *k*–precision parameter; $\alpha 95$ –cone of confidence; Dec–declination; Inc–inclination. Geographic (Geo) and tilt-corrected (Strat) declination and inclinations shown; VGP lat–latitude of the virtual geomagnetic pole; Class–orientation and statistical data listed for class I, II, III, and IV sites; class V values not determined (nd); Lith–texture: mudstone (ms), sandstone (ss), volcanic ash (ash); Bedding–left-hand rule of azimuth/dip, in degrees.

Appendix C. Supplemental Data

Supplemental data for stratigraphic sections measured for the Ceja Formation
(Tables C1 & C2) at El Rincón, CDRP-CL, and Los Lunas volcano (LLVN & LLVS).

Table C1. Largest gravel sizes in the Ceja Formation.

Stratigraphic section sample number	Map unit	Dist. from top of section (m)	No.	Mean max. width $\pm 1\sigma$ (cm)	Mean intermediate width $\pm 1\sigma$ (cm)
ER19	Tca	64	12	8.8 \pm 1.5	4.5 \pm 1.7
ER27	Tca	56	14	8.5 \pm 1.9	5.8 \pm 1.4
ER35	Tca	48	10	1.6 \pm 0.7	0.8 \pm 0.3
ER46 & CDRP- CL49 & ER50	Tca	34	31	7.9 \pm 2.7	5.2 \pm 1.9
ER57	Tca	26	10	16.8 \pm 4.1	11.4 \pm 3.1
CDRP-CL57 & SGN18	Tcrp	24	22	22.2 \pm 8.7	15.7 \pm 6.6
CDRP-CL62	Tcrp	20	12	27.3 \pm 10.0	20 \pm 6.2
ER87	Tcrp	6	10	17.3 \pm 5.8	11.8 \pm 3.6
Top of Ceja Fm	Tcrp	<1	1	1100	nd

Notes: Largest gravel sizes encountered along a bedding parallel transect of 30 m. Distance from top of section refers to depth below the Llano de Albuquerque surface. No. refers to number of clasts measured. Mean max. and intermediate width refers to the arithmetic mean of the maximum and intermediate dimensions of the measured clasts (nd = not determined).

Stratigraphic sections include the type section of the Ceja Formation at El Rincón (ER, Connell, 2008a), and at CDRP-CL (Bernalillo-Sandoval County Line section); SGN (Shooting Gallery, north) refers to deposits along the Ceja del Rio Puerco, about 1.5 km north of CDRP-CL. The Ceja Formation (Tc) includes the Atrisco (Tc) and Rio Puerco (Tcrp) Members (Connell, 2008a).

Table C2. Proportions of muddy, sandy, and gravelly beds estimated in measured stratigraphic sections in the Ceja Formation).

Stratigraphic section	Map unit	Unit thickness (m)	Muddy beds (%)	Sandy beds (%)	Gravelly beds (%)
ER	Tc	84	9	56	35
ER	Tca	50	13	69	18
ER	Tcrp	33	2	37	61
CDCRP-CL	Tc	57	19	60	24
CDCRP-CL	Tca	37	25	73	3
CDCRP-CL	Tcrp	20	19	60	24
CDRP3	Tc	52	26	55	20
CDRP3	Tca	27	46	50	4
CDRP3	Tcrp	24	2	60	37
LLVN	Tc	170	14	68	18
LLVN	Tca	132	17	71	13
LLVN	Tcrp	39	6	59	35
LLVS	Tc	24	15	84	1
Combined	Tca	---	17	64	19
Combined	Tcrp	---	3	49	48

Notes: Stratigraphic sections include the type section of the Ceja Formation at El Rincón (ER, Connell, 2008a), CDRP-CL (Bernalillo-Sandoval County Line section), and Los Lunas volcano (LLVS & LLVN). The Ceja Formation (Tc) includes the Atrisco (Tc) and Rio Puerco (Tcrp) Members (Connell, 2008a). Combined refers to mean proportions of deposit texture in these measured sections.